DNA 5280F

FUEL-AIR EXPLOSIVE SIMULATION OF FAR-FIELD NUCLEAR AIRBLASTS

T. H. Pierce
R. T. Sedgwick
S-CUBED
P.O. Box 1620
La Jolla, California 92038

31 December 1979

Final Report for Period 9 May 1977—31 December 1979

CONTRACT No. DNA 001-77-C-0251

APPROVED FOR PUBLIC RELEASE;
DISTRIBUTION UNLIMITED.

THIS WORK WAS SPONSORED BY THE DEFENSE NUCLEAR AGENCY
UNDER RDT&E RMSS CODE B344078464 Y99QAXSD07034 H2590D.

Prepared for
Director
DEFENSE NUCLEAR AGENCY
Washington, DC 20305

Destroy this report when it is no longer needed. Do not return to sender.

PLEASE NOTIFY THE DEFENSE NUCLEAR AGENCY, ATTN: STTI, WASHINGTON, D.C. 20305, IF YOUR ADDRESS IS INCORRECT, IF YOU WISH TO BE DELETED FROM THE DISTRIBUTION LIST, OR IF THE ADDRESSEE IS NO LONGER EMPLOYED BY YOUR ORGANIZATION.

UNCLASSIFIED

SECURITY CLASSIFICATION OF THIS PAGE (When Data Entered)

REPORT DOCUMENTATION PAGE		READ INSTRUCTIONS BEFORE COMPLETING FORM
1. REPORT NUMBER DNA 5280F	2. GOVT ACCESSION NO. AD-A135042	3. RECIPIENT'S CATALOG NUMBER
4. TITLE (and Subtitle) FUEL-AIR EXPLOSIVE SIMULATION OF FAR-FIELD NUCLEAR AIRBLASTS		5. TYPE OF REPORT & PERIOD COVERED Final Report for Period 9 May 77—31 Dec 79 6. PERFORMING ORG. REPORT NUMBER SSS-R-80-4366
7. AUTHOR(s) T. H. Pierce R. T. Sedgwick		8. CONTRACT OR GRANT NUMBER(s) DNA 001-77-C-0251
9. PERFORMING ORGANIZATION NAME AND ADDRESS S-CUBED P.O. Box 1620 La Jolla, California 92038		10. PROGRAM ELEMENT, PROJECT, TASK AREA & WORK UNIT NUMBERS Subtask Y99QAXSD070-34
11. CONTROLLING OFFICE NAME AND ADDRESS Director Defense Nuclear Agency Washington, DC 20305		12. REPORT DATE 31 December 1979 13. NUMBER OF PAGES 242
14. MONITORING AGENCY NAME & ADDRESS(if different from Controlling Office)		15. SECURITY CLASS. (of this report) UNCLASSIFIED 15a. DECLASSIFICATION/DOWNGRADING SCHEDULE N/A since UNCLASSIFIED

16. DISTRIBUTION STATEMENT (of this Report)

Approved for Public Release; Distribution Unlimited

17. DISTRIBUTION STATEMENT (of the abstract entered in Block 20, if different from Report)

18. SUPPLEMENTARY NOTES

This work was sponsored by the Defense Nuclear Agency under RDT&E RMSS Code B344078464 Y99QAXSD07034 H2590D.

19. KEY WORDS (Continue on reverse side if necessary and identify by block number)

Fuel-Air Explosive	Turbulent Jet
Airblast Simulation	Jet Breakup
Blastwave	Fuel Injection
Nuclear Explosion	Detonation
Fuel Dispersion	

20. ABSTRACT (Continue on reverse side if necessary and identify by block number)

Fuel-air explosions (FAE) have been investigated in the context of far-field nuclear airblast simulation. The objective of the investigation is to determine the feasibility of a reusable FAE simulator at the one kiloton level. Two issues have been researched in parallel efforts. These are the mechanisms by which largescale FAE clouds of controlled shape can be reliably and repeatedly formed and detonated, and the quality

DD FORM 1 JAN 73 1473 EDITION OF 1 NOV 65 IS OBSOLETE

UNCLASSIFIED

SECURITY CLASSIFICATION OF THIS PAGE (When Data Entered)

20. ABSTRACT (Continued)

of nuclear airblast simulation that is achieved when such FAE clouds are detonated.

The formation of hemispherical clouds by simultaneous, impulsive liquid fuel injection through a large number of radially directed, centrally clustered nozzles is discussed in detail. Specific fuel dispenser designs are considered and use experience with two of these is described. Survey experiments dealing with the atomization and penetration characteristics of large-diameter, impulsively formed single liquid jets are discussed. Small-scale hemispherical cloud formation experiments are also discussed.

A new reusable facility for testing FAE simulation of nuclear airblasts at the 1/4-ton scale is described. Preliminary surface-burst experiments at that scale using propylene oxide and heptane as fuels are discussed. The results from these experiments are scaled and compared with 1 KT nuclear curvefits. The agreement is judged to be reasonable at this scale.

Numerical calculations of the airblast that emerges from a detonated heptane-air cloud have also been carried out. The calculated results are compared with the nuclear curves. The quality of simulation at the 1 KT level is generally good and becomes excellent at ranges corresponding to overpressures below about 70 kPa (10 psi)

SUMMARY

The progress of an experimental and theoretical research program is reported in which simulation of far-field nuclear airblast by means of fuel-air explosions (FAE) is being investigated. The advantages of a full-scale reusable FAE blast simulator include the absence of cratering, ejecta, and significant ground shock, short turn-around times between blastwave experiments, and relatively lower costs per experiment when compared with other means of blast simulation. The existence of such a simulator should greatly enhance the state-of-the-art of blastwave simulation and provide a means for accelerating our knowledge of blastwave-structural interactions.

The present investigation has focused specifically on explosions of hemispherical fuel-air clouds formed from a point source, using multiple-nozzle liquid fuel injection. The research involves two areas. First is an assessment of the degree of correspondence between FAE and nuclear airblasts in terms of peak and time-resolved static and stagnation pressures, static impulse, positive-phase duration, and wave-front decay rates. A small-scale instrumented FAE facility (cloud diameter ~9 m (30 ft)) has been developed for this purpose. The second research area involves examining the engineering requirements for scale-up of this facility to a one kiloton nuclear equivalent. In particular, impulsive liquid fuel injection has been investigated with nozles ranging from 2 to 10 cm (0.75-4 in.) in diameter. The ultimate vertical reach, degree of atomization, fuel-air distribution, and transverse spreading rate of the jets are considered to be the basic dependent variables, with initial jet velocity, nozzle diameter, nozzle length, quantity of fuel dispensed per nozzle, and fuel properties (density, viscosity, surface tension, and vapor pressure) taken as independent variables. Current estimates indicate that a one kiloton FAE simulation using propylene oxide would require a hemispherical cloud 142 m (466 ft) in

diameter if the global fuel-air ratio were stoichiometric. The individual nozzles that would be required to form such a cloud must therefore be capable of injection to 71 m (233 ft).

The small-scale experimental facility consists of a concrete test pad with continuous runways connecting inlaid instrumentation modules. Instrumentation consists of stagnation and static piezo-electric pressure transducers as well as high-speed photography. Test sequencing is controlled electronically. Two impulsive fuel dispensers have been built. In one of these, high-pressure gas (such as compressed air or nitrogen) is discharged through a sonic orifice to drive a piston which forces fuel through the nozzle(s). In the other, the piston is driven by a gas generator.

Observations of large-diameter, impulsively injected single liquid jets have indicated that several breakup mechanisms may simultaneously be operative. Breakup at the head of the jet appears to result from a recurring instability. This might be a Taylor acceleration instability. Breakup along the sides of the jet also occurs and may result from shear layer stripping or from a Helmholtz instability. Due to internal turbulent motion the jet ceases to possess a contiguous core above some height. The end or tail of the jet breaks up in what appears to be a response to periodic vortex shedding. Material removed from the jet as droplets or strands presumably undergoes successive aerodynamic shattering and subsequent vaporization. By these combined mechanisms fuel vapor is added to the air along the entire jet trajectory. Tail breakup appears to limit jet reach if insufficient fuel is dispensed through the nozzle.

Small-scale FAE clouds have been formed by injection of fuel through a large number (600-1400) of radially-directed nozzles. Visually uniform spray distributions have been

achieved; however, interactions between the expanding spray cloud and the air can lead to shape distortions if the injection velocity is too high.

The small-scale experiments with detonated fuel-air clouds are believed to exhibit reasonable nuclear/FAE airblast fidelity. Experiments in this area are continuing with the recently upgraded hardware and instrumentation. The experimentally-determined effective blastwave energy of the FAE, with respect to a scaled 1 KT nuclear explosion, is on the order of 40-75% of the constant-pressure heat of the combustion depending on the fuel used and the way in which the FAE cloud is formed. A theoretical calculation of the airblast emerging from a heptane FAE has indicated that under ideal conditions the higher values could be anticipated. Experiments have shown that the FAE airblast characteristics are repeatable and azimuthally symmetrical. The quality of the nuclear airblast simulation was found to improve with range in both the experimental and the theoretical work.

TABLE OF CONTENTS

Section		Page
SUMMARY		1
1	INTRODUCTION	15
2	FUEL DISPENSING SYSTEM	19
	2.1 U-Tube Dispenser	22
	2.2 Linear Dispenser	28
3	TURBULENT LIQUID JETS	39
	3.1 Steady-State Jets	40
	3.2 Impulsive Jets	51
4	HEMISPHERICAL FUEL-AIR CLOUD FORMATION	71
	4.1 Cloud Size Requirements	71
	4.2 Fuel Distribution Uniformity	76
	4.3 Cloud Formation from Multiple Jets	80
	4.4 Experimental Investigations	82
	4.5 Dispenser Scaleup Requirements	90
5	FAE SIMULATION OF FAR-FIELD NUCLEAR AIRBLAST.	101
	5.1 Characteristics of Nuclear Airblast in the Far-Field	101
	5.2 Experimental Investigations	110
	5.3 Theoretical Investigations	148
6	CONCLUDING REMARKS	197
7	REFERENCES	203
APPENDIX		
A	EXPERIMENTAL FACILITY	209
	A.1 Test Pad	209

TABLE OF CONTENTS (continued)

Section		Page
	A.2 Control and Instruments	216
	A.3 Photography	218
APPENDIX		
B	LINEAR DISPENSER GAS GENERATOR	221

LIST OF ILLUSTRATIONS

Figure		Page
1	Fuel dispenser design options	20
2	Schematic diagram showing the U-tube used in the experimental investigation for disseminating fuel to form hemispherical fuel-air explosive clouds	23
3	Schematic of linear fuel dispenser	29
4	Photograph of linear fuel dispenser	30
5	Nozzle inlet pressure as a function of time during operation of U-tube fuel dispenser . .	34
6	Nozzle inlet pressure as a function of time during operation of linear fuel dispenser . .	36
7	Water jet breakup classification according to Ohnsorge	41
8	Sketch of five-nozzle head used in quasi-steady small diameter jet experiments	48
9	Jet reach vs. nozzle pressure drop and jet velocity, small diameter jets	49
10	Ultimate jet reach versus nozzle diameter . .	50

LIST OF ILLUSTRATIONS (continued)

Figure		Page
11	Exaggerated schematic representation illustrating features of impulsively injected liquid jets	54
12	Head and surface breakup	55
13	Tail breakup	56
14	Early jet spreading	57
15	Jet spreading at later times	58
16	Estimated minimum dispensed liquid volume versus nozzle diameter	63
17	Ultimate jet reach vs. fuel quantity dispensed	64
18	Average jet width vs. time for propylene oxide jet from 1.91 cm diameter nozzle . . .	65
19	Comparison of water and propylene oxide stream height from two experiments involving projection from a 3.81 cm diameter nozzle at initial velocities of 72 m/s	66
20	Comparison of stream height as a function of time for two experiments involving the projection of propylene oxide from a 3.81 cm diameter nozzle	67
21	Ultimate jet reach versus pressure drop and velocity for heptane, 1.27 cm diameter nozzle	70
22	Photograph of 1400-nozzle head used with linear dispenser to produce hemispherical fuel-air clouds	84
23	Examples of clouds formed with 600-nozzle dispenser head	85
24	Cloud formed with 1400-nozzle dispenser head.	86

LIST OF ILLUSTRATIONS (continued)

Figure		Page
25	Distortions of expanding point-source spray clouds induced by aerodynamic interactions between spray and air	88
26	Schematic flow diagram of simulator design code	92
27	Semi-smoothed surface burst nuclear data and fully smoothed nuclear form curve	102
28	Semi-smoothed surface burst nuclear data and fully smoothed nuclear form curve	103
29	Nuclear surface burst reference curve for peak overpressure versus range	105
30	Nuclear surface burst reference curve for positive-phase static overpressure impulse versus range	106
31	Nuclear surface reference curve for static overpressure positive-phase duration versus range	107
32	Nuclear surface burst reference curve for peak dynamic pressure versus range	108
33	Schematic flow diagram of data reduction program	112
34	Comparison of measured overpressure as a function of time with a nuclear blast waveform (test 2536)	118
35	Comparison of measured overpressure as a function of time with a nuclear blast waveform (test 2536)	119
36	Comparison of measured overpressure as a function of time with a nuclear blast waveform (test 2536)	120
37	Comparison of measured overpressure as a function of time with a nuclear blast waveform (test 2536)	121

LIST OF ILLUSTRATIONS (continued)

Figure		Page
38	Comparison of measured positive phase impulse with nuclear data (test 2536)	122
39	Comparison of measured positive phase impulse with nuclear data (test 2536)	123
40	Comparison of measured positive phase impulse with nuclear data (test 2536)	124
41	Comparison of measured positive phase impulse with nuclear data (test 2536)	125
42	Plot of measured stagnation overpressure as a function of time at the 12.2 m station from three separate experiments	126
43	Plot of measured static overpressure as a function of time at the 24.4 m station from three separate experiments	127
44	Plot of measured static overpressure as a function of time from a single experiment (test 2571)	128
45	Plot of measured static overpressure as a function of time taken from a single experiment (test 2574)	129
46	Peak static pressure versus range for hemispherical and spherical blastwaves	130
47	Positive-phase static overpressure impulse versus range	131
48	Raw and semi-smoothed static pressure data from FAE test CD-6 at R = 13.9 m, transducer position no. 4	134
49	Characteristic explosion length versus range for test CD-6	135
50	Peak static overpressure versus range for test CD-6	136
51	Peak static overpressure impulse versus range for test CD-6	137

LIST OF ILLUSTRATIONS (continued)

Figure		Page
52	Static overpressure positive phase duration versus range for test CD-6	138
53	Peak dynamic pressure versus range for test CD-6	139
54	Static overpressure versus time during test CD-6 at R/R_o = 0.782, transducer position no. 2	140
55	Static overpressure versus time during test CD-6 at R/R_o = 1.31, transducer position no. 3	141
56	Static overpressure versus time during test CD-6 at R/R_o = 1.84, transducer position no. 4	142
57	Static overpressure versus time during test CD-6 at R/R_o = 2.51, transducer position no. 5	143
58	Static overpressure versus time during test CD-6 at R/R_o = 3.17, transducer position no. 6	144
59	Static overpressure versus time during test CD-6 at R/R_o = 3.97, transducer position no. 7	145
60	Dynamic pressure versus time during test CD-6 at R/R_o = 1.31, transducer position no. 3	146
61	Dynamic pressure versus time during test CD-6 at R/R_o = 2.51, transducer location no. 5	147
62	Unconfined detonation velocity versus equivalence ratio in two-phase propylene oxide and heptane fuel-air mixtures	151
63	Particle velocity behind unconfined two-phase heptane and propylene oxide detonations in air	152

LIST OF ILLUSTRATIONS (continued)

Figure		Page
64	Absolute static pressure behind unconfined two-phase heptane and propylene-oxide detonations in air	153
65	Density behind unconfined two-phase heptane and propylene oxide detonations in air . . .	154
66	Product mixture specific-heats ratio behind unconfined two-phase heptane and propylene oxide detonations in air	155
67	Product mixture molecular weight behind unconfined two-phase heptane and propylene oxide detonations in air	156
68	Self-similar absolute static pressure profile within expansion wave behind stoichiometric, two-phase heptane-air detonation	161
69	Self-similar density profile in expansion wave behind stoichiometric, unconfined, two-phase heptane-air detonation	162
70	Self-similar absolute velocity profile in expansion wave behind stoichiometric, unconfined, two-phase heptane-air detonation.	163
71	Calculated static overpressure profile within FAE airblast at fixed times	167
72	Calculated static overpressure profiles within FAE airblast at fixed times	168
73	Calculated static overpressure versus time at fixed range from hemispherical FAE airblast	169
74	Calculated static overpressure versus time at fixed range from hemispherical FAE airblast	170
75	Calculated static overpressure versus time at fixed range from hemispherical FAE airblast	171
76	Calculated static overpressure versus time at fixed range from FAE airblast	172

LIST OF ILLUSTRATIONS (continued)

Figure		Page
77	Calculated static overpressure versus time at fixed range from hemispherical FAE air blast	173
78	Calculated static overpressure versus time at fixed range from FAE airblast	174
79	Trajectory of interface between combustion products and air in terms of time after detonation reaches cloud boundary	175
80	Inferred characteristic blastwave radius in hemispherical geometry for experimental scale stoichiometric heptane-air FAE	177
81	Calculated peak static overpressure from FAE versus range, compared against nuclear reference curve	178
82	Calculated positive-phase static overpressure impulse from FAE versus range, compared against nuclear reference curve	179
83	Calculated peak dynamic pressure from FAE versus range, compared with nuclear reference curve	180
84	Calculated static overpressure positive-phase duration versus range from FAE, compared with nuclear reference curve	181
85	Calculated heptane-air FAE static overpressure versus time after shock arrival compared with nuclear reference curve, at R/R_o = 0.603	182
86	Calculated heptane-air FAE static overpressure versus time after shock arrival compared with nuclear reference curve, at R/R_o = 1.01	183
87	Calculated heptane-air FAE static overpressure versus time after shock arrival compared with nuclear reference curve, at R/R_o = 1.42	184

LIST OF ILLUSTRATIONS (continued)

Figure		Page
88	Calculated heptane-air static overpressure versus time after shock arrival compared with nuclear reference curve, at R/R_o = 1.93	185
89	Calculated heptane-air side-on overpressure versus time after shock arrival compared with nuclear reference curve, at R/R_o = 2.43	186
90	Calculated heptane-air static overpressure versus time after shock arrival compared with nuclear reference curve, at R/R_o = 3.04	187
91	Calculated heptane-air dynamic pressure versus time after shock arrival compared with nuclear reference curve, at R/R_o = 0.603	188
92	Calculated heptane-air dynamic pressure versus time after shock arrival compared with nuclear reference curve, at R/R_o = 1.01	189
93	Calculated heptane-air dynamic pressure versus time after shock arrival compared with nuclear reference curve, at R/R_o = 1.42	190
94	Calculated heptane-air dynamic pressure versus time after shock arrival compared with nuclear reference curve, at R/R_o = 1.93	191
95	Calculated heptane-air dynamic pressure versus time after shock arrival compared with nuclear reference curve, at R/R_o = 2.43	192
96	Calculated heptane-air dynamic pressure versus time after shock arrival compared with nuclear reference curve, at R/R_o = 3.04	193
A-1	Plan view of concrete FAE test pad showing instrumentation trough locations	211

LIST OF ILLUSTRATIONS (continued)

Figure		Page
A-2	Photograph of FAE test pad	212
A-3	Cross-sectional view of instrumentation trough	213
A-4	Photograph of stagnation pressure sting mounted in instrumentation trough	214
A-5	Photograph of FAE control console	217
B-1	Sketch of linear fuel dispenser gas generator.	222
B-2	Photograph of gas generator used with linear fuel dispenser	223
B-3	Burning velocity of Red Dot smokeless powder .	224
B-4	Cross-sectional view of gas generator igniter.	225
B-5	Loss-free theoretical pressure developed in free volume tank after gas generator blowdown.	230
B-6	Required gas generator orifice as a function of free volume and pressure in the free volume, for 20 ms blowdown time	234

SECTION 1

INTRODUCTION

There exists an ongoing defense requirement to assess the response of various objects to airblast loading resulting from nuclear explosions. Since the 1963 ban on above-ground nuclear weapons testing, it has been necessary to conduct such experiments by simulated means. For far-field airblast simulation of surface bursts, the predominant technique has been the use of high explosives. Ground-plane hemispheres and surface-tangent spheres constructed of stacked high-explosives have been detonated for this purpose. This technique has the advantage of being relatively straightforward, and the quality of airblast simulation obtained is reasonably satisfactory at overpressure levels below about 1 MPa (150 psi).

Unfortunately, inexpensive surplus TNT has become very scarce. As of March 1979 an estimate of the bulk cost of TNT was about 2.75 $/kg (1.25 $/lbm). Since approximately 4.54×10^5 kg (10^6 lbm) of TNT are required for a 1 KT nuclear simulation, a program of frequent simulated testing at this energy-release level would be prohibitively expensive.

In addition to cost, high explosive (HE) simulation has other drawbacks. A substantial crater is formed at the explosion center during a test. For subsequent testing this necessitates either relocation of all instrumentation to a new test area, or considerable earthmoving to refill the crater. Either operation is time-consuming and costly. Furthermore, high explosives generate a ground shock which in the far-field is not representative of a nuclear ground shock. The ground shock therefore tends to interfere with experiments intended to test solely for airblast-loading. Finally, a substantial amount of high velocity debris and ejecta accompanies HE detonations. Impingement of these materials upon test objects is clearly undesirable.

For these reasons, concepts for alternate simulated far-field airblast sources have been explored. In particular, attention has recently focused on the use of fuel-air explosions for this purpose (References 1-9). A fuel-air explosion results from fast combustion of a cloud comprising fuel that has been dispersed into atmospheric air. The event includes both the combustion process within the cloud itself and the cumulative subsequent interactions with the ambient air.

Two modes of FAE cloud combustion are possible. Deflagration alone will occur if the cloud is not too large and if it is initiated with a low energy blast source or a thermal ignition source (such as a flame). Detonation will occur if the cloud is initiated by a blastwave or other shock source of sufficient strength and duration. The explosions that result from these two modes possess similar characteristics in the extreme far-field ($\lesssim$7000 Pa (1 psig)) but they are very different at higher overpressures. The highest overpressure attained by a deflagrative explosion is a function of the deflagration velocity and is in general significantly less than that generated by a detonative explosion. Since it is desirable to extend the blast simulation to the highest pressure levels possible, only detonative explosions are of present interest.

The characteristic size of the fuel-air cloud that would be required to simulate a 1 KT nuclear airblast is exemplified by estimates assuming propylene oxide as the fuel. In this case at stoichiometric proportions the cloud volume would be 7.50×10^5 m^3 (2.65×10^7 ft^3) and would contain 85,400 kg (188,000 lbm) of fuel. For a hemispherically shaped cloud, the diameter would be 142 m (466 ft).

Two fundamental issues are being addressed by the present research program. The first involves the determination of a satisfactory means by which a cloud having the required

dimensions can be formed. The second involves the determination of the degree of correspondence, or fidelity, between FAE and far-field nuclear airblasts.

For tests requiring peak overpressure levels above about 7 kPa (11 psi), it has been considered preferable to form hemispherically-shaped clouds. A hemispherical FAE is theoretically the most efficient shape (Reference 10). Its symmetry assures the minimum number of undesirable secondary waves (due to reflections), and allows predictable testing in all directions at the highest overpressure levels possible.

Several techniques for forming hemispherical FAE clouds have been suggested. These include balloon containment, explosive fuel dissemination from an array of canisters, rockets propelled by the fuel that is to be dispersed, and large-scale hydraulic fuel injection.

Of these techniques, hydraulic fuel injection appears at present to be the most viable. Liquid fuel is impulsively injected into the atmosphere at high velocity through a large number of nozzles. Each liquid jet is atomized hydraulically, that is, without induced swirl or coaxial air injection. The spray columns from these many jets overlap to fill in the cloud. The jets can be injected either radially from a central (point) source or vertically from distributed ground positions. The former seems preferable, because the reach required of each jet would be the same and because the amount of plumbing would be minimized due to the smaller ground area covered by the dispensing system.

With this technique, the cost of materials expended per test would be minimized. No above-ground structure is required, and potentially harmful debris is not produced. On the other hand, such a technique has not been previously developed. Investigation has been required to determine

whether or not it is in fact possible to impulsively generate jets with the necessary reach, degree of atomization, and fuel distribution. The technology needed to impulsively inject a large number of such jets simultaneously has also required development. The technique has, however, been shown to be feasible in preliminary small-scale experiments (References 2-5) and is discussed in detail in this report.

Regardless of the specific technique chosen for fuel air cloud formation, the quality of the simulated far-field nuclear airblast is of fundamental concern. In particular, the correspondence between the positive-phase static and dynamic pressure profiles as functions both of radius and time needs to be evaluated in terms of peak pressures, positive phase durations, impulse, and the extent of secondary shocks and other aberrations in the pressure-time profiles. Blastwave symmetry and repeatability are also of importance. The results of investigations in these areas are discussed in this report.

The report is structured as follows. First, experimental fuel dispensing systems that have been considered and those that have been tested at small scale are described in Section 2. In Section 3 the experimentally observed atomization characteristics of liquid jets are discussed, while Section 4 deals with the formation of hemispherical clouds using a large number of such jets. In Section 5 the results of theoretical and experimental investigations of nuclear airblast simulation by fuel-air explosions are discussed. A concluding discussion is provided in Section 6.

SECTION 2

FUEL DISPENSING SYSTEM

Point-source fuel dissemination requires a dispensing system capable of impulsively forming a large number of radially-directed jets simultaneously. The specific requirements for such a dispenser are closely coupled to the dynamics of breakup of individual liquid jets. (Jet breakup is the subject of Section 3.) However, since an impulsive dispenser is required to investigate jet breakup, development of the dispenser has been iterative. In this section dispenser hardware concepts are described generally and experience with two specific designs is discussed.

Several concepts have been considered and schematic sketches of them are shown in Figure 1. The first of these, which appears to be the least complex, operates on a principle similar to that of a common aerosol dispenser. A gas generator raises the pressure above a liquid supply which is then ejected through a dip tube. The gas generator is located at the top of the dispenser to facilitate reloading. This design (Figure 1(a)) had been previously suggested as a candidate system (Reference 5).

There are three problem areas with this design. First, it is questionable whether the liquid in the dispenser tank can be fully ejected. After the liquid level drops below the bottom of the dip tube the liquid column remaining in the tube would be unstable. Secondly, even if this last fluid were to be dispensed smoothly, subsequent gas ejection through the nozzles would disturb the spray. This would be detrimental to the formation of a predictable spray pattern. Finally, the hot products from the gas generator might ignite the fuel inside the dispenser, or these gases could ignite the spray cloud as they issue from the nozzle.

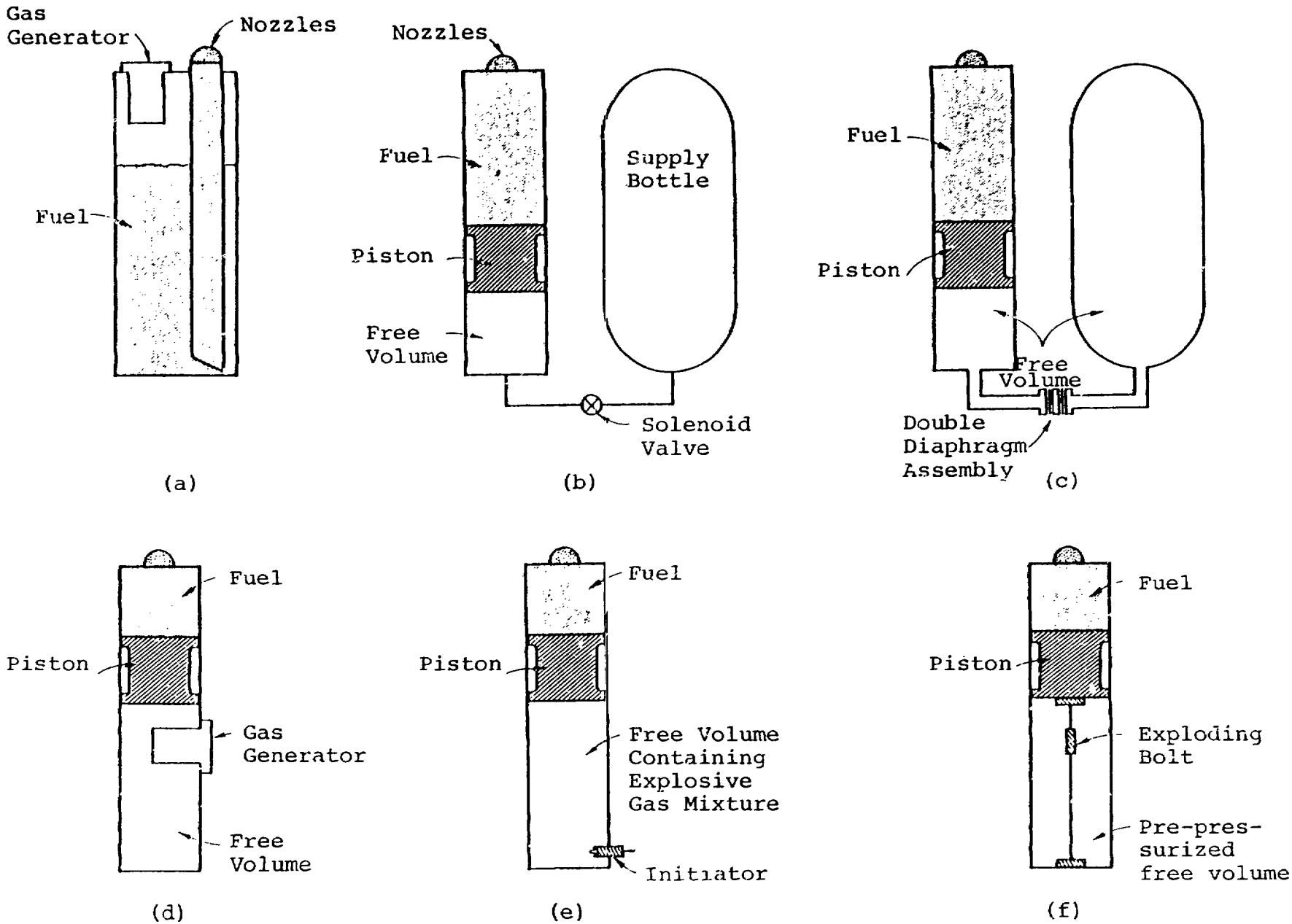

Figure 1. Fuel dispenser design options.

All of the remaining dispenser concepts in Figure 1 incorporate an interface between the propelling gas and the fuel. This avoids the potential problems of the aerosol dispenser design. The first of these concepts is illustrated in Figure 1(b). A piston driven by gas that is admitted through a solenoid valve into a free volume behind it forces fuel through the nozzles(s). The valve acts as a choked (sonic) orifice, limiting the gas flow rate from a high pressure supply bottle. In this design the valve opening time also limits the rate of initial piston acceleration. This can be problematic if the acceleration time is comparable to the total fuel dispensing time. Also, rather high supply bottle pressures are required to achieve useful working pressures behind the piston. This design might be improved by incorporating a fast-acting double-diaphragm type of valve, such as that used in shock tubes. A sketch of this alternate arrangement is shown in Figure 1(c).

A high pressure supply bottle can be avoided through the use of a gas generator in a configuration such as that shown in Figure 1(a). A propellant grain with variable burn rate might be used so as to tailor the dispensing pressure to any time-varying profile desired.

Another concept involving combustion is shown in Figure 1(e). In this case, however, the free-volume is filled with a combustible gas mixture. Dispensing is initiated by detonating this mixture. The pressure will then decrease due to gas expansion as the piston displaces the fuel. The pressure dropoff rate is governed by the free volume size and by gas properties, but it is not otherwise controllable.

An arrangement that does not involve sudden pressurization by combustion or by means of valving is shown in Figure 1(f). Here the free volume pressure is raised in advance to the appropriate initial level with a suitable gas (at ambient

temperature). The piston is restrained by a cable that can be severed by an explosive device (such as an exploding bolt). As in the preceding device concept, this design permits only a limited amount of control over the pressure dropoff rate. However, high temperature gases are not involved. This would simplify construction and eliminate driver-gas energy losses due to heat transfer.

All of the schemes shown in Figure 1 use gas pressure to force the fuel out of the dispenser. However other, more novel techniques might also be feasible. As examples, the piston could be driven by a rocket motor or perhaps even by a large spring.

Two dispenser concepts (Figures 1(b) and 1(d)) have been examined at a size compatible both with small-scale fuel-air cloud formation experiments and with large scale single-jet reach and breakup experiments.

2.1 U-TUBE DISPENSER

A rudimentary dispenser system was used exclusively during the early phases of the present research program (Reference 5). It is essentially an adaptation of the choked-orifice arrangement of Figure 1(b). A sketch of the dispenser is shown in Figure 2. Because of its shape it has been referred to as the U-tube dispenser. It is 2.75 m (9 ft) long overall, constructed of 15.2 cm (6 in.) schedule 40 wrought steel pipe. The maximum amount of liquid that can be dispensed is about 0.036 m^3 (9.5 gal.). The centerline distance between the two legs is 46 cm (18 in.). The piston shown is 15.2 cm (6 in.) long and is fitted with two teflon seals. High pressure nitrogen is discharged into the free volume through a solenoid valve with a 1.9 cm (0.75 in.)

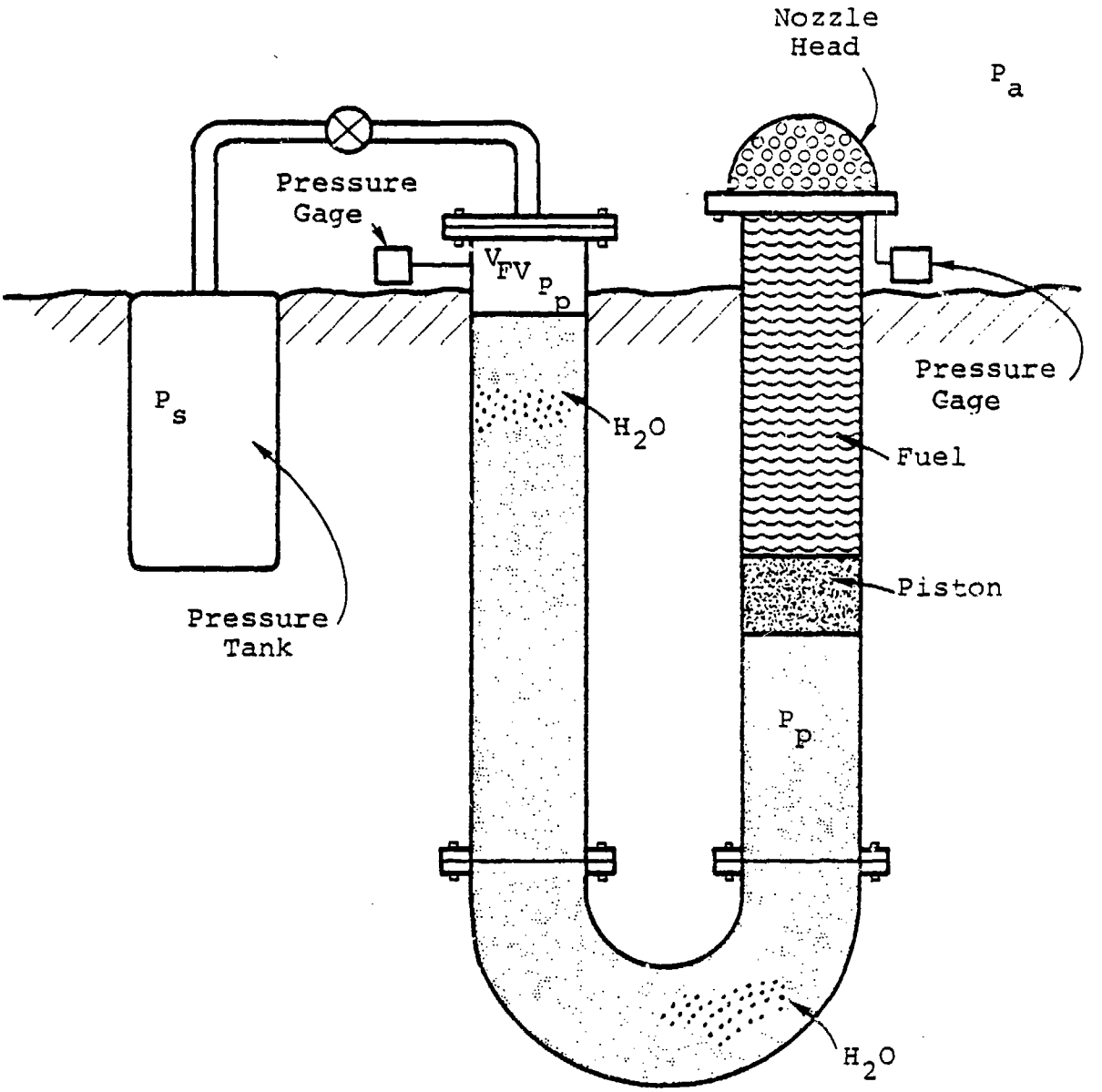

Figure 2. Schematic diagram showing the U-tube used in the experimental investigation for disseminating fuel to form hemispherical fuel-air explosive clouds. One leg of the U-tube was pressurized in order to force the fuel through a nozzle head attached to the other leg of the U-tube.

effective orifice diameter. The nitrogen is supplied from two manifolded cylinders having a total volume of 0.71 m^3 (2.5 ft^3).

In use this dispenser was buried in the ground. The volume behind the piston was filled with water which effectively formed a flexible U-shaped extension of the solid piston. The back side of the extended piston was then accessible from the surface. The amount of water behind the piston could be adjusted so as to permit some control over the initial free volume.

The pressure level required in the supply bottles is much higher than that in the free volume behind the piston. An estimate of the necessary supply pressure was obtained by assuming quasi-steady-state dispensing (constant piston velocity) and ignoring the dropoff in supply bottle pressure. In that case the pressure on both sides of the piston is the same and constant, and the rate of increase in the free volume equals the rate of fuel volume efflux through the nozzle(s). Referring to the notation in Figure 2, this condition can be expressed as

$$\dot{V}_{FV} = \dot{V}_{\ell} \quad , \tag{1}$$

where

$$\dot{V}_{\ell} = \frac{\dot{m}_{\ell}}{\rho_{\ell}} \tag{2}$$

is the volume flow rate of the liquid fuel and m_{ℓ}, ρ_{ℓ} are the fuel mass flow rate and the liquid density respectively. The rate of increase in free volume, $\dot{V}_{FV}$, can be written as

$$\dot{V}_{FV} = \frac{d}{dt}\left(\frac{m\bar{R}T}{P_p W}\right) \quad . \tag{3}$$

Here, the perfect gas law has been used to express the instantaneous free volume magnitude in terms of the mass of gas contained within it, m; the pressure, P_p; molecular weight, W; temperature, T of the gas; and R, the universal gas constant. Equating Eqs. (2) and (3) according to Eq. (1) gives, with P_p and T constant,

$$\frac{\dot{m}_\ell}{\rho_\ell} = \frac{\bar{R}T}{P_p W}\dot{m} \quad , \tag{4}$$

where $\dot{m} = dm/dt$ represents the rate at which gas flows from the supply bottle into the free volume.

Now, if the nozzle area, A_N and the U-tube cross-sectional area, A_u are such that

$$(A_N/A_u)^2 << 1 \quad ,$$

then the liquid mass flow through N such nozzles can be expressed as

$$\dot{m}_\ell = NA_N[2\rho_\ell(P_p - P_A)]^{\frac{1}{2}} \quad , \tag{5}$$

where it has been assumed that the nozzle discharge coefficient is equal to unity. On the other hand, the gas mass flow rate through the orifice (solenoid valve) is given by

$$\dot{m} = A_E P_S \left(\frac{\gamma W}{\bar{R}T}\right)^{\frac{1}{2}} f(M_E) \quad , \tag{6}$$

where A_E is the orifice area and

$$f(M_E) \equiv M_E \left(1 + \frac{\gamma-1}{2} M_E^2\right)^{-\frac{\gamma+1}{2(\gamma-1)}} \quad . \tag{7}$$

The orifice Mach number in Eq. (7) is

$$M_E = \left\{\left(\frac{2}{\gamma-1}\right)\left[\left(\frac{P_s}{P_p}\right)^{\frac{\gamma-1}{\gamma}} - 1\right]\right\}^{\frac{1}{2}} \quad , \tag{8}$$

and γ is the ratio of specific heats of the gas. The maximum value of M_E is unity, corresponding to a critical ratio P_s/P_p that can be calculated from Eq. (8). This is the choking point. At larger ratios of P_s/P_p, achieved by reducing P_p, the mass flow $\dot{m}$ does not increase further.

Combining Eq. (4)-(6) gives

$$P_s = P_p(P_p - P_A)^{\frac{1}{2}} \left(\frac{2W}{\gamma \rho_\ell \bar{R}T}\right)^{\frac{1}{2}} \left(\frac{N A_N}{A_E f(M_E)}\right) \quad . \tag{9}$$

This equation is not in closed form since $f(M_E)$ is a function of P_S. However, at the choking point, $M_E = 1$, and in that case Eq. (9) becomes

$$P_s = P_p(P_p - P_A)^{\frac{1}{2}} \left(\frac{2W}{\gamma \rho_\ell \bar{R}T}\right)^{\frac{1}{2}} \left(\frac{N A_N}{A_E}\right)\left(\frac{\gamma+1}{2}\right)^{\frac{\gamma+1}{2(\gamma-1)}} \quad . \tag{10}$$

For a fixed choked orifice area A_E, Equation (10) indicates that the required supply bottle pressure increases linearly with the liquid nozzle area and with the number of these nozzles. As an example, for a single 7.62 cm (3 in.) diameter nozzle driven at P_P = 1.38 MPa (200 psi), and with P_A = 1 x 10^5 Pa (14.7 psi), W = 28, γ = 1.4, and ρ_ℓ = 1000 kg/m^3 (62.5 lbm/ft^3), the supply bottle pressure required in conjunction with a 1.91 cm (0.75 in.) diameter choked orifice at room temperature would be P_S = 5.47 MPa (658 psi

Higher free volume pressures can be achieved without excessive supply bottle pressure by increasing the solenoid valve orifice area. Larger valves generally have longer opening times, however, and since fuel dispensing times are characteristically in the range 100-500 ms, valve opening times must be kept very short. In the case of the U-tube system, the solenoid valve opening time was estimated to be on the order of 50 ms. Together with the large effective mass of the dispenser piston (including the water) this resulted in rather sluggish behavior during the initial startup period. Transient oscillations were also observed on occasion during startup. Free volume pressures above 1.4 MPa (200 psi) could not be easily obtained when testing large nozzles (or with a large number of small nozzles) because of the unreasonably high supply pressures that would be required according to Eq. (10).

The principal advantage of a choked-orifice driven dispenser is that the free volume pressure does not decrease as rapidly as does the pressure in the supply bottle during the dispensing operation. This can be seen in Eq. (10). A design of this kind with a fast valve (for example, a double diaphragm) and no moving water mass remains open for consideration. However, it is felt at present that the use of a solenoid-actuated or similar valve is not totally satisfactory and that the U-tube configuration is not optimum.

2.2 LINEAR DISPENSER

A dispenser of the type sketched in Figure 1(d) was also designed and built and has been employed in more recent experimental work. A schematic to scale of this device appears in Figure 3 and a photograph is shown in Figure 4. This was originally referred to as the linear dispenser to distinguish it from the earlier U-tube. The piston in this case is driven by pressure developed from a gas generator. Details of the gas generator are given in Appendix B. In addition to testing the gas generator concept, this dispenser was designed to improve performance and reliability over that of the U-tube. Water can be added to the tank below the piston so as to adjust the initial free volume; however the water does not move with the piston. This results in greatly improved inertial start-up response. The piston acceleration time was reduced further by increasing its diameter.

One disadvantage of the linear design is that, unlike the U-tube, the linear dispenser must be removed from the ground in order to change the water level in the free volume tank or to reload the gas generator between runs. In the present installation this effectively constrains the overall dispenser length to about 3 m (10 ft) due to the reach limit of the equipment on hand that is used to r- -e the dispenser. For this reason the linear dispenser capacity was limited to a maximum of 0.0273 m^3 (7.2 gal.) of liquid. This is slightly greater than the quantity of fuel needed for the hemispherical cloud detonation experiments, but it is somewhat less than the capacity of the U-tube.

For design purposes the start-up inertial response of the linear dispenser was analyzed to first order. The gas generator was assumed to develop the initial pressure P_{P_0} in the initial free volume, V_{FV_0}, in negligible time. The mass of fluid in the nozzle was small compared with that of the remaining fluid and the piston mass, and was therefore ignored.

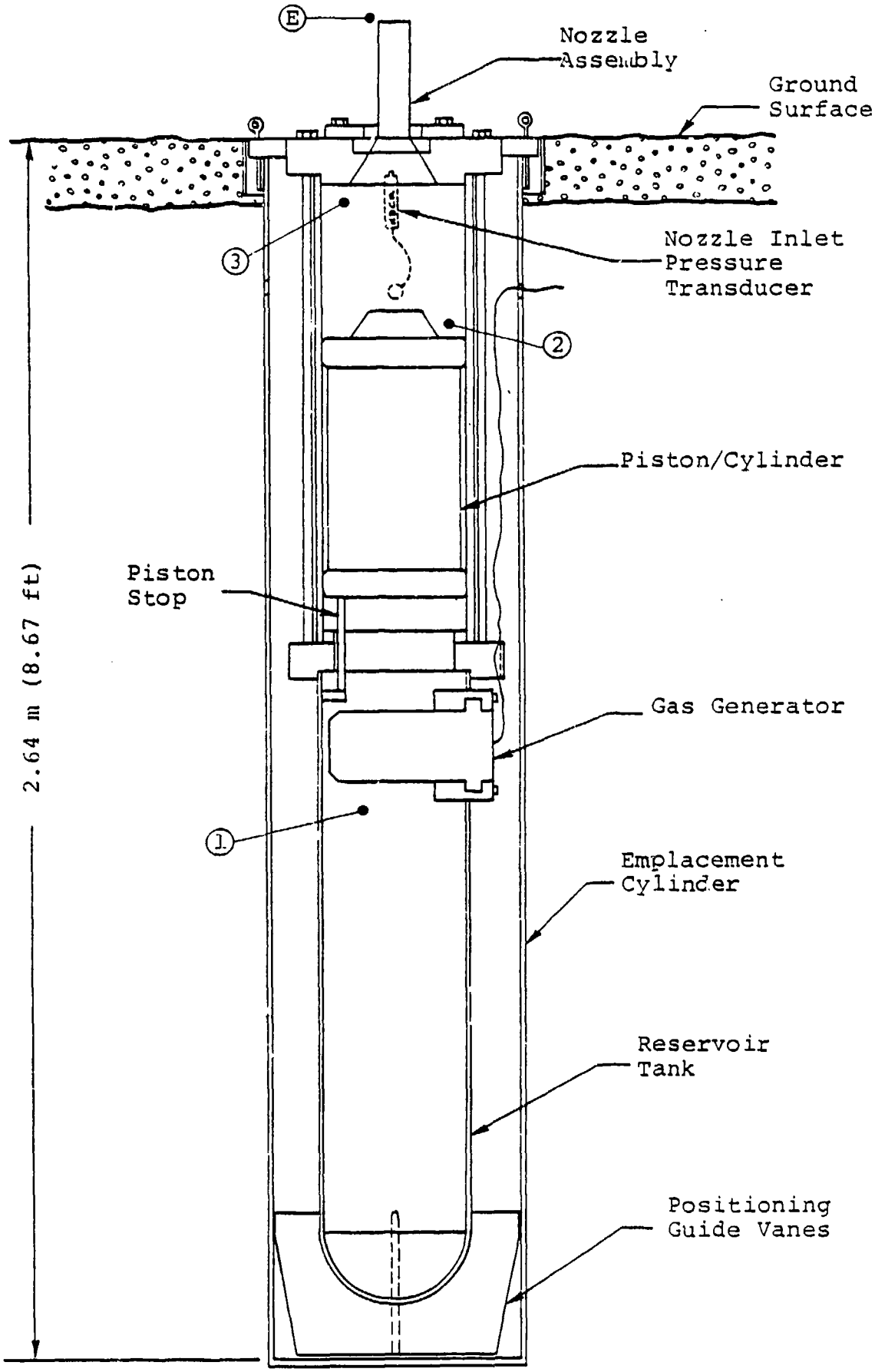

Figure 3. Schematic of linear fuel dispenser. Circled symbols refer to points designated in the theoretical performance calculations.

Figure 4. Photograph of linear fuel dispenser. A 10.2 cm (4 in.) I.D. x 102 cm (40 in.) long nozzle is installed. The dispenser is standing on the center area of the concrete test pad. In use it is lowered into the adjacent hole.

The fluid between the piston and nozzle was assumed to move as block flow (uniform velocity throughout). The motion was further assumed to be quasi-steady so that the Bernoulli equation

$$P_e + \tfrac{1}{2}\rho_\ell u_3^2 = P_A + \tfrac{1}{2}\rho_\ell u_E^2 \tag{11}$$

and steady-state conservation of mass,

$$u_E = u_3 \frac{A_P}{A_N} \tag{12}$$

could be used. In these relationships, points "3" and "E" (see Figure 3) designate the nozzle inlet and exit planes respectively, A_P and A_N are the piston and nozzle areas, and P_A is the ambient pressure.

The equation of motion for the piston plus fluid plug is simply

$$(m_\ell + m_p) \frac{du_p}{dt} = (P_p - P_3) A_p \quad , \tag{13}$$

in which m_ℓ and m_p are the masses of the liquid and the piston, P_p is the instantaneous pressure behind the piston, and u_p is the piston velocity. This equation by itself shows that the pressure drop across the piston plus fluid plug goes to zero as the piston attains constant velocity. In that condition $P_p = P_3$ and the pressure drop to P_A takes place entirely within the nozzle.

Combining Eqs. (11)-(13), with $u_3 = u_p$, gives

$$\frac{(m_\ell + m_p)}{A_p} \frac{du_p}{dt} = (P_p - P_A) - \tfrac{1}{2}\rho_\ell u_p^2 \left[\left(\frac{A_p}{A_N}\right)^2 - 1\right] \quad . \tag{14}$$

It should be noted in this equation that if $A_P = A_N$ (equal piston and nozzle areas), the piston will continue to accelerate indefinitely as long as $P_P > P_A$ and no steady velocity will be reached in that case. It is also clear that increases in A_P will enhance the inertial reponse and that an increase in the ratio A_P/A_N will reduce the time to reach a near-steady velocity.

In reality the free volume pressure P_p drops off continuously as the result of gas expansion during dispensing. The rate of free volume increase is

$$\frac{dV_{FV}}{dt} = A_P u_P \quad . \tag{15}$$

The volume increase is related to the rate of fuel expulsion by

$$\frac{dm_\ell}{dt} = -\rho_\ell \frac{dV_{FV}}{dt} \quad ,$$

and assuming isentropic expansion, the pressure changes according to

$$\frac{P_P}{P_{P_0}} = \left(\frac{V_{FV_0}}{V_{FV}}\right)^\gamma \quad . \tag{16}$$

Equations (14)-(16) were solved with the intial conditions $P_P = P_{P_0}$, $V_{FV} = V_{FV_0}$, and $u_P = 0$ at $t = 0$. This yielded the piston velocity as a function of time. The nozzle inlet pressure was then calculated from

$$P_3 = P_A + \tfrac{1}{2}\rho_\ell u_P^2 \left[\left(\frac{A_P}{A_N}\right)^2 - 1\right] \quad , \tag{17}$$

obtained by combining Eq. (11) and (12). Since $u_p = 0$ at $t = 0$, it is clear that P_3 is initially equal to P_A.

It was originally felt that the U-tube could be adapted for gas-generator driven dispensing. This would be done by eliminating the water behind the piston and mounting the gas generator at the top of the left-hand leg shown in Figure 2. If the U-tube could have been adapted in this way a new dispenser might not have been needed. A calculation of the type just described was carried out to estimate the response of the U-tube if it were used in this manner. With a 7.62 cm (3 in.) nozzle, the pertinent values are $A_P/A_N = 4.0$, $A_P = 0.0182$ m^2 (0.196 ft), and $m_p = 7.51$ kg (16.5 lbm). Characteristic values of the following parameters were used: $m_\ell = 26.5$ kg (7 gal. of water), $P_{P_0} = 1.83$ MPa (265 psi), $V_{FV_0} = 0.0708$ m^3 (2.5 ft^3), $\gamma = 1.3$, $P_A = 1 \times 10^5$ Pa (14.7 psi), and $\rho_p = 1000$ kg/m^3 (62.5 lbm/ft^3).

The result is plotted in Figure 5. As can be seen the pressure at the nozzle inlet continues to rise during nearly 30 percent of the dispensing period. The resulting fluid efflux would therefore not be impulsive in character. The use of the U-tube modified for gas-generator operation was therefore rejected. In order to obtain a more impulsive response a larger piston area was clearly required.

The linear dispenser was accordingly designed with a piston diameter of 29 cm (11.5 in.), nearly twice that of the U-tube. An even larger piston would have been desirable; however, machining costs rise very rapidly with piston diameter, and the availability of materials was limiting.

With this larger piston the start-up dynamics were improved. The actual area and mass of the piston are $A_P = 0.0670$ m^2 (0.721 ft^2) and $m_p = 43.1$ kg (94.9 lbm). In conjunction with a 7.62 cm (3 in.) nozzle, the piston-to-

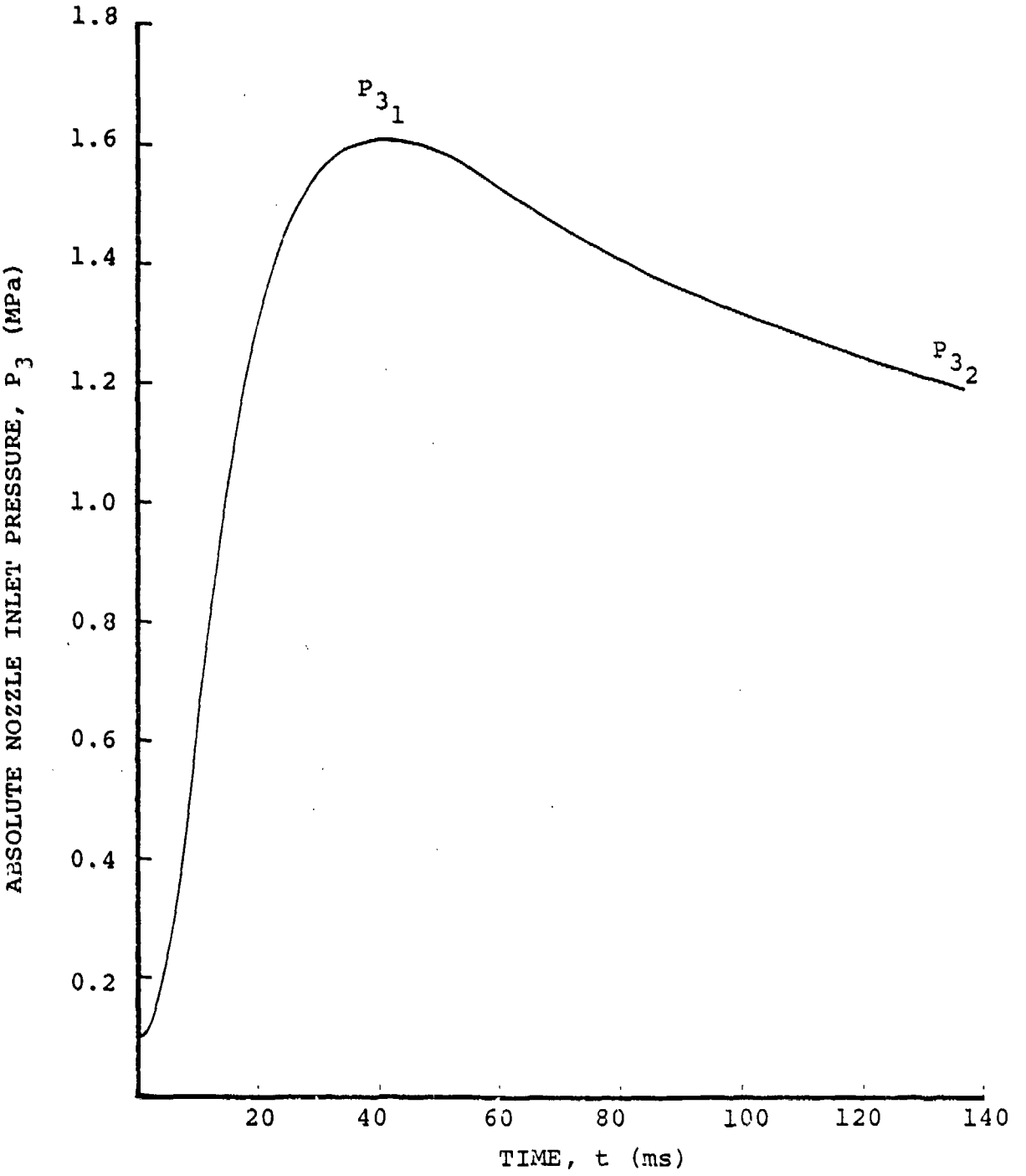

Figure 5. Nozzle inlet pressure as a function of time during operation of U-tube fuel dispenser. Values used in calculation are m_ℓ = 26.5 kg, P_{P_0} = 1.83 x 10^6 Pa, V_o = 0.0708 m^3, γ = 1.3, P_A = 1 x 10^5 Pa, ρ_e = 1000 kg/m^3, D_P/D_N = 2, A_p = 0.0182 m^2, m_p = 7.51 kg.

nozzle area ratio is A_P/A_N = 14.7. With other quantities the same as in the previous calculation for the U-tube, the inertial response that was expected is shown in Figure 6. The time to reach maximum nozzle inlet pressure (or maximum nozzle exit velocity) is in this case only six percent of the total dispensing time.

The piston was constructed of 6061-T6 aluminum alloy. To minimize its weight it was assembled from 27.3 cm (10.75 in.) OD x 0.93 cm (0.365 in.) wall tubing with welded end caps. The overall length of the piston is 56 cm (22 in.). A 6.4 cm (2.5 in.) long nose with a 60° taper angle was included to provide cushioning during piston deceleration (stopping). The maximum stroke of the piston is 41 cm (16 in.). At the upper limit of its travel it is stopped by an annular shoulder. In this position the nose mates with the nozzle inlet wall with a 0.5 mm (0.020 in.) gap between the tapered surfaces.

Two piston seals are employed on each of the two piston end caps. The three uppermost seals are 4.8 mm (3/16 in.) diameter teflon-encapsulated viton o-rings manufactured by Chesterton, Inc. These are more flexible and remain resilient longer than solid teflon. They can endure sustained exposure to solvent fuels (in particular, propylene oxide). A single teflon spiral-type backup o-ring is used with each of these three seals. The lowermost seal is a 6.4 mm (0.25 in.) wide aluminum/bronze step-cut piston ring. This ring is needed to protect the other seals from potentially damaging exposure to the hot products from gas-generator combustion and it also serves as a cylinder wiper.

The cylinder in which the piston travels was fabricated from 32 cm (12.75 in.) OD by 28 cm (11.1 in.) ID A106 grade B seamless black pipe. This was bored to 29 cm (11.5 in.) ID, honed, flash chrome plated, and then re-honed. The chrome plating was applied to provide corrosion protection. The

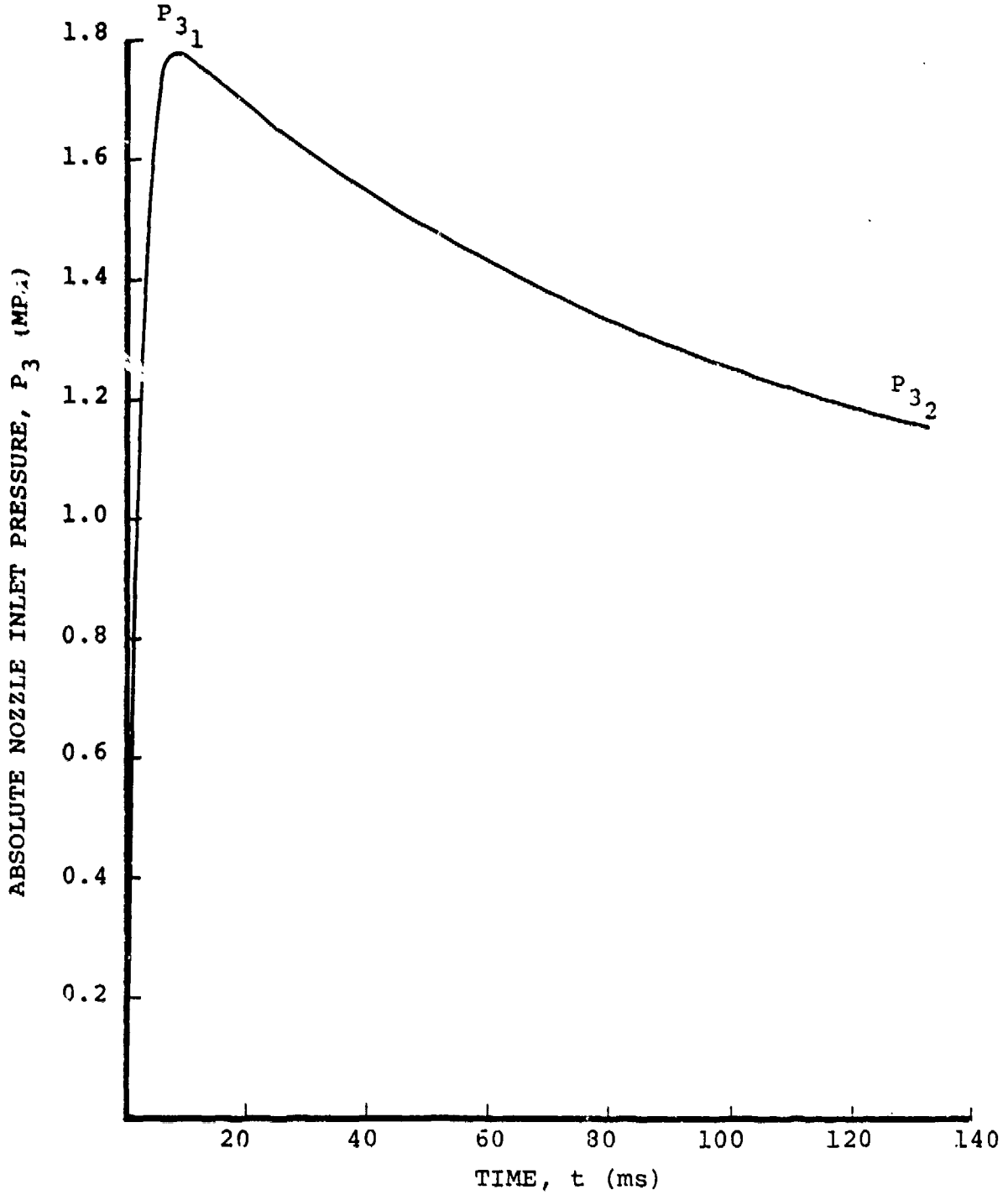

Figure 6. Nozzle inlet pressure as a function of time during operation of linear fuel dispenser. Values used in calculation are m_ℓ = 26.5 kg, P_{P_0} = 1.83 x 10^6 Pa, V_o = 0.0708 m^3, γ = 1.3, P_A = 1 x 10^5 Pa, ρ_ℓ = 1000 kg/m^3, Dp/D_N = 3.83, A_p = 0.0670 m^2, m_p = 43.1 kg.

piston/cylinder assembly was attached to the other dispenser parts using the techniques of hydraulic cylinder construction. Eight 1.9 cm (0.75 in.) tie bolts connect the cylinder to the free volume chamber. The free volume is about 0.093 m^3 (3.3 ft^3) with the gas generator installed and without any water fill.

In use the linear dispenser is installed below grade in a steel cylinder that is 51 cm (20 in.) ID by 2.6 m (103 in.) long and has a 2.5 cm (1 in.) thick welded steel base plate. This cylindrical housing was constructed from the gas bottle of a surplus torpedo. A fork lift truck is used when it is necessary to remove the dispenser from the housing. A 2.7 m (9 ft) A-frame gantry with hoist is used when raising the dispenser just far enough to service the gas generator.

Experience with the linear dispenser has been for the most part positive, with the exception of difficulties associated with the gas generator (Appendix B). An additional problem was experienced with the method used to vary the internal volume of the free volume tank. It was found that adding water to the free volume tank would lead to a substantial loss of dispensing pressure. This was apparently due to energy absorption by the water which was evidently penetrated by the exhaust jet. The effect was aggravated with greater amounts of water present. No suitable alternate fill to replace water was found. Any suitable alternate fill must be unaffected by exposure to high temperature, violently turbulent gases. It should generate no dust or grit which could damage the piston or cylinder, and it should not be propelled by the high velocity jet into damaging projectiles. Heavy steel chain was tried as a fill but this, like the water, apparently absorbed much of the gas energy.

SECTION 3

TURBULENT LIQUID JETS

The projection and atomization characteristics of impulsive, turbulent liquid jets are of importance to the point-source FAE cloud formation technique described in the Introduction. The breakup of steady, laminar liquid jets has been studied extensively and a substantial body of literature is available. Turbulent liquid jets on the other hand have received comparatively little attention. In any case the primary breakup characteristic investigated by other researchers has been the point of jet rupture. This is the point along the jet trajectory beyond which there is no continuous path that connects fluid particles to the nozzle. Very few experiments are reported in which ultimate jet penetration distances (reach) have been measured.

Impulsive hydraulic fuel injection has also received little previous attention other than in the areas of high-pressure jet cutting and diesel fuel injection. In both of these applications very small diameter jets are involved. Except for earlier work at Systems, Science and Software (Reference 5) and that reported herein, it appears that no prior systematic experiments have been conducted with large diameter (to 10 cm (4 in.)), impulsively injected, turbulent liquid jets in the intermediate pressure range (2.8 MPa (400 psi)).

Impulsive (single-pulse or finite column length) jets are distinguished from steady state (continuous or infinite column length) jets on the basis of their duration. If the time for an element of jet fluid to traverse the distance from the nozzle exit to the point of ultimate jet reach is short compared to the total dispensing time, the jet can be considered steady state. If these two times are comparable, the jet is considered impulsive.

The dispensing time is approximately

$$t_D = \frac{V_F}{u_D A_N} \tag{18}$$

where V_F is the total volume of fluid that is dispensed at constant velocity, u_D, through a nozzle of area A_N. The time, t_R, for a fluid element to attain full reach, R_C, is

$$t_R = \frac{R_C}{u_D} \quad . \tag{19}$$

Therefore the condition for an impulsive jet is

$$t_{D_{MAX}} \sim t_R \quad ,$$

or, in terms of volume dispensed

$$V_{F_{MAX}} \sim A_N R_C \quad . \tag{20}$$

This is just the volume that would be contained in a virtual liquid column of length R_C and cross-sectional area A_N. If the actual fuel volume dispensed is very much larger than this value the virtual liquid column is said to be of infinite length and the jet is essentially steady.

3.1 STEADY-STATE JETS

An early classification of jet breakup characteristics was given by Ohnsorge (Reference 11). This is reproduced in Figure 7. The classification was developed in terms of the liquid Reynolds number,

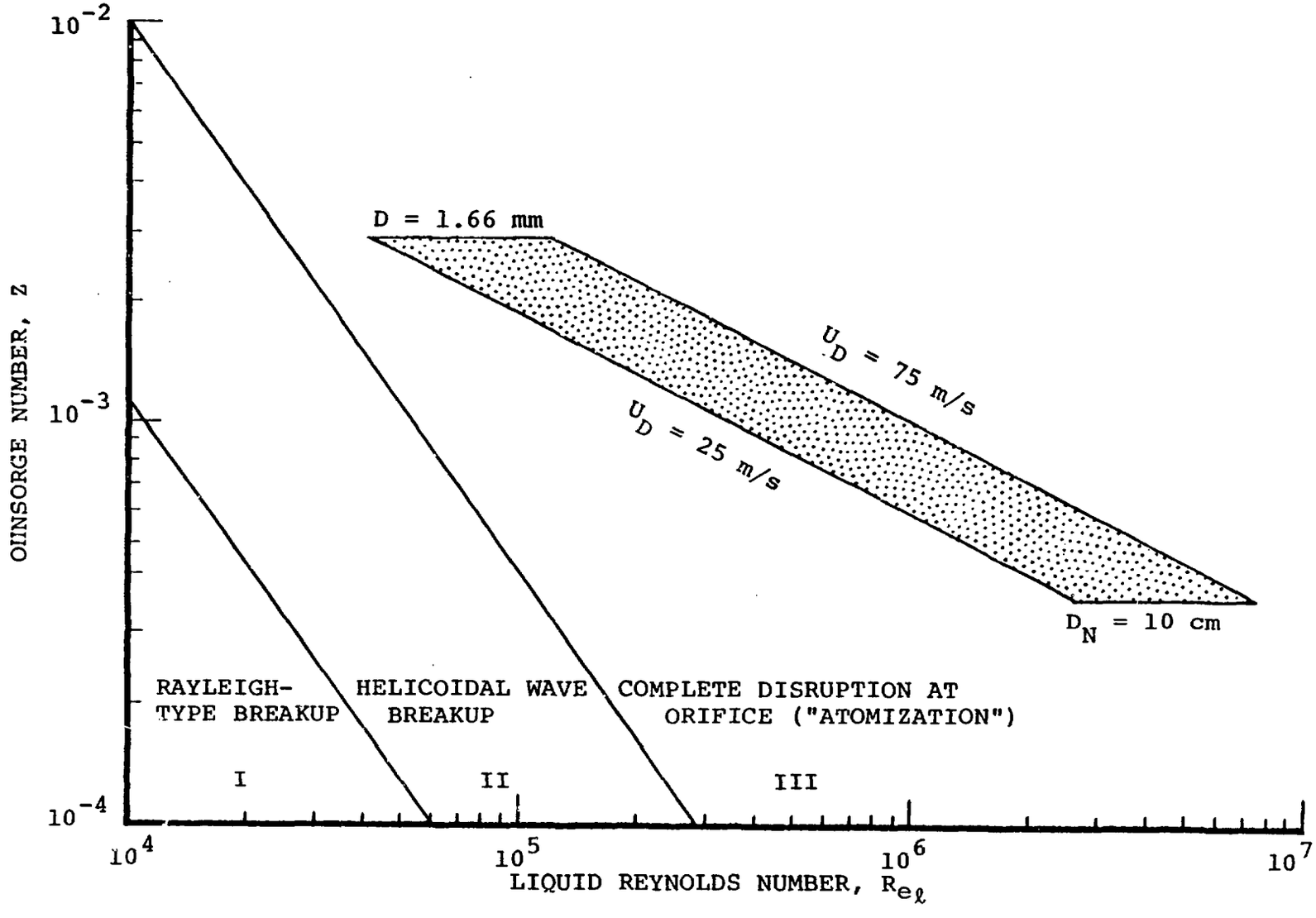

Figure 7. Water jet breakup classification according to Ohnsorge (Ref. 13). The regime corresponding to conditions of present interest is shaded.

$$R_{e_\ell} \equiv \frac{\rho_\ell u_D D_N}{\mu_\ell}$$

and the Ohnsorge number

$$Z \equiv \frac{\mu_\ell}{(\rho_\ell D_N \sigma_\ell)^{\frac{1}{2}}} \quad ,$$

where D_N is the nozzle diameter and μ_ℓ and σ_ℓ are the liquid viscosity and surface tension. As the velocity of the jet is increased at fixed diameter, the dominating breakup mechanism changes from symmetrical varicose surface wave growth (Reference 12) to helicoidal wave developement (Reference 13). At still higher velocities, Ohnsorge reported that the jets were fully disrupted or atomized at the nozzle exit.

For reference the regime of interest to the present investigation is designated by the shaded area in Figure 7. The regime spans the range 0.35 MPa $\leq \Delta P \leq$ 2.8 MPa, 1.6 $\leq D_N \leq$ 100 mm (50 $\leq \Delta P \leq$ 400 psi, 1/16 $\leq D_N \leq$ 4 in.). It is noted that nozzle pressure drop, ΔP, and jet velocity, u_D are related by

$$\Delta P = \tfrac{1}{2}\rho_\ell u_D^2 \qquad (21)$$

assuming loss-free flow in the nozzle. As can be seen on the figure, all of the jets of interest lie in the complete atomization regime according to the Ohnsorge classification.

Complete jet disintegration at the nozzle exit does not however appear to be an accurate description of turbulent jet breakup in many cases. More recent investigations clearly show that, although surface atomization begins in high-velocity turbulent jets at the nozzle exit, a self-contiguous central jet core persists for a considerable distance. In terms of the liquid Weber number

$$We_{\ell} \equiv \frac{\rho_{\ell} u_D^2 D_N}{\sigma_{\ell}} \quad ,$$

the distance to this rupture point, x_B, has been correlated empirically by Grant and Middleman (Reference 14) as

$$\frac{x_B}{D_N} = 8.51 \, We_{\ell}^{0.32} \quad , \tag{22}$$

for $100 \leq We \leq 10^5$, and by Phinney (Reference 15) as

$$\frac{x_B}{D_N} = 55 + 1.085 \, We_{\ell}^{\frac{1}{2}} \tag{23}$$

for the approximate range $35 \leq We_{\ell} \leq 6 \times 10^4$. These two relations do not agree well with one another. They do show however that for example at $We_{\ell} \sim 10^5$ the distance to the rupture point can be as much as 400 diameters from the nozzle exit. It should be noted that in turbulent jets, this rupture does not appear to occur abruptly. Rather, the jet core is dissociated gradually and the rupture point simply designates the furthest position of self-continuity of the core.

Many investigators have concluded that turbulent liquid jets are ultimately shattered by the unconstrained radial motion of internal eddies (References 15-20). The smallest of these perturb the surface but appear to be contained by it. Those eddies with sufficient radial momentum penetrate the surface and are swept away by aerodynamic forces. The amount of material stripped from the jet by this mechanism is relatively small. However, the resulting spray partially conceals the inner jet core, which has an irregular, mottled surface. It is the large-scale, low-momentum eddies which

eventually produce surface disturbances of sufficient magnitude as to induce utlimate varicose breakup of the jet core.

The intensity and character of turbulence upstream of the nozzle exit therefore play key roles in determining both the extent of early spray removal and the ultimate reach of the jet. The turbulent intensity is increased by surface roughness, by increasing the nozzle length, and by non-smooth plumbing transitions*. Other characteristics of specific nozzle geometry seem to be of little consequence (References 16 and 21). Differences in the scale and intensity of turbulence at the nozzle exit could perhaps account for the differing descriptions given of turbulent jet breakup by the various investigators.

The distance to the rupture point of a turbulent liquid jet and its ultimate penetration distance (reach) are not directly related. Rupture is associated with the formation of liquid strands or ligaments (Reference 22) which subsequently collapse under the action of surface tension into droplets. Larger liquid globules with diameters on the order of the intial jet diameter may also be formed (References 23 and 24). The droplets and globules are then broken up into a finer spray by aerodynamic shattering if their velocity is high enough. In fact, the process of aerodynamic shattering can be expected to be repeated with the formation of successively smaller droplets until the spray momentum has been largely depleted. The surviving droplets then presumably undergo phase change by convection-assisted evaporation. In jets with a vertical velocity component, these may or may not pass through a trajectory extremum and fall to the ground before being fully vaporized.

*It should be noted that the nozzles used in the development of Eqs. (22) and (23) were very long (L/D $\sim$ 100), so that the turbulence was presumably well developed.

Aerodynamic shattering of liquid droplets is a complex phenomenon. A good summary discussion is given in Reference 25. Shattering occurs when the gas-liquid Weber number for the droplet, $W_e \equiv \rho_A u^2 D/\mu_\ell$ is greater than about ten. The mode of shattering changes as W_e is increased. At low Weber numbers ($W_e \lesssim 100$) the parent droplet is broken into relatively large secondary drops, while for $W_e \gtrsim 1000$ the parent droplet is atomized into a fine microspray, typically 1/100 of the parent droplet size. Breakup times and droplet trajectories have been correlated with coarse accuracy by a number of researchers (Reference 25). This information could conceivably by used at some future time to predict jet penetration beyond the rupture point; however, neither the droplet size distribution nor the droplet velocity at the rupture point is presently known with sufficient accuracy for that purpose.

For these reasons the determination of ultimate jet reach is best obtained experimentally. Data of this type are very limited, even for steady state jets. Prior interest in jet reach has been confined largely to studies of fire stream projection (Reference 26). In most cases the maximum distance that the jet remains suitable for firefighting has been measured, rather than the ultimate jet reach. However, Box (Reference 27) and Freeman (Reference 21) give ultimate jet reaches for vertical fire streams up to 5 cm (2 in.) diameter and at pressures to 0.5 MPa (70 psi). A correlation in this range given by Freeman, rewritten here in dimensionless format, is

$$\frac{R_c}{D_N} = \lambda - 1.12 \times 10^{-4} \lambda^2 \quad , \tag{24}$$

where

$$\lambda \equiv \frac{\Delta P}{\rho_\ell g D_N} = \frac{u_D^2}{2gD_N} \quad .$$

Here, ΔP is the pressure drop across the nozzle, ρ_ℓ = 1000 kg/m^3 (62.5 lbm/ft^3), g = 9.80 m/s^2 (32.2 ft/sec^2) is the acceleration due to gravity, and D_N is the nozzle diameter. It is interesting to note that ultimate dimensionless reach as given by Eq. (24) decreases with increasing nozzle diameter (at fixed velocity), while the dimensionless rupture distance, given by Eqs. (22) and (23) increases. However, the ranges of validity of these three empirical relations do not coincide.

The accuracy of Eq. (24) rapidly diminishes for nozzle sizes larger than about 3.8 cm (1.5 in.), and for pressures above about 0.5 MPa (70 psi). Increasing the diameter or pressure beyond these limits leads to much less increase in actual reach than is predicted by Eq. (24). At sufficiently high pressures a decrease in the reach of these water jets has been observed. The physical constraints that limit the upper bound on the reach that could be achieved by an arbitrarily large jet are not presently known. However the greatest vertical jet reach that has been documented is 170 m (560 ft) (Reference 28). This is a steady state water jet that is developed from an annular nozzle at 2.8 MPa (400 psi).

A limited number of survey experiments were performed at Systems, Science and Software with small diameter, quasi-steady liquid jets at pressures to 2 MPa (300 psi). These small diameter jets are relevant to the formation of small-scale experimental FAE clouds. The individual jets were produced using the U-tube dispenser. A total of 0.011 m^3 (3 gal.) of liquid was discharged through five nozzles. The nozzles were

drilled into a blind end flange as shown in Figure 8. All of the nozzle bores were 13 mm (0.50 in.) in length so that the nozzles had length-to-diameter ratios varying between 3.5 and 8.5. The U-tube was pressurized by nitrogen gas from a 9.8 x 10^{-4} m^3 (60 in^3) supply bottle. During dispensing the pressure in this bottle dropped from an initial value near 2 MPa (300 psi) to atmospheric pressure. This took place in about 10 s. The reach of each jet was measured as a function of time on films taken during a test and correlated with the measured nozzle entry pressure.

Results from tests with JP4 kerosene, NAPTHA, and propylene oxide (P.O.) were qualitatively similar. Characteristic data from these tests is given in Figures 9 and 10. Below about 0.34 MPa (50 psi) the jet reach was found to increase rapidly with pressure. However the lack of atomization in this range made the jets nearly invisible on the films and reach measurements could not be taken. This difficulty accounts for the considerable data scatter near 0.34 MPa (50 psi). It should also be noted that in all cases, accurate definition of the instantaneous jet reach was very difficult and could account for some of the data scatter. Above 0.34 MPa (50 psi) jet atomization was substantial and increased subjectively with increasing pressure. The jets became visible on the films allowing reach to be measured. The reach remained roughly constant and in some cases decreased somewhat in this range. This implies balancing competition between increasing jet momentum and the increased drag per unit mass that results from the formation of smaller spray droplets at the higher injection velocities. In essence the ultimate jet reach was found to be a function only of nozzle diameter above some minimum jet velocity.

It should be noted that during the early experiments of this kind, only cursory attention was given to prevailing atmospheric winds. These were estimated at the time to be no

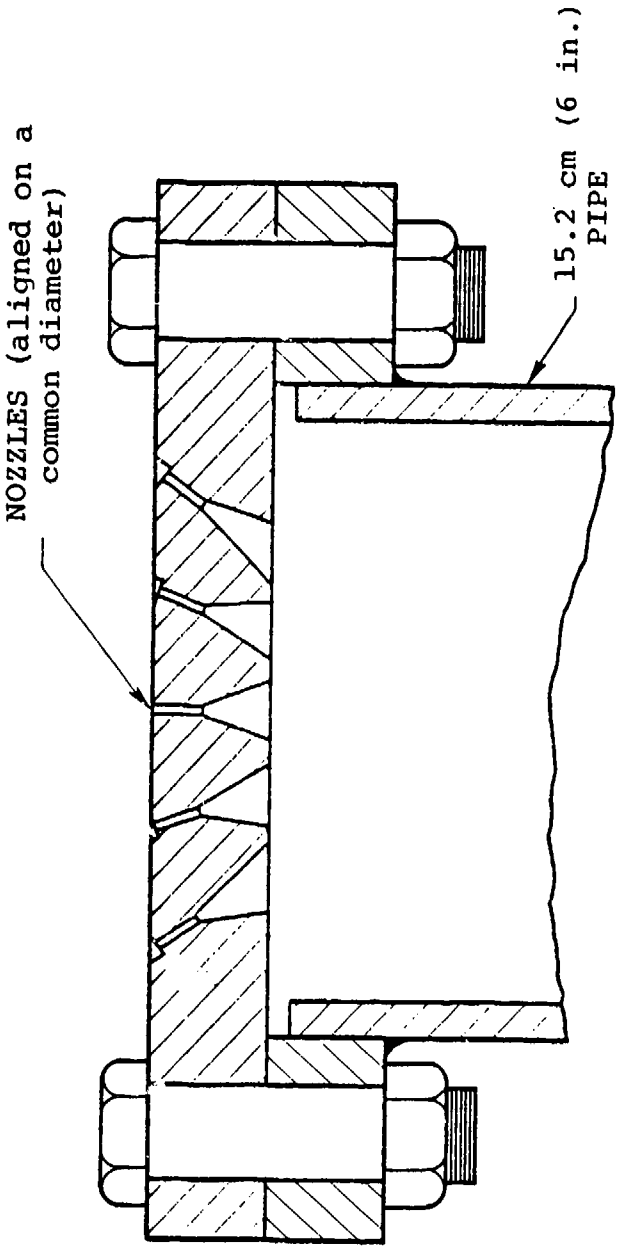

Figure 8. Sketch of five-nozzle head used in quasi-steady small diameter jet experiments.

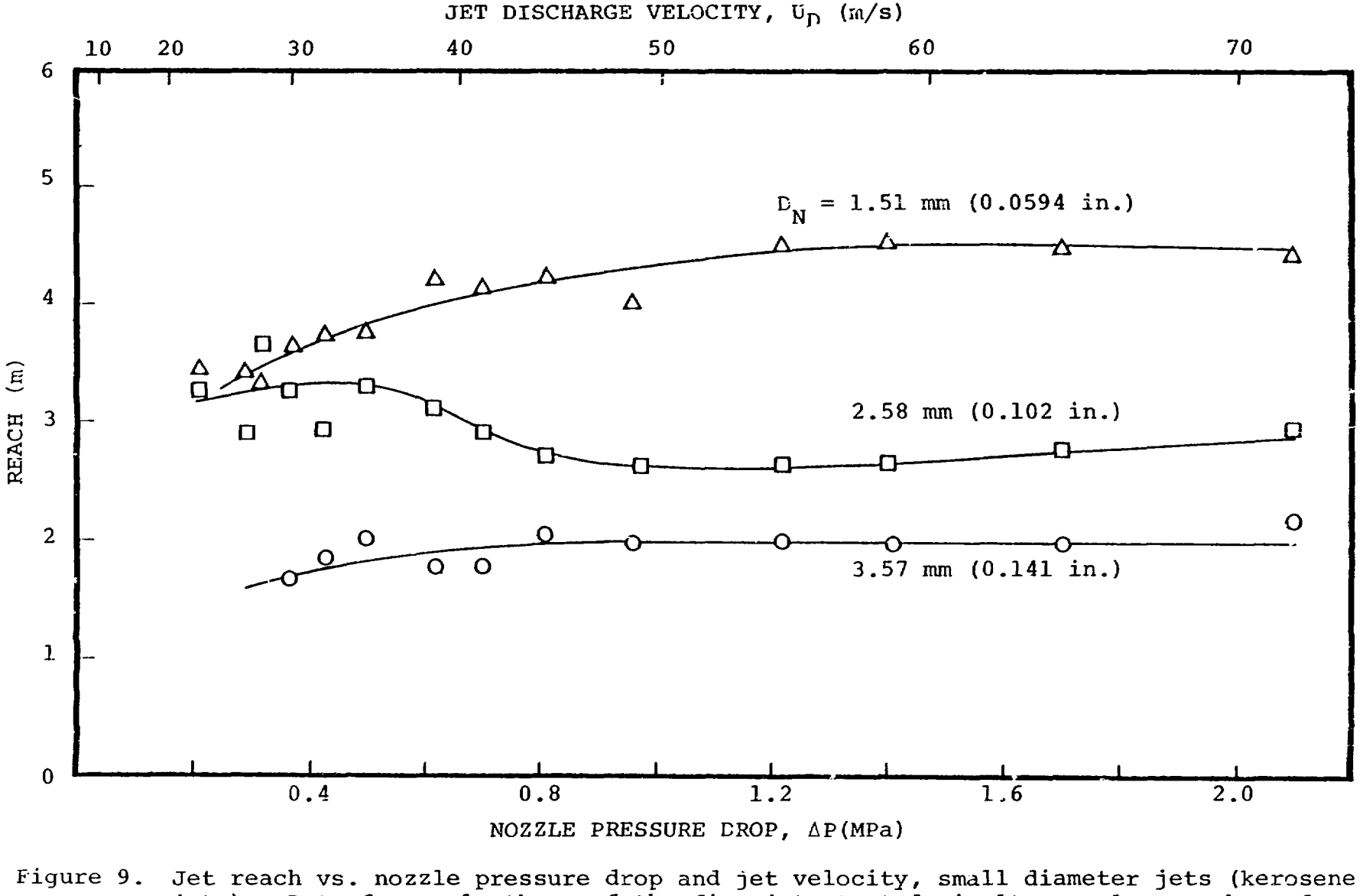

Figure 9. Jet reach vs. nozzle pressure drop and jet velocity, small diameter jets (kerosene jets). Data from only three of the five jets tested simultanecusly are shown for clarity.

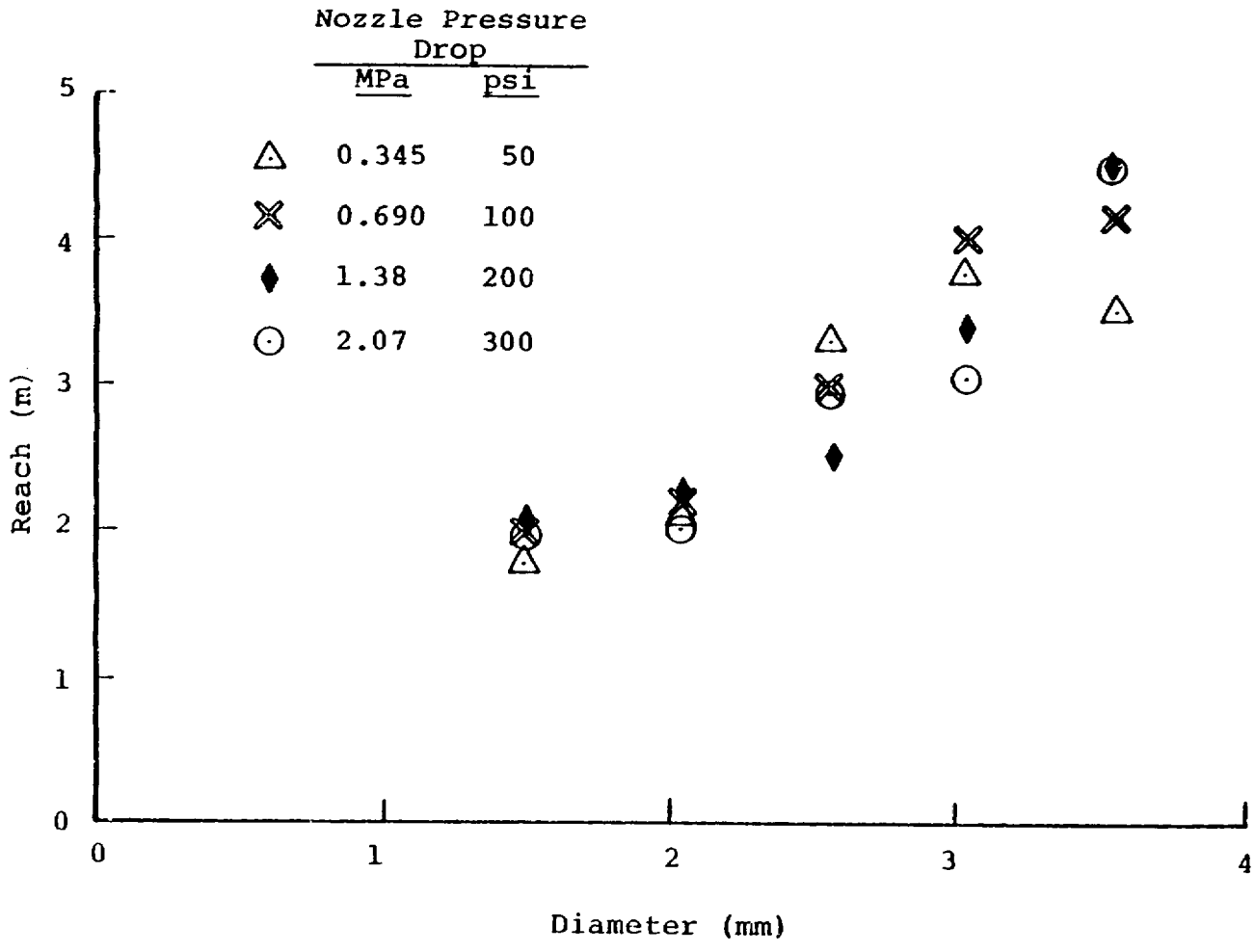

Figure 10. Ultimate jet reach versus nozzle diameter (kerosene jets).

more than about 1.3 m/s (3 MPH). Some of the tests were later repeated during completely quiescent weather. These later tests were also of greater duration. About 0.036 m^3 (9.5 gal.) of fuel was dispensed and the pressurized supply bottle volume was increased to 0.033 m^3 (1.17 ft^3). These changes resulted in a dispensing time of about 30 seconds. The pressure range covered was 0.7-2 MPa (100-300 psi). The jet reaches measured in these later tests were substantially greater than those in the earlier experiments (by as much as a factor of two), but it is believed that the increases were virtual. It is felt that in a very still atmosphere the extremely fine spray droplets hovered in a cloud near the jet peak. These fine droplets were then displaced vertically by air currents induced by the jet. As a result, the apparent jet reach was increased. With any slight breeze or with much shorter dispensing period, this phenomenon could not occur. It is believed for this reason that the earlier tests are the more credible.

Some of the data scatter in Figures 9 and 10 is no doubt due to momentary wind gusts that occurred during the experiments. In consequence the trends indicated by the curves are probably accurate only within, say, about ±10%. The general sensitivity of ultimate reach to wind has been noticed by other investigators even in large diameter jets at lower pressures (with comensurately larger spray droplets) (Reference 10).

3.2 IMPULSIVE JETS

Impulsively injected jets are of greater interest to the present investigation than are steady-state jets. A hemispherical fuel-air cloud having a radius on the order of 70 m (230 ft) is required to simulate the far-field airblast of a 1 KT nuclear explosion. To form this cloud a large number of radially-directed jets are to be discharged from a central point source. The cloud must be formed in less than about two

seconds to avoid cloud distortion and drift due to atmospheric winds. Therefore steady-state jets are unsuitable.

An impulsive jet from a single nozzle would ideally atomize fully into a uniform, fine spray and would attain the required reach. Unfortunately, techniques to enhance jet atomization tend to diminish jet reach. For example, it is well known that induced swirl and impinging or coaxial air jets promote early liquid jet atomization and the formation of small droplets. These benefits however accrue at the expense of reach. Maximum jet reach is instead obtained by sustaining jet coherence over the greatest possible trajectory length and by encouraging the initial formation of large droplets upon jet rupture. For this latter purpose a simple, converging hydraulic nozzle that is terminated at the orifice has been found to be the most effective (Reference 16). Additives such as long-chain, high molecular weight polymers can additionally be used to dramatically increase jet coherence (References 19 and 29). However, for the application to spray cloud formation, excessive jet coherence is also not desirable. Highly coherent jets would not atomize sufficiently to fill in the voids between them in clusters of jets and the extremely large droplets would be difficult to detonate. Therefore, a hydraulic nozzle designed to generate moderate but not minimum turbulent intensity is believed to be the best practical tradeoff. This will produce a reasonably coherent jet that however will ultimately atomize into a detonable spray.

Impulsive jet breakup has been investigated at Systems, Science and Software in part with the U-tube facility and in part with the linear dispenser. The linear dispenser driven by the smokeless-powder gas generator as described in Appendix B is currently limited to 1.4 MPa (200 psi). In order to conduct experiments at higher pressures an alternate technique was used. In tests above 1.4 MPa (200 psi), a brass diaphragm was

placed over the nozzle inlet and the dispenser freevolume was pressurized with nitrogen to within about 0.17 MPa (25 psi) of the diaphragm rupture point. To start a test, nitrogen gas from a large-volume supply bottle at 5.5 MPa (800 psi) was allowed to flow rapidly into the freevolume tank. This quickly raised the pressure in the freevolume tank causing the diaphragm to rupture. This procedure was considered a contingency measure since there was some question as to the influence of the diaphragm on the jet breakup.

Impulsively dispensed jets from nozzles having diameters between 2.5-10 cm (1-4 in.) have been examined. In all cases the nozzle design is very simple, consisting of a 60° conical inlet that converges to the required exit diameter. This is followed by a straight section that is ten nozzle diameters in length. The junction between these two sections is rounded with a 2.5 cm (1 in.) radius of curvature. The straight section was added to allow a limited amount of turbulence to develop.

The characteristics of impulsive jet breakup are illustrated stylistically in Figure 11, while Figures 12 through 15 are outline sketches traced from high speed films taken during the experiments. It should be noted that the samples chosen for this group of figures involve different liquids and nozzle sizes.

Many breakup features of impulsive jets are similar to those of steady-state jets. The mechanism of jet surface penetration by turbulent eddies is believed to be primarily responsible for jet rupture. This is a process that for a given moving fluid element is essentially independent of events ahead of or behind that element. It should therefore be little affected by the jet duration. Similarly, those mechanisms leading to jet surface erosion as well as those associated with

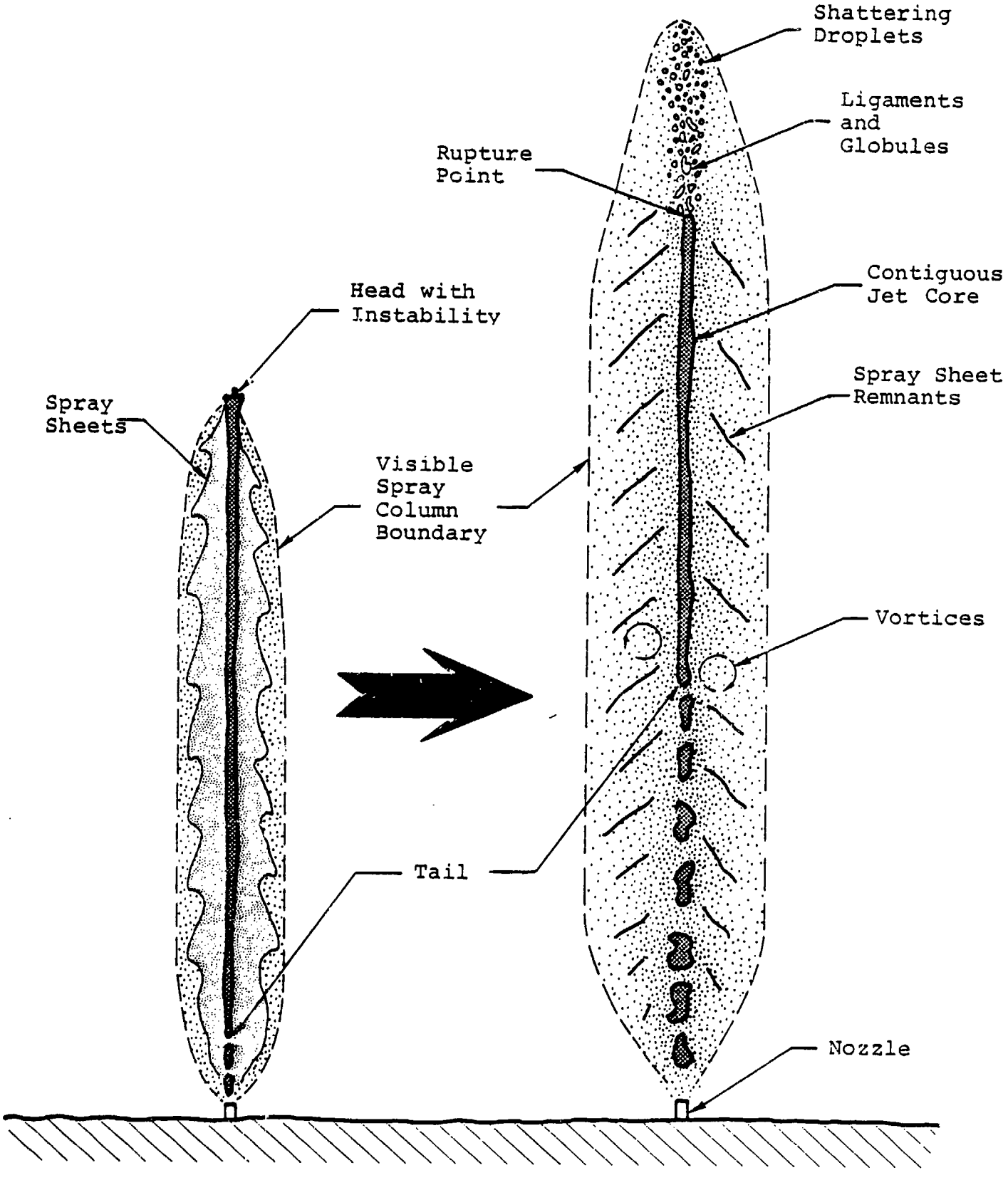

Figure 11. Exaggerated schematic representation illustrating features of impulsively injected liquid jets.

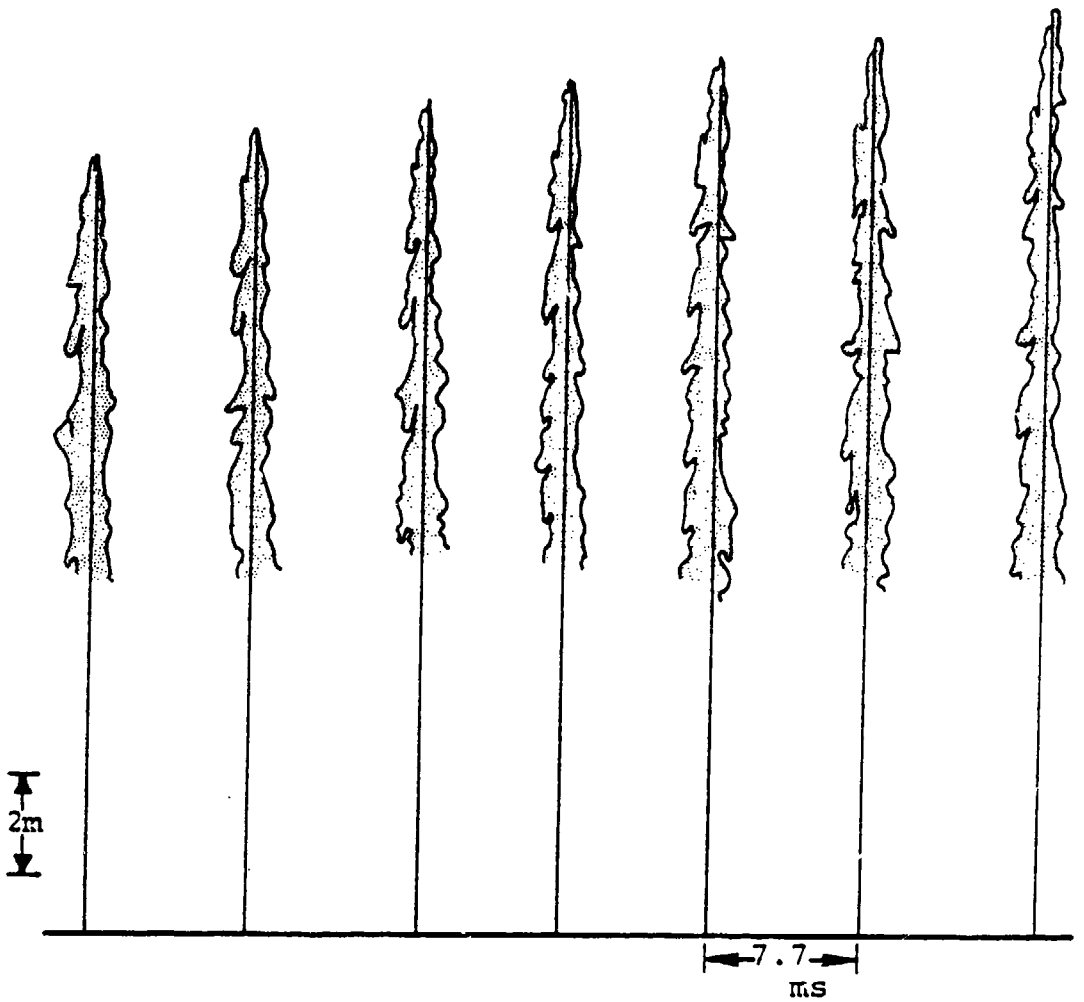

Figure 12. Head and surface breakup. Propylene oxide jet from 1.91 cm (0.75 in) diameter nozzle at 1.07 MPa (155 psi) driving pressure drop. (Only the dense spray near the core is shown.)

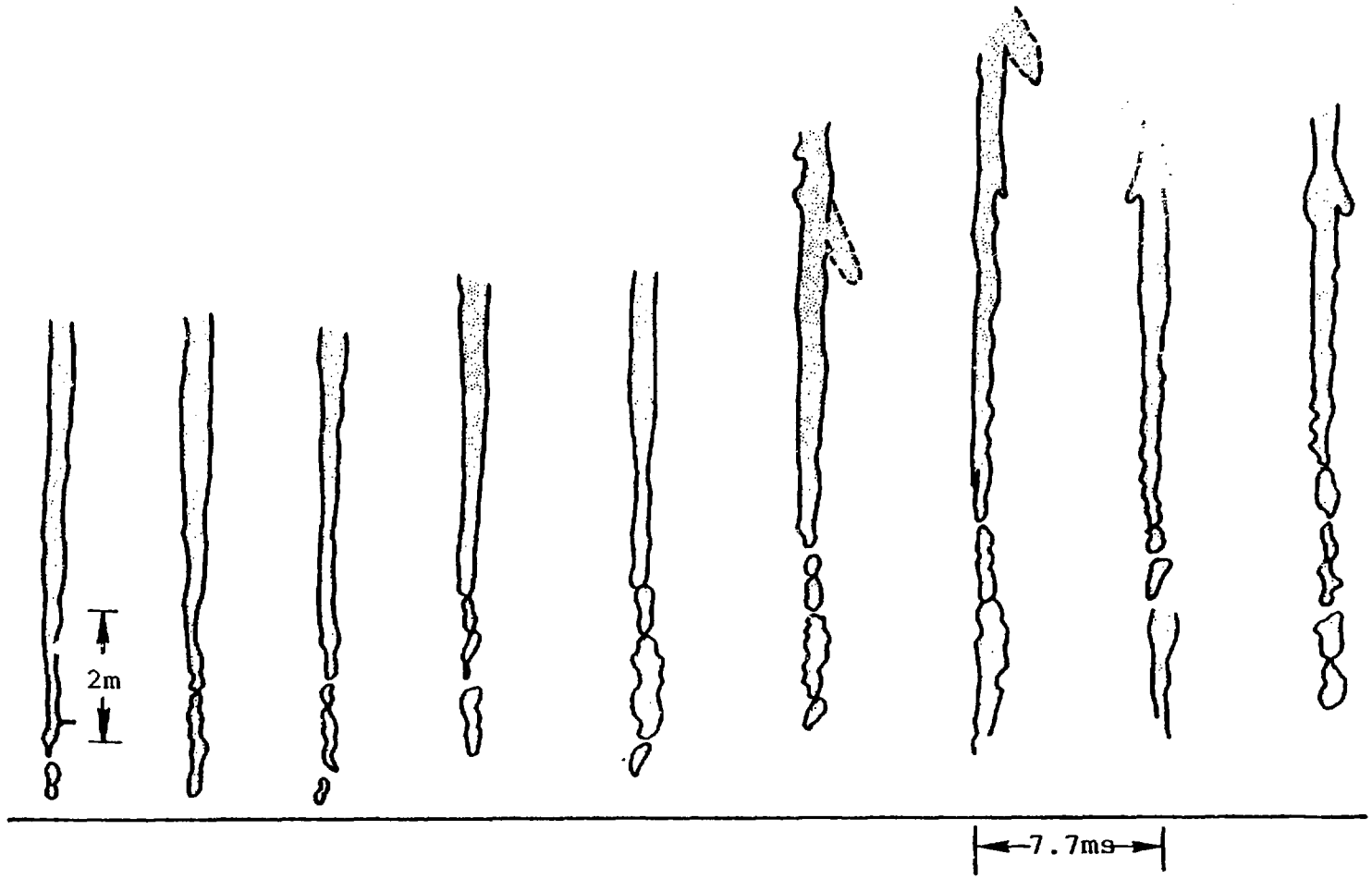

Figure 13. Tail breakup. Water jet from 3.81 cm (1.5 in) diameter nozzle at 1.38 MPa (200 psi) driving pressure drop. (Only the dense spray near the core is shown.)

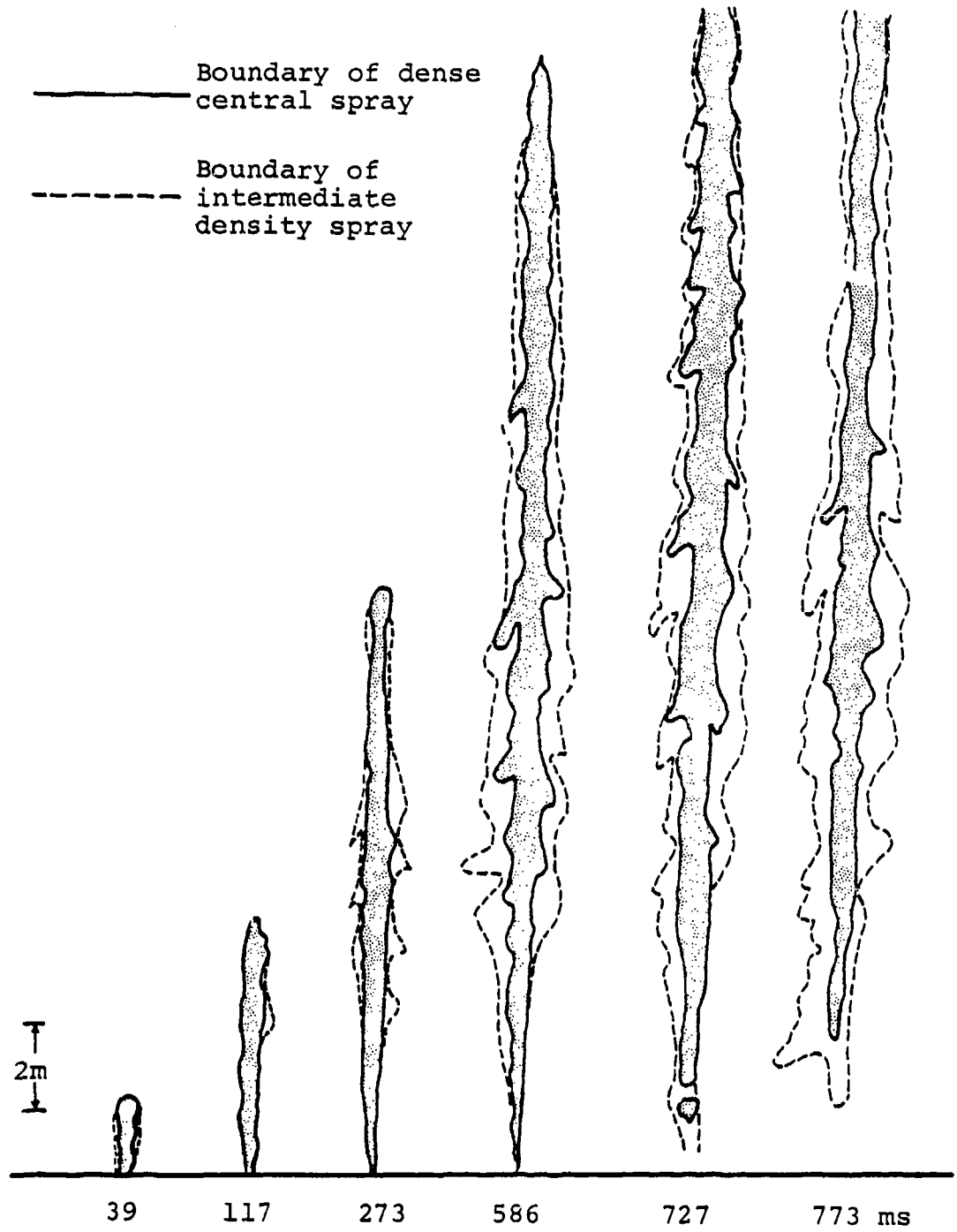

Figure 14. Early jet spreading. Water jet from 1.91 cm (0.75 in) diameter nozzle; nozzle pressure 1.03 MPa (150 psi).

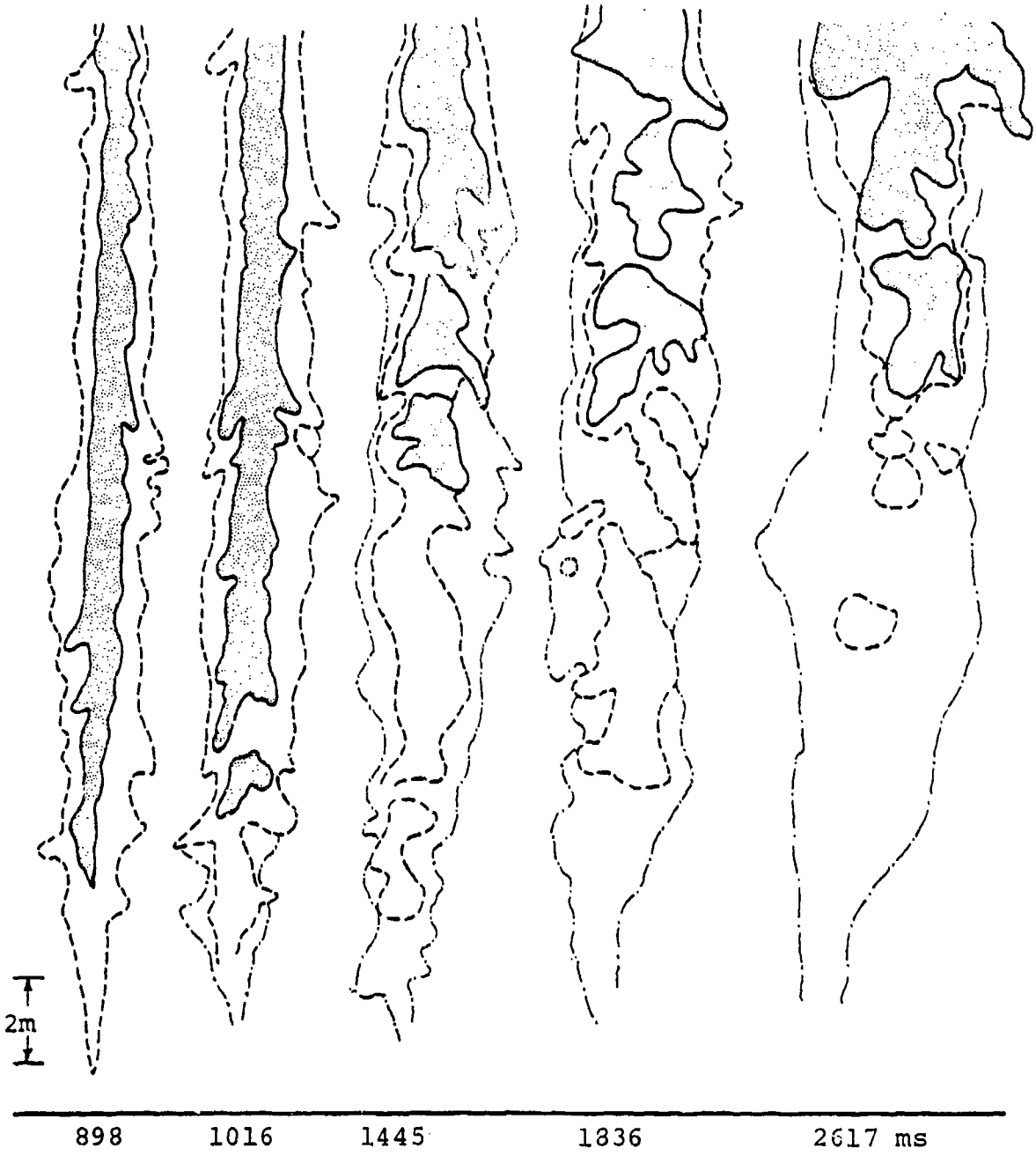

Figure 15. Jet spreading at later times. Water jet from 1.91 cm (0.75 in) diameter nozzle; nozzle pressure 1.03 MPa (150 psi).

the behavior of droplets, ligaments, and globules formed after rupture appear to be quite similar for both steady-state and impulsive jets.

On the other hand, impulsive jets differ signficantly from steady-state jets because of the existence of both a leading front (head or nose) and a terminating tail. These influence the quantity and distribution of residual spray along the jet path.

As an impulsive jet initially emerges from a nozzle, its head appears to undergo recurring instabilities which result in the periodic shedding of spray sheets. Qualitatively these have the appearance of Taylor instabilities; that is, acceleration induced waves which grow within the liquid at the jet head until they are removed by aerodynamic drag. It appears that the removed liquid forms a spray which rapidly decelerates. The suddenly exposed liquid core at the jet head passes through this spray and the instability cycle repeats. This repeating process contributes to the Christmas-tree character of the early-time spray immediately adjacent to the jet core, which is apparent in Figure 12. In other investigations similar behavior has been observed with impulsively started fuel jets of small diameter (200 μm (0.008 in.)) (Reference 22).

The tail of an impulsive jet appears to have a much greater effect on jet breakup than that at either the head or external surfaces. An example of the appearance of an impulsive jet in the vicinity of its tail is given in Figure 13. Only the dense region near the core (not the entire spray outline) has been traced on this figure. The average velocity of the instantaneous tail of the contiguous column exceeds that of the head by a factor of 1.5 to 2. This indicates that material breaks off from the end of the jet core in a continuing process. The tail breakup could for example be the result of unbalanced lateral forces associated with periodic vortex

shedding. In any case, material removed from the tail is very rapidly dispersed as a spray. The passage of the tail is always accompanied by a considerable widening of the residual spray column below the rupture point.

Tail breakup is very beneficial in the present context because it is primarily responsible for the majority of residual spray in the first several hundred jet diameters from the nozzle exit. The only other contributions to the spray in this region are from jet surface atomization and from remnants of spray shed during passage of the head. On the other hand, the tail breakup process can reduce jet reach. As the total quantity of liquid dispensed impulsively through the nozzle is reduced, a condition may be obtained in which the advancing jet tail overtakes the head. If this occurs before the head reaches the normal rupture point, the jet will be broken up at a distance closer to the nozzle than is usual. This would in turn result in diminished total jet travel or reach. The minimum quantity of liquid that can be dispensed through a given nozzle without reach reduction by this mechanism corresponds to the condition in which the advancing tail breakup point overtakes the head at exactly the normal jet rupture point.

An estimate of this minimum quantity of liquid that must be dispensed can be obtained from a simple analysis. Neglecting jet surface and head atomization and assuming that the jet moves at a constant velocity, u_D, its length at the moment of tail emergence from the nozzle is

$$L_o = \frac{4V_F}{\pi D_N^2} \quad . \tag{25}$$

Assuming that the tail breakoff point propagates along the jet at twice the jet velocity relative to the ground, the rate of change in the contiguous jet length L would be

$$\frac{dL}{dt} = - u_D$$

so that

$$L = L_o - u_D t \quad .$$

Thus at time $t^* = L_o/u_D$ after tail emergence, the jet tail would reach the jet head. The distance from the nozzle to the head, at the moment of tail emergence, is $x = L_o$. Hence at the time t^* it will be at

$$x^* = L_o + u_D(L_o/u_D) \quad ,$$

that is, $x^* = 2L_o$. If this position is set equal to the rupture distance, then the condition for the minimum virtual column length is $L_{o_{min}} = x_{B/2}$. Using Eq. (25), the corresponding minimum required dispensed volume of liquid is

$$V_{F_{min}} = \frac{\pi D_N^2 x_B}{8} \quad .$$

At large liquid Weber numbers, Eq. (23) becomes

$$x_B \doteq 1.09 \; D_N We_\ell^{1/2}$$

so that in this regime

$$V_{F_{min}} \doteq 0.428 \; u_D \left(\frac{\rho_\ell D_N^7}{\sigma_\ell} \right)^{1/2} \quad . \qquad (26)$$

A plot of this equation for water and heptane at an injection velocity of u_D = 60 m/s (200 ft/s) is given in Figure 16.

Tests with heptane discharged vertically through a 2.5 cm (1 in.) diameter nozzle at u_D = 60 m/s (200 ft/s) were carried out to determine if this anticipated phenomenon is in fact operative. The minimum volume estimated by Eq. (26) under these conditions is $V_{F_{min}} \doteq 0.012\ m^3$ (3.2 gal). This is about half the capacity of the linear dispenser so that testing both at dispensed volumes above and below the predicted minimum was possible. Results from these experiments are plotted in Figure 17. Reach measurements were made from films taken during the tests. These were checked against measurements taken from a simple hand-held sight stick. Reduced reach was experienced when less than $0.0076\ m^3$ (2 gal) of heptane was dispensed. These results are certainly in the predicted direction but it is felt that more tests will be required to conclusively verify the tail breakup effect.

Before the tail of an impulsive jet emerges, the shape of the jet spray in the immediate vicinity of the nozzle is conical. This is due to surface atomization and subsequent air entrainment of droplets by the two-phase (droplets/air) mixture in that region. The remaining spray column shape is roughly cylindrical except at the jet head. After the tail emerges the spray column also becomes cylindrical near the nozzle. This can be seen in Figures 14 and 15.

The average spray column width and height continue to increase for a considerable time after dispensing has ended. This is evident in Figures 18-20. (The dispensing times for all tests plotted in these figures were less than 0.6 s.) Figure 18 shows the increase in average jet width as a funtion of time and Figures 19 and 20 are plots of the head trajectories of characteristic vertical jets. In both of the latter two figures, a calculated trajectory assuming simple

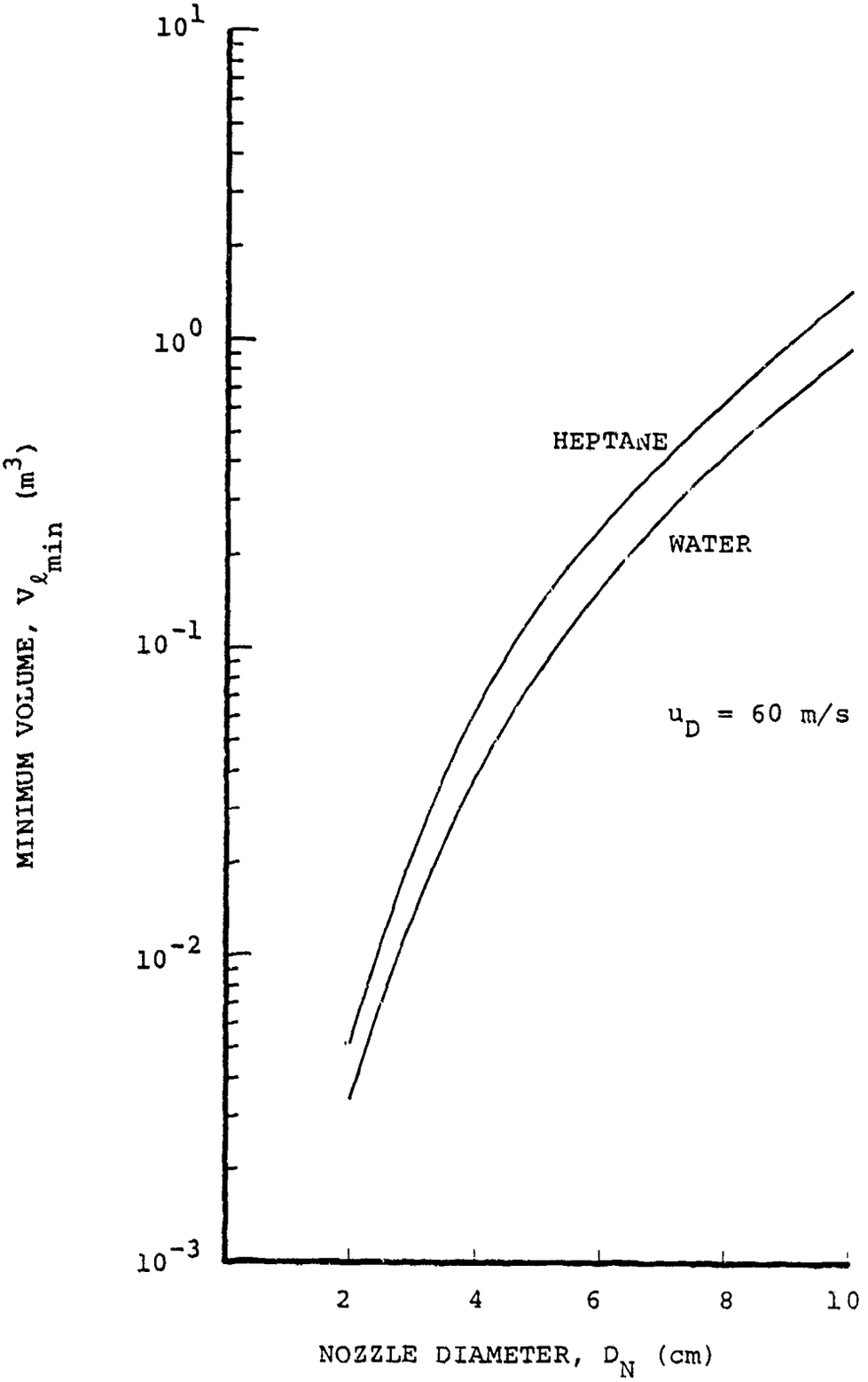

Figure 16. Estimated minimum dispensed liquid volume versus nozzle diameter.

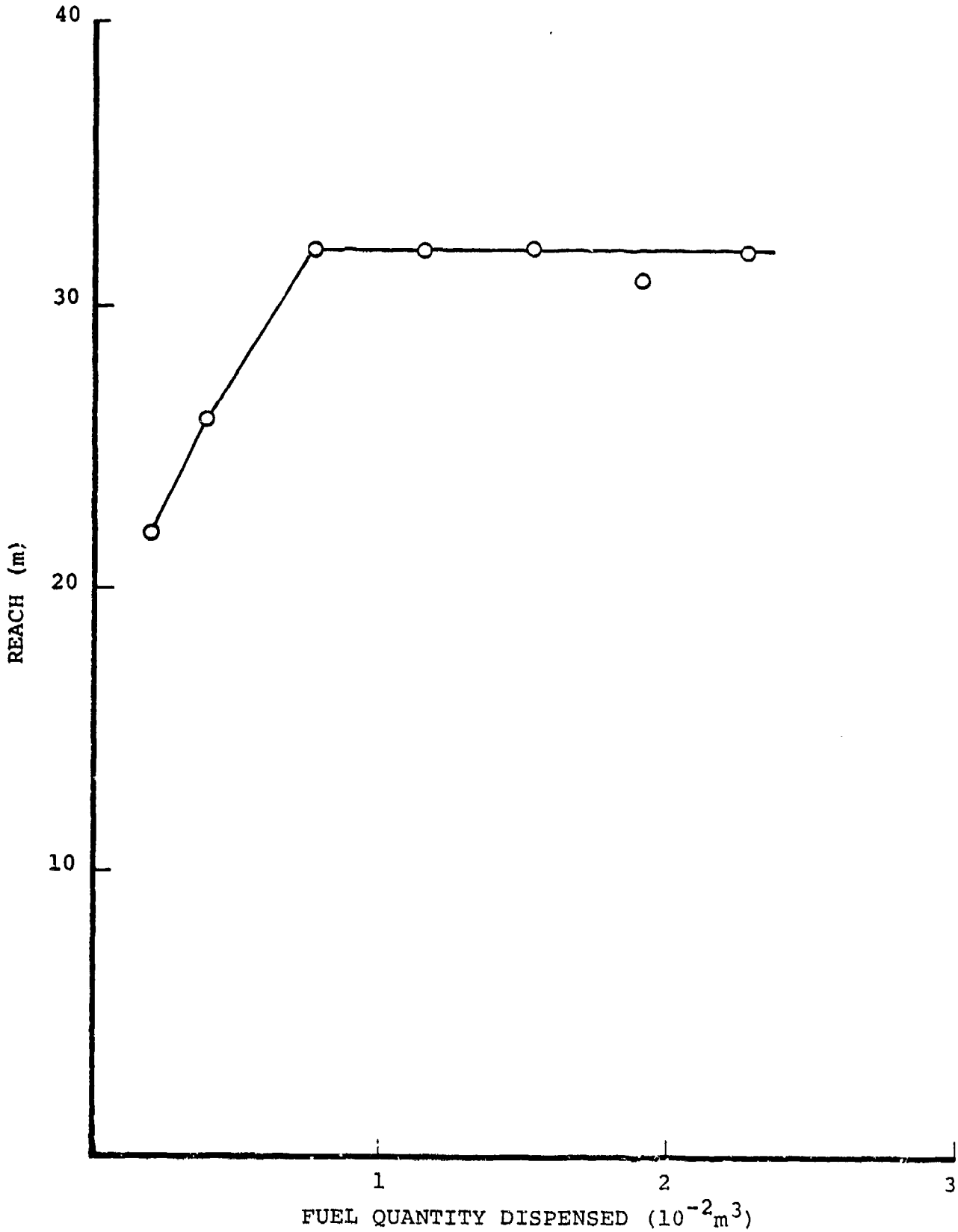

Figure 17. Ultimate jet reach vs. fuel quantity dispensed. (2.54 cm (1 in.) diameter nozzle, heptane, nominal driving pressure = 1.23 MPa (180 psi)).

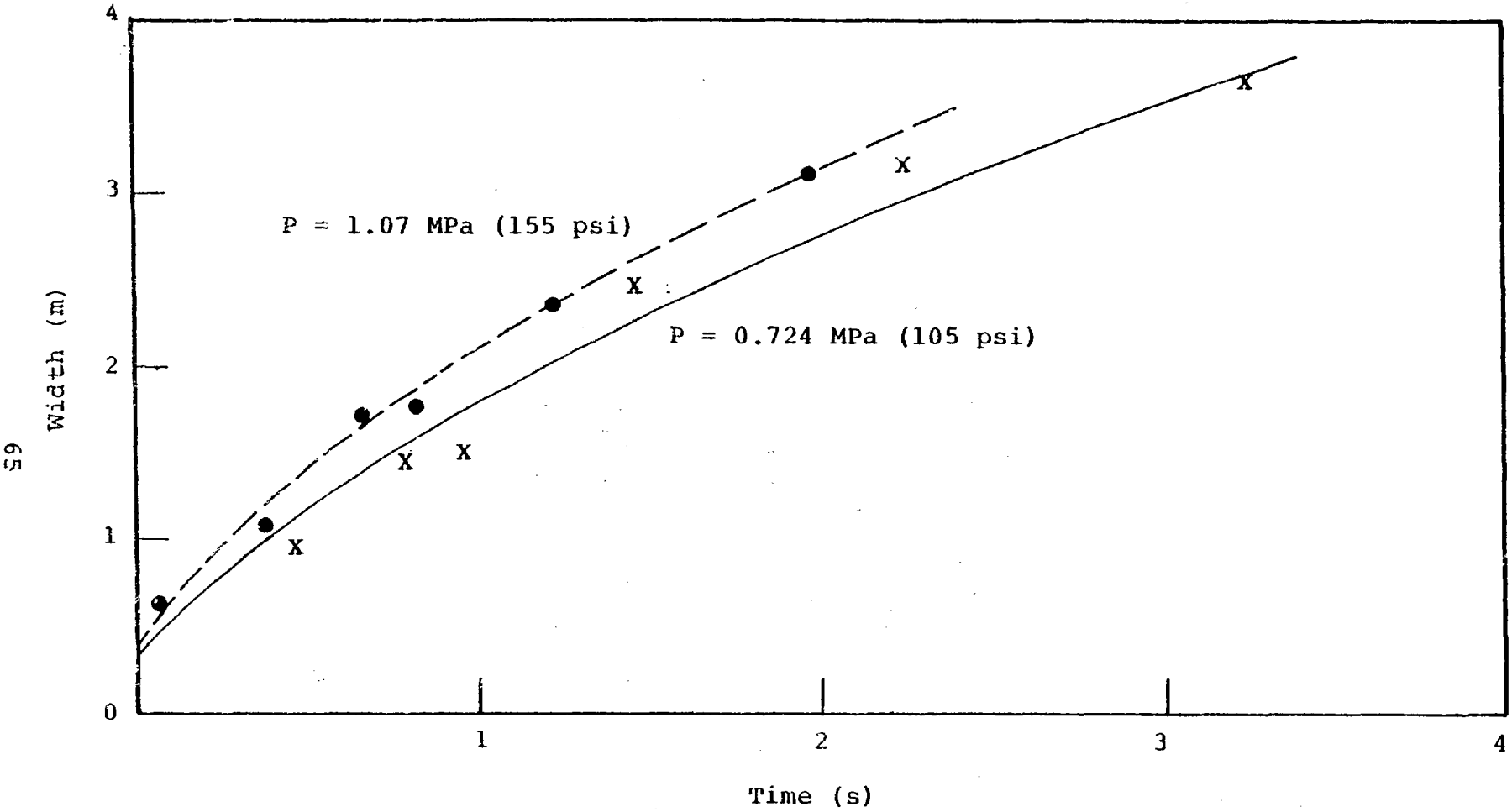

Figure 18. Average jet width vs. time for propylene oxide jet from 1.91 cm (0.75 in) diameter nozzle.

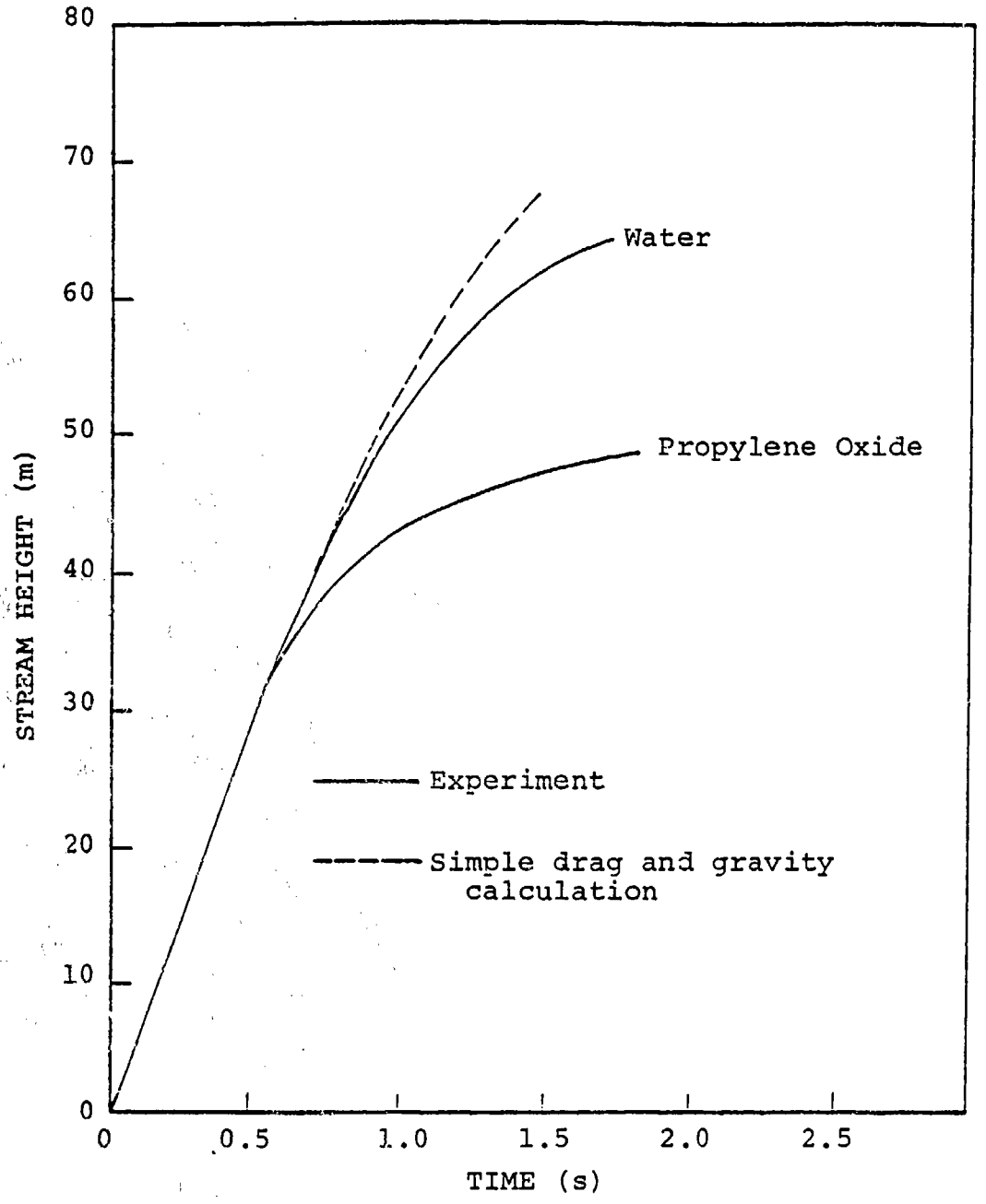

Figure 19. Comparison of water and propylene oxide stream height from two experiments involving projection from a 3.81 cm (1.5 in.) diameter nozzle at initial velocities of 72 m/s (236 ft/s).

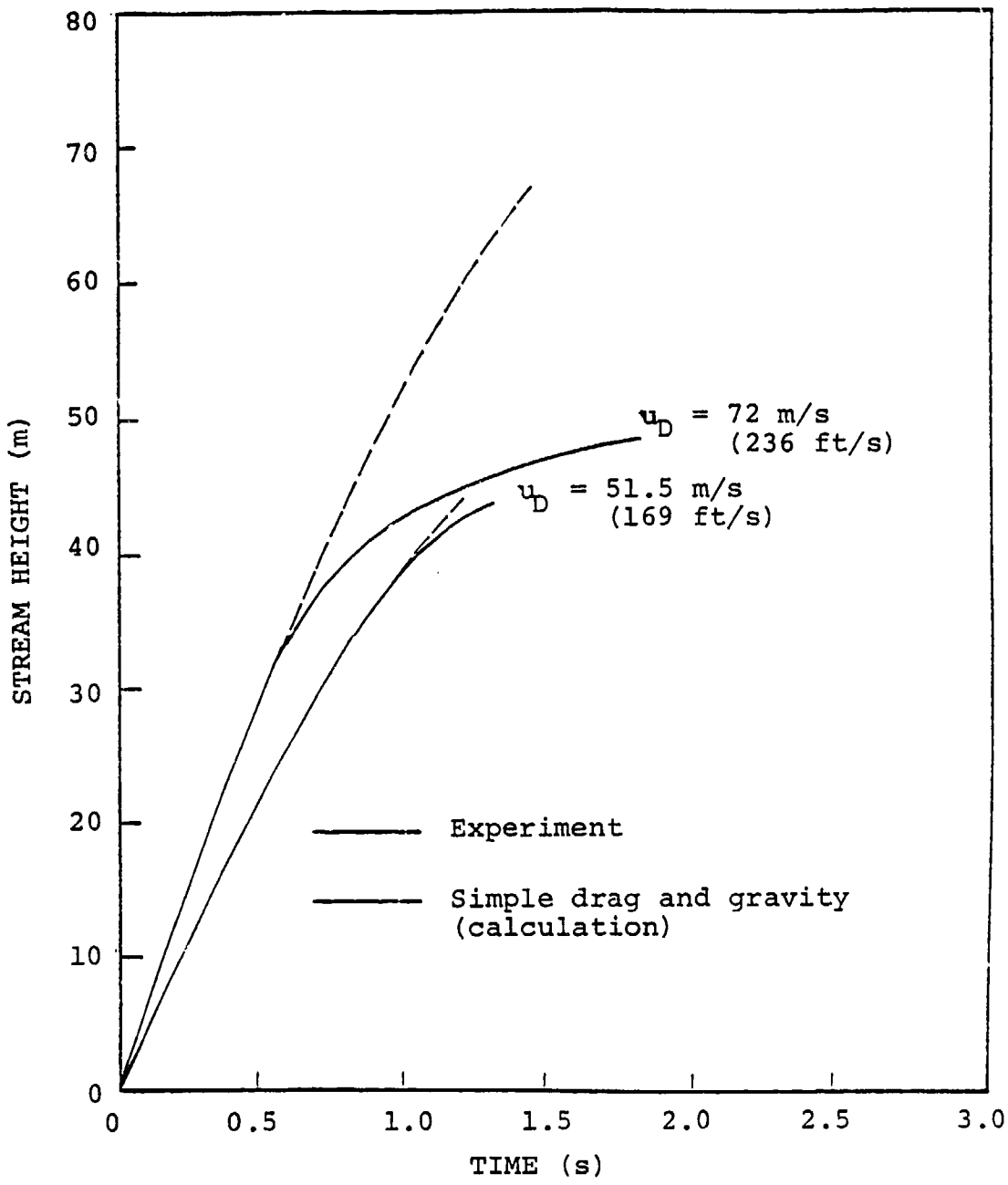

Figure 20. Comparison of stream height as a function of time for two experiments involving the projection of propylene oxide from a 3.81 cm (1.5 in.) diameter nozzle.

lateral aerodynamic surface drag in conjunction with gravitational deceleration has been plotted for reference. Below some breakaway point this curve can be made to agree quite well with the measured trajectories using a drag coefficient of $C_D = 0.25$. The influence of gravity is small compared to the aerodynamic drag. The rapid reduction in jet velocity beyond the breakaway point is presumably associated with aerodynamic drag on spray droplets following jet rupture. The breakaway points in these experiments did not however correlate with the rupture distances given by either Eq. (22) or Eq. (23).

Ultimately the jet attains a trajectory maximum after which the spray droplets vaporize or else fall partially or fully to the ground, depending on the liquid volatility and droplet size. Jet widths in excess of 250 nozzle diameters have been observed at these late times. However the jets are nearly if not fully atomized at much earlier times. Since it is of importance to minimize spray formation times, the earliest moment at which the jet has developed into a detonable cylindrical cloud is of interest. On the films of impulsive jets it appears that this moment occurs shortly after the tail reaches the vicinity of the rupture point or the breakaway point. On that basis a tentative definition for the formation time of an impulsive jet, measured from the beginning of the dispensing period, is

$$t_F \equiv t_D + \frac{500 D_N}{u_D} \quad ,$$

where t_D is the dispensing time. Making use of Eq. (18) this can be written

$$t_F = \frac{1}{u_D} \left(\frac{4V_F}{\pi D_N^2} + 500 D_N \right) \quad . \tag{27}$$

This definition is somewhat arbitrary. The second term represents an upper limit estimate of the time for the contiguous jet tail to reach the rupture point. In writing that term it was assumed that normal jet rupture occurs at distances less than 1000 nozzle diameters and that the jet tail moves at twice the velocity of the head. Since ultimate jet reach is typically 1200-2000 nozzle diameters it represents a reasonable upper estimate.

Some measurements of impulsive jet reach, taken approximately at the formation time, are given in Figure 21 as a function of jet velocity. In this figure the fuel is heptane, the nozzle size is 1.3 cm (0.5 in.), and 0.0064 m^3 (1.7 gal) of fuel were dispensed. The reach behavior of impulsive jets appears to be similar to that of steady jets when sufficient liquid is dispensed. Beyond a certain minimum jet velocity the reach appears to be essentially constant. The knee of the reach curve (the point at which the curve begins to level off) also corresponds roughly to the minimum jet velocity for which atomization can be visually observed.

In future work, it is recommended that jet reach and width at the formation time be measured systematically as functions of jet velocity and diameter. The minimum volumes of fuel that can be dispensed in order to achieve these reaches, and the minimum jet velocity for sufficient atomization should be determined.

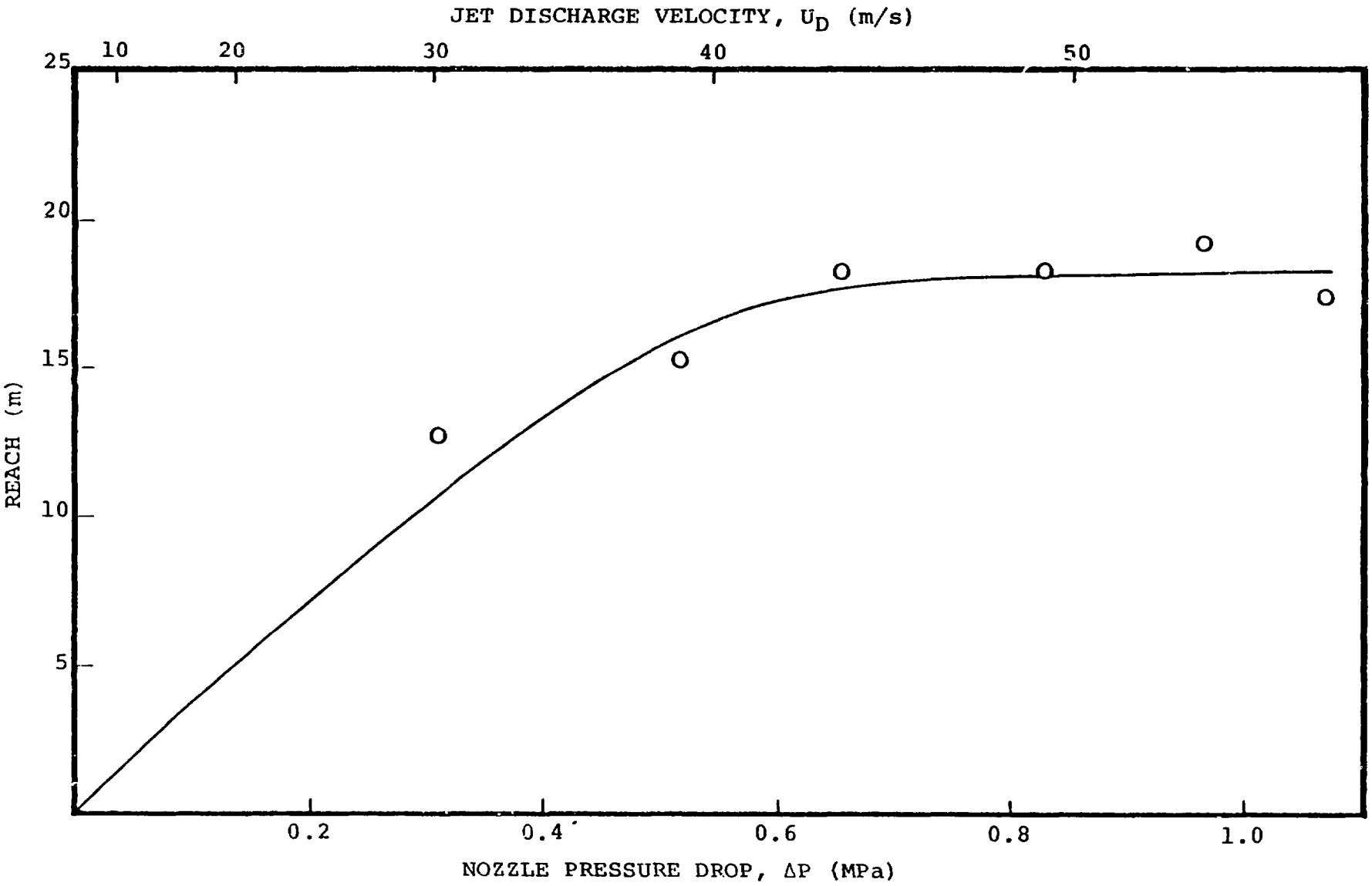

Figure 21. Ultimate jet reach versus pressure drop and velocity for heptane, 1.27 cm (0.5 in.) diameter nozzle.

SECTION 4

HEMISPHERICAL FUEL-AIR CLOUD FORMATION

4.1 CLOUD SIZE REQUIREMENTS

The volume of the fuel-air cloud and the quantity of fuel required are fixed by the nuclear yield to be simulated. The relationships are not straightforward but are asociated with the energy release available through combustion of the fuel-air cloud and with the way in which this energy is disposed hydrodynamically.

The total energy release resulting from the detonation of a fuel-lean or stoichiometric fuel-air cloud is

$$E_{O_{T,F}} = m_F H_C \tag{28}$$

where m_F is the mass of fuel in the cloud and H_C is the low-temperature, constant pressure heat of combustion per unit mass of fuel. This expression assumes that the considerably dissociated detonation products achieve low temperature equilibrium during the expansion that follows airblast development from the fully reacted cloud.

Due to the finite spacial and temporal distribution of the energy released, the airblast produced by a fuel-air explosion differs from a point source blastwave of the same energy, $E_{O_{T,F}}$. However, at fixed range from an FAE, the variables of interest (such as overpressure and overpressure impulse) may individually or collectively exhibit point-source (or nuclear source) characteristics. If so, it is possible to define an effective energy, $E_{O_{E,F}}$ for the FAE airblast at that range. This is the energy of a point or nuclear source which at the same range would yield the same values for the variable or variables of interest.

In general, the value of $E_{o_{E,F}}$ so determined will vary with range and with the particular blast variable(s) being considered, as well as with the reference airblast itself (point source or nuclear). Over limited range intervals, the variation in $E_{o_{E,F}}$ with range may, however, be small enough that a single average value can be used with acceptable accuracy. The extent to which a single value of $E_{o_{E,F}}$ is successful in specifying FAE/nuclear airblast equivalence has been examined in the present investigation. The procedure followed to establish a value for $E_{o_{E,F}}$ is discussed in Section 5. It has also been found useful for discussion purposes to normalize the effective blastwave energy by defining an effective airblast efficiency; i.e.,

$$\eta_F = \frac{E_{o_{E,F}}}{E_{o_{T,F}}} \quad . \tag{29}$$

It should be emphasized, however, that the value of η_F does not physically represent the amount of energy that is partitioned to hydrodynamic blast.

Substituting Eq. (28) into (29) and solving for m_F gives

$$m_F = \frac{E_{o_{E,F}}}{\eta_F H_c} \quad . \tag{30}$$

This is the quantity of fuel required in order to yield a specified effective blast source energy on the presumption that η_F is known. The quantity of air that is required for combustion with this amount of fuel is simply

$$m_a = m_F/\phi_A \quad , \tag{31}$$

where ϕ_A is the fuel-air ratio by mass. (Stoichiometric proportions are designated by ϕ_A^*.)

The size of the cloud that contains the required amount of air depends on whether the fuel is dispersed as a vapor or as a spray. If dispersed as a condensed spray, the volume occupied by the spray, V_F, is normally negligible compared with the volume occupied by the air, V_A. I.e., from Eq. (31),

$$\frac{V_F}{V_A} = \frac{\rho_A \phi_A}{\rho_\ell} \quad .$$

This ratio is typically of the order 10^{-3} to 10^{-4}. The size of the fuel-air cloud in this case is essentially the volume of air containing mass m_a. That is,

$$V \doteq V_A = \frac{m_a \bar{R} T_a}{P_a \bar{W}_a} \quad .$$

Using Eq. (30) and (31) and solving for the radius of a hemisphere containing this volume leads to

$$R_{c_s} = \left(\frac{3 \bar{R} T_a E_{o_{E,F}}}{2\pi \eta_F \phi_A \bar{W}_a P_a H_c} \right)^{1/3} \quad . \tag{32}$$

If on the other hand, the fuel is dispersed as a vapor, or as a spray which then fully evaporates, the volume of the mixture is

$$V = \frac{m \bar{R} T_a}{P_a \bar{W}} \quad ,$$

where the mixture mass and molecular weight are related to those of the fuel and air by

$$\frac{m}{W} = \frac{m_F}{W_F} + \frac{m_a}{W_a} \quad .$$

These relations, along with Eqs. (30) and (31) give a cloud radius of

$$R_{C_v} = \left[\frac{3\bar{R}T_a E_{o_{E,F}}}{2\pi\eta_F P_a H_c} \left(\frac{1}{W_F} + \frac{1}{\phi_A W_a} \right) \right]^{1/3} \quad . \tag{33}$$

The difference in cloud size calculated in these two ways is small. For example, for $E_{o_{E,F}} = 2.09 \times 10^{12}$ J (the effective far field blast source energy of a 1 KT nuclear explosion), assuming a stoichiometric mixture of propylene oxide and air, and using $\eta_F = 0.744$*, a spray cloud radius of $R_{C_S} = 69.2$ m and a vaporized cloud radius of $R_{C_V} = 70.4$ m are predicted. (Physical properties of selected fuels are given in Table 1.)

The temperature and pressure used in the preceding example were ordinary atmospheric values. Actually, if the cloud is formed as a spray and then evaporates, the cloud temperature will be reduced somewhat. To estimate the magnitude of this effect, the evaporation can be treated as a simple heat removal process from the air, for which at constant pressure the energy equation is

$$Q = H_2 - H_1 \quad .$$

---

*This value was determined experimentally in small-scale FAE tests using propylene oxide and is discussed in Section 5.

Table 1. Properties of selected fuels.

Fuel	ρ_ℓ (kg/m^3)	μ_ℓ (N-s/m^2)	σ_ℓ (N/m)	W (kg/kmol)	ϕ_A*	H_c (1) (J/kg)	L (2) (J/kg)
Propylene oxide	831	3.27×10^{-4}	0.023	58.1	0.106	3.27×10^7	5.27×10^5
Heptane	683	4.14	0.0209	100.0	0.0662	4.44	3.18
Kerosene	819	14.9	0.0268	150.0	0.0684	4.72	2.91
Gasoline	751	5.29	0.0226	120.0	0.0664	4.39	3.39
Ethylene oxide	880	3.1	0.0245	44.0	0.128	2.76	5.82

(1) Heat of combustion per unit mass of fuel, lower value

(2) Latent heat of vaporization

The heat effectively added is $Q = -m_F L$ where L is the latent heat of vaporization per unit mass of fuel. Treating the air as calorically perfect, the energy equation then gives

$$-m_F L = m_a C_{P_A} \Delta T$$

or

$$\Delta T = -\phi_A L / C_{P_A} \quad . \tag{34}$$

This effect can account for an absolute temperature drop on the order of 10% which may be sufficient to be considered in cloud formation schemes involving fuel spray evaporation.

4.2 FUEL DISTRIBUTION UNIFORMITY

At the present time it is felt preferable to form spray clouds that will not largely vaporize prior to detonation initiation. This implies low vapor-pressure fuels which are advantageous in that boiling-induced jet breakup (Reference 30) is minimized or eliminated. The more essential basis for this judgement, however, derives from fundamental differences between gas- and two-phase detonations.

Detonations which occur in premixed gas-phase reactants possess a hydrodynamic reaction zone that is typically no more than a few millimeters thick. The reaction zone is characterized by regularly recurring localized ignition centers. Fast reaction at the ignition centers produces blastwaves which interact with the detonation front and with adjacent, similarly produced blastwaves. Their collisions in the directions transverse to the wavefront produce new ignition centers. Combustion is also augmented behind these transverse shocks. The

propagation velocity and detonation limits of gas-phase detonation depend on the stoichiometry (at given pressure and temperature). This is because the fuel and oxidizer are mixed on a molecular level in advance of the detonation so that reaction mechanisms involving all of the species initially present can occur at once in the gas-phase and are limited only by the chemical kinetics. A fuel-air explosion to be generated from a cloud in which the fuel is initially fully vaporized should therefore possess a near-stoichiometric global equivalence ratio to optimize the energy release per unit mass of mixture. Moreover, uniform mixing throughout the FAE cloud would represent an engineering objective for the fuel disseminator in this case. Either fuel-rich or fuel-lean pockets in the cloud would reduce the total cloud energy release.

Detonations in two-phase mixtures in which the fuel is dispersed as a fog with very small ($\sim$2 μm) droplets exhibit most of the characteristics of gas-phase detonations (Reference 31). However, when the droplets are larger the time for their conversion to vapor is increased. The reaction zone of a detonation in such a spray is protracted and its character becomes significantly altered (Reference 32-36). Mixing of fuel with the oxidizer occurs only after it has been removed from the droplets by a process of mass stripping. This results while the droplets are accelerating in the convective oxidizer gas flow behind the detonation shock front. Stripping appears to involve liquid boundary layer removal, Helmholtz surface waves, and shattering from a Taylor acceleration instability.

With some fuel/oxidizer combinations, fuel removed from the droplets in the early stages of stripping accumulates in the recirculation zones of the individual droplet wakes. After a delay period localized explosions occur in these wakes. Other fuel/oxidizer combinations do not exhibit explosive

ignitions. In all cases, however, the energy release rate in the reaction zone is limited by the mass stripping processes rather than by chemical kinetics. The long reaction zones which result are responsible for a generally one-dimensional structure that is very different from that of gas-phase detonations.

Because the mass-stripping process in two-phase detonations is rate limiting, the initial fuel (droplet) distribution uniformity is not as critical as it is in gas-phase detonations. The fuel that is stripped from a given droplet mixes in the intensely turbulent reaction zone with gases originating an appreciable distance away. The droplets can thus be conceptually viewed as moving sources of fuel vapor within the well-stirred environment of the reaction zone.

The propagation velocity of a fuel-lean two-phase detonation depends as would be expected on the global fuel/air stoichiometry. However, evidence exists in the literature indicating that condensed-phase fuel in excess of the amount required for a globallly stoichiometric mixture does not participate in the detonation. In one study (Reference 37) identical detonation velocity and structure results were obtained with stoichiometric and with very fuel-rich two-phase (spray) mixtures. In a similar investigation (Reference 38) the fuel-rich limit could not be determined. Additional studies (References 31, 39, and 40) have demonstrated detonability of fuel <u>films</u> at global equivalence ratios as high as 600. All these results suggest that the condensed fuel vaporizes, mixes with the oxidizer gas, and reacts as quickly as it is removed from the parent droplet (or liquid layer, in the case of films). Except in the final stages of oxygen consumption, combustion of the fuel vapor therefore continuously occurs in a globally fuel-<u>lean</u> environment, regardless of the quantity of fuel that is latently available in the condensed-phase at any given moment. Combustion

essentially ceases when all of the oxygen in the oxidizer has been consumed. It appears that fuel vapor added to the products by further droplet stripping beyond that point does not affect the detonation, even though the equilibrium composition of the products would be shifted. All these processes are absent from a gas-phase detonation in which the fuel and oxidizer are premixed on a molecular level so that all of the fuel initially present affects the instantaneous combustion chemistry, as mentioned earlier.

The requirements for uniform fuel distribution and local stoichiometry in the formation of a two-phase fuel-air cloud are therefore not exacting, provided that some moderate sacrifices in fuel economy can be tolerated. Any quantity of liquid fuel can evidently be dispersed into a given volume of air provided that (1) the fuel in condensed form does not occupy a significant fraction of the total spacial volume either locally or globally, and (2) the droplets are not spaced so far from one another in any local region as to preclude involvement of all of the adjoining air in the combustion processes*. When these two conditions are met, the total energy release is expected to be proportional to the mass of air enveloped by the cloud, and to be relatively independent of the amount of fuel, provided an excess above stoichiometric exists everywhere. The behavior expected of the detonation is as though the cloud were uniformly stoichiometric. Only the expansion wave properties would be modified.

---

*In this context is it noted that typical droplet spacings are on the order of ten droplet diameters in documented spray detonations.

4.3 CLOUD FORMATION FROM MULTIPLE JETS

A current objective has been to generate hemispherical clouds comprising unevaporated fuel sprays that are distributed so as to be at least sightly fuel-rich throughout. The actual fuel distribution however is produced in a very complex way which at present is not fully understood. The fuel distribution is affected by the breakup and spreading processes of individual jets from which the hemispherical cloud is to be formed, and by the interactions between adjacent jets including the manner in which they overlap.

The effect of adjacent jet overlap on the fuel distribution in a hemispherical cloud can be assessed to first order by assuming that the spray cloud from each individual jet is cylindrical and that adjacent spray cylinders diffuse into one another without interaction and geometric distortion. These assumptions may be reasonable for dilute sprays as is the case in FAE clouds. If two adjacent spray cylinders of radius R_J originate from the same point (the nozzle cluster), and if the angle between their centerlines is θ, then it is straightforward to show that they will overlap to a distance

$$R_F' = \frac{R_J\sqrt{2(1 + \cos\theta)}}{\sin\theta} \qquad (35)$$

from the vertex. If $R_F < R_C$ (the cloud radius), then at radii between R_F and R_C the spray cylinders will not overlap. In this case the cloud will consist of a core region of overlapped spray cylinders and an outer region characterized by non-overlapping finger-like projections (the appearance has been compared to that of a sea urchin). It is clearly desirable to design the dispensing system so that $R_F = R_C$. Since typically $R_J/D_N \sim 50$ and $R_C/D_N \sim 1500$ at the formation time, setting $R_F = R_C$ in Eq. (35) implies $\theta \sim 3.8°$.

Due to jet spray overlap, a uniform spray distribution in the hemispherical cloud would not result from uniform distribution in the individual spray cylinders. The total mass of fuel in one isolated spray cylinder is m_F/N where N is the total number of jets used to form the cloud. If the spacial density of fuel in this cylinder is ρ_F', then clearly

$$\frac{m_F}{N} = \int_o^{R_C} \rho_F' A_J dR \quad . \tag{36}$$

In this equation, A_J is the cross-sectional area of the spray cylinder (jet) and ρ_F is considered to be a function of R. Now the contribution by this single jet to the total mass of fuel in a hemispherical shell of thickness dR at radius $R < R_C$ from the nozzle cluster is

$$dm_F' = \rho_F' A_J dR \quad .$$

Therefore the total mass in the shell contributed by all N overlapping jets, assuming that $R_F = R_C$, is

$$dm_F = N dm_F' = N\rho_F' A_J dR \quad .$$

The volume of this differential shell is $dV = 2\pi R^2 dR$. Hence the fuel spray density at radius R resulting from the overlapping jets has an average value of

$$\bar{\rho}_F = \frac{dm_F}{dV} \quad .$$

that is,

$$\bar{\rho}_F = \frac{NA_J\rho'_F}{2\pi R^2} \quad . \tag{37}$$

It is emphasized that this is an average value. Since the degree of overlap varies with radius the distribution would actually vary additionally with both azimuth and elevation.

The implication from Eqs. (36) and (37) is that, as a result of jet spray overlap, uniform average cloud density obtains only when the spray density of individual jet cylinders increases as R^2. That is, if $\rho'_F \propto R^2$, those two equations lead to

$$\bar{\rho}_F = \frac{3m_F}{2\pi R_C^3} \quad .$$

Any other variation in ρ'_F will result in a non-constant $\bar{\rho}_F$. This is somewhat fortuitous. Although attempts have not been made to measure ρ'_F experimentally, on the films it appears subjectively that the spray in fully-formed, impulsive single jets is in fact distributed non-uniformly. The spray density near the nozzle is low and it increases gradually in what appears to be an accelerating fashion with respect to increasing radius. This has provided some encouragement that hemispherical clouds with adequate spray distribution uniformity can in fact be formed.

4.4 EXPERIMENTAL INVESTIGATIONS

Experiments to investigate hemispherical cloud formation by means of multiple, radially injected impulsive jets have been conducted on a small scale ($R_C \doteq 4.6$ m (15 ft)). Both the U-tube and linear dispensers have been used at different

times. Nozzle clusters have consisted of a number of countersunk radial holes drilled into machined hemispherical steel or spun aluminum domes. One of these domes in shown in Figure 22. This particular dome nozzle was designed in accordance with Eq. (35); i.e., with $R_F = R_C$. Other domes have been tested having 600 to 1400 holes (nozzles). Hole sizes between 1.6-3.2 mm (1/16-1/8 in.) and dispensing pressures from 0.34-1.4 MPa (50-200 psig) have been tested. In most of the experiments the volume of liquid dispensed was 0.0265 m^3 (7 gal). Liquids tested have included water, propylene oxide and heptane.

Examples of tests illustrating the features of these clouds are shown in Figures 23 and 24. The four clouds that appear in Figure 23 were generated from domes having 600 3.2 mm (1/8 in.) diameter holes. The photogrpahs are frames from high-speed films. The angle between jets was about 6°, which is considerably greater than the value of 3.8° discussed earlier as being required for complete jet spray overlap throughout the cloud. The resulting shape (which has been likened to that of a sea urchin) is apparent in Figures 23(b) and (d).

Since is advantageous to minimize the number of nozzles (so as to reduce the complexity and cost of the dispenser), it was at first felt that the problem of inadequate overlap could be overcome by dispensing at higher pressures. That would produce individual jet sprays of greater diameter, thereby increasing R_F. Presumably $R_F = R_C$ could in that way be reached without changing θ (see Eq. (35)). Hence the number of nozzles could be held to 600. Dispensing at higher pressures also would increase the jet velocity, reduce the dispensing time and the cloud formation time, and produce a more finely atomized spray, with little if any effect on jet reach.

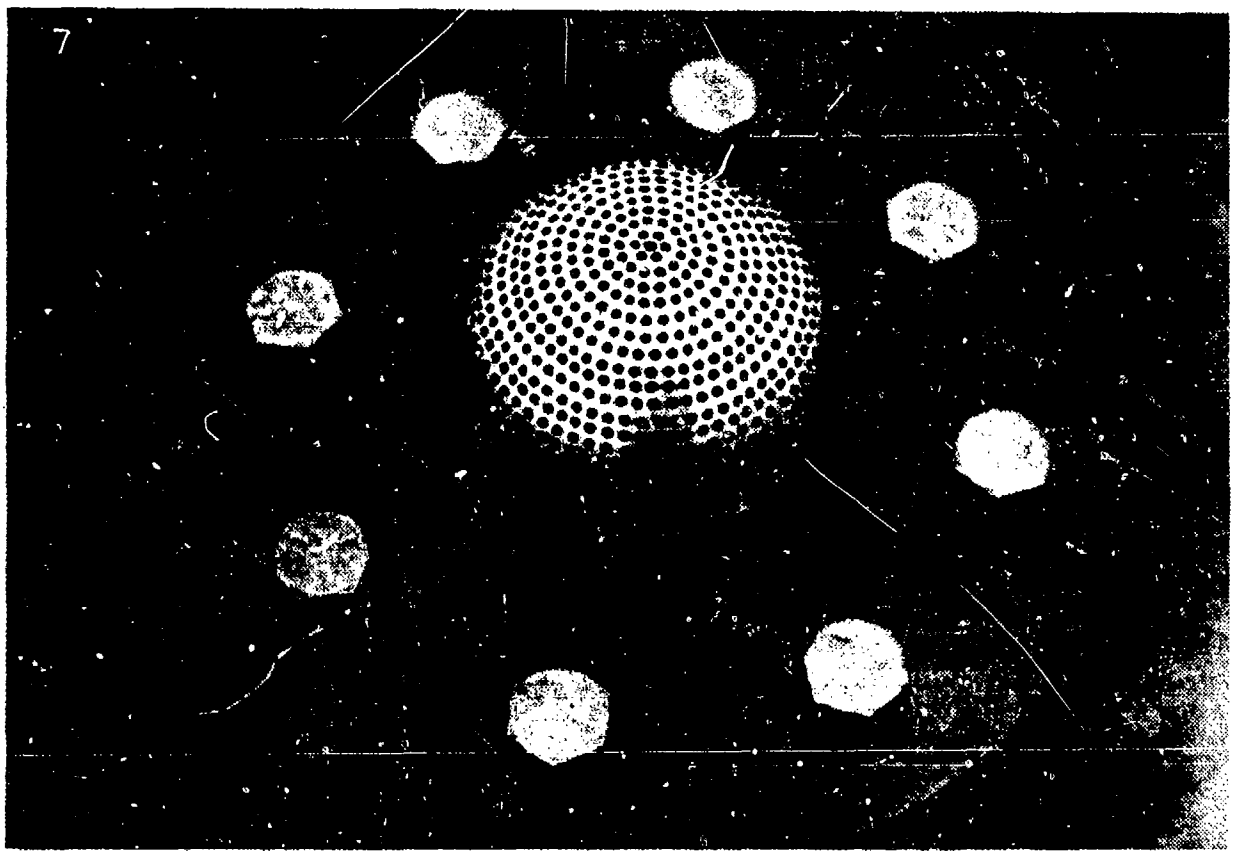

Figure 22. Photograph of 1400-nozzle head used with linear dispenser to produce hemispherical fuel-air clouds. Outside diameter is 12.7 cm (5 in.).

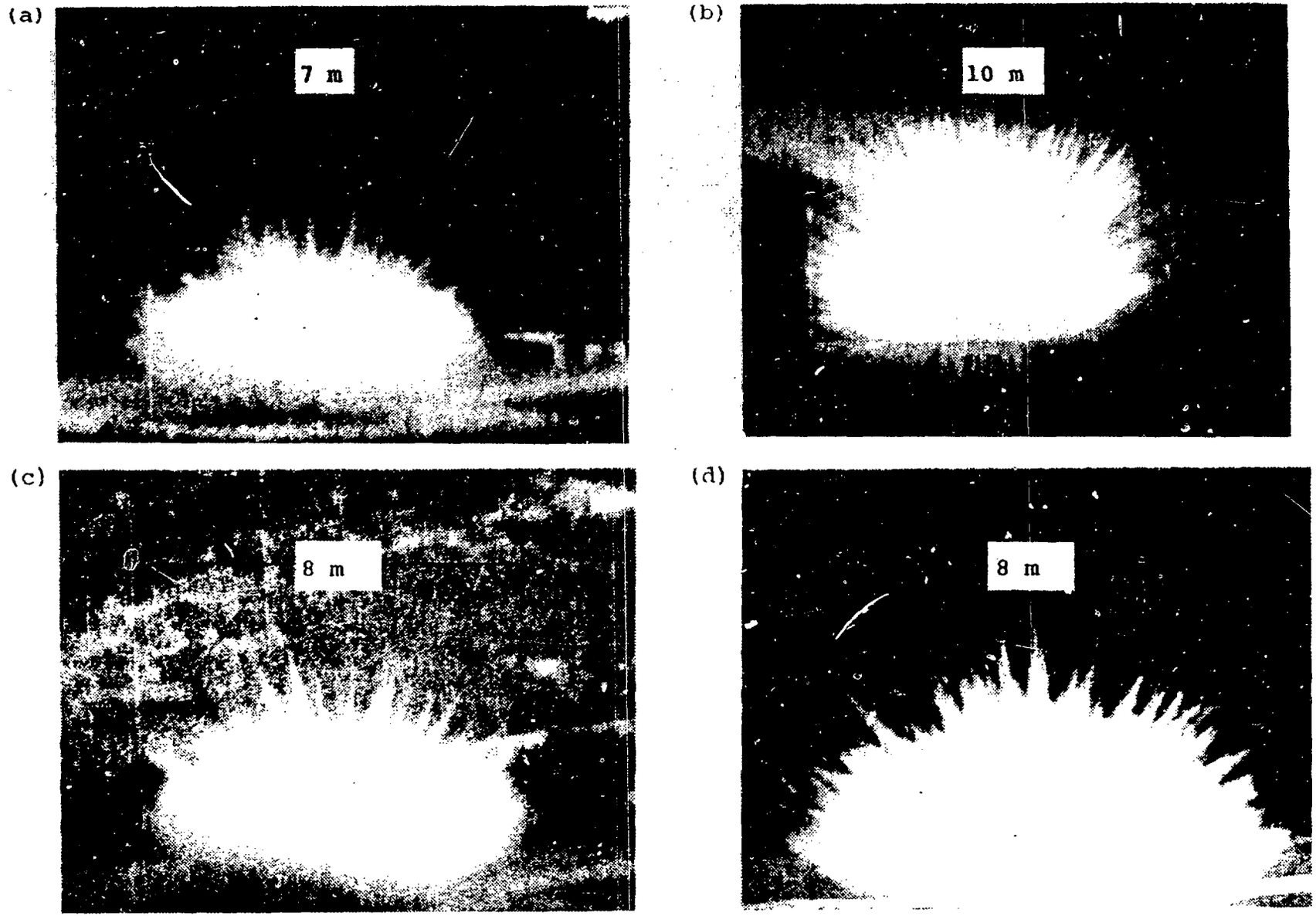

Figure 23. Examples of clouds formed with 600-nozzle dispenser head. (a) Propylene oxide at 1.24 MPa (180 (psi), (b) P.O. at 0.414 MPa (60 psi), (c) heptane at 1.24 MPa (180 psi), (d) heptane at 0.965 MPa (140 psi). Dimensions given on the photographs are approximate.

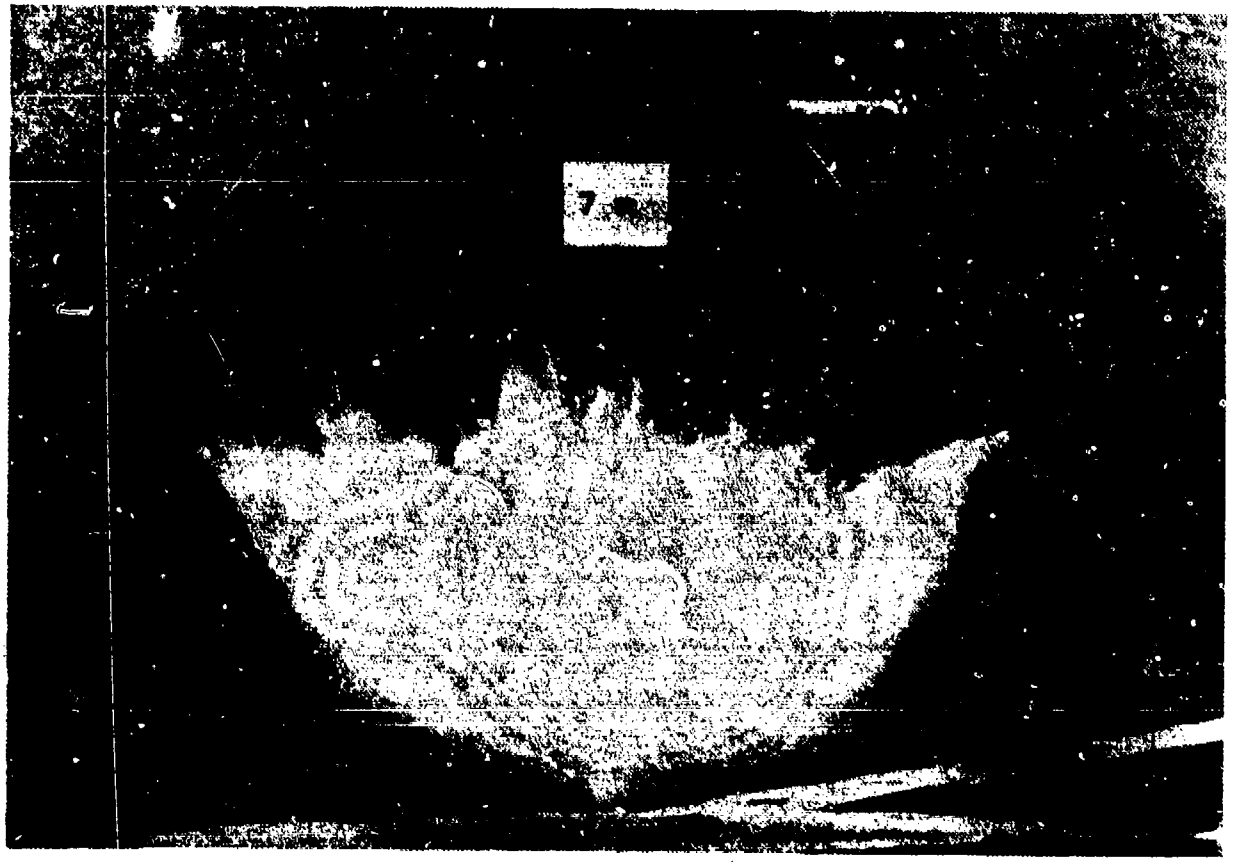

Figure 24. Cloud formed with 1400-nozzle dispenser head. Heptane at 0.965 MPa (140 psi). The dimension given on the drawing is approximate.

Unfortunately, it was found that increases in jet velocity lead to cloud shape distortions. These distortions are the result of air motions induced by momentum transfer from the expanding spray. The character of the distortion changed from relatively insignificant edge lifting to severe, large-scale dishing as the jet velocity was increased. The magnitude of these effects can be seen by comparing Figures 23(a) and (b) or Figures 23(c) and (d).

Based on these results it was concluded that jet overlap would have to be accomplished by increasing the number of nozzles rather than by increasing the jet velocity. The number of nozzles was accordingly increased from 600 to 1400, which gives $\theta \sim 4°$. Clouds produced with the 1400-nozzle head were then very uniform in visual appearance and did not have the spiked sea urchin character. However, they were now surprisingly dished, even at pressures as low as 0.3 MPa (45 psi) which corresponds to a heptane jet velocity of 30 m/s (100 ft/s). This is illustrated by the example in Figure 24.

The origin of these cloud-shape distortions has been examined by observing the trajectories of spray droplets that are visible on the high-speed films. In some of the experiments, oblong (peanut-shaped) styrofoam packing material was stacked in a radial row along the concrete test pad, in a direction perpendicular to the camera line of sight. The motion of these lightweight chips was very clear on the film.

On the basis of observations from these experiments, the following explanation is offered. A sketch of an ideal, expanding hemispherical cloud is shown in Figure 25(a). The spray is distributed uniformly within the cloud and extends fully to the ground. As the front of the spray cloud advances, momentum is added continuously to newly and previously engulfed air by drag from the droplets. This sets the air in motion radially which lowers the center-cloud pressure and compresses

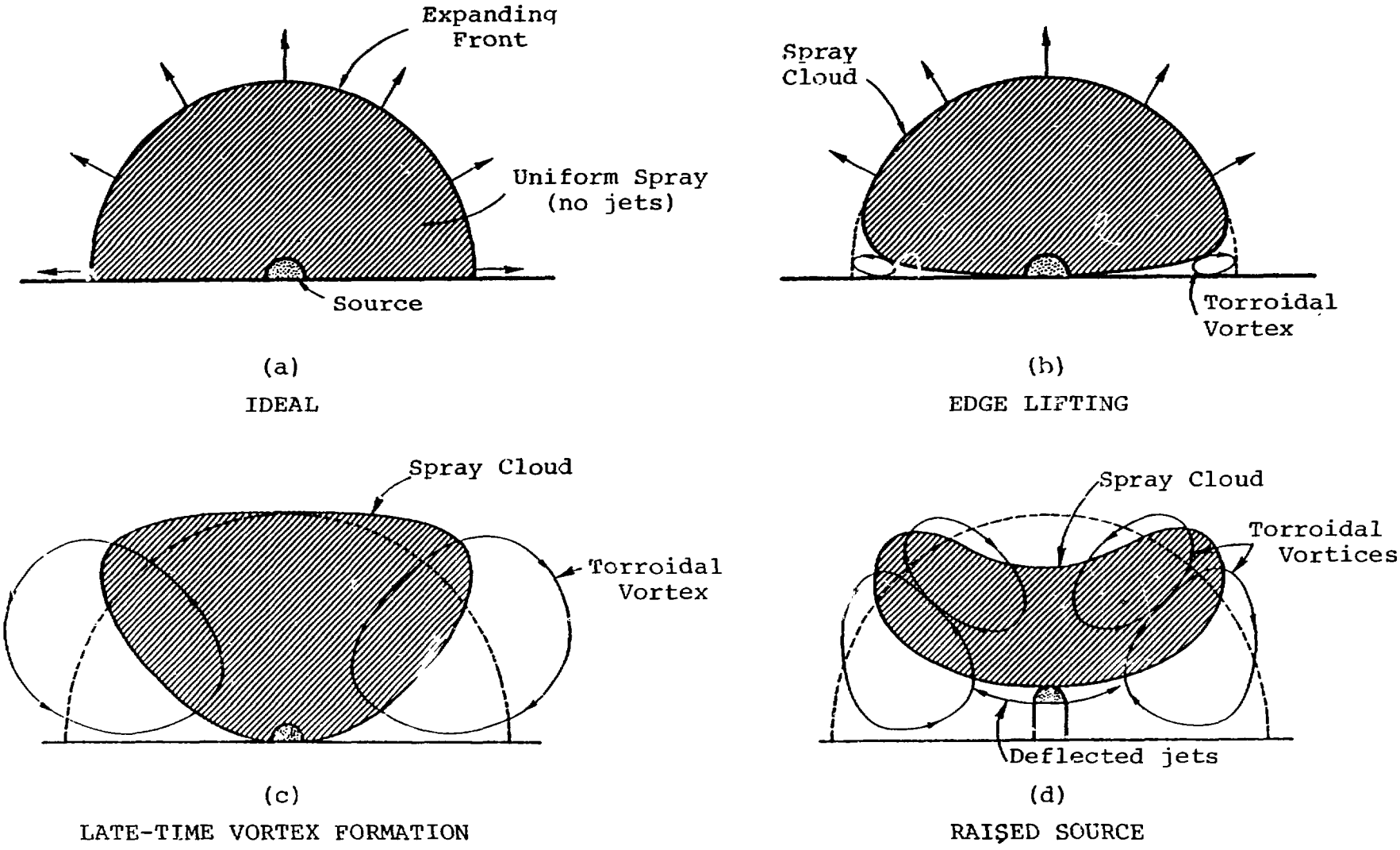

Figure 25. Distortions of expanding point-source spray clouds induced by aerodynamic interactions between spray and air. The dashed lines represent the desired hemispherical shape.

the air ahead of the expanding front. A pressure profile is therefore developed which rises from a subatmospheric value in the center of the cloud to an above-atmospheric level just ahead of the front, and then drops back to atmospheric pressure at a somewhat greater radius. Air flow continues to be outward from the center until the retarding internal pressure gradient becomes sufficiently steep as to stop the air movement locally.

This process cannot apply to the boundary layer. Near the ground the same radial pressure profile is impressed, but the air in this region experiences an additional, radially-inward acceleration due to viscous forces. Gas elements in the boundary layer will therefore be stopped before the air above it stops, and under continued action of the pressure gradient these will begin to flow toward the center. This movement is directed upward upon collision with outward moving or stagnant surface layer air, and a separation vortex results. In the case of an expanding hemispherical cloud this vortex would be torroidal in shape, as sketched in Figure 25(b). This vortex is believed to be responsible for cloud edge lifting.

At the end of the dispensing period the pressure gradient near the center of the cloud is no longer supported by a momentum influx from the spray nozzles. However droplets still in motion near the expanding front continue to drag on the air in that region. Air begins to accelerate towards the cloud center. This acceleration is greatest in the air layers on the underside of the cloud which do not experience droplet drag. The result is the development at late times of a large-scale torroidal vortex, as depicted in Figure 25(c).

If the dispenser source is raised above the ground, boundary layer effects no longer influence the cloud. However, large-scale vortices now begin to form immediately after the start of dispensing because the reduced center-cloud pressure in this case causes air to be drawn under the cloud, toward the

center. Vertical deflection of the horizontally directed jets has been observed in this case as these jets emerge from the nozzle cluster. When the large-scale vortex motion is sufficiently severe, secondary vortices are visible. The result is a dish-shaped cloud as sketched in Figure 25(d).

The distortions described are induced more readily in clouds with greater jet overlap, i.e., smaller θ. Air paths between the fingers of spiked clouds provide partial relief for some of the pressure gradients. The distortions are also aggravated by increased spray momentum and by decreased droplet size. Smaller droplets tend to follow the motion of vortices more readily, producing more pronounced cloud distortions. Since the size of the droplets generated by an atomizing jet decreases with increasing jet velocity, such increases very rapidly produce cloud shape distortions. Some control might be exercised over droplet size by appropriate fuel selection or through the use of additives, but for a given fuel the jet velocity must be limited. The relationship between the maximum tolerable jet velocity and cloud scale is not presently known since all of the experiments to date have been with 4.6 m (15 ft) radius clouds. This is an important area which requires further investigation.

4.5 DISPENSER SCALEUP REQUIREMENTS

Although all questions regarding scaleup of the impulsive cloud formation concept have not as yet been resolved, an attempt has been made with what is known to anticipate the fundamental design requirements of large dispensing systems. A computer program has been developed in which all presently recognized design constraints are considered and an optimum design within these constraints is sought. This program will be updated as the understanding of cloud formation improves. The program does not dictate all design details, but at present

it is assumed that a piston is incorporated in the design to act as an interface that separates the fuel being dispensed from the driver gases.

An outline flow diagram of the dispenser design code is given in Figure 26. The mass of fuel and the cloud radius required for a specified far-field, effective blast source energy are first calculated directly from Eqs. (30) and (33). The individual nozzle size required is then obtained from

$$D_N = \frac{R_C}{\bar{R}_C} \tag{38}$$

in which $\bar{R}_C \equiv R_C/D_N$ is the dimensionless reach, a function generally of the jet velocity and D_N when sufficient fuel is dispensed.

The minimum number of nozzles, as discussed earlier, approximately corresponds to a configuration in which all of the radial jet cylinders overlap and are tangent on the cloud surface. The area on the cloud surface that is allocated to each jet in this array is that of a spherical hexagon. If approximated as a planar hexagon, this area is just $A = 2\sqrt{3}\, R_J^2$ where R_J is the radius of the spray cylinder inscribed within the hexagonal space. Equating the total area of all such hexagons to the surface area of the hemispherical cloud leads to the approximation

$$N_{N_{min}} = \frac{\pi}{\sqrt{3}} \left(\frac{\bar{R}_C}{\bar{R}_J}\right)^2 \tag{39}$$

for the minimum number of nozzles, where $\bar{R}_J \equiv R_J/D_N$ is the dimensionless jet radius.

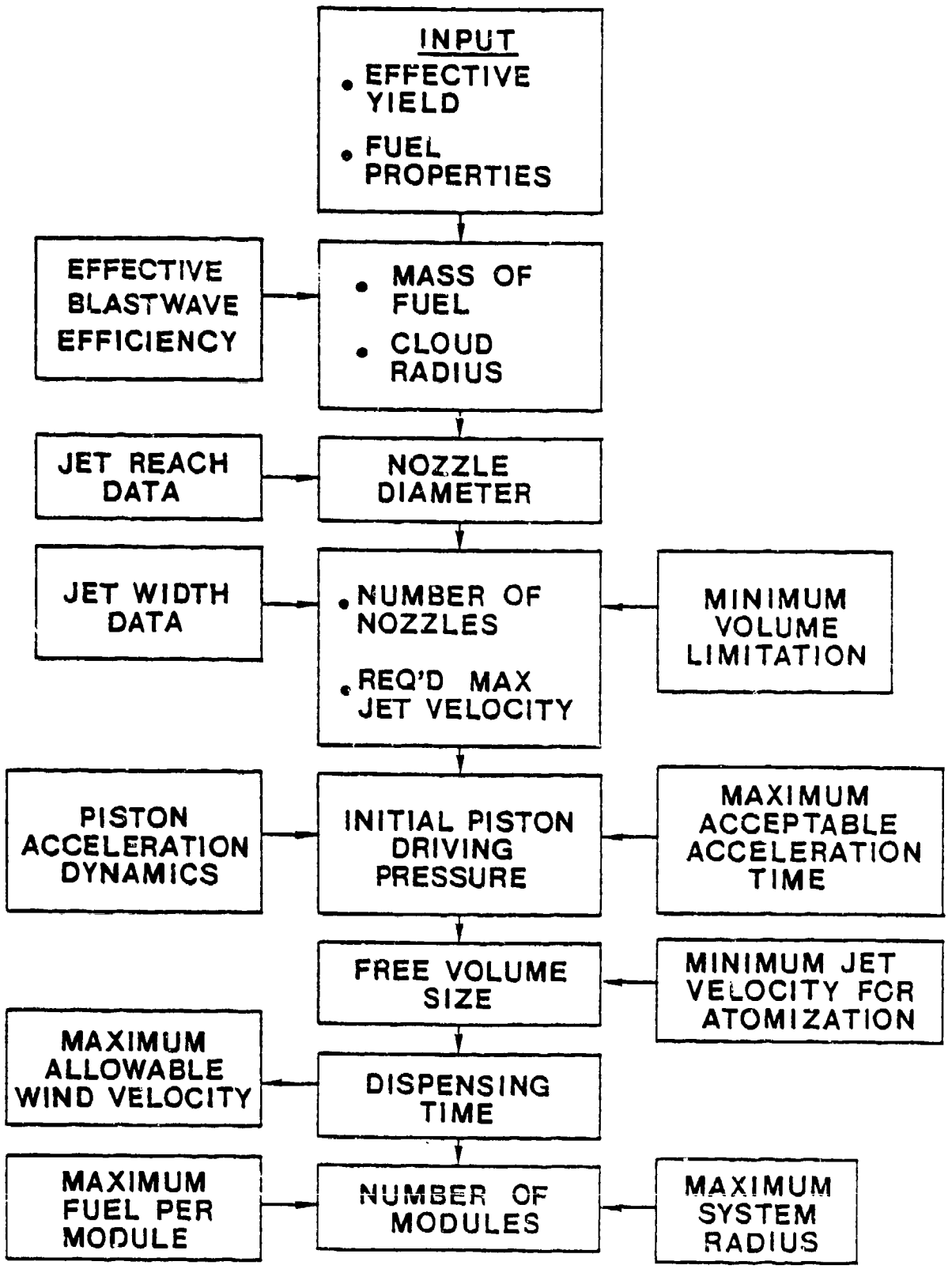

Figure 26. Schematic flow diagram of simulator design code.

The upper limit on the number of nozzles is at present presumed to be fixed by the minimum volume that can be impulsively injected through a single nozzle without reach loss due to tail breakup interference, as described in Section 3; that is

$$N_{N_{max}} = \frac{m_F/\rho_\ell}{V_{F_{min}}} \quad .$$

Using the expression for $V_{F_{min}}$ given by Eq. (26), this can be written

$$N_{N_{max}} = \frac{m_F}{0.428\rho_\ell U_{D_1} D_N^{7/2}} \left(\frac{\sigma_\ell}{\rho_\ell}\right)^{1/2} \quad . \tag{40}$$

As a conservative measure, the maximum dispensing velocity, $U_D = U_{D1}$, (which corresponds to the peak dispensing pressure $P3_1$ in Figures 5 and 6) is presently being used in this equation.

For a given set of design conditions, the maximum atmospheric wind velocity that can be tolerated during a test is an important consideration. For the present it is assumed that the cloud will be detonated at the formation time, t_F. This time is calculated from Eq. (27) with $U_D = U_{D_2}$ (corresponding to $P3_2$ in Figures 5 and 6) to be conservative. If the cloud displacement due to wind during this period is to be no more than a small fraction C_1 of the cloud radius, then the maximum permissible wind velocity is

$$U_{w_{max}} = \frac{C_1 R_C}{t_F} \quad . \tag{41}$$

If the value of $U_{w_{max}}$ calculated in this way is not realistic, either t_F or R_C must be changed.

During the dispensing period the jet velocity must be high enough for atomization, but it cannot be so high as to induce serious vortex-induced cloud shape distortions. Thus, there is a minimum and a maximum jet velocity. Since for all dispensing systems presently being considered, $U_{D_1} > U_{D_2}$, this means that

$$U_{D_1} \leq U_{D_{max}} \tag{42.1}$$

and

$$U_{D_2} \geq U_{D_{min}} \tag{42.2}$$

are required. The lower jet velocity limit $U_{D_{min}}$ is associated with the knee of the curve of reach as a function of dispensing velocity (see Figure 21). The upper limit, $U_{D_{max}}$, has not been well established as yet but it appears to be not far removed from $U_{D_{min}}$.

As presently conceived, the dispensing system to produce large clouds would consist of a cluster of N_P modules, close-packed at the center of the test arena into a circular region of overall radius R_{dis}. Each module would comprise a piston of diameter D_F in a cylinder assembly of diameter D_{PN}. Behind each piston a time-varying free volume $\tilde{V}$ is to be provided. The total instantaneous free volume for the entire system is $V_o = N_P\tilde{V}$.

A particular module would dispense an amount of fuel $\tilde{m}_F = m_F/N_P$ through $\tilde{N}_N = N_N/N_P$ nozzles into a designated sector of the cloud. The modules would be identical in construction; that is, all of the pistons would have identical diameter, D_P,

mass, m_p, and length, L_p. The total nozzle cross-sectional area that is driven by one piston is $\tilde{A}_N = \tilde{N}_N A_N$, where A_N is the area of one nozzle.

If all of the nozzles are to be the same size and if they are all driven at the same pressure, they will have the same reach. If the dispenser cluster radius were comparable to the cloud radius, the cloud from these nozzles could not be hemispherically shaped. To minimize such cloud shape aberrations, it is therefore necessary that $R_{dis} \leq C_3 R_C$, where C_3 is a small number.

The dynamics of individual modules are predicted by Equations (11) through (17). (Appropriate notational modifications are needed to adapt those equations to the present context.) The intial conditions are $P_p = P_{p_o}$, $u_p = 0$, $\tilde{V} = \tilde{V}_o$, and $\tilde{m}_\ell = \tilde{m}_F$ at $t = 0$. From an integration of these equations the time t_1 to reach peak dispensing velocity U_{D1} and also the dispensing time t_D (which corresponds to $m_\ell = 0$, $U_D = U_{D_2}$) are determined. To confine the degradation of jet quality that is due to piston acceleration to a minimum initial period requires

$$t_1 \leq C_2 t_D$$

where C_2 is small. It is noted that Eq. (16) applies only to systems in which the freevolume expansion is isentropic. It would not apply, for example, to a tailored gas generator or to a choked-orifice dispensing system. These designs would require separate treatment.

In any dispenser with a driving pressure that decreases during the dispensing process, successive jet segments possess progressively lower velocities. This tends to stretch the jet. That is, at the nozzle exit $\partial P/\partial x = 0$ along the jet axis, and so the inviscid equation of (one-dimensional) motion near that point is

$$\frac{\partial U_D}{\partial x} = - \frac{1}{U_D} \frac{\partial U_D}{\partial t} \quad .$$

If $\partial U_D/\partial t < 0$ as the result of $d\Delta P/dt < 0$ (see Eq. (11)), then $\partial U_D/\partial x < 0$, implying a stretching. Since the cohesive resistance to tensile forces in a liquid is very small, this effect will contribute to accelerated jet disruption if it is too large. No satisfactory criterion for the maximum tolerable velocity gradient has as yet been proposed and no experiments have as yet addressed this question directly. However, to provide some ceiling on the nozzle-exit velocity gradient (for purposes of developing the dispenser design code), the velocity difference U_D resulting from a velocity gradient that acts over a distance equal to half the jet reach is arbitrarily limited to no more than the average dispensing velocity $\bar{U}_D$. That is,

$$- \left(\frac{\Delta U_D}{\bar{U}_D t_D} \right) \left(\frac{R_C}{2} \right) \leq \bar{U}_D$$

or

$$R_C \leq - \frac{2\bar{U}_D^2 t_D}{\Delta U_D} \quad , \tag{43}$$

where

$$\bar{U}_D \equiv (U_{D_1} + U_{D_2})/2$$

and

$$\Delta U_D \equiv U_{D_2} - U_{D_1} \quad .$$

This velocity gradient can be reduced by increasing the free volume (which lowers ΔU_D), but a very large freevolume tank would be costly. An understanding of the effects of a velocity gradient on jet breakup would be helpful in establishing the smallest usable free volume.

To be complete, the list of dispenser design considerations should include hardware and installation cost equations. The design which satisfies all of the engineering constraints at minimum cost would be sought. Although this has not as yet been done, some limitations based on economy have been tentatively incorporated into the code. To minimize the total number of nozzles, Eqs. (39) and (40) are set equal. This effectively establishes an upper bound on U_{D_1} which replaces that expressed by Eq. (42) if it is smaller. In addition, the diameter of the individual dispenser module pistons is presently limited in the program to 29.2 cm (11.5 in.), and the length of each piston cylinder is limited to 2.5 m (100 in.). These limits were established because it was felt that the costs of fabricating the piston and cylinder would increase very rapidly for larger sizes. The freevolume size is also minimized by setting $U_{D_2} = U_{D_{min}}$. This replaces Eq. (42.2).

The program as written iterates on P_{P_o}, $\tilde{V}_o$, and N_p (which must be an integer) until a solution satisfying all constraints is found. If this cannot be done, the constraints that are violated are indicated.

Preliminary calculations using the design code have been carried out at scales corresponding to 0.267, 20, and 1000 ton nuclear equivalents, with propylene oxide as the assumed fuel. (The smallest of these corresponds approximately to the scale of early experimental tests conducted by Systems, Science and Software.) The program output is presented in Table 2. In the calculations, $\bar{R}_C = 1500$ and $\bar{R}_J = 50$ were assumed. Also, $C_1 = C_2 = C_3 = 0.05$ was used. It was assumed that $D_{PN} = 1.5\ D_P$, and also that $m_p = \rho_p A_p L_p$, where $L_p/D_p = 1.91$ and $\rho_p = 1150\ kg/m^3$ ($72\ lb/ft^3$) are based on the design of the linear dispenser. A value of $\eta_F = 0.74$ was used as an estimate of the effective blastwave efficiency of the propylene oxide FAE clouds (see Section 5.2.3). The freevolume (driving) gas was assumed to have a specific heat ratio $\gamma = 1.4$.

The calculations that are summarized in Table 2 were performed after the linear dispenser had already been fabricated. For that reason the calculated dimensions do not coincide completely with the actual design. Values of $U_{D_{min}}$ were crudely estimated for generating the calculation. The results in the table should accordingly be regarded as very rough approximations.

One observation from these approximations is that the peak dispensing velocities specified for the two smaller scales are quite high. Cloud distortion effects due to induced air motions are therefore almost certain to occur at the 0.267 ton scale, and would be likely at the 20-ton scale if the values of Pp_o listed were to be used. The dispensing velocity required at the 1 KT scale is more reasonable and at the same time the velocity gradient is also quite low, but a very large free volume would be needed in that case. Also, at the 1 KT scale the overall dispenser cluster radius is nearly 9% of the cloud radius. If cylinders longer than 2.5 m (100 in.) were permitted however, the dispenser cluster radius could be reduced.

Table 2. Approximate simulator system design at three scales using propylene oxide as fuel.

	Scale (tons)		
	0.267	20	1000
CLOUD CHARACTERISTICS			
Radius, R_c (m)	4.43	18.7	68.9
Total fuel mass, m_F (kg)	22.7	1704.0	85,200.0
Total condensed fuel volume, $V_{..}$ (m^3)	0.0265	1.99.	99.7
Cloud formation time, t_F (s)	0.0601	0.324	1.71
DISPENSER MODULE CHARACTERISTICS			
Piston diameter, D_p (m)	0.292	0.292	0.292
Piston mass, m_p (kg)	43.0	43.0	43.0
Overall cylinder length, L_{cp} (m)	0.952	2.2	2.5
Module overall diameter, D_{pn} (m)	0.439	0.439	0.439
Fuel mass per module, $\tilde{m}_F$ (kg)	22.7	94.7	112.0
Nozzles per module, $\tilde{N}_n$	1632.0	91.0	2.14
Fuel mass per nozzle, $\hat{m}_F$ (kg)	0.0139	1.04	52.2
Single nozzle diameter, D_n (m)	0.00296	0.0125	0.0459
Individual jet spray column diameter, D_j (m)	0.310	1.31	4.82
Free volume per module, $\tilde{V}_0$ (m^3)	0.00413	0.119	7.98
Peak dispensing velocity, U_{D_1} (m/s)	138.0*	67.7	35.3
Time to reach $0.9U_{D_1}$, t_1 (s)	0.00168	0.0138	0.0122
Dispensing time, t_D (s)	0.0305	0.185	1.05
Dispensing velocity at t_D, U_{D_2} (m/s)	50.0	45.0	35.0
Ratio t_1/t_D	0.055*	0.0743*	0.0117
Initial driving pressure, P_{P0} (MPa)	17.3	2.35	0.636
DISPENSER SYSTEM CHARACTERISTICS			
Number of modules, N_p	1.0	18.0	762.0
Dispenser system radius, R_{dis} (m)	0.219	0.930	6.05
Ratio R_{dis}/R_c	0.0494	0.0497	0.0878*
Total number of nozzles, N_n	1632.0	1632.0	1632.0
Total free volume, V_o (m^3)	0.00413	2.15	5080.0

*Does not satisfy specified constraint

SECTION 5

FAE SIMULATION OF FAR-FIELD NUCLEAR AIRBLAST

5.1 CHARACTERISTICS OF NUCLEAR AIRBLAST IN THE FAR-FIELD

The degree of correspondence or fidelity between FAE and surface nuclear airblasts is usually discussed in terms of positive-phase blastwave characteristics. These are peak static overpressure, peak dynamic pressure, and the associated positive-phase durations and impulses, all as functions of radius; and the static overpressure, dynamic pressure, and the associated impulses as functions of time at fixed radii.

However, a complete set of universally accepted nuclear data that could be used for a comparative basis is not presently available. Sources of experimental and theoretical nuclear data (as well as some TNT airblast data) are listed in References 41-62. Some of the data in these sources are conflicting. Presumably a certain amount of the conflict is due to differences in instrumentation, data reduction, and curvefitting procedures.

For example, much of the nuclear static overpressure data were obtained with variable reluctance or strain gage transducers in conjunction with magnetic tape recording systems. The overall risetime capability of these systems was on the order of one millisecond. Self-recording mechanical gages (developed by Ballistic Research Laboratory) with risetimes of 3-5 ms were also used. Characteristic samples of semi-smoothed nuclear data are given in Figures 27 and 28. High frequency noise has been filtered out of these samples, but lower frequency pressure excursions (which carry real or apparent impulse) have been retained.

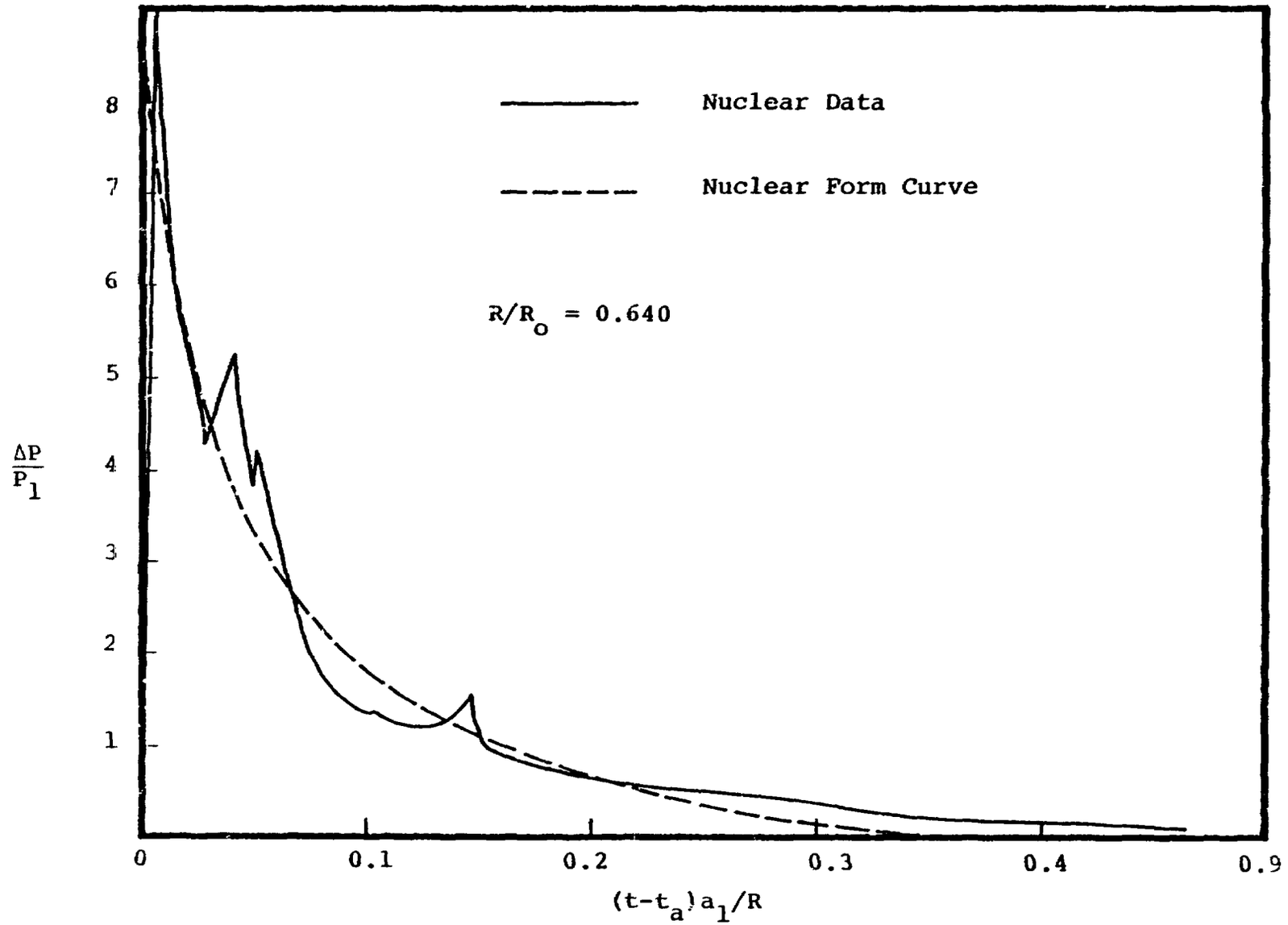

Figure 27. Semi-smoothed surface burst nuclear data (Reference 41) and fully smoothed nuclear form curve (Reference 52). The arrival time is t_a.

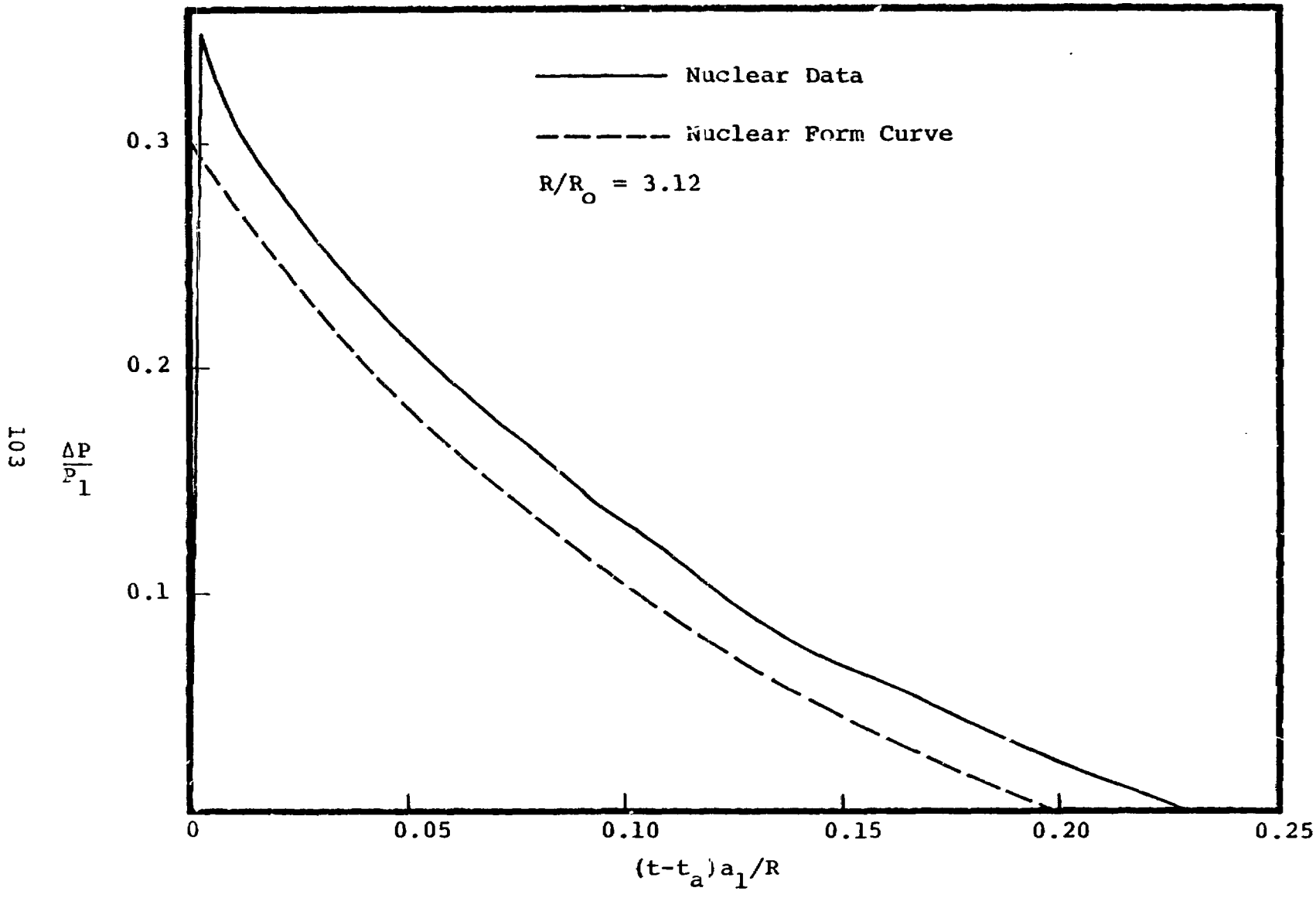

Figure 28. Semi-smoothed surface burst nuclear data (Reference (41) and fully smoothed nuclear form curve (Reference 52). The arrival time is t_a.

In reporting peak overpressures, the first crest of the initial pressure rise, as recorded by the instrumentation, was used by Reference 44. On the other hand, in Reference 41 an extrapolation procedure to compensate for the equipment rise-times was followed. On a semi-logarithmic plot with overpressure on the logarithmic scale and time on the linear scale, a straight line was drawn through the data points near t = 0. This was extrapolated to time zero in order to infer the peak overpressure.

Experimental nuclear airblast data for measurements other than static overpressure (and impulse) are more scarce and contain more scatter. This is particularly true of the time variation, positive-phase duration, and impulse associated with dynamic pressure.

In the current investigation, the nuclear-data curvefits given by Brode (Reference 52) were used as the reference against which FAE airblasts are compared. Examples of overpressure-time curvefits from this reference are included in Figures 27 and 28. These are fully smoothed curvefits, in the sense that all excursions from the average profiles have been excluded. The Brode nuclear curves for peak static overpressure, peak dynamic pressure, static overpressure impulse and positive phase duration appear in Figures 29-32. The peak static overpressure ΔP_{max} and peak dynamic pressure, q_{max}, have been made dimensionless in these plots with respect to $P_1 = 1.01 \times 10^5$ Pa (14.7 psi). The positive phase duration has been normalized with respect to the characteristic time R/a_1, where R is the range from the explosion center and a_1 = 341 m/s (1116 ft/s) is the sea level speed of sound in air. Impulse is made dimensionless with respect to both the time R/a_1 and pressure P_1. Finally, the range is expressed as the dimensionless variable

$$\bar{R} \equiv \frac{R}{R_o} \quad . \tag{44}$$

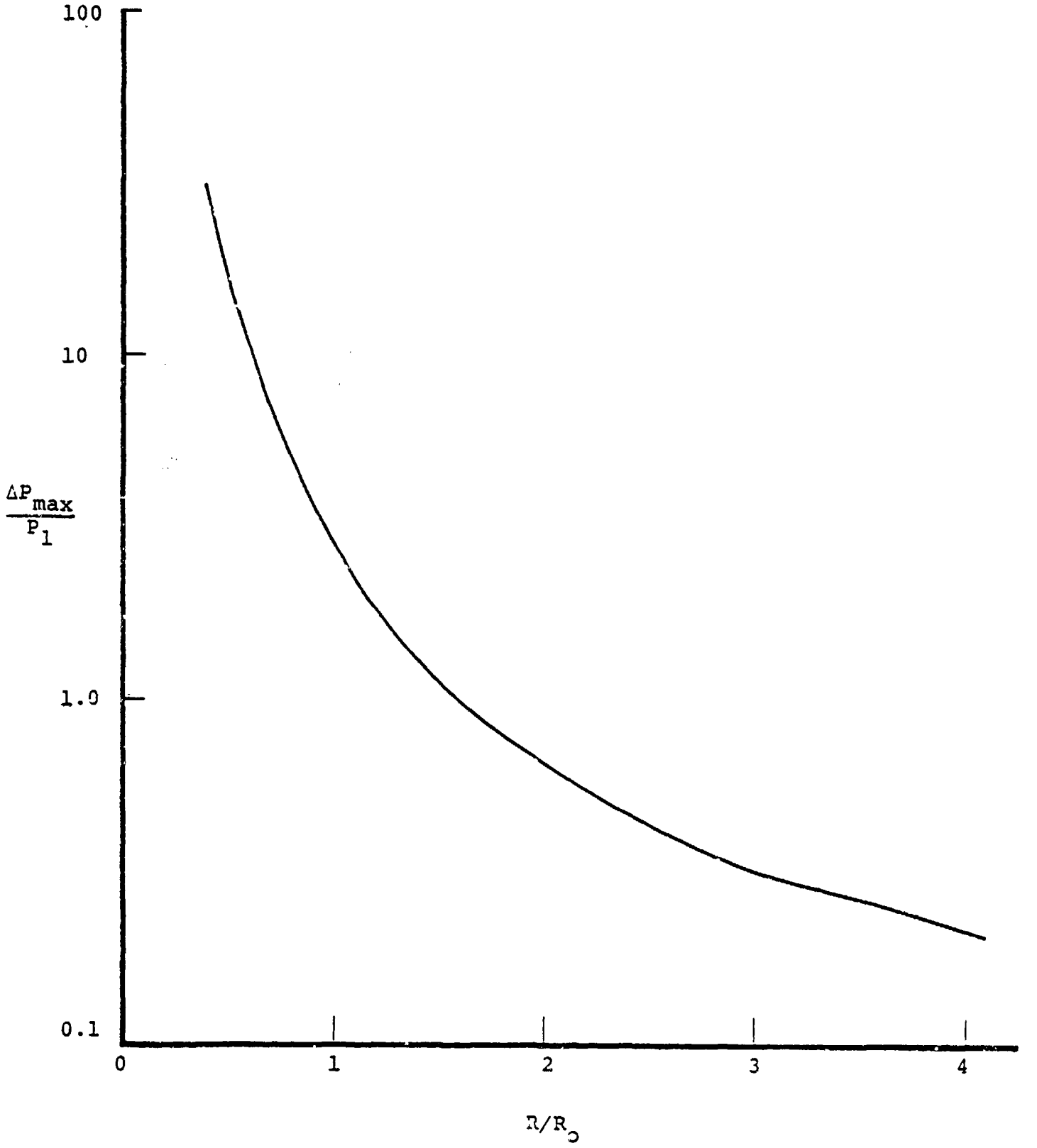

Figure 29. Nuclear Surface Burst Reference Curve for Peak Overpressure versus Range (Reference 52).

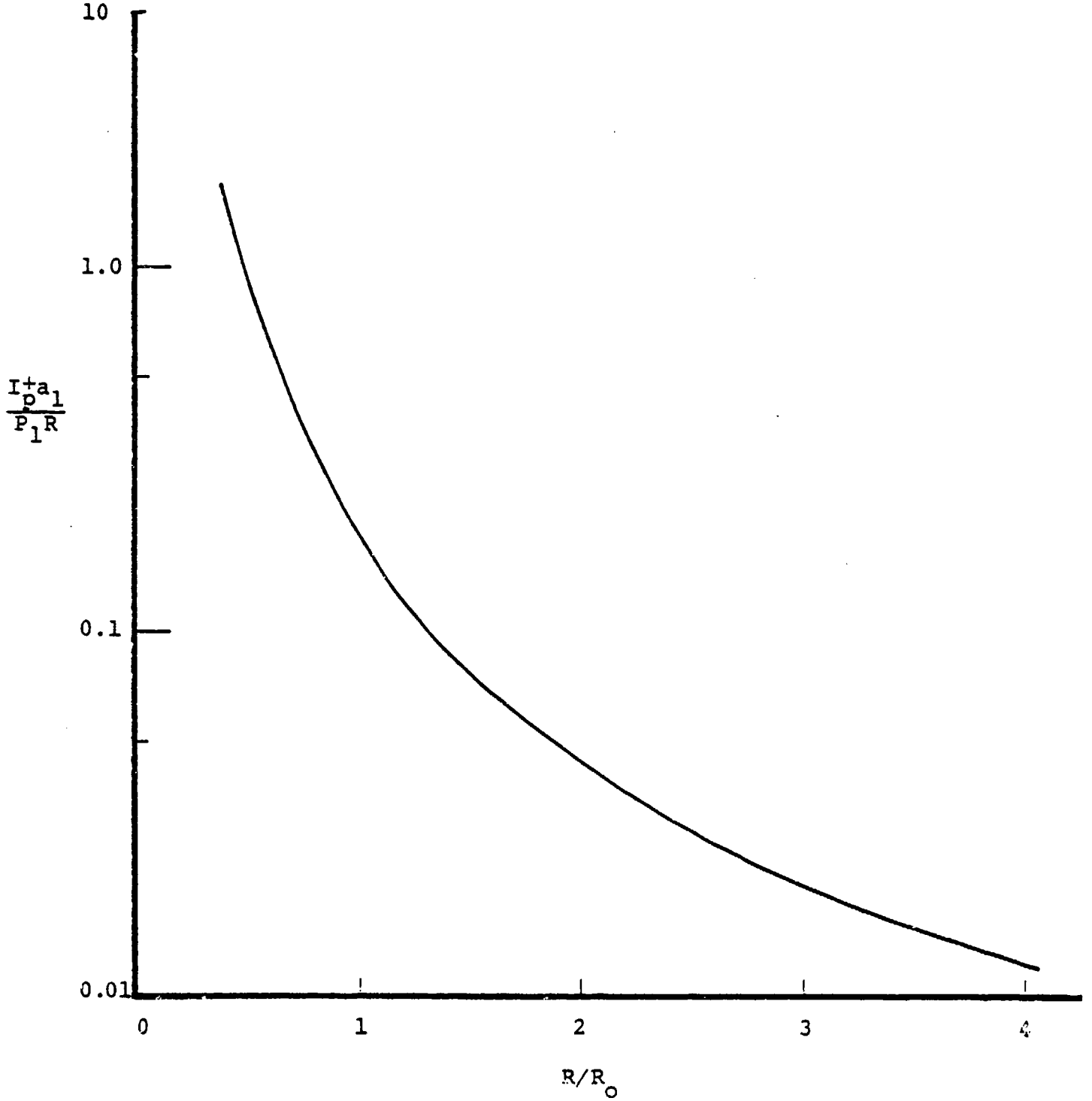

Figure 30. Nuclear Surface Burst Reference Curve for Positive-Phase Static Overpressure Impulse Versus Range (Reference 52).

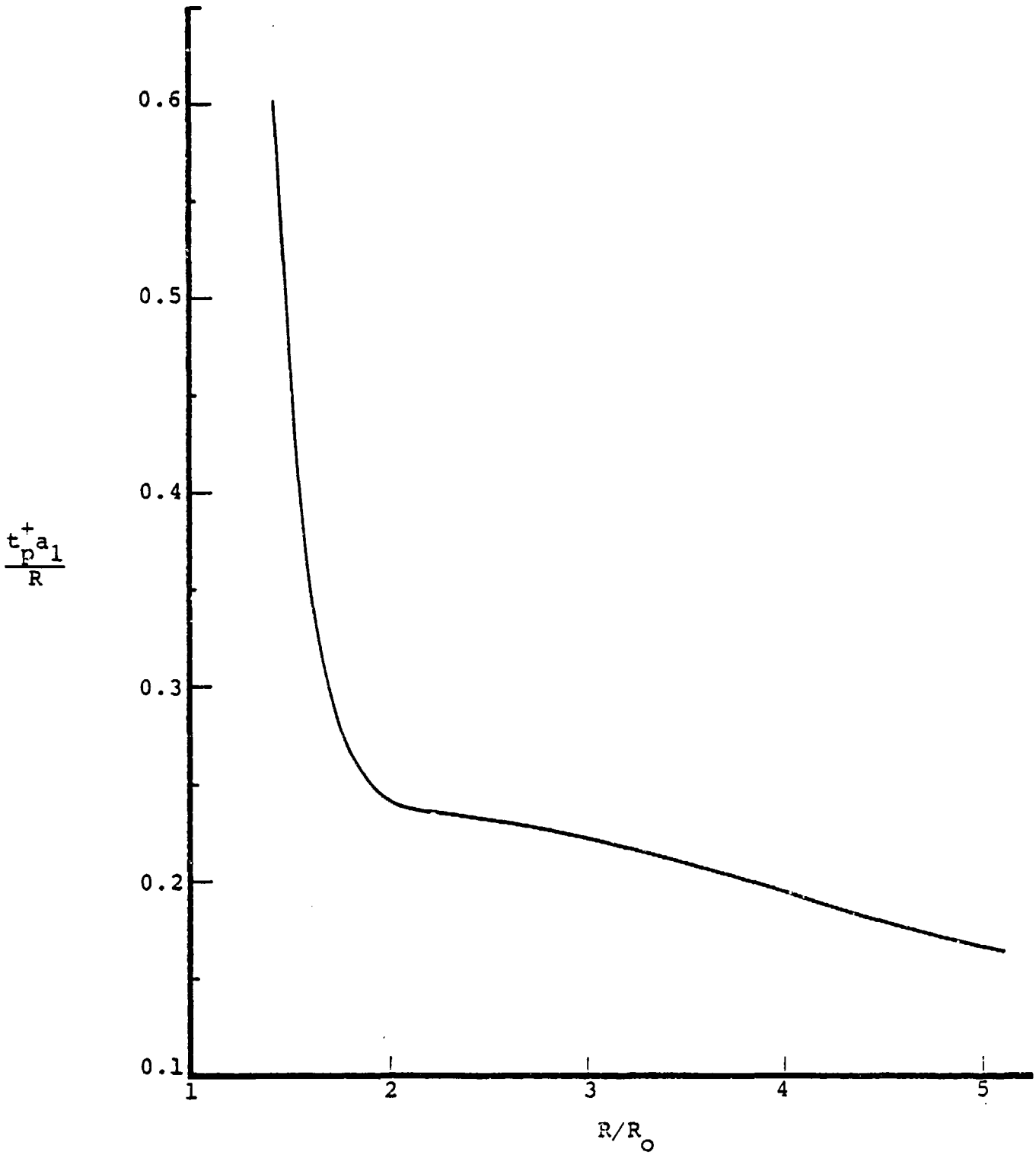

Figure 31. Nuclear Surface Reference Curve for Static Overpressure Positive-Phase Duration Versus Range (Reference 52).

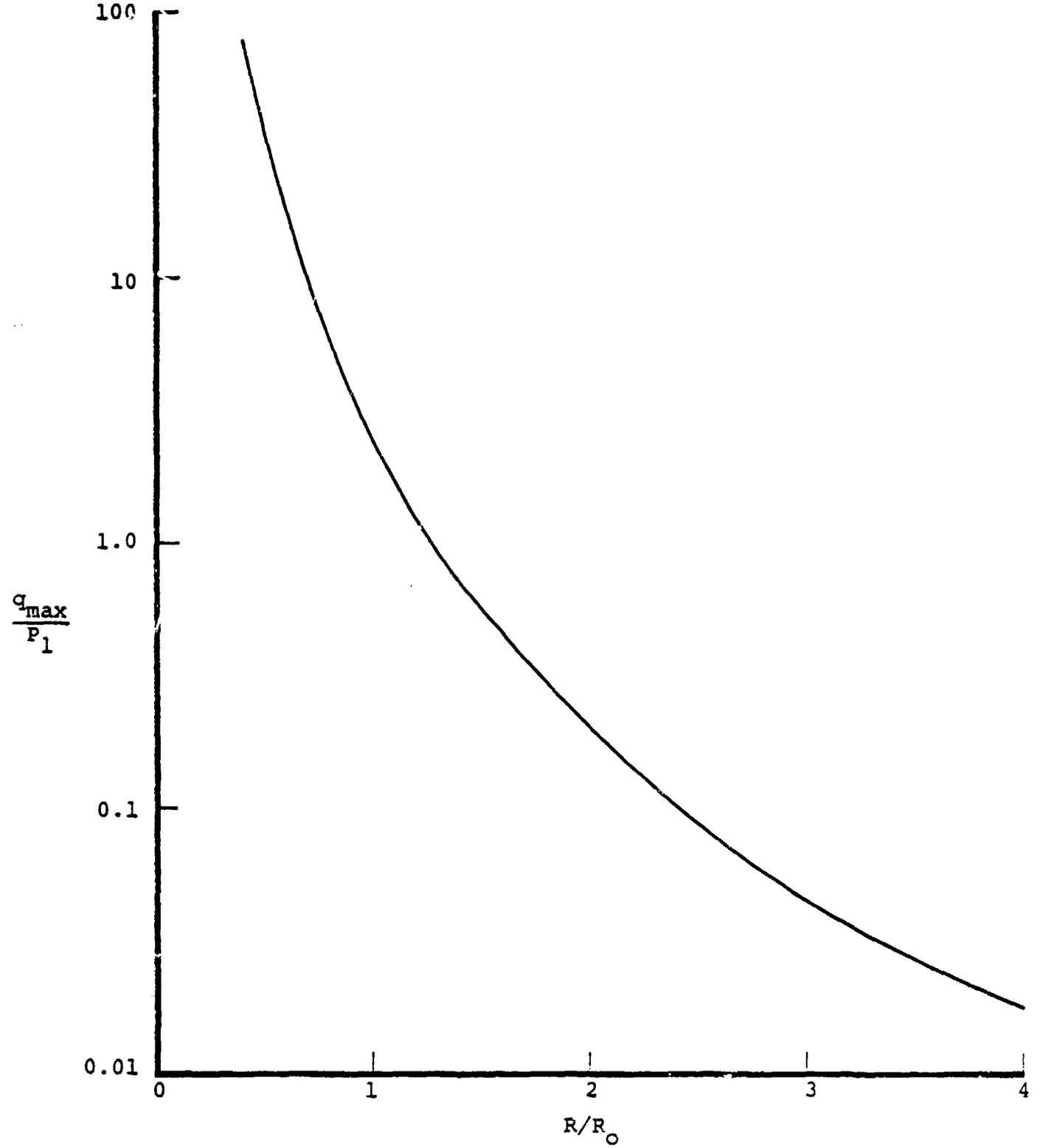

Figure 32. Nuclear Surface Burst Reference Curve for Peak Dynamic Pressure Versus Range (Reference 52).

Here the characteristic radius R_o is defined by

$$R_o \equiv \left(\frac{E_o}{\nu \pi P_1}\right)^{1/3} , \tag{45}$$

where

$$\nu = \begin{cases} 2, \text{ hemispherical geometry} \\ 4, \text{ spherical geometry} \end{cases}$$

The energy E_o in this expression is the effective or apparent blast yield, which for a nuclear explosion is designated by $E_{o_{E,N}}$. Effective yield is a concept that was discussed in Section 4.1. Values of $E_{o_{E,N}}$ are usually given in terms of equivalence with respect to TNT airblasts. The effective blast yield varies with range and with the variable chosen as a basis for comparsion. However, over a limited range interval the variation in $E_{o_{E,N}}$ may be small enough that a single average value can be used.

It has been found useful to define the effective airblast efficiency (or effectiveness) of a nuclear explosion by

$$\eta_N \equiv \frac{E_{o_{E,N}}}{E_{o_{T,N}}} . \tag{46}$$

This definition parallels Eq. (29) which was written for a fuel-air explosion. Based on overpressure decay in the far field, a suitable average value of η_N is approximately 0.5. This value has been used for the purposes of this reporrt. For a 1 KT nuclear explosion, the total energy release is $E^*_{o_{T,N}}$ = 4.18×10^{12} J (3.96×10^9 Btu) (Reference 45) and so for

$\nu = 2$, $R^*_{E,N} = 149$ m (489 ft), assuming $P_1 = 1.01 \times 10^5$ Pa (14.7 psi). (The asterisk is used to designate the 1 KT level.) This value of R_o, which corresponds to the effective blastwave energy of a 1 KT nuclear explosion, was used in preparing Figures 29-32. To the extent that cube-root scaling as implied by Eq. (45) can be considered valid, these dimensionless figures then apply to any scale of nuclear explosion.

5.2 EXPERIMENTAL INVESTIGATIONS

5.2.1 Test Setup and Procedure

The experimental facility presently being used to investigate small-scale FAE airblasts (~1/4 ton nuclear equivalent) is described in Appendix A. The facility comprises two perpendicular concrete runways extending from the explosion center. Along these runways there are instrumentation troughs located as listed in Table A.1. The principle instrumentation consists of stagnation and static pressure measurements at each trough. In addition, high-speed films are taken. FAE clouds are impulsively generated at the explosion center using the linear dispenser (described in Section 2) with a multi-nozzle hemispherical head of the type shown in Figure 22. Tests are normally conducted in the early morning hours to minimize wind effects. Following a suitable delay after impulsive cloud formation, the cloud is detonated. Detonation is initiated with a small (50-500 gm) H.E. charge suspended directly above the dispenser head at a minimum height. The minimum height is determined by considering the number of jets that are blocked by the H.E. charge, or by the potential for damage to the dispenser.

5.2.2 Data Reduction

Pressure data gathered during a test are digitized and the bulk of the data reduction is then machine processed. A schematic flow chart outlining the data reduction procedure is given in Figure 33.

At each instrumentation position, the time of blastwave arrival, the peak static overpressure, and the peak reflected stagnation pressure are measured. The positive-phase impulse is obtained from the static pressure record at that location by integration. From these four measurements an average value of K_o is determined. This is done as follows. A curve is smoothed through the time-of-arrival versus range data. From this curve the wave front velocity U_s at the instrumentation location in question is determined. The shock Mach number M_s is computed from $M_s \equiv U_s/a_1$. Separately, the Mach number is calculated from the peak static overpressure ΔP_{max} using

$$M_s^2 = 1 + \frac{\gamma + 1}{2\gamma} \left(\frac{\Delta P_{max}}{P_1}\right) \quad , \tag{47}$$

and from the peak reflected head-on overpressure ΔP_R through

$$\frac{\Delta P_R}{P_1} = 2(\bar{P} - 1) + \frac{(\gamma + 1)(\bar{P} - 1)^2}{2\gamma + (\gamma - 1)(\bar{P} - 1)} \quad , \tag{48}$$

where

$$\bar{P} \equiv \frac{P_2}{P_1} = 1 + \frac{\Delta P_{max}}{P_1} \quad ,$$

and $\gamma = 1.4$ is the specific heats ratio for air. The value of $\bar{P}$ is determined from Eq. (48) and then M_s is calculated from

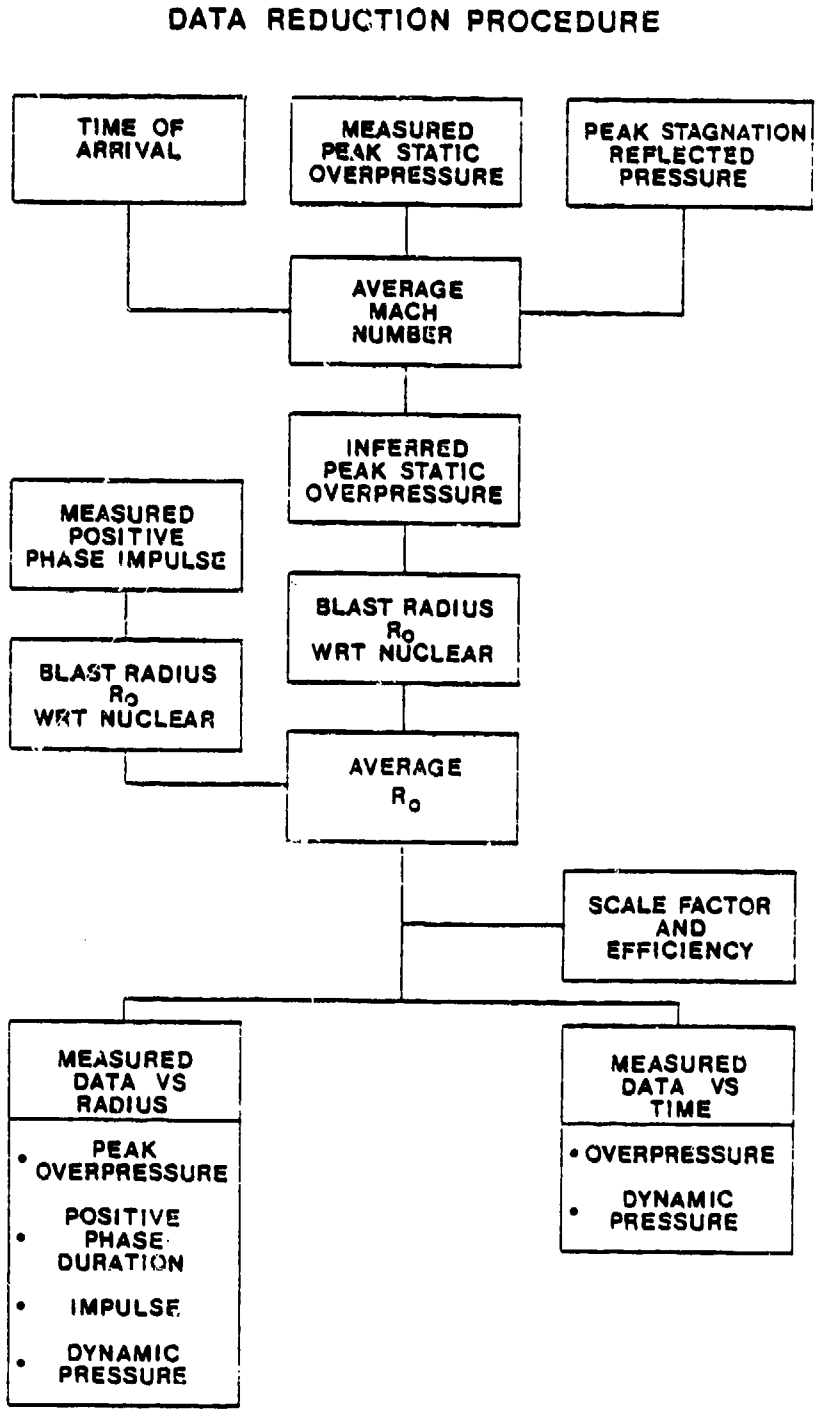

Figure 33. Schematic flow diagram of data reduction program.

Eq. (47). The three values of M_s are averaged. Eq. (47) is next used to infer a mean of value of ΔP_{max}. The corresponding characteristic radius R_o can then be obtained from Figure 29 since the measurement range R is of course known. In the same way, R_o is obtained from the measured positive phase impulse, by reference to Figure 30. These two values of R_o are then averaged. The same procedure is followed at all other instrumentation locations and a final, overall average value for R_o is generated. This is the effective characteristic radius for the FAE airblast with respect to the Brode nuclear curves and is designated $R_{OE,F}$. The corresponding effective blastwave energy is $E_{OE,F}$, calculated from Eq. (45). The measured peak overpressure, positive phase duration and impulse, and the dynamic pressure can then be plotted versus $R/R_{OE,F}$ and compared directly with Figures 29-32. The overpressure as a function of time is also plotted and compared with the Brode curvefit (Reference 52).

Dynamic pressure is derived from the stagnation and static pressure measurements. The dynamic pressure

$$q \equiv 1/2\ \rho u^2$$

can readily be shown to be

$$q = 1/2\ \gamma P M^2 \qquad (49)$$

for a perfect gas, where P is the absolute static pressure (not overpressure) and the local flow Mach number is $M = u/a$. The peak value of q, that is, q_2 or q_{max}, can be calculated directly.* This is because $P_{max} \equiv P_2 = \Delta P_{max} + P_1$ is measured,

*Point "2" is used to designate conditions just being the blast-wave shock front in theoretical work described later in this report.

and the flow Mach number just behind the blastwave shock, M_2, is related to the shock Mach number by

$$M_2 = \frac{2(M_s^2 + 1)}{\sqrt{[2\gamma M_s^2 - (\gamma - 1)][2 + (\gamma - 1) M_s^2]}} \quad . \tag{50}$$

The shock Mach number is determined from Eq. (47), so the stagnation pressure measurement is not needed to obtain q_{max}. However, at later times the local flow Mach number at a fixed radial position is not related to the shock front strength. The stagnation probe pressure measurement is, therefore, needed in order to obtain q(t). If the flow into the stagnation pressure probe is subsonic, the pressure as measured by that probe, P_o', is equal to the freestream stagnation pressure, P_o. The flow Mach number (needed in Eq. (49)) is in this case found from

$$\frac{P}{P_o} = \left(1 + \frac{\gamma - 1}{2} M^2\right)^{-\frac{\gamma}{\gamma - 1}} \quad , \tag{51}$$

where P and P_o are absolute pressures.

On the other hand, if the flow into the stagnation pressure probe is supersonic, then the measured pressure P_o' is not the actual stagnation pressure P_o. At the first moment following the passage of the blastwave leading shock, the pressure at the stagnation probe reaches its peak reflected value; i.e., $P_o' = P_R$ at that moment. Within a few microseconds (depending on the probe dimensions), the reflected shock moves upstream of the probe face and a quasi-stationary bow shock is formed. Thereafter, the absolute static and stagnation probe pressures are related by

$$\frac{P}{P_o'} = \left\{ \frac{2\gamma M^2 - (\gamma-1)}{(\gamma+1)\left[\left(\frac{\gamma+1}{2}\right)M^2\right]^{\gamma}} \right\}^{\frac{1}{\gamma-1}} \quad . \tag{52}$$

It can be demonstrated that if at any time the measured ratio P/P_o' exceeds 0.528 (for $\gamma = 1.4$), then the flow at that moment is subsonic. Conversely, if $P/P_o' < 0.528$, then the flow is supersonic. This criterion is invoked to determine which of Eqs. (51) or (52) should be used to compute M at a given instant. Once M is known, Eq. (49) is used to calculate q. The moment in time at which $q = 0$ ($M = 0$, $u = 0$) defines the positive phase dynamic pressure duration, t_q^+.

The effective airblast efficiency of the FAE is calculated by combining

$$R_{o_{E,F}} \equiv \left(\frac{E_{o_{E,F}}}{\nu\pi P_1} \right)^{1/3} \tag{53}$$

with Eqs. (28) and (29), which gives

$$\eta_F = \frac{\nu\pi P_1 R_{o_{E,F}}^3}{m_F H_c} \quad . \tag{54}$$

It should be noted that other investigators have defined blastwave efficiencies differently. For example (Reference 63), a blastwave efficiency can be defined as the ratio of the actual mechanical positive-phase work done by the expanding, burned cloud/air interface to the total combustion energy based on a heat of combustion. However, by itself this particular definition of efficiency cannot be used to determine the amount

of fuel needed to simulate the airblast characteristics of a point blast or a nuclear source of specified strength. In conjunction with this efficiency, an "equivalent blast energy ratio" must be used in order to calculate the necessary quantity of fuel. When point source and FAE decay curves are matched over the same range of blastwave radii, the product of the interface-work efficiency and the "equivalent blast energy ratio" should yield a value that is approximately equal to the effective blast efficiency defined in this report.

An explosion scale factor with respect to a 1 KT nuclear explosion is also calculated as part of the data reduction. Cube-root scaling implies, for fixed atmospheric conditions, that

$$\left(\frac{E^*_{o_{E,N}}}{E_{o_{E,F}}}\right)^{1/3} = \frac{R^*_N}{R_F} = \frac{I^{+*}_{P_N}}{I^{+}_{P_F}} = \frac{t^{+*}_{P_N}}{t^{+}_{P_F}} = \frac{t_N}{t_F}$$

where again the subscript "N" designates "nuclear" and "F" designates "FAE". The scale factor, s, is accordingly defined by

$$s \equiv \left(\frac{E^*_{o_{E,N}}}{E_{o_{E,F}}}\right)^{1/3} . \qquad (55)$$

That is, the scale factor is written in terms of the effective blastwave energies of the fuel-air and 1 KT nuclear explosions. This can also be expressed as

$$s = \frac{R^*_{o_{E,N}}}{R_{o_{E,F}}} \qquad (56)$$

by using Eq. (45).

5.2.3 Experimental Results and Discussion

As noted in Appendix A, preliminary experiments were carried out with somewnat less sophistication than the more recent work described in the present section. The early results, however, were sufficient to demonstrate the fundamental feasibility of nuclear airblast simulation by means of two-phase fuel-air explosions, when the FAE cloud is generated from a central source by means of multiple nozzle, impulsive hydraulic fuel injection. Those experiments are discussed in detail in Reference 5 and only a brief summary is given here. Approximately stoichiometric, 4.6 m (15 ft) radius hemispherical propylene-oxide/air clouds were detonated in the experiments. Relatively long delay times (up to 2500 ms) between the start of the fuel dispensing and cloud detonation were used. These delays were in considerable excess of the minimum cloud formation times (Eq. (27)) so that due to settling of the fuel sprays the clouds were usually flatter than the optimum hemispherical shape.

Characteristic records of static overpressure versus time from one of these tests are given in Figures 34-37. The fully smoothed nuclear curvefits of Brode are superimposed on the figures for reference. The corresponding experimental static-overpressure impulse plots and smoothed nuclear curves are given in Figures 38-41. The degree of repeatability between tests can observed in Figures 42 and 43. The symmetry of the blastwaves produced by the FAE source is represented by the samples in Figures 44 and 45. In Figures 46 and 47, the peak overpressures and total positive phase impulses versus range are plotted and compared against the nuclear curves. Also shown on these two figures are the theoretical point-source blastwave curves (Reference 62), which coincide closely with the Brode nuclear curves in this range of pressures.

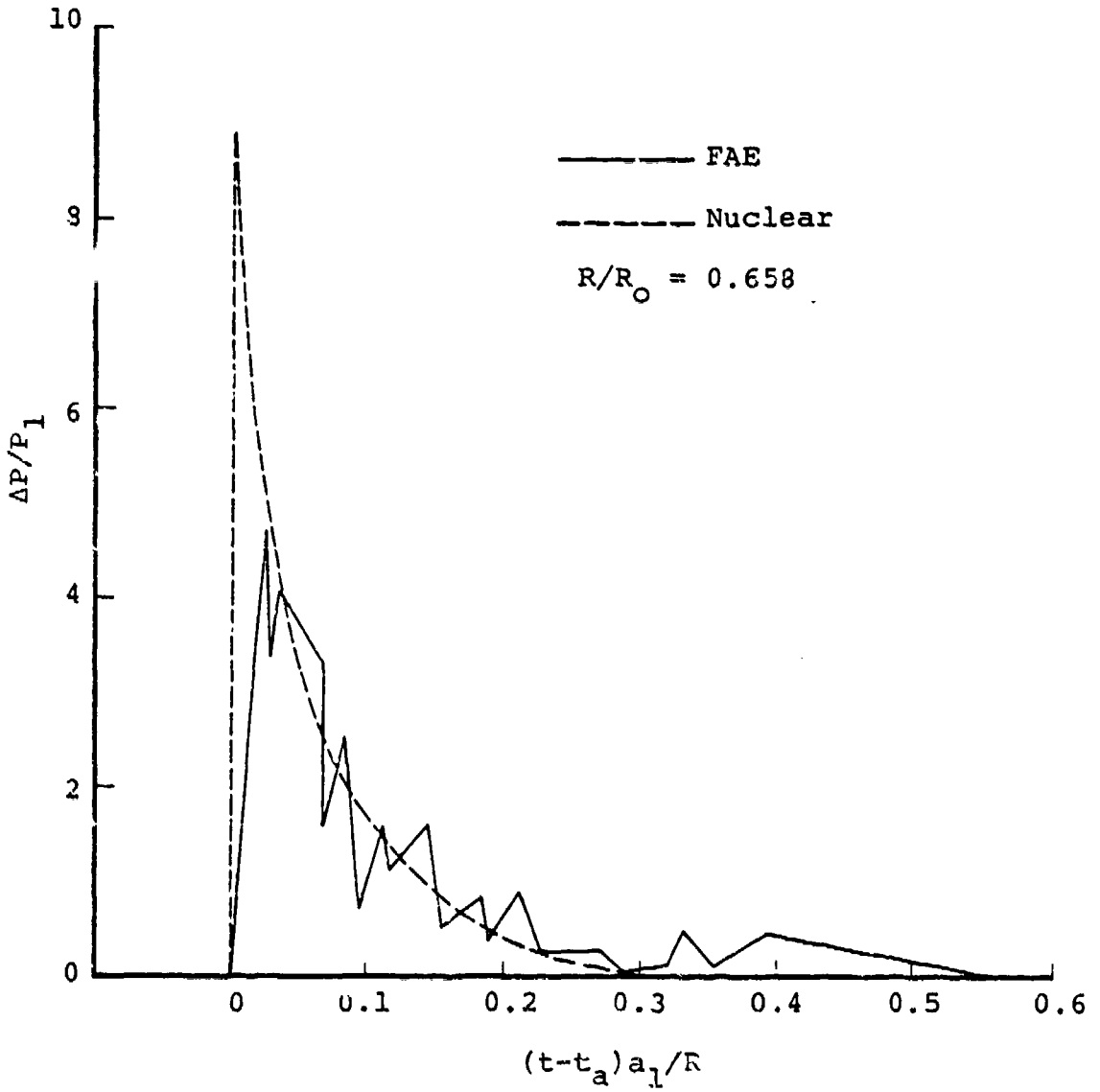

Figure 34. Comparison of Measured Overpressure as a Function of Time with a Nuclear Blast Waveform. The experimental data were taken from test 2536 (t_a is arrival time).

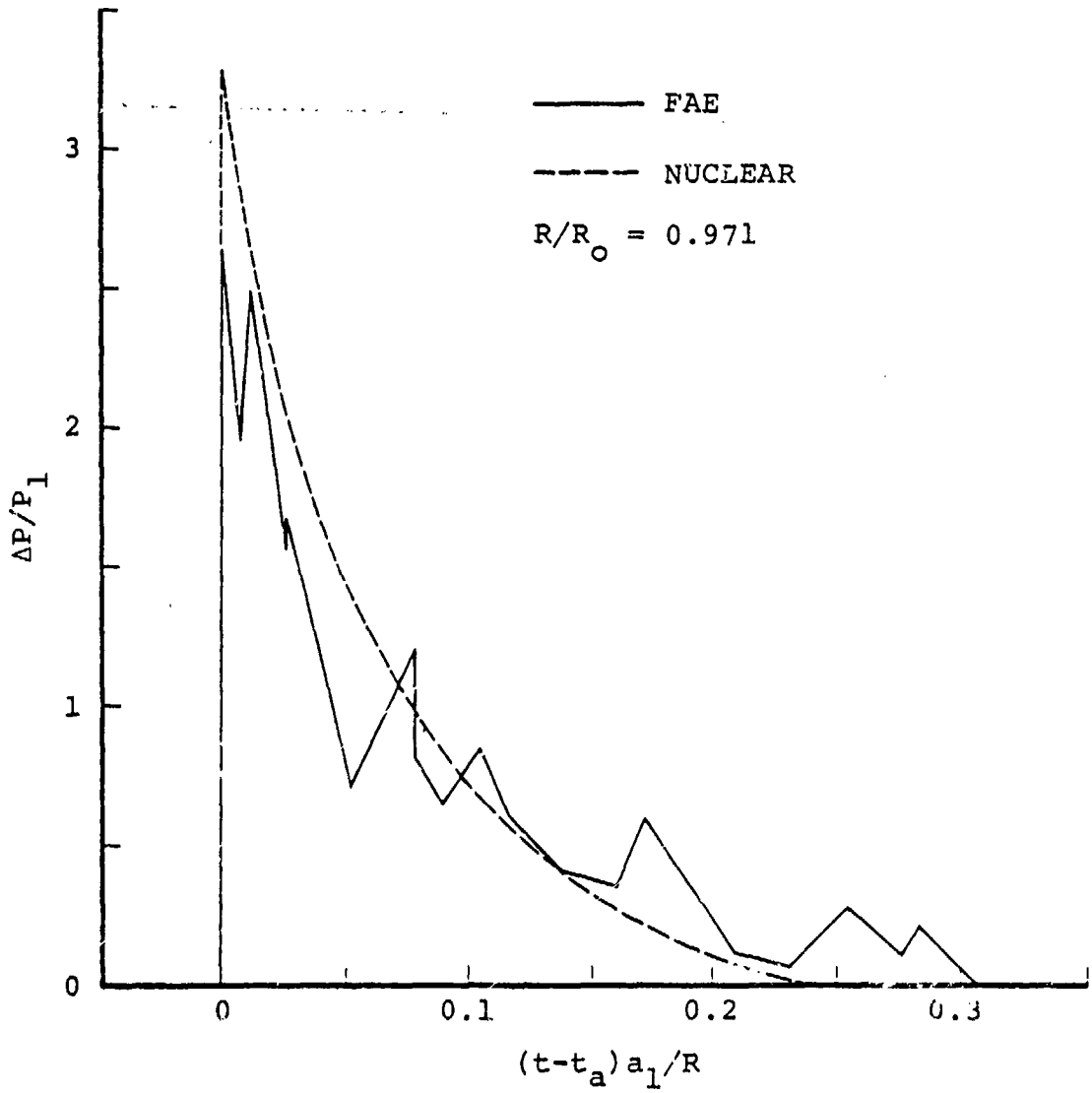

Figure 35. Comparison of Measured Overpressure as a Function of Time with a Nuclear Blast Waveform. The experimental data were taken from Test 2536 (t_a is arrival time).

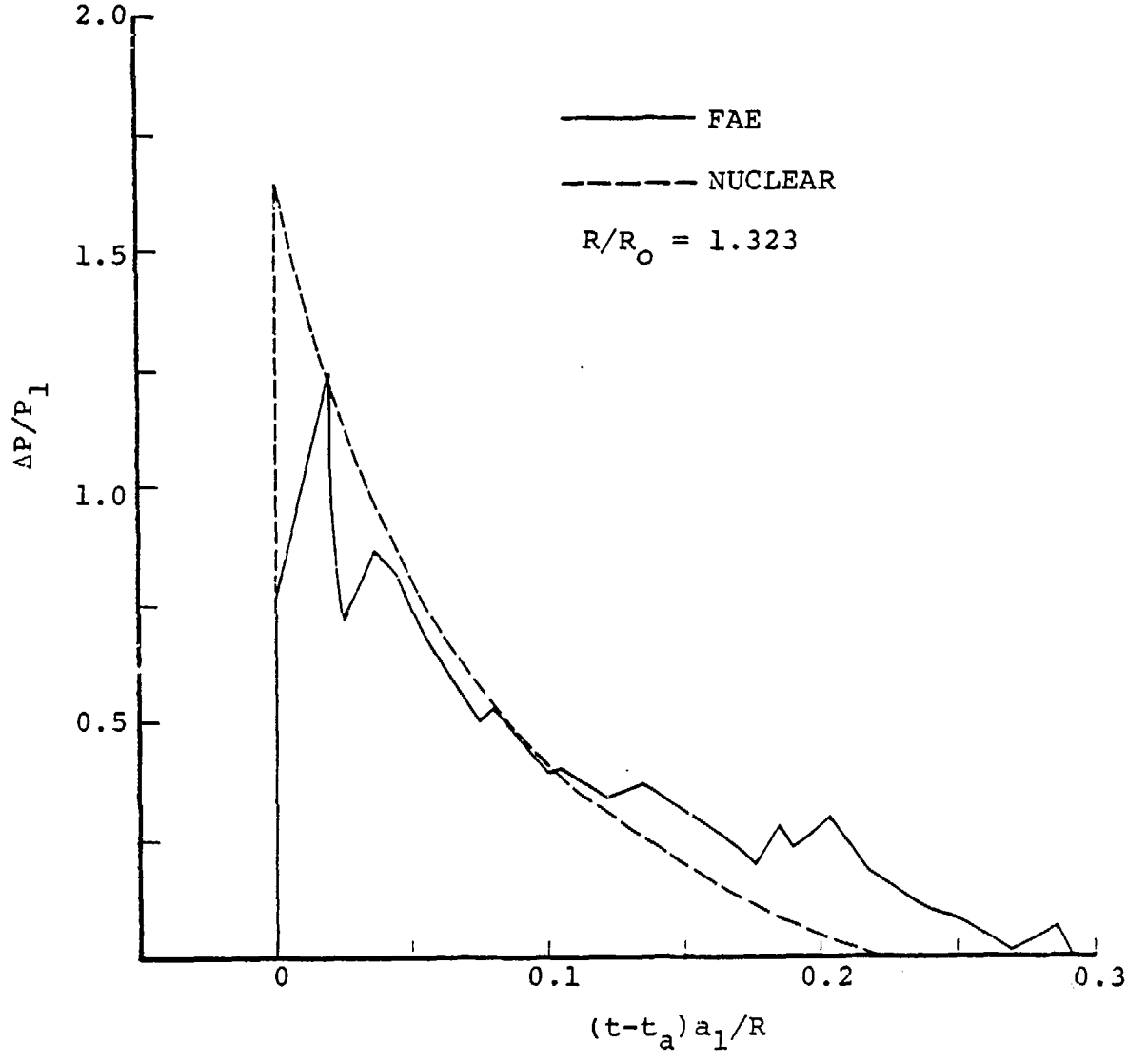

Figure 36. Comparison of Measured Overpressure as a Function of Time with a Nuclear Blast Waveform. The experimental data were taken from Test 2536 (t_a is arrival time).

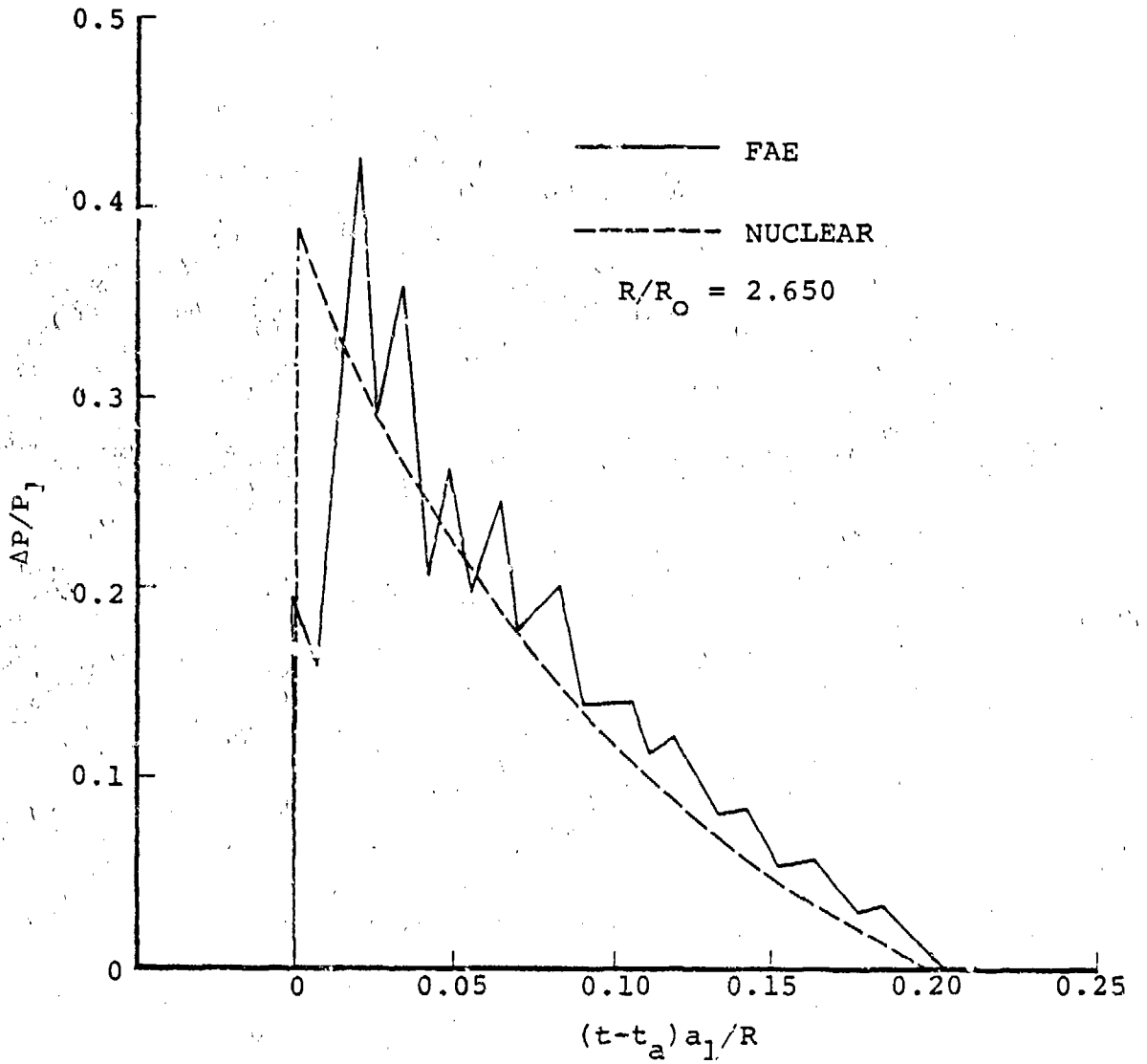

Figure 37. Comparison of Measured Overpressure as a Function of Time with a Nuclear Blast Waveform. The experimental data were taken from Test 2536 (t_a is arrival time).

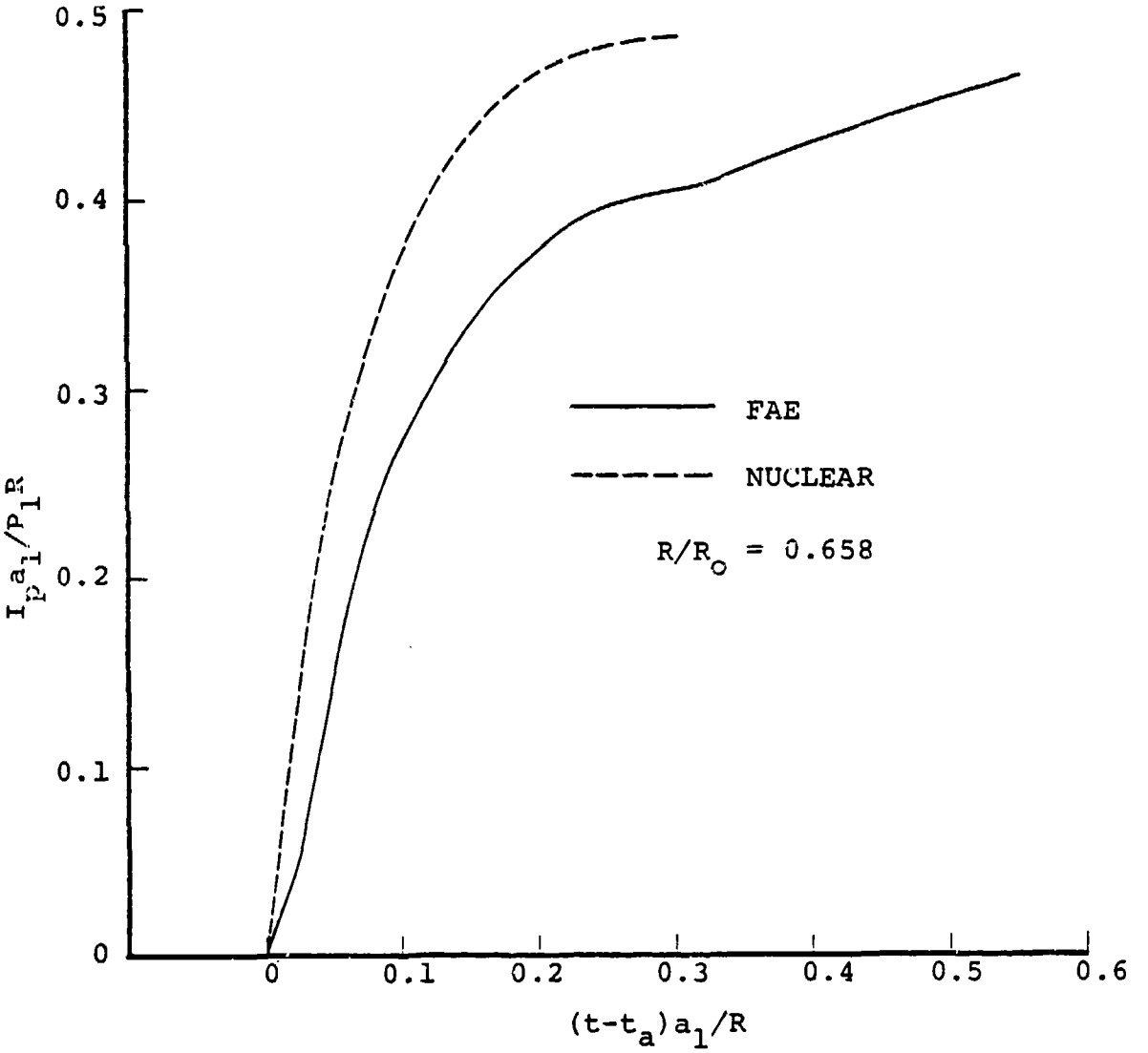

Figure 38. Comparison of Measured Positive Phase Impulse with Nuclear Data. The experimental data were taken from Test 2536 (t_a is arrival time).

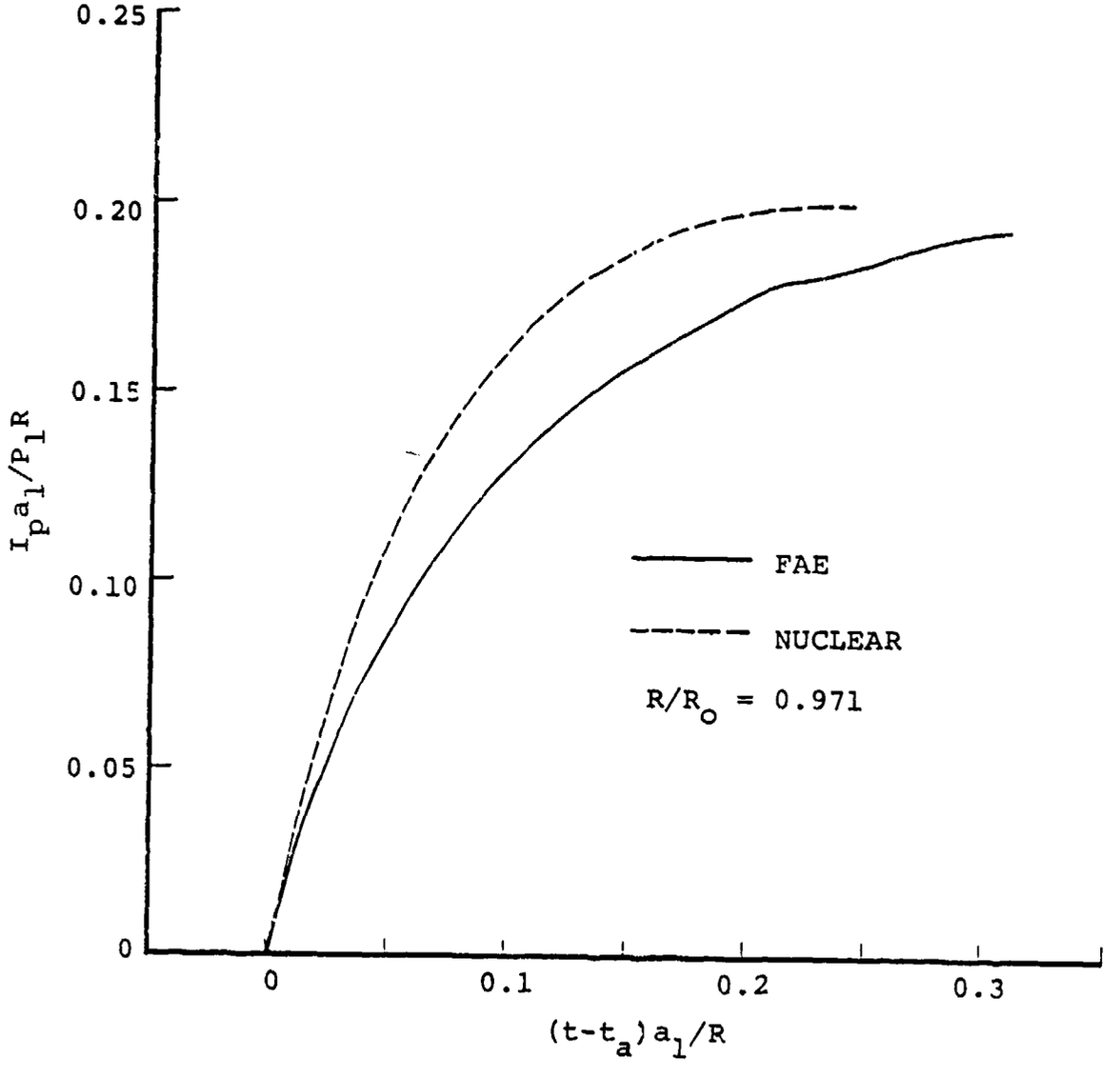

Figure 39. Comparison of Measured Positive Phase Impulse with Nuclear Data. The experimental data were taken from Test 2536 (t_a is arrival arrival time).

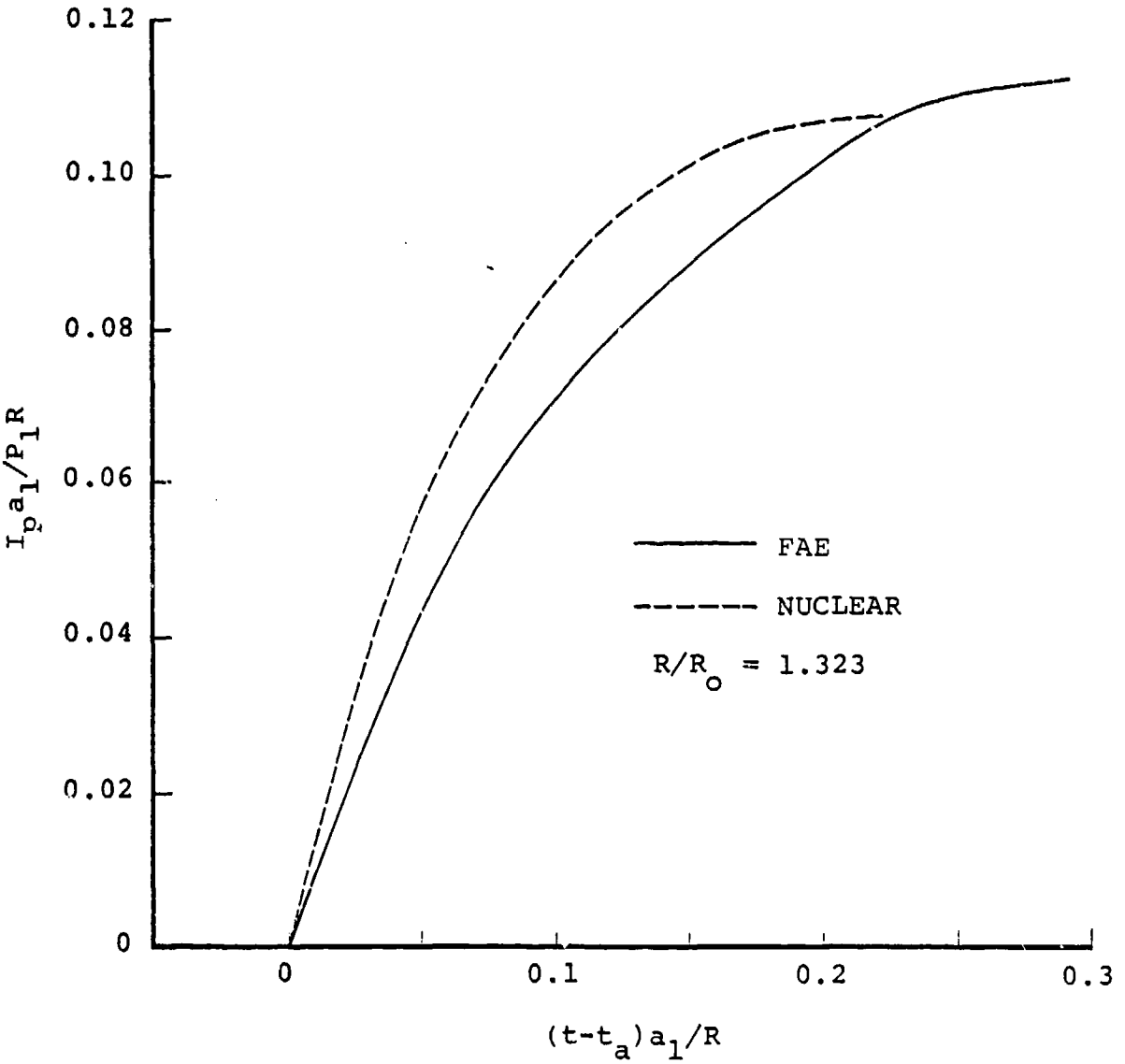

Figure 40. Comparison of measured positive phase impulse with nuclear data. The experimental data were taken from Test 2536 (t_a is arrival time).

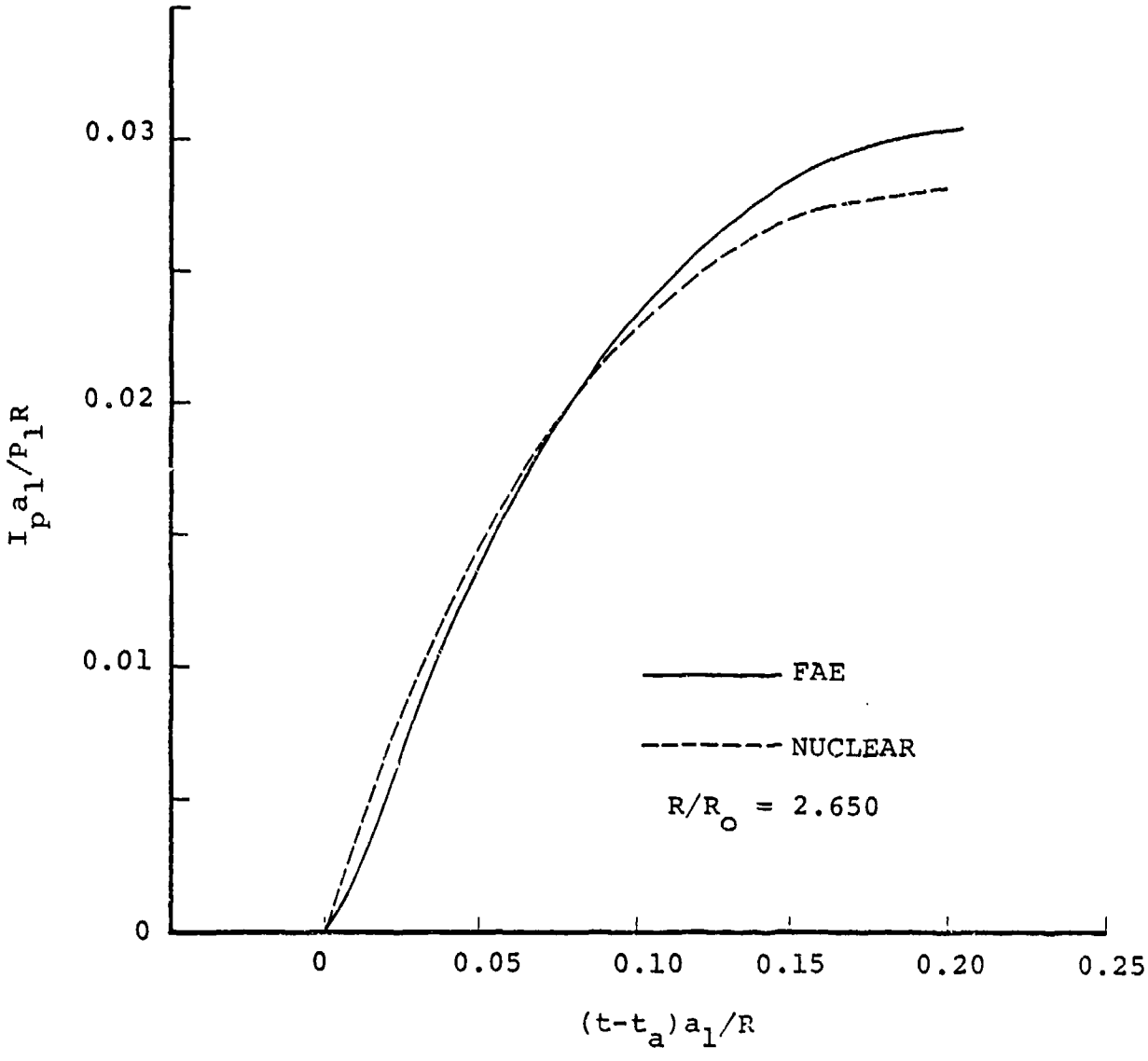

Figure 41. Comparison of measured positive phase impulse with nuclear data. The experimental data were taken from Test 2536 (t_a is arrival time).

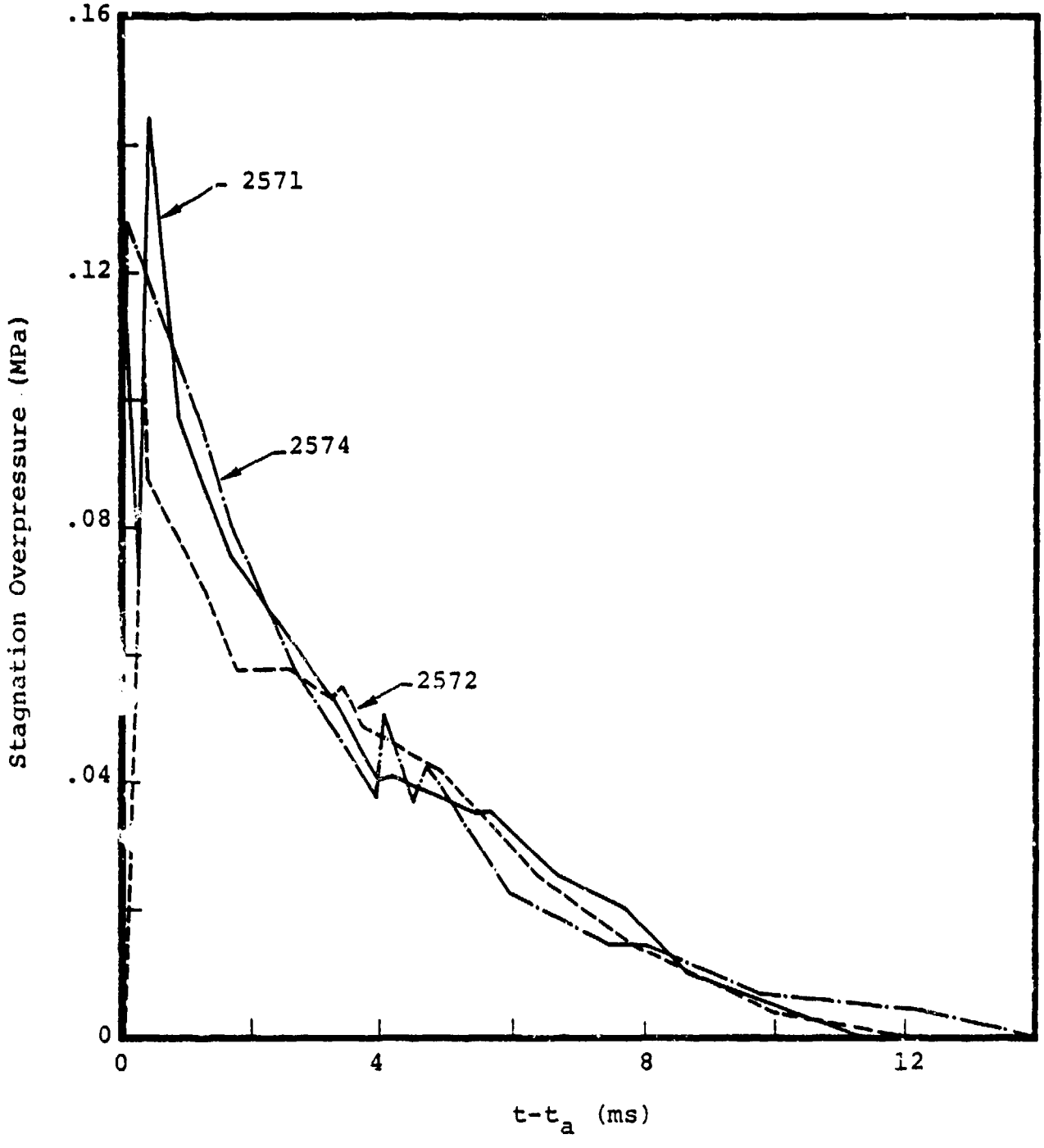

Figure 42. Plot of measured stagnation overpressure as a function of time at the 12.2 m (40 ft) station from three separate experiments (t_a is arrival time).

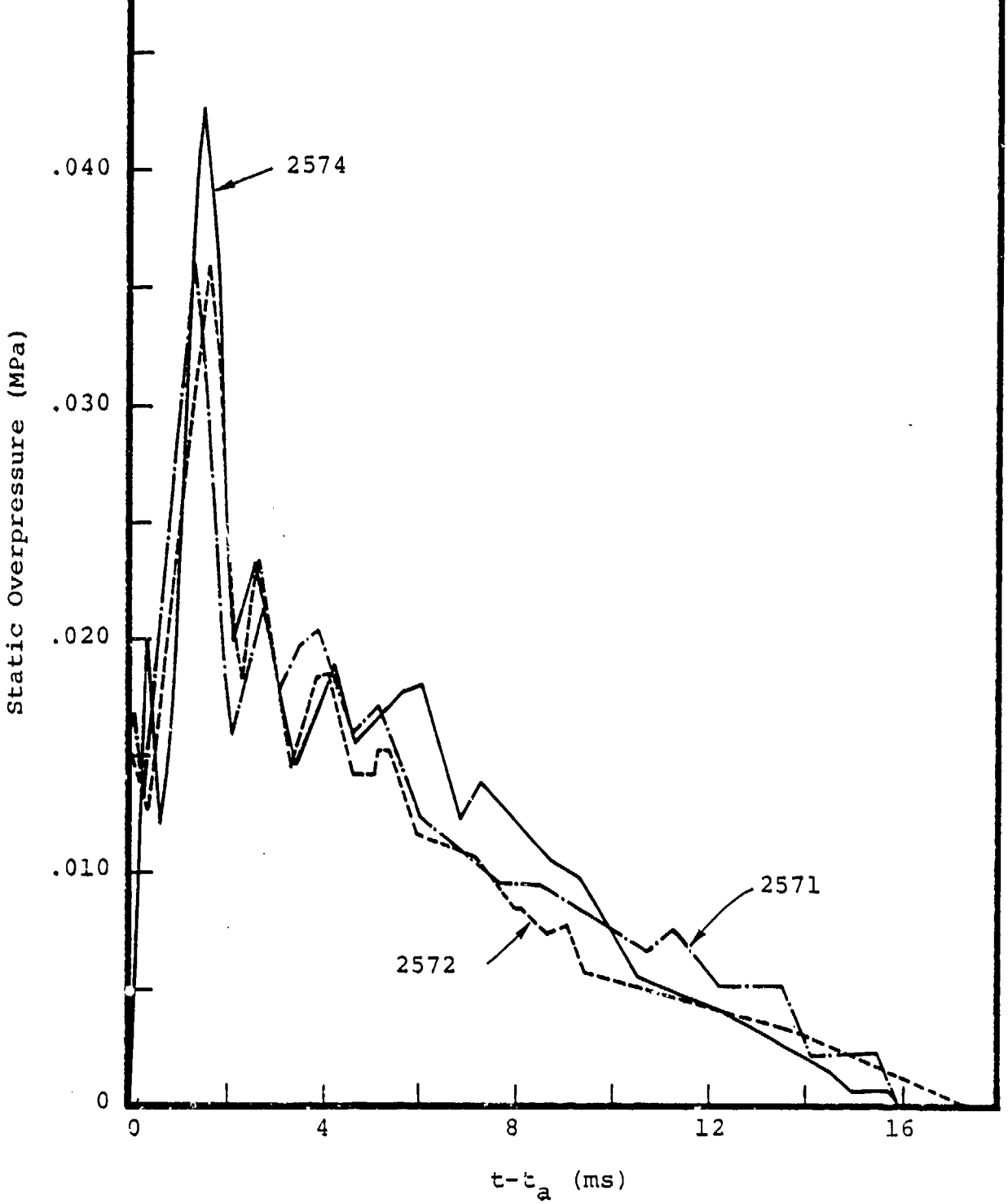

Figure 43. Plot of measured static overpressure as a function of time at the 24.4 m (80 ft) station from three separate experiments (t_a is arrival time).

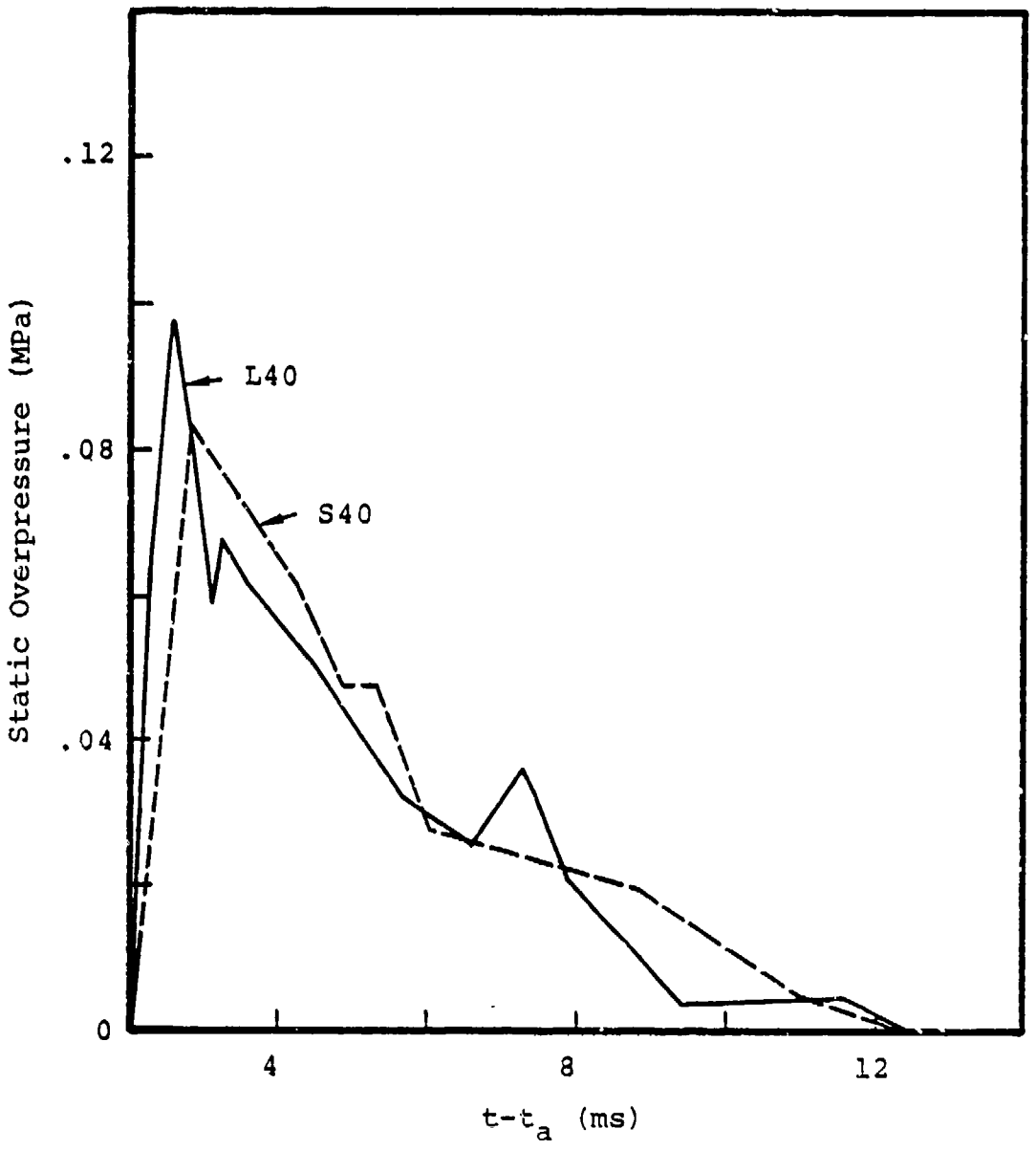

Figure 44. Plot of measured static overpressure as a function of time from a single experiment. The gauges were both located at a range of 12.2 m (40 ft) but were separated by 90 degrees. The experimental data were taken from Test 2571 (t_a is arrival time).

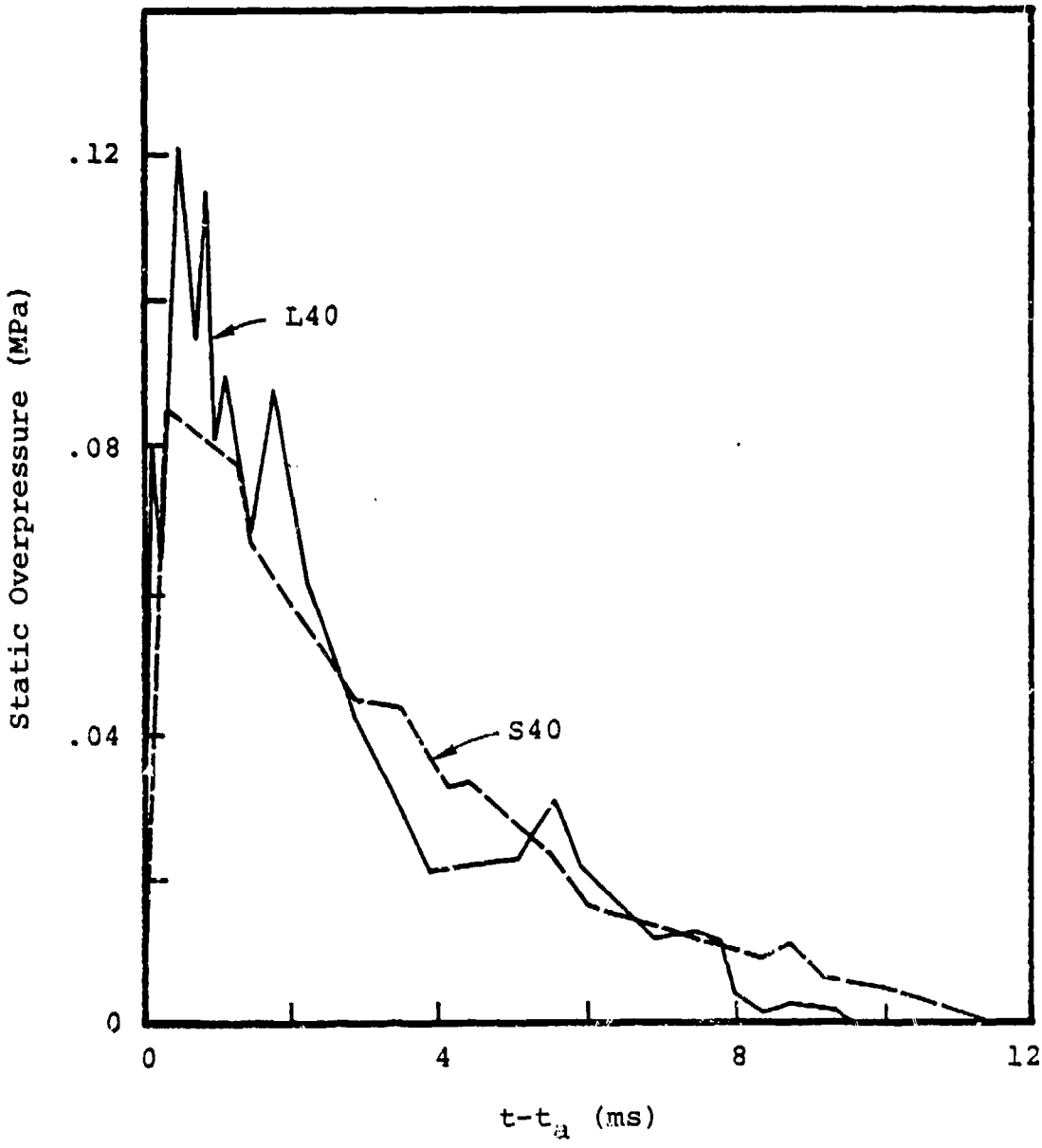

Figure 45. Plot of measured static overpressure as a function of time taken from a single experiment. Both gauges were located at range of 12.2 m (40 ft) but separated by 90 degrees. The comparison is similar to that shown in Figure 15 except that the data plotted are from Test 2574 (t_a is arrival time).

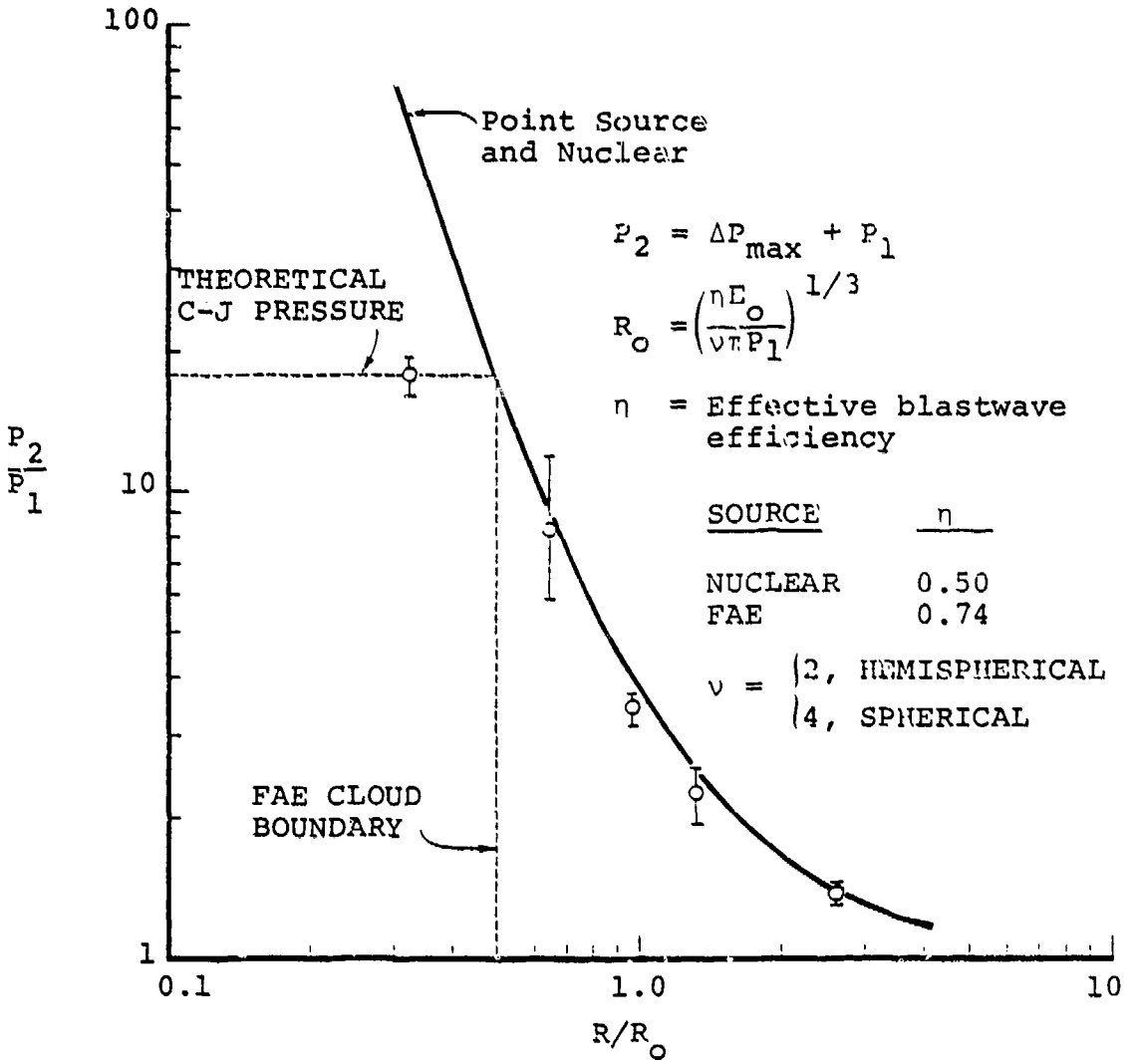

Figure 46. Peak static pressure versus range for hemispherical and spherical blastwaves. FAE data derived from tests with stoichiometric propylene oxide.

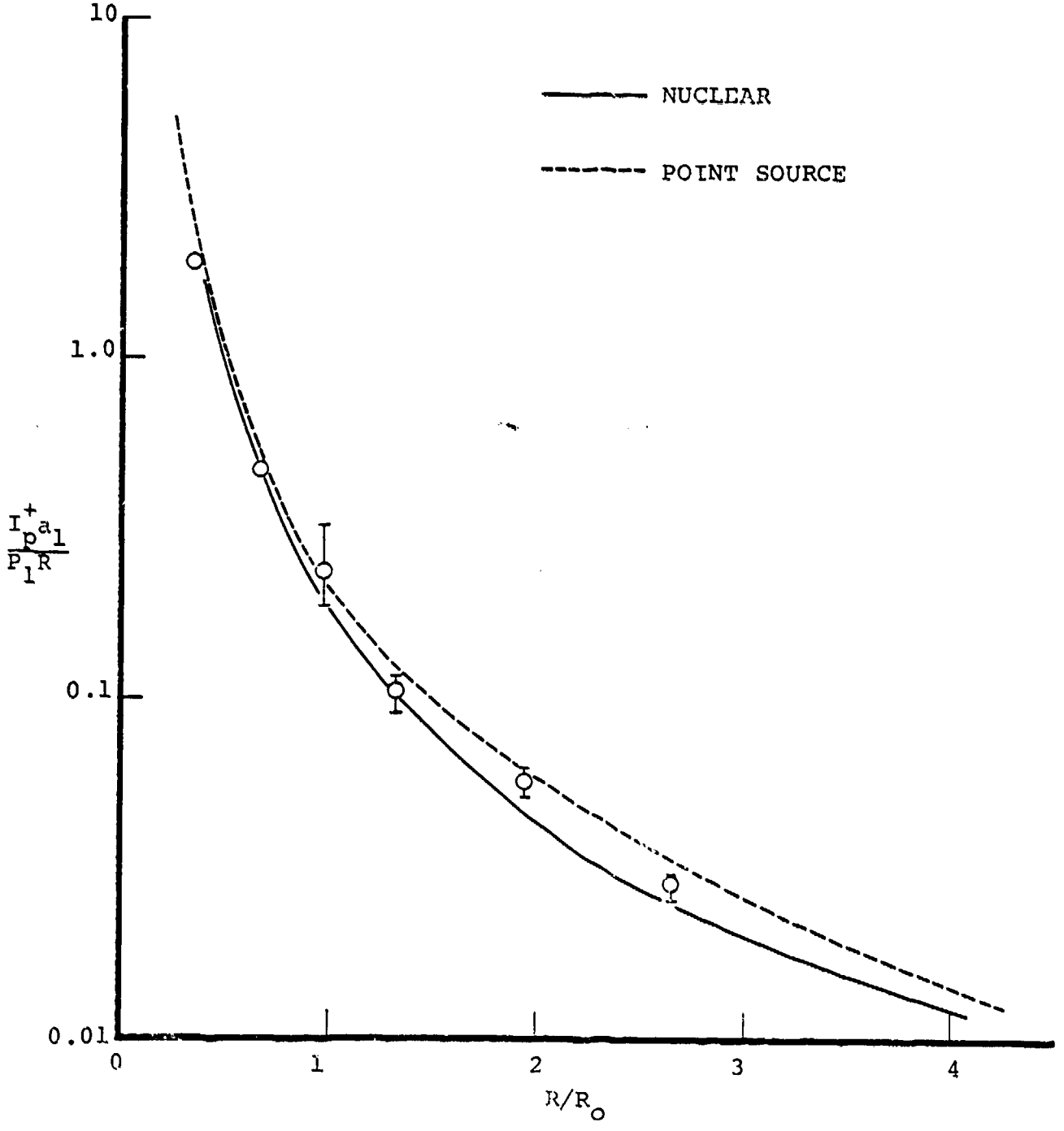

Figure 47. Positive-phase static overpressure impulse versus range. Comparison of FAE data (propylene oxide tests) with reference nuclear curve and point source blastwaves.

The general agreement between the FAE and nuclear data as well as the reasonable degree of symmetry and repeatability were encouraging in these early tests. However, the strain gauge pressure transducers were too slow to yield accurate peak overpressure values at the small experimental scale. Those plotted in Figure 46 were accordingly considered to be low by some undertermined amount. Rather than extrapolate to infer peak values, the peaks from the raw data were reported as ΔP_{max}. Scale factors and effective blast coupling efficiencies were, therefore, determined from the positive phase impulse measurements alone, since impulse is less sensitive to inaccuracies in ΔP_{max}. The averages of these two parameters among all tests were $s \doteq 16$ and $\eta_F \doteq 0.74$.

In addition to rounded peaks, the static pressure data also exhibit numerous excursions. These precluded credible dynamic pressure and positive-phase duration determinations which are quite sensitive to small measurements errors. It is true, of course, that raw nuclear airblast data are also irregular in time (see Figures 27 and 28). However, it was not known if the pressure excursions in the FAE tests were inherent to the explosion process. It was considered likely that the excursions were at least in part the result of reflections from surface irregularities in the vicinity of the transducers or reflections from ground slopes surrounding the test area that was in use at the time. Questions of this nature were considered sufficient justification to warrant the improvement and relocation of the test facility.

A limited number of FAE tests utilizing the new facilities, hardware, instrumentation, and data reduction software were conducted. These tests were intended to exercise the new equipment and procedures, and to attempt detonation of clouds after minimal formation time. A problem was experienced in this test series with what appeared to be oscillatory noise caused by vibration of the transducer mounting plates (see

Figures A-3 and A-4). Unfortunately this problem was not corrected by simple modifications of the plates (such as installing the transducers in delrin or teflon inserts).

A sample of the raw data taken from a test (CD-6) in this series appears in Figure 48. The semi-smoothed profile used for data reduction is superimposed on the raw data in this figure. Experiment CD-6 was a test in which a nominally stoichiometric, propylene-oxide/air cloud was detonated. The linear dispenser was used with a 600-hole nozzle head. The peak fuel dispensing pressure was about 1.3 MPa (190 psi). Detonation of the cloud was initiated by a 0.5 kg (1.1 lb) ball of H.E. (C-4) mounted 0.38 m (15 in.) above the nozzle head. The initiator was fired 0.6 s after the start of fuel dispensing, at which time the appearance of the fuel/air cloud was similar to that in Figure 23(a).

The data from test CD-6 was fully reduced. Characteristic explosion lengths as inferred from peak static overpressure and from overpressure impulse measurements are plotted in Figure 49. The arithmetic average of these is R_o = 7.54 m (24.7 ft), which leads to η_F = 0.392 and s = 19.8. The low efficiency and high scale factor are attributed to the short time allowed for cloud formation. That is, the fuel spray jets had not spread sufficiently to engulf the air between them at the cloud boundaries. The short cloud formation times were, however, consistent with the requirement that the FAE simulator be capable of operation in moderate winds. Improvements in technique should permit fast cloud formation with increased effective blastwave efficiency.

The reduced data from test CD-6 are presented in Figures 50-61. The peak static overpressure, overpressure impulse, overpressure positive phase duration, and dynamic pressure are plotted as functions of range in Figures 50-53. Semi-smoothed

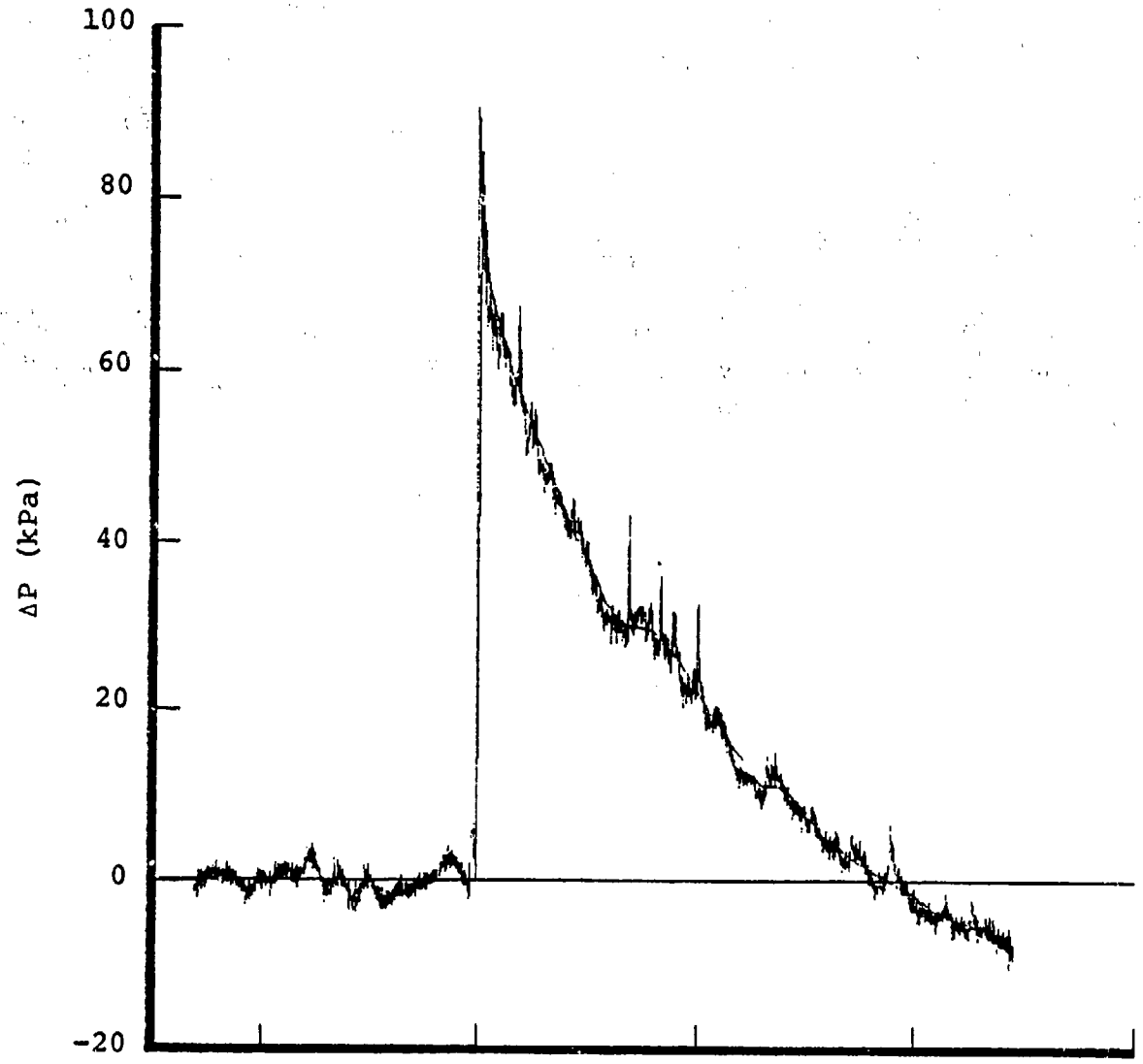

Figure 48. Raw and semi-smoothed static pressure data from FAE test CD-6 at R = 13.9 m (45.6 ft), transducer position no. 4 (t_a is arrival time).

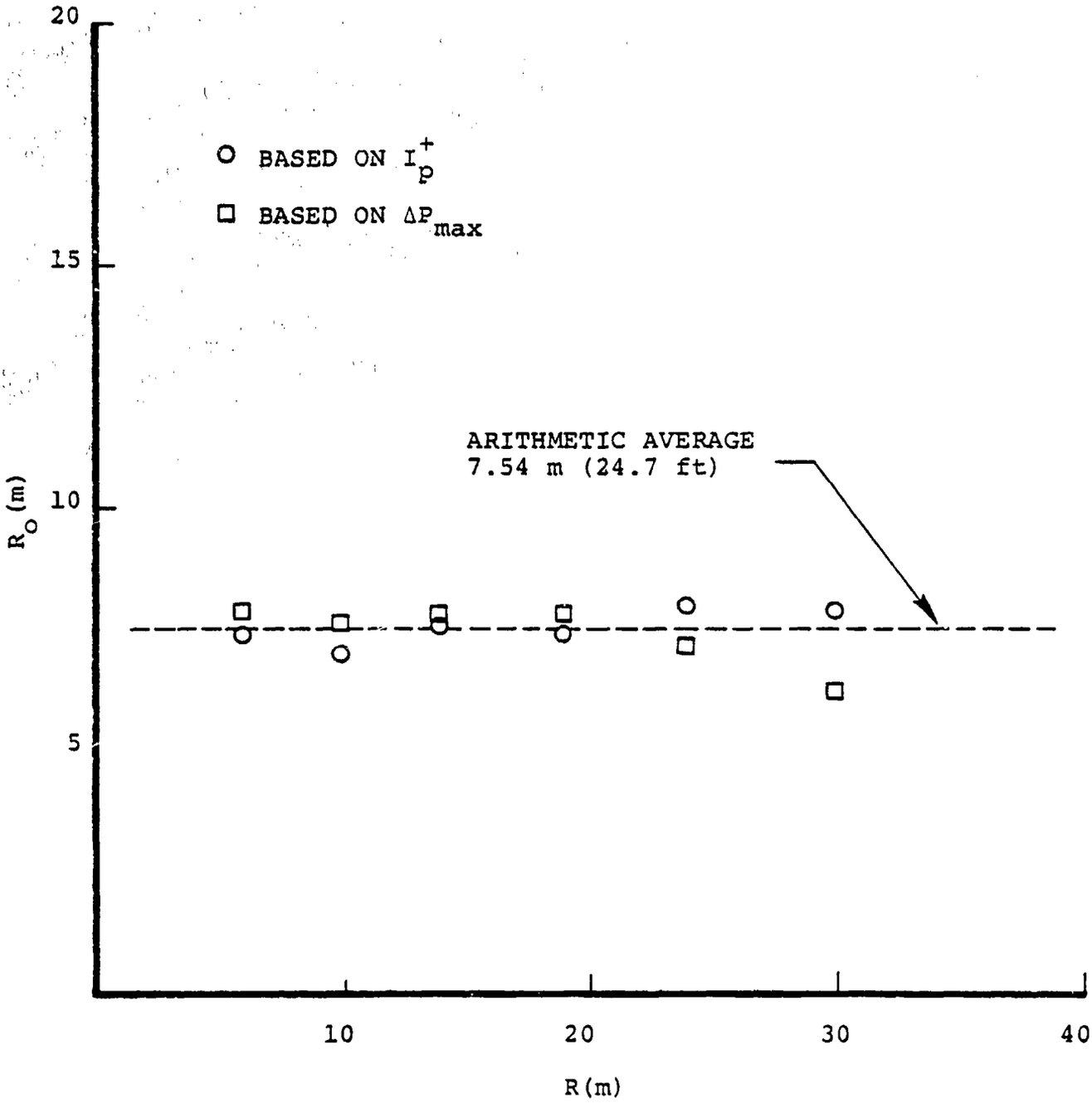

Figure 49. Characteristic explosion length versus range for test CD-6.

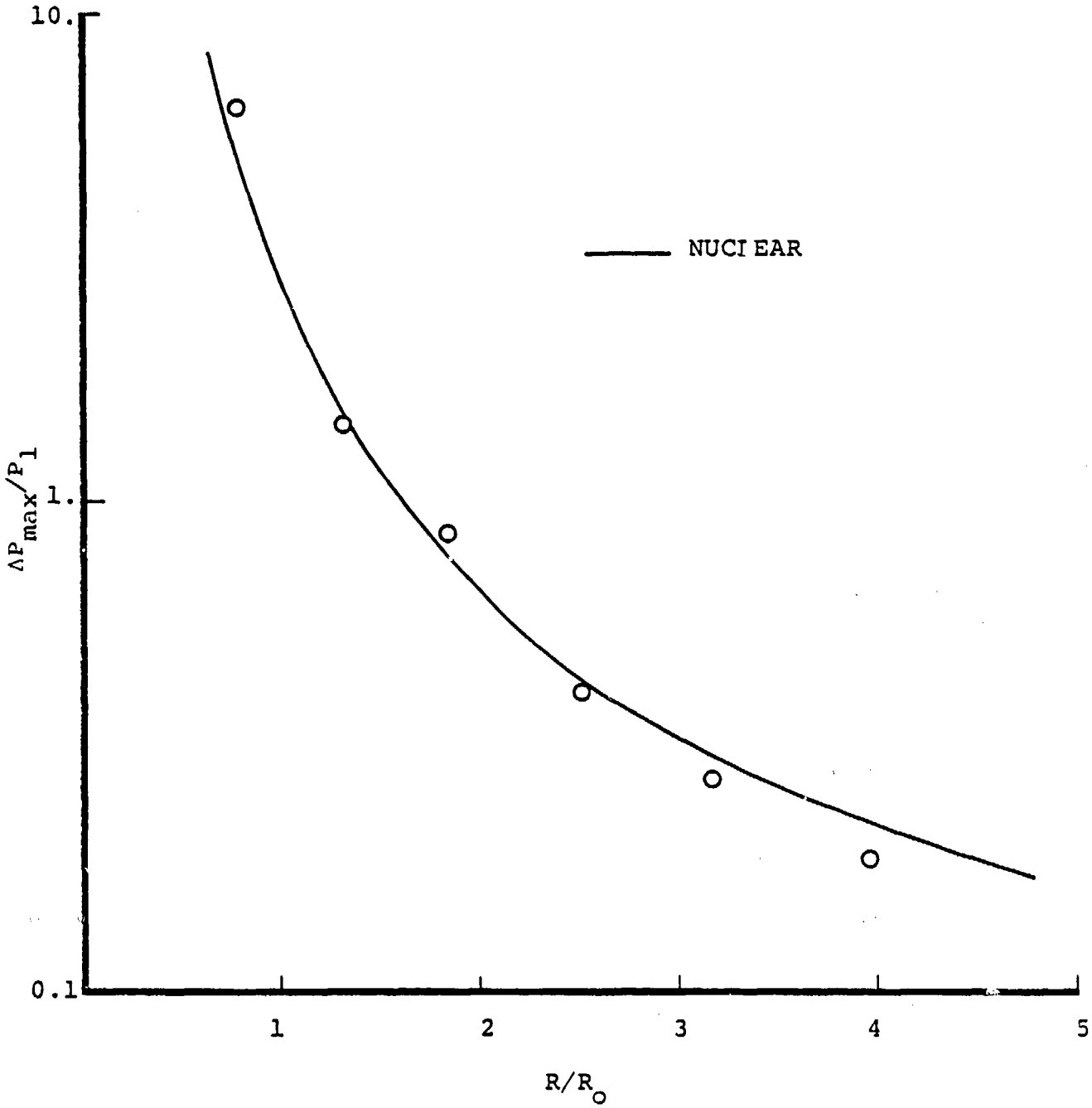

Figure 50. Peak static overpressure versus range for test CD-6.

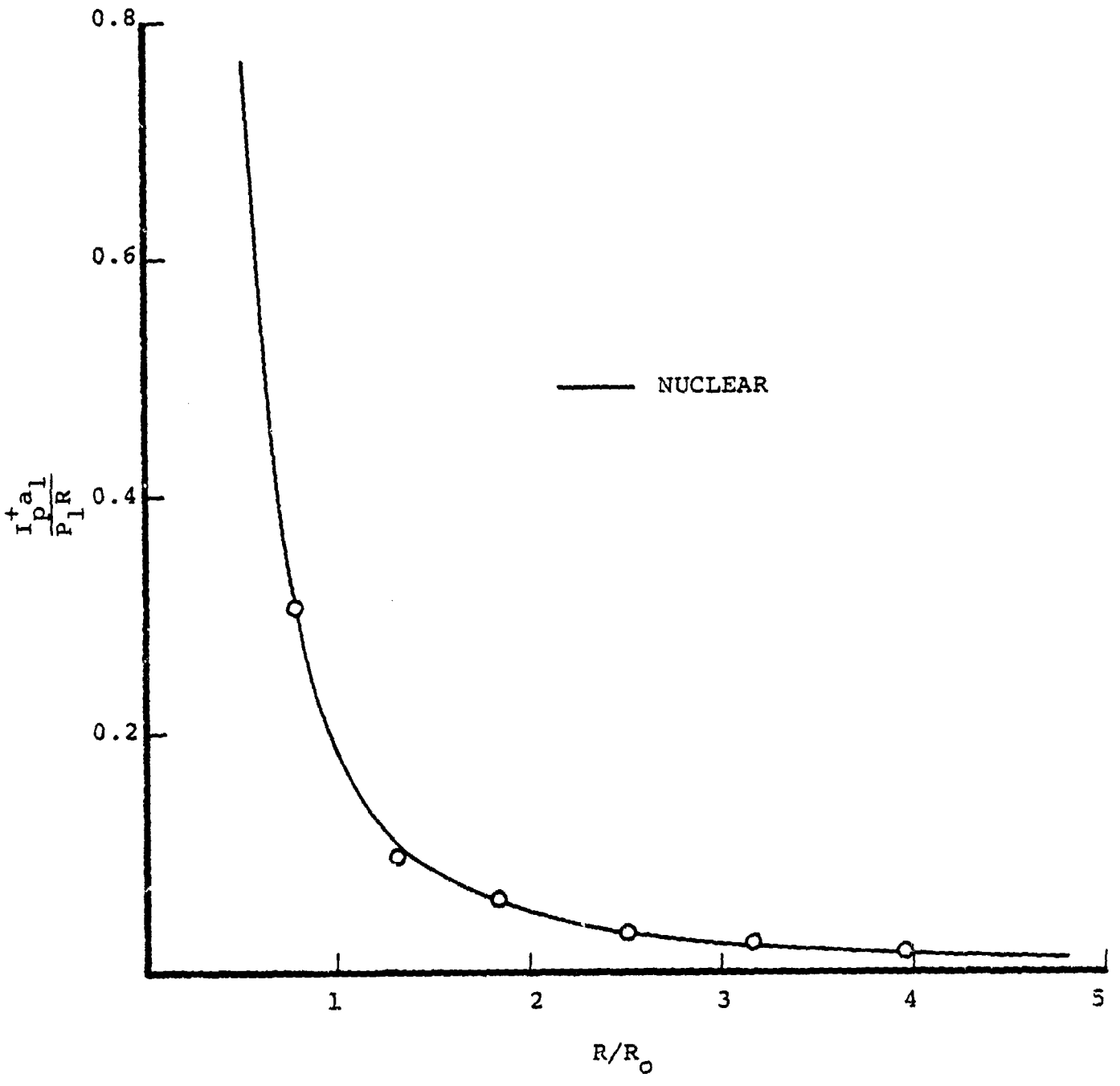

Figure 51. Peak static overpressure impulse versus range for test CD-6.

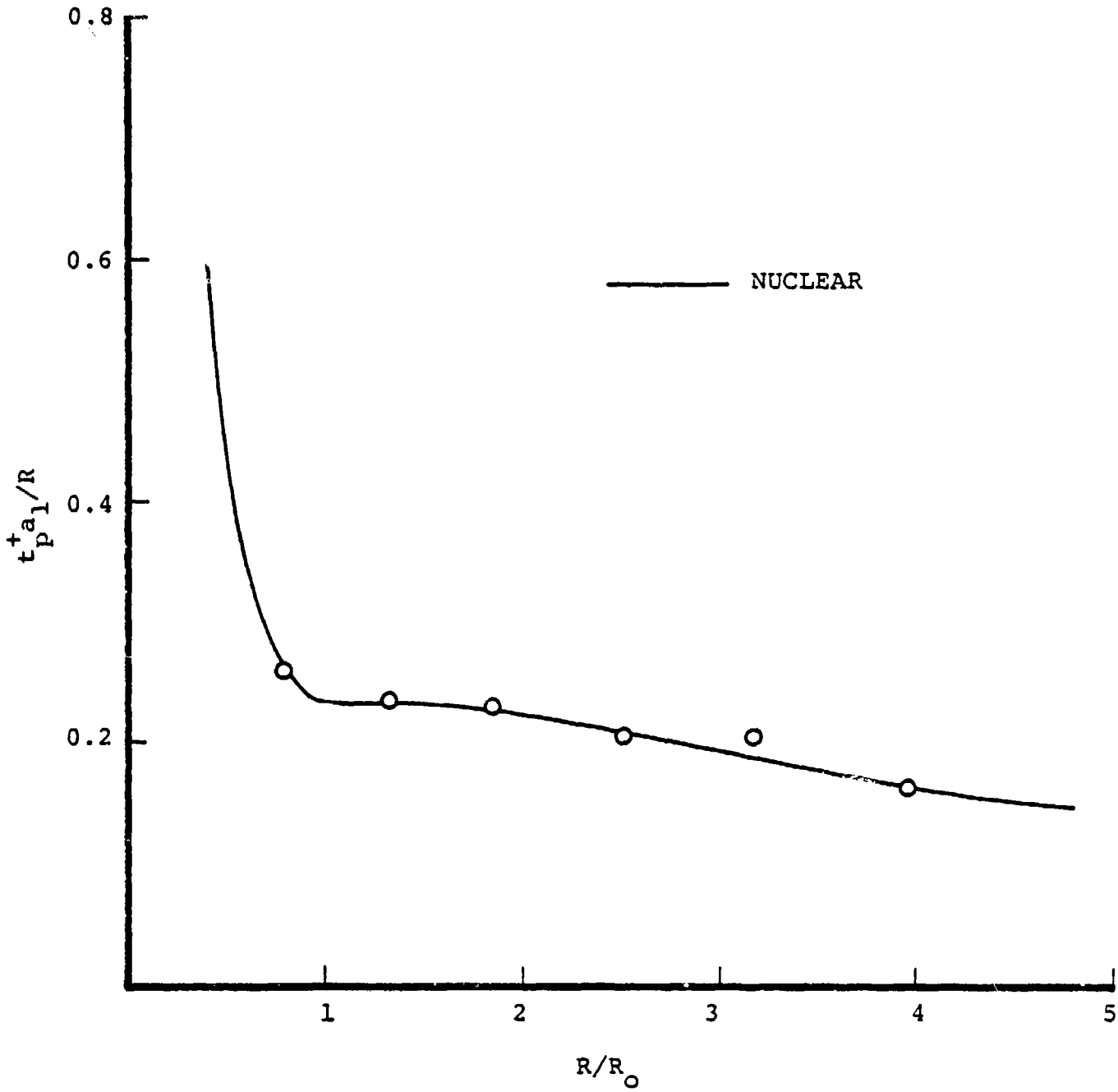

Figure 52. Static overpressure positive phase duration versus range for test CD-6.

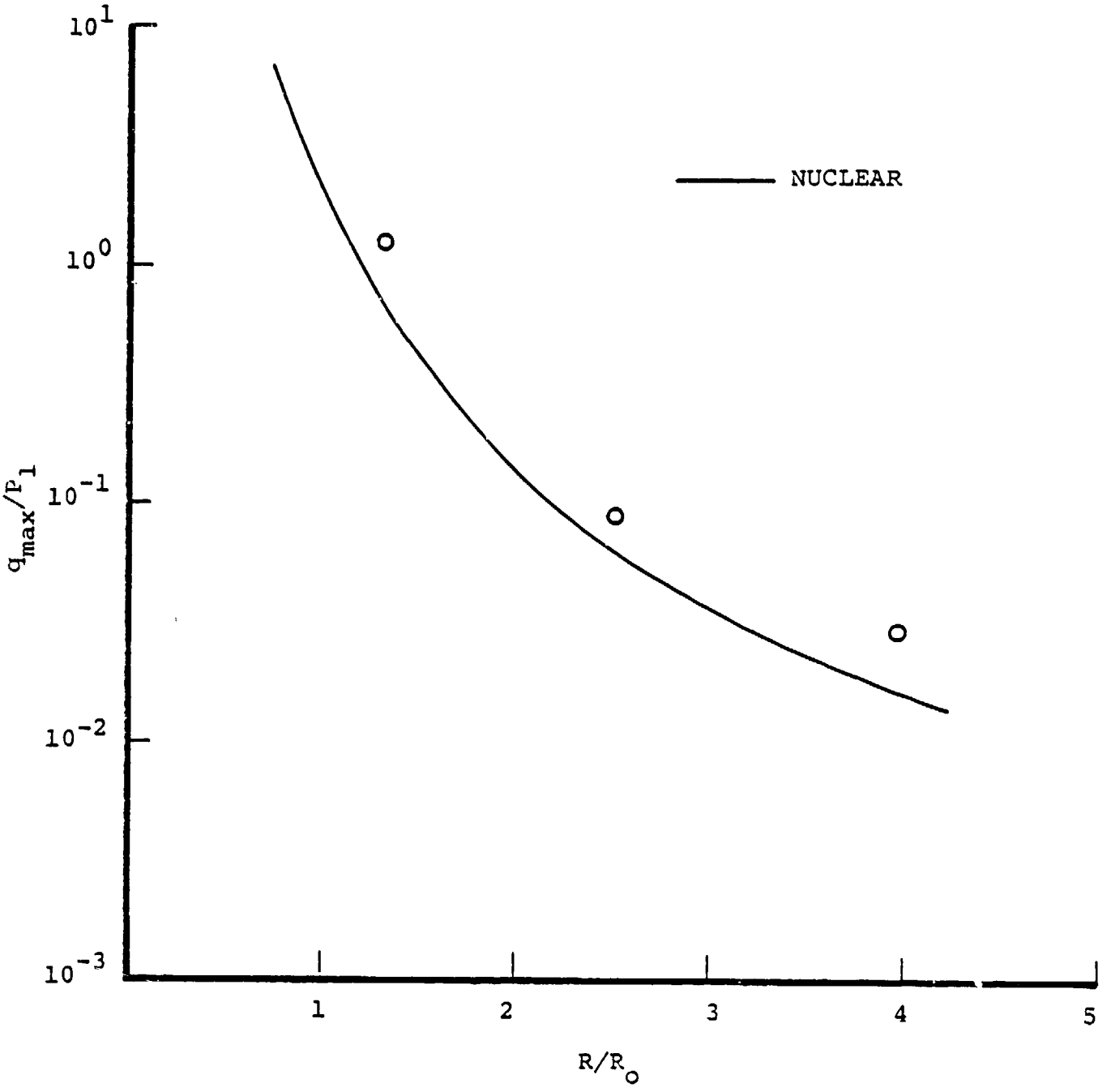

Figure 53. Peak dynamic pressure versus range for test CD-6.

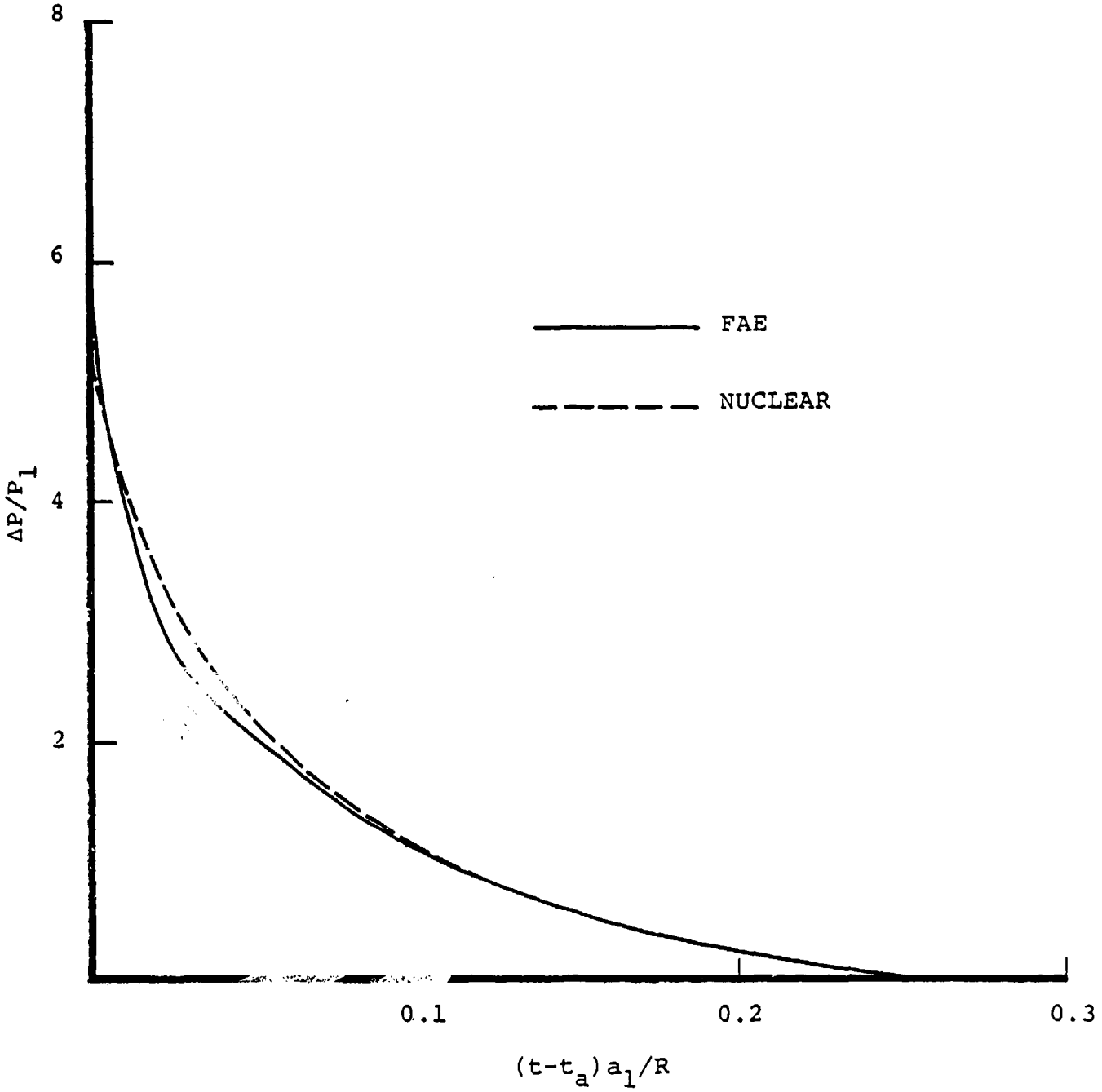

Figure 54. Static overpressure versus time during test CD-6 at R/R_o = 0.782, transducer position no. 2 (t_a is arrival time).

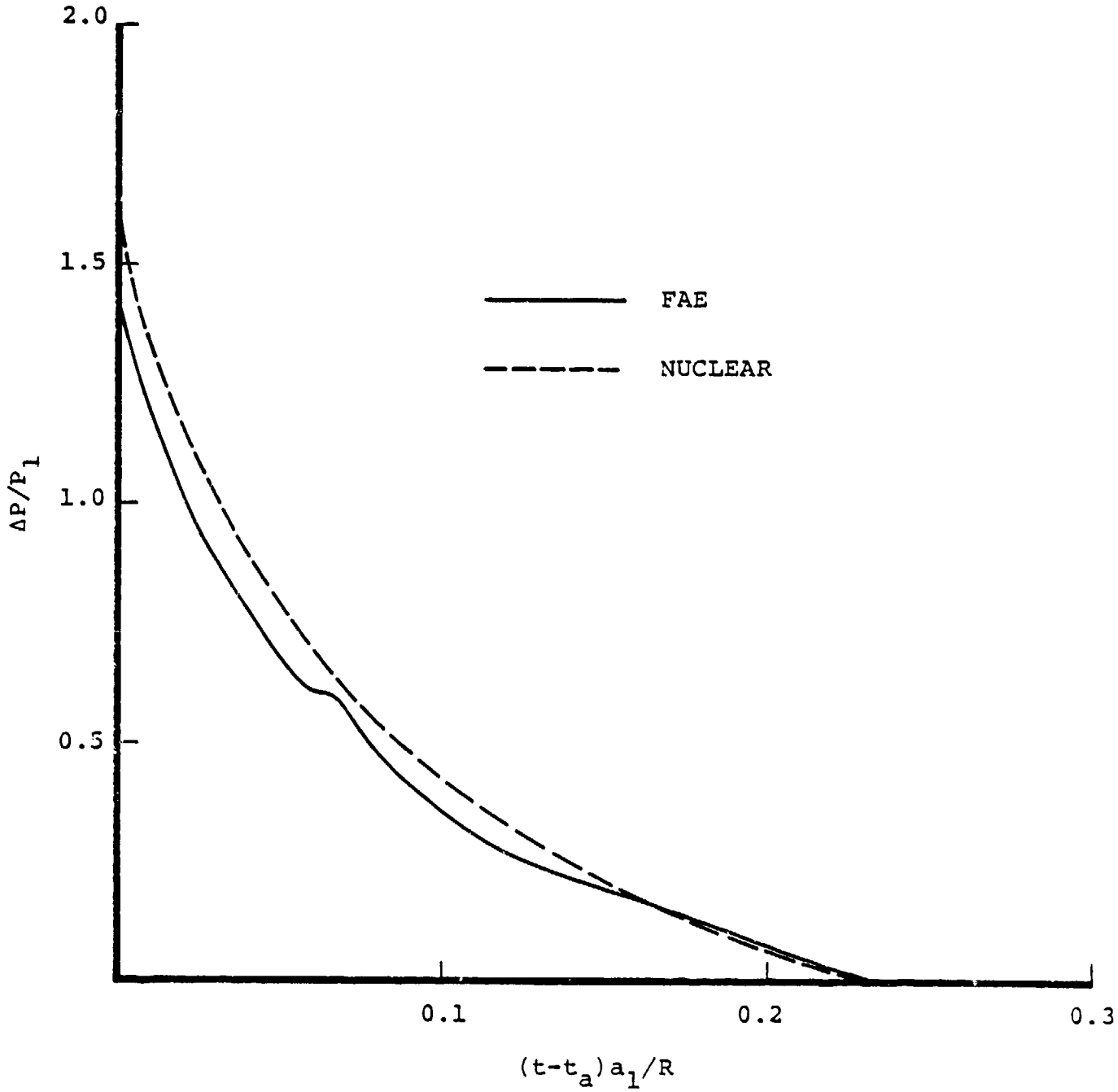

Figure 55. Static overpressure versus time during test CD-6 at R/R_o = 1.31, transducer position no. 3 (t_a is arrival time).

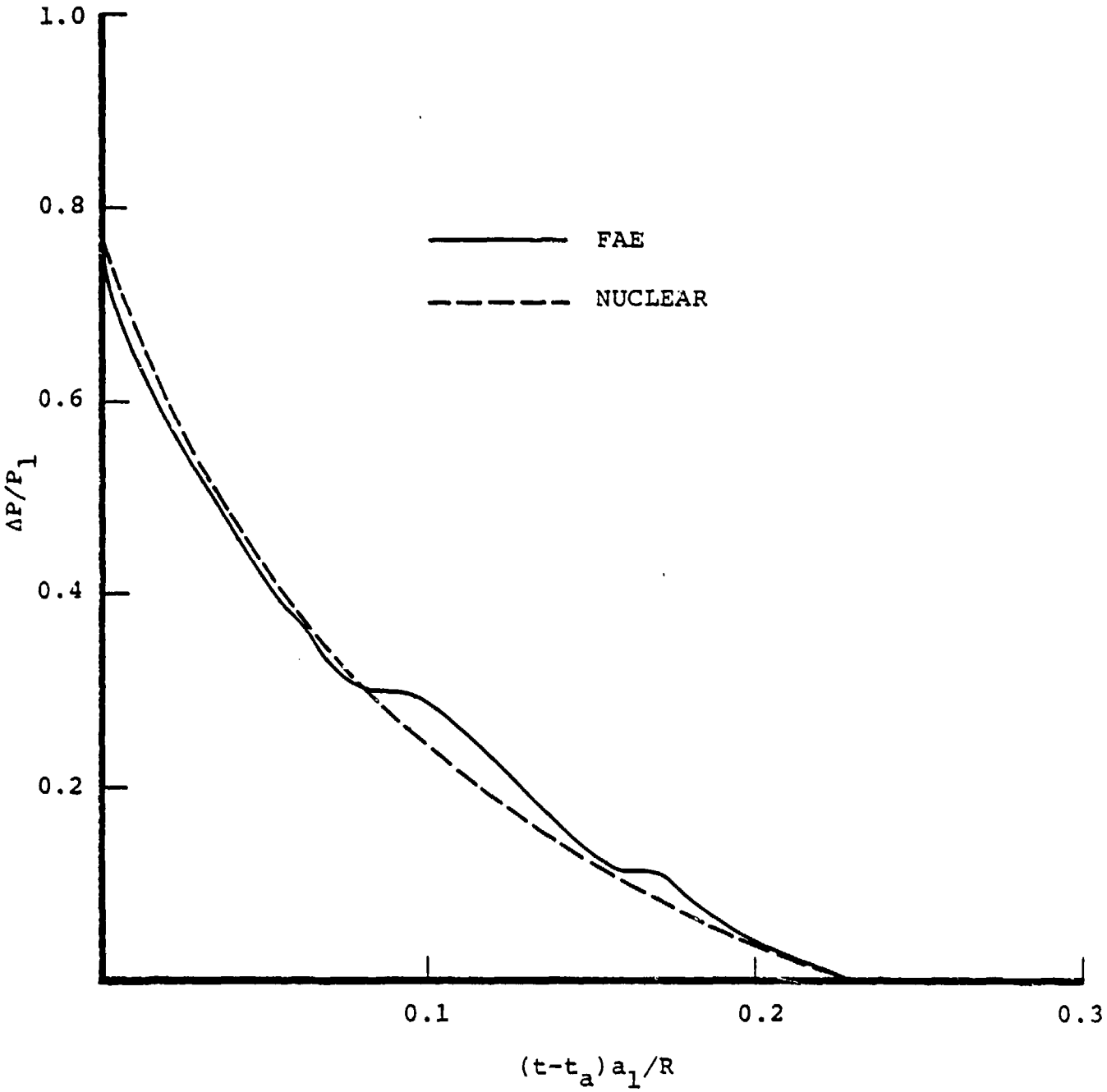

Figure 56. Static overpressure versus time during test CD-6 at R/R_o = 1.84, transducer position no. 4 (t_a is arrival time).

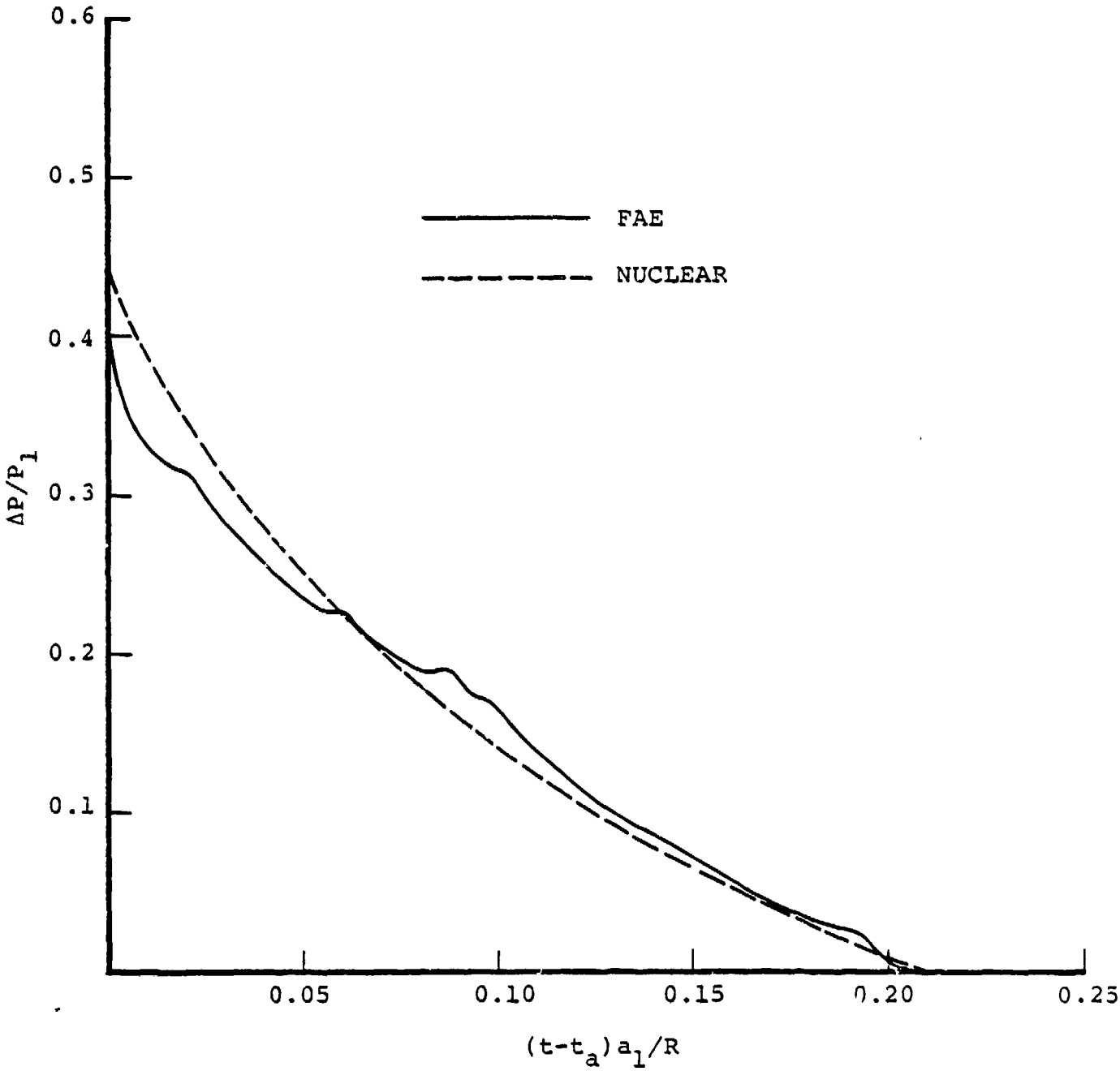

Figure 57. Static overpressure versus time during test CD-6 at R/R_o = 2.51, transducer position no. 5 (t_a is arrival time).

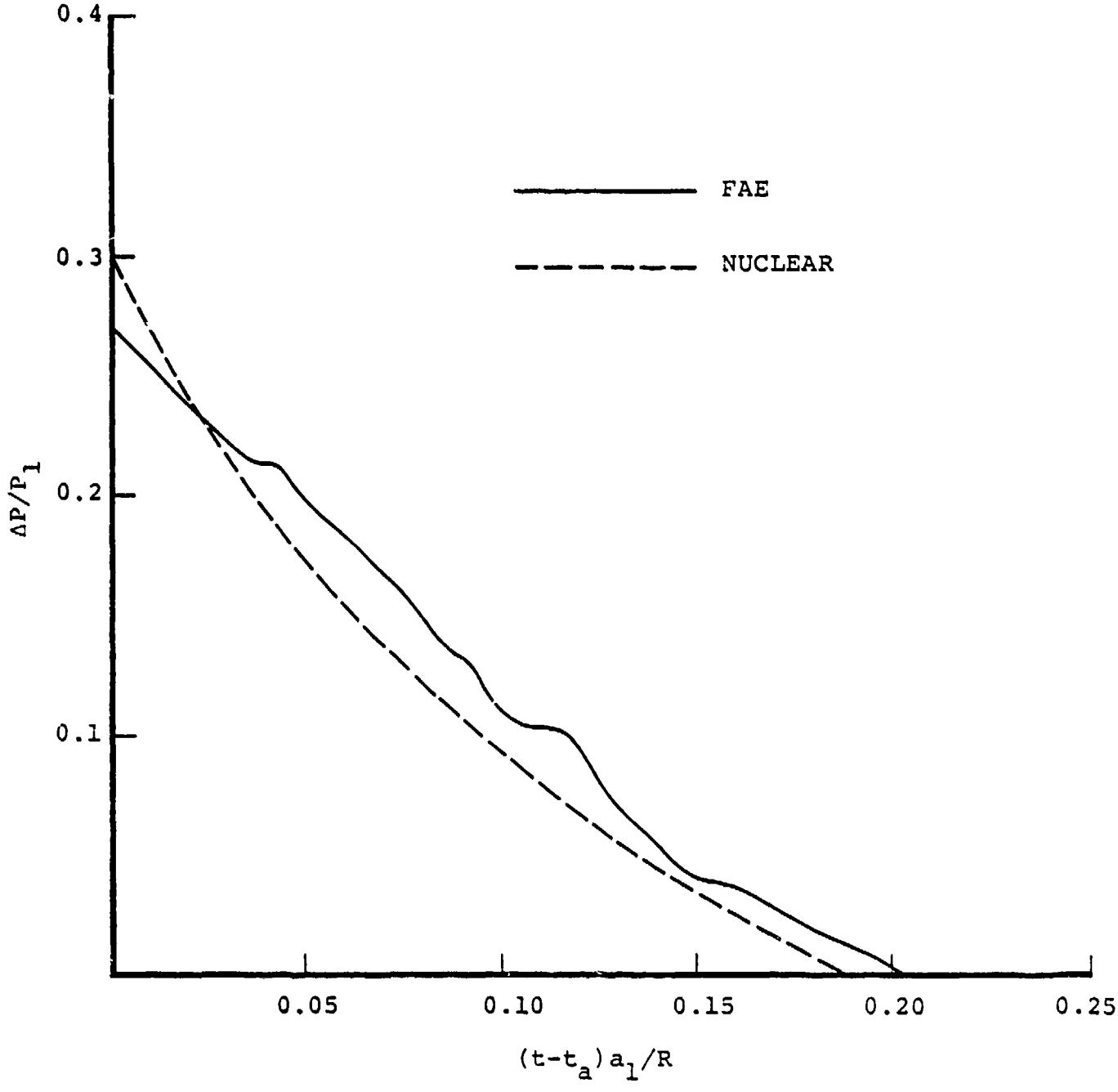

Figure 58. Static overpressure versus time during test CD-6 at R/R_o = 3.17, transducer position no. 6 (t_a is arrival time).

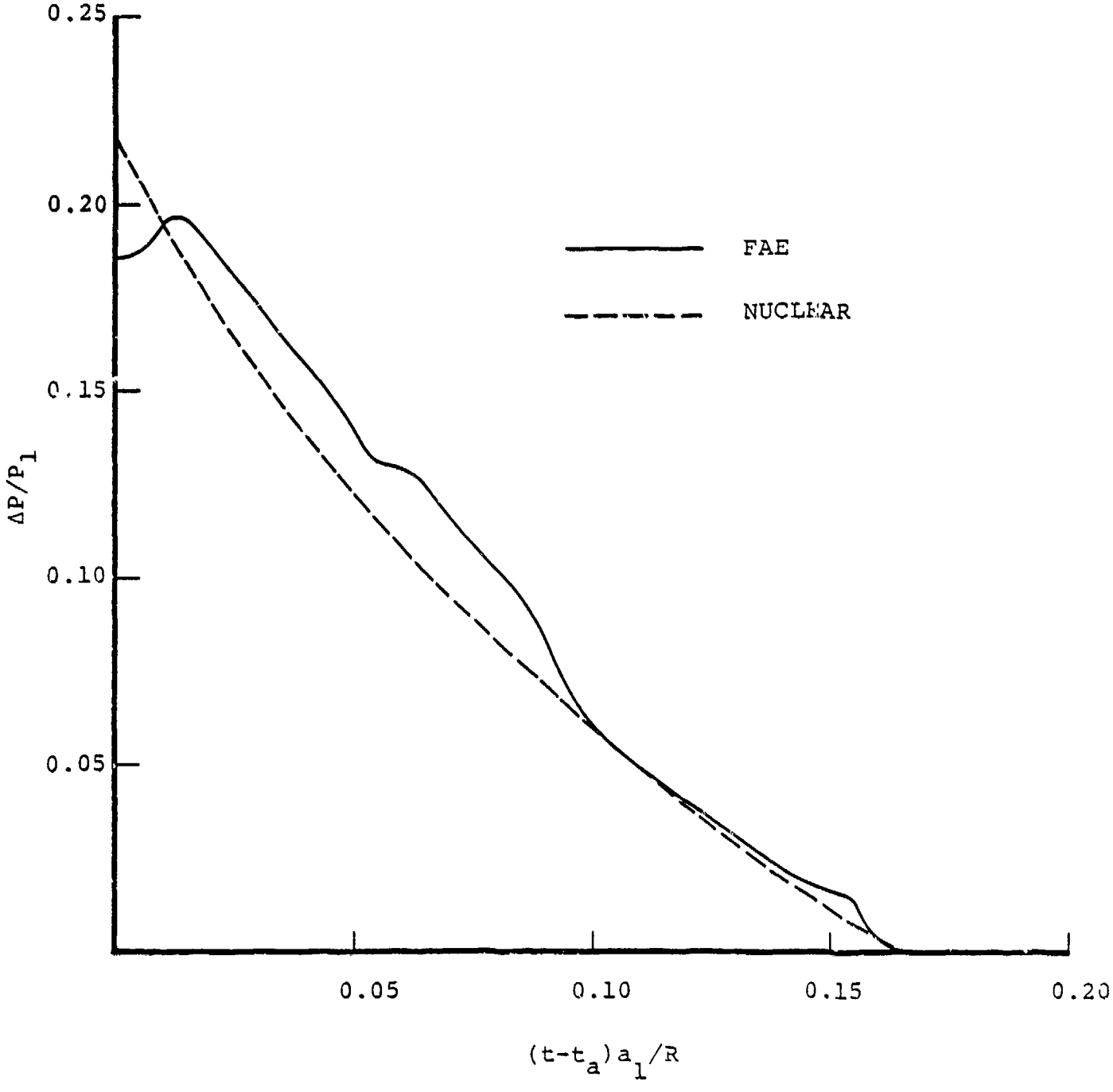

Figure 59. Static overpressure versus time during test CD-6 at R/R_o = 3.97, transducer position no. 7 (t_a is arrival time).

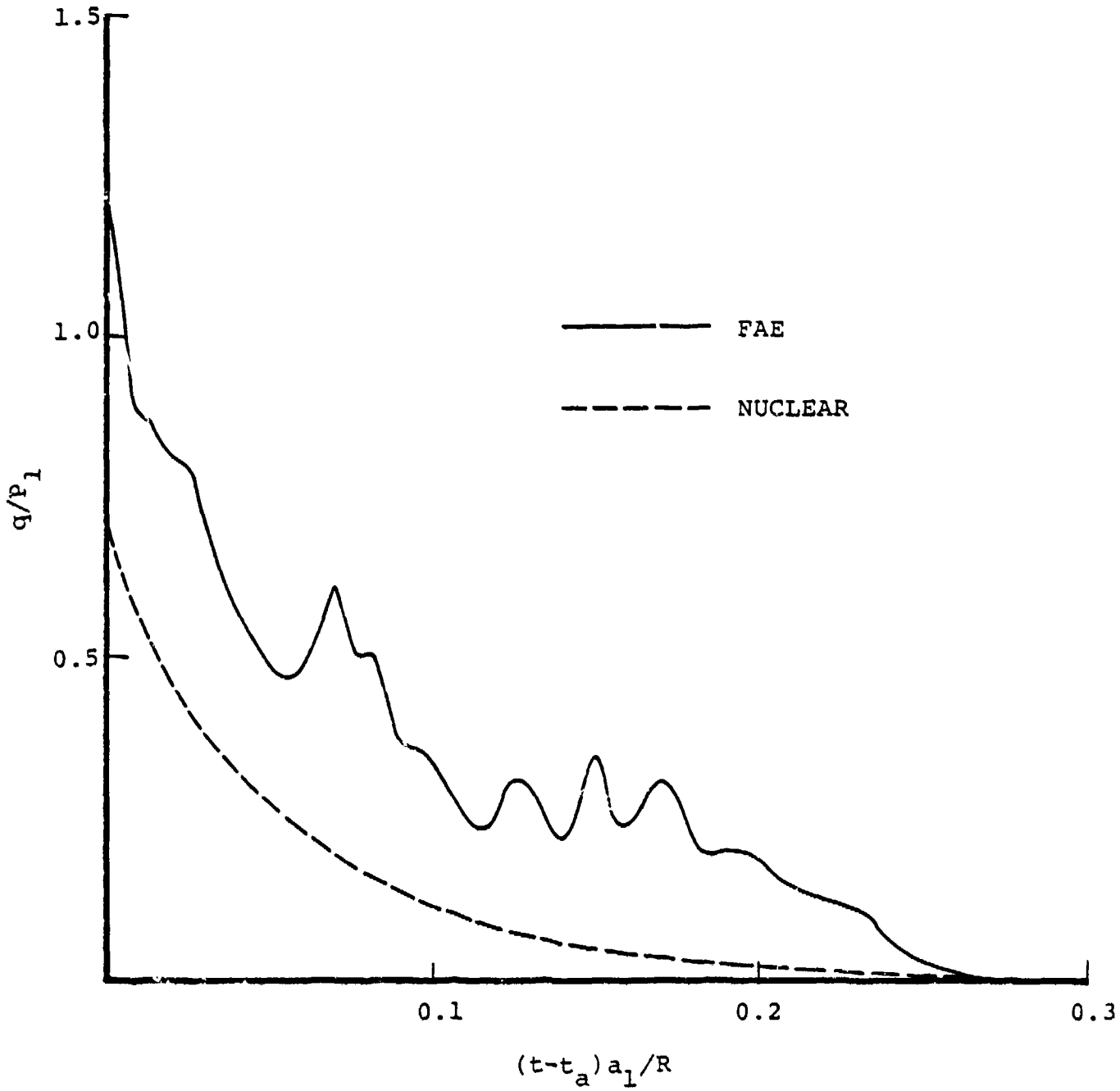

Figure 60. Dynamic pressure versus time during test CD-6 at R/R_o = 1.31, transducer position no. 3 (t_a is arrival time).

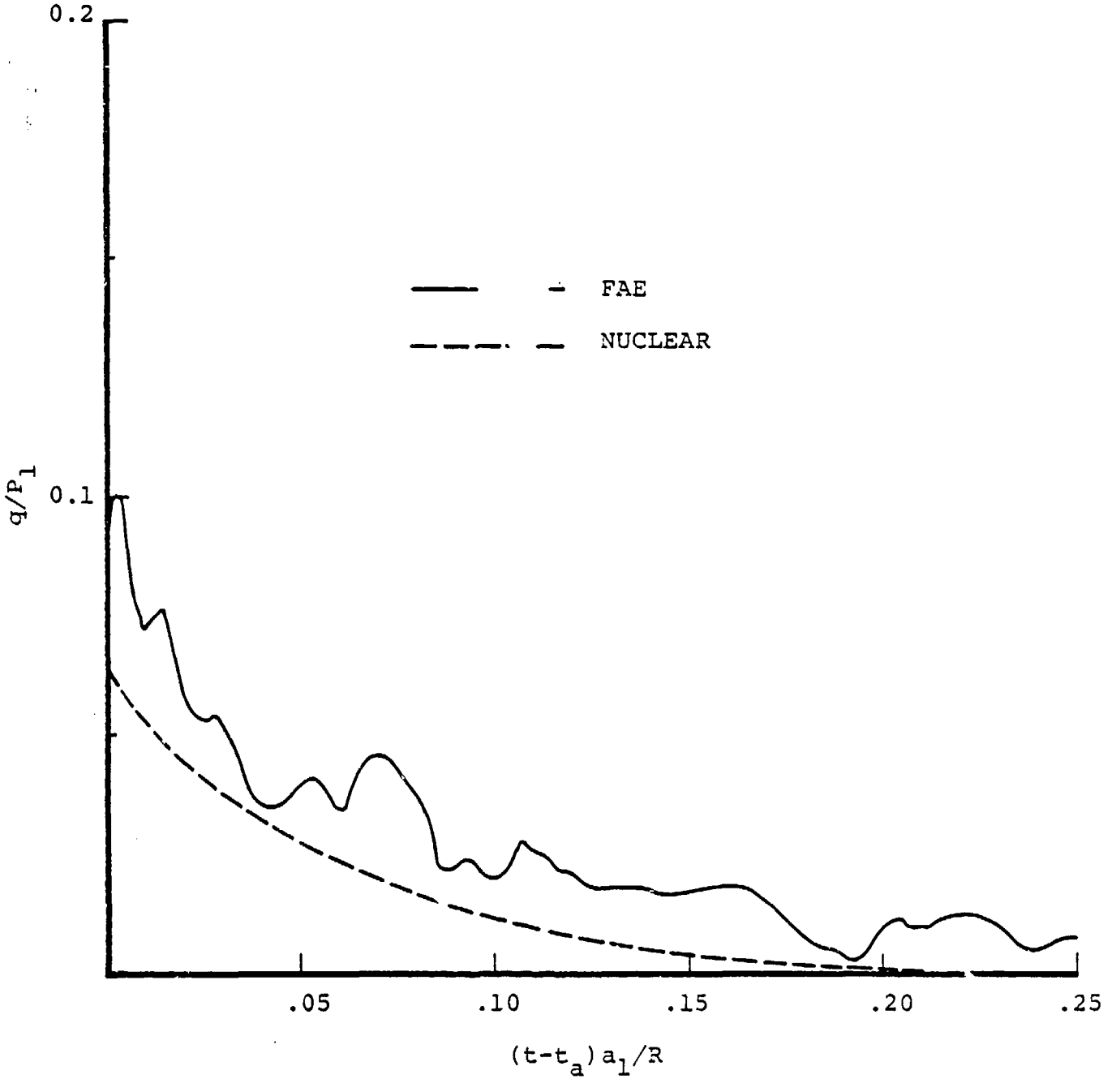

Figure 61. Dynamic pressure versus time during test CD-6 at R/R_o = 2.51, transducer location no. 5 (t_a is arrival time).

static overpressure versus time curves are given in Figure 54-59 at the various transducer locations. Fully smoothed nuclear form curves are superimposed on these figures for comparison.

Semi-smoothed dynamic pressure versus time curves and the corresponding nuclear reference curves appear for two instrumentation locations in Figures 60 and 61. The ragged character of the FAE curves is due to the sensitivity of calculated dynamic pressure to small errors in measured static and stagnation pressures, when the two pressures are nearly equal. Although three stagnation pressure probes were used during test CD-6 the oscillations in dynamic pressure at the most distant were so great that dynamic pressure at this location has been excluded from final data presentation, except for the peak value (Figure 53). A fourth stagnation pressure probe was not functional at the time CD-6 was conducted.

5.3 THEORETICAL INVESTIGATIONS

A centrally initiated fuel-air cloud can be exploded either as deflagration or as a detonation. In the case of a deflagrative explosion, compression waves induced by the accelerating flame front do not fully coalesce into a shock for an appreciable distance from the cloud boundary. The explosion does not assume a blastwave character until the shock overpressure is quite low (typically, $\sim$7 KPa (1 psi)). On the other hand, if the cloud is detonated, transition to blastwave behavior occurs at much higher pressures. Detonative explosion is, therefore, the preferred mode if the range of the simulated nuclear far-field airblast is to be as wide as possible.

When the fuel is dispersed uniformly throughout the cloud and initiated with an adequately strong shock source, a spherical (or hemispherical) detonation having constant radial

propagation velocity $dR_s/dt = U_s$ will quickly develop. The front velocity corresponds closely to the well-known Chapman-Jouget condition. The structure of the flowfield between the explosion center and the detonation front is approximately self-similar as the front expands.

Upon crossing the interface at the cloud boundary, the shock front strength drops somewhat as a result of the change in acoustic impedance. A U-shaped expansion-wave pressure profile forms near the shock front, centered behind the cloud/air interface. A part of this expansion wave moves inward toward the explosion center. The other part interacts with the leading shock. The shock decays because it is no longer protected from this interior rarefaction by a sonic barrier at the Chapman-Jouget point. The inward moving wave eventually reflects at the explosion center causing a dramatic, momentary drop in pressure there. Combustion products then flow inward toward the center. The pressure again rises at the center until a weak compression wave, which later steepens to a weak shock, emerges. Somewhat after this occurs, the positive-phase pressure profile behind the front and the front decay rate begin to develop point blastwave characteristics. Further wave interactions within the cloud remnant continue beyond this time but with diminishing magnitude. A considerable residual amount of the energy released by combustion remains at later times in the expanding burned cloud, primarily in the form of internal energy. In an equivalent central region, this is also true of ideal point blastwaves, but rough calculations have indicated that in fuel-air explosions the fractional amount of residual energy may be relatively greater.

A calculation has been carried out of the airblast that develops from a detonated hemispherical fuel/air cloud. This was done in order to assess the magnitude of secondary shocks from these explosions, to investigate the initial curvature of

the pressure-time decay at fixed radii, to provide a means to test the experimental data reduction progr ', and to determine theoretical values for η_F and s.

The calculation was executed in three st· ·s. First, the detonation front characteristics were determined. These were then used as boundary conditions to compute the self-similar detonation wave interior profiles. Finally, the self-similar detonation profiles at the time the front reaches the cloud boundary were used as initial conditions in a calculation of the subsequent time-varying blastwave flowfield.

5.3.1 Detonation Front Characteristics

The properties of Chapman-Jouget detonation waves were calculated using the Systems, Science and Software's ORAKL code. This program is a modification of the TIGER code written for BRL by SRI (Reference 64). Chemical equilibrium is assumed at the C-J point. The program calculates the detonation front velocity, the product composition, the thermal and thermodynamic product mixture properties, and the product velocity. Some of the calculated characteristics of propylene oxide and heptane detonations in air are plotted in Figures 62-67 as functions of equivalence ratio ϕ. This is the ratio of the actual fuel/air mass ratio, ϕ_A, to the stoichiometric fuel/air mass ratio, ϕ_A^*; i.e.,

$$\phi \equiv \phi_A/\phi_A^* \quad . \tag{57}$$

The calculations were carried out for the two-phase case; that is, initially the fuel was disposed as an unevaporated spray of liquid droplets. Chemical species considered in the product gases include H, H_2, O, O_2, H_2O, OH, HO_2, CO, CO_2, N_2, NO, NO_2, and C(s).

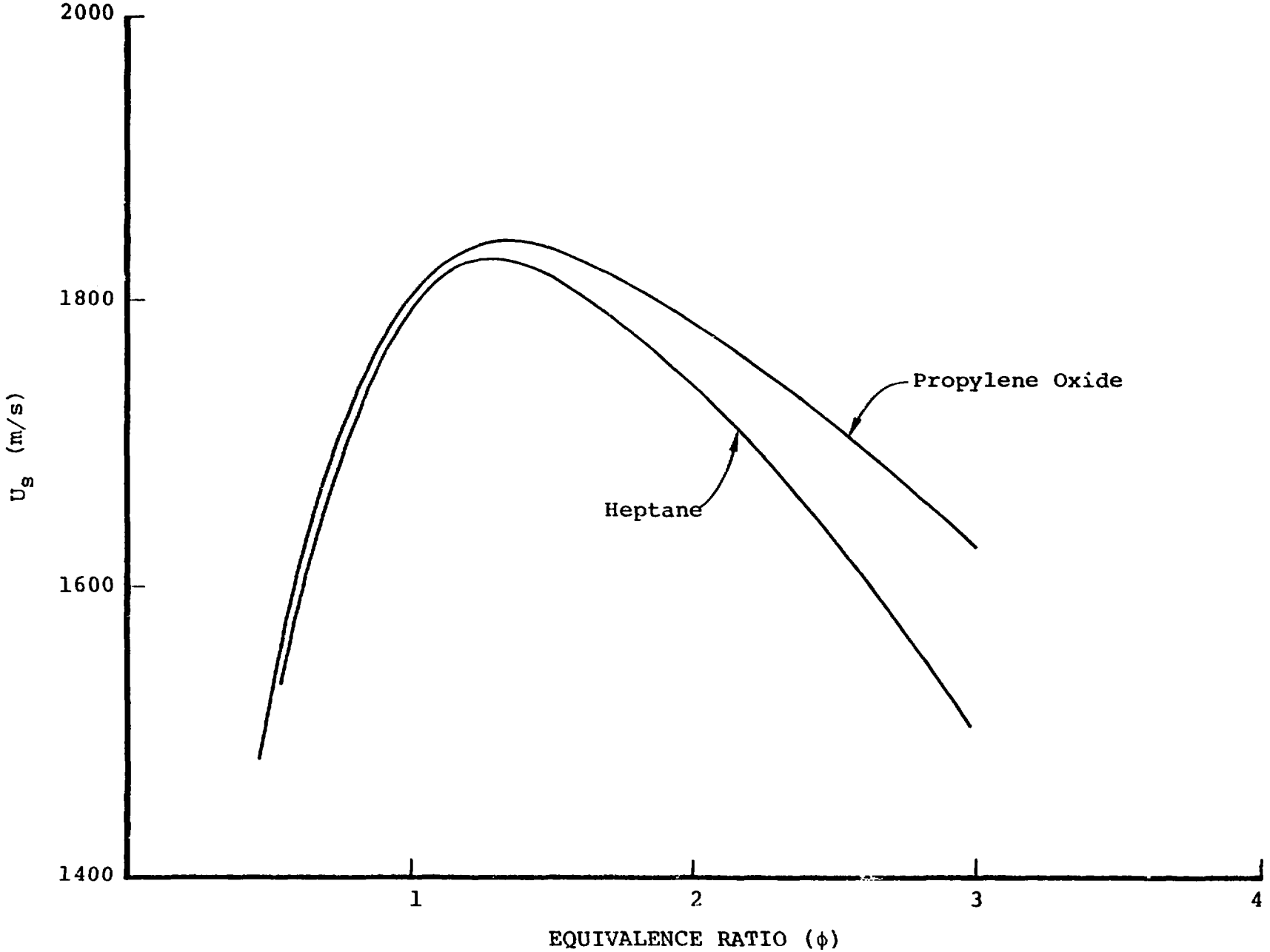

Figure 62. Unconfined detonation velocity versus equivalence ratio in two-phase propylene oxide and heptane fuel-air mixtures.

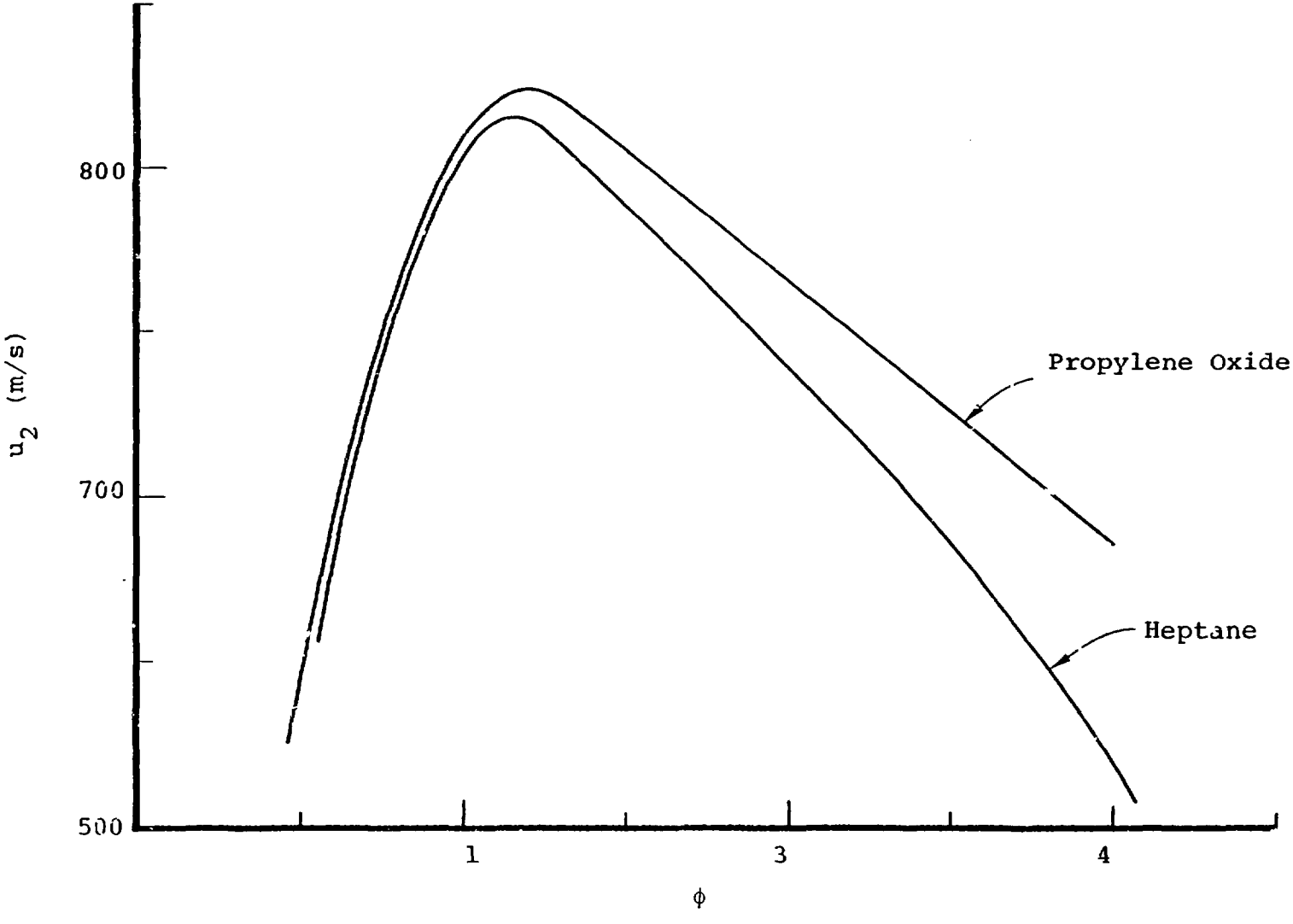

Figure 63. Particle velocity behind unconfined two-phase heptane and propylene oxide detonations in air.

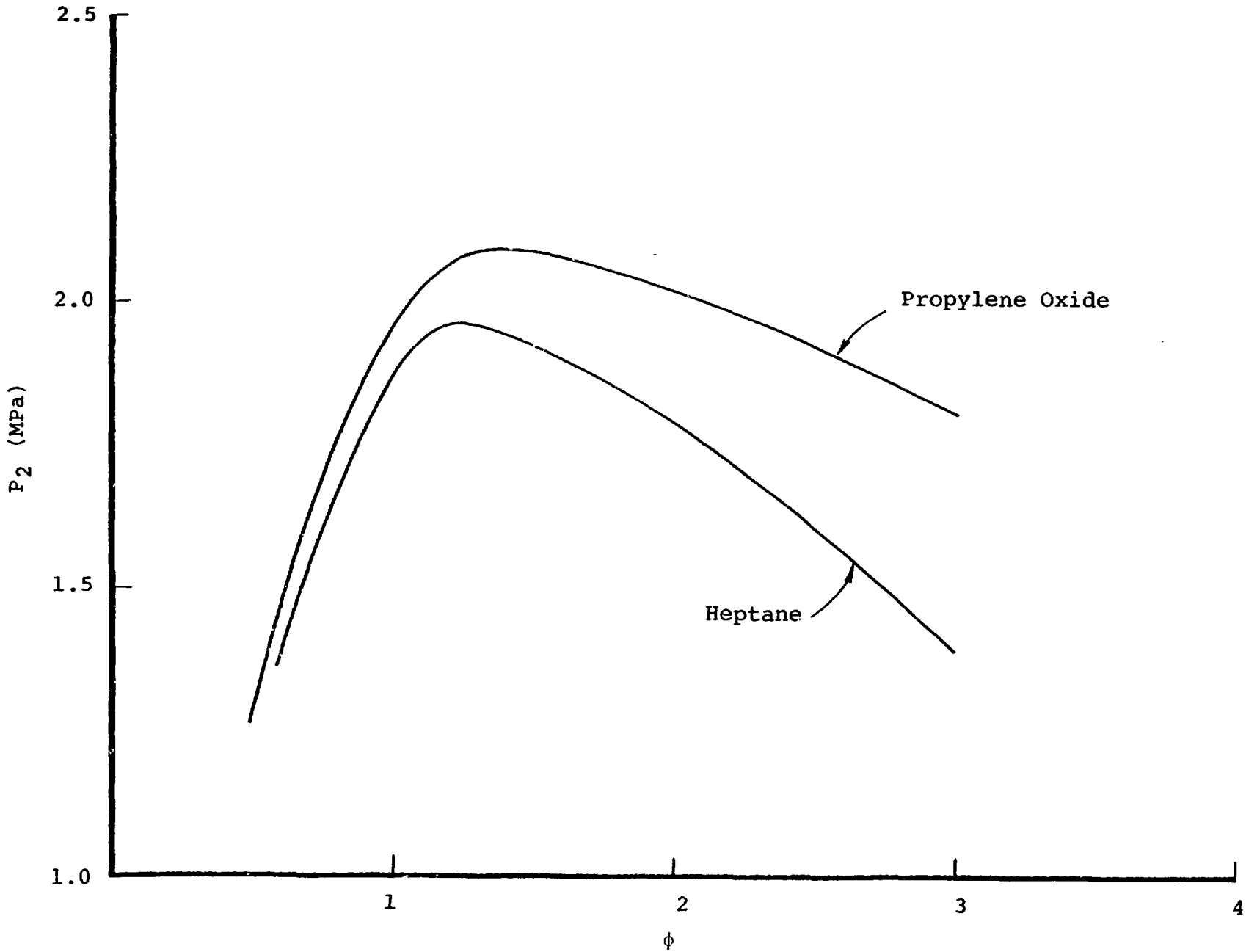

Figure 64. Absolute static pressure behind unconfined two-phase heptane and propylene-oxide detonations in air.

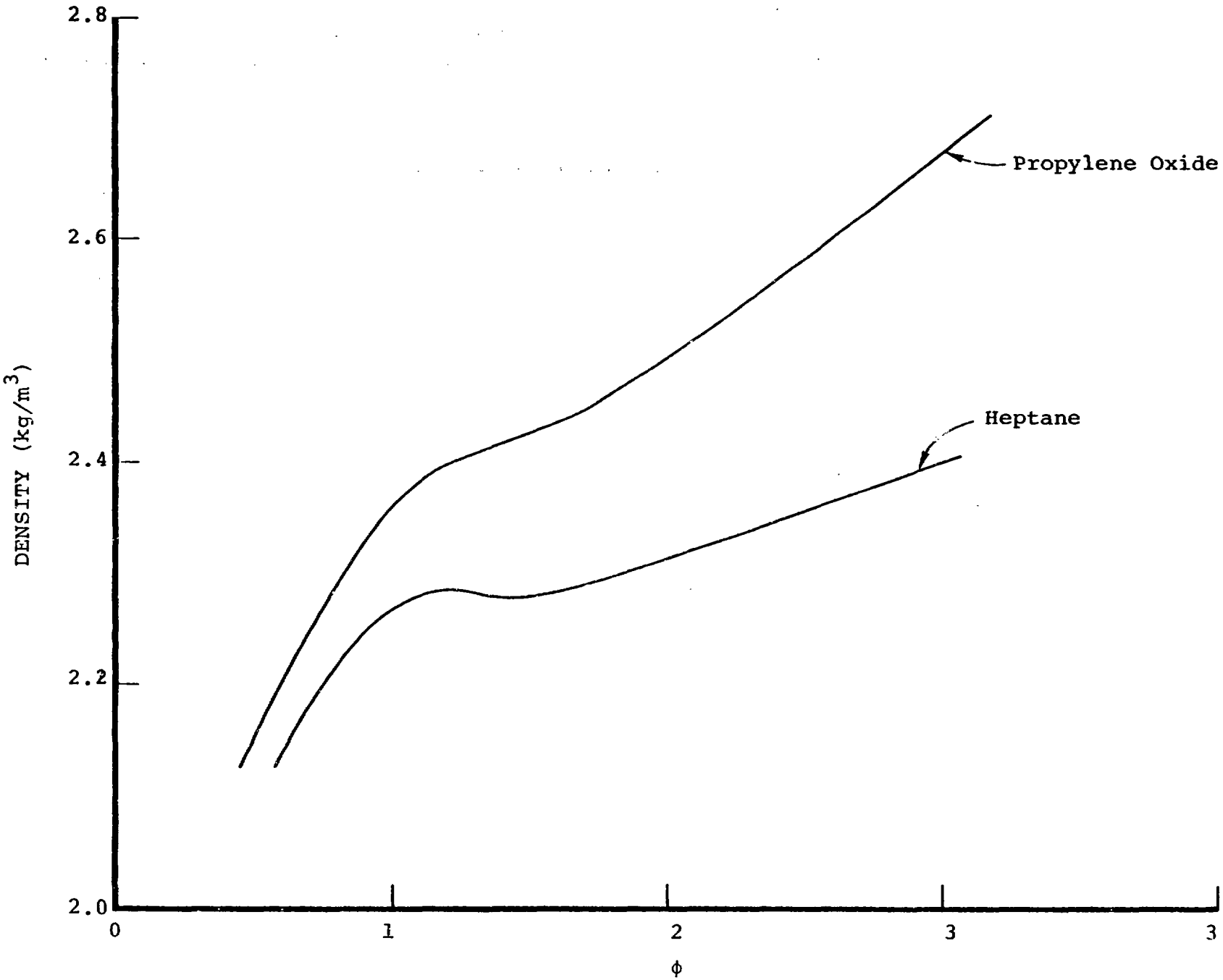

Figure 65. Density behind unconfined two-phase heptane and propylene oxide detonations in air.

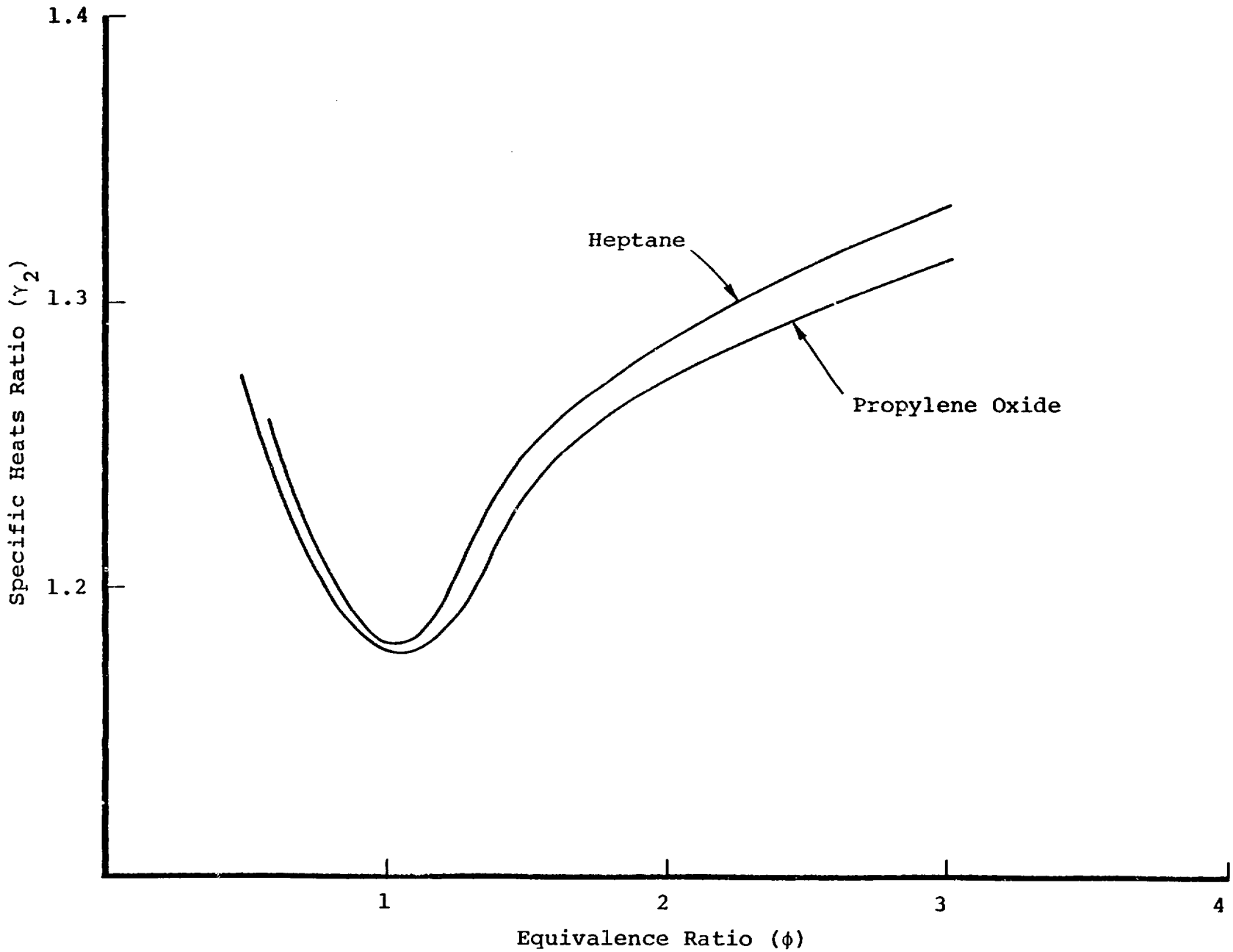

Figure 66. Product mixture specific-heats ratio behind unconfined two-phase heptane and propylene oxide detonations in air.

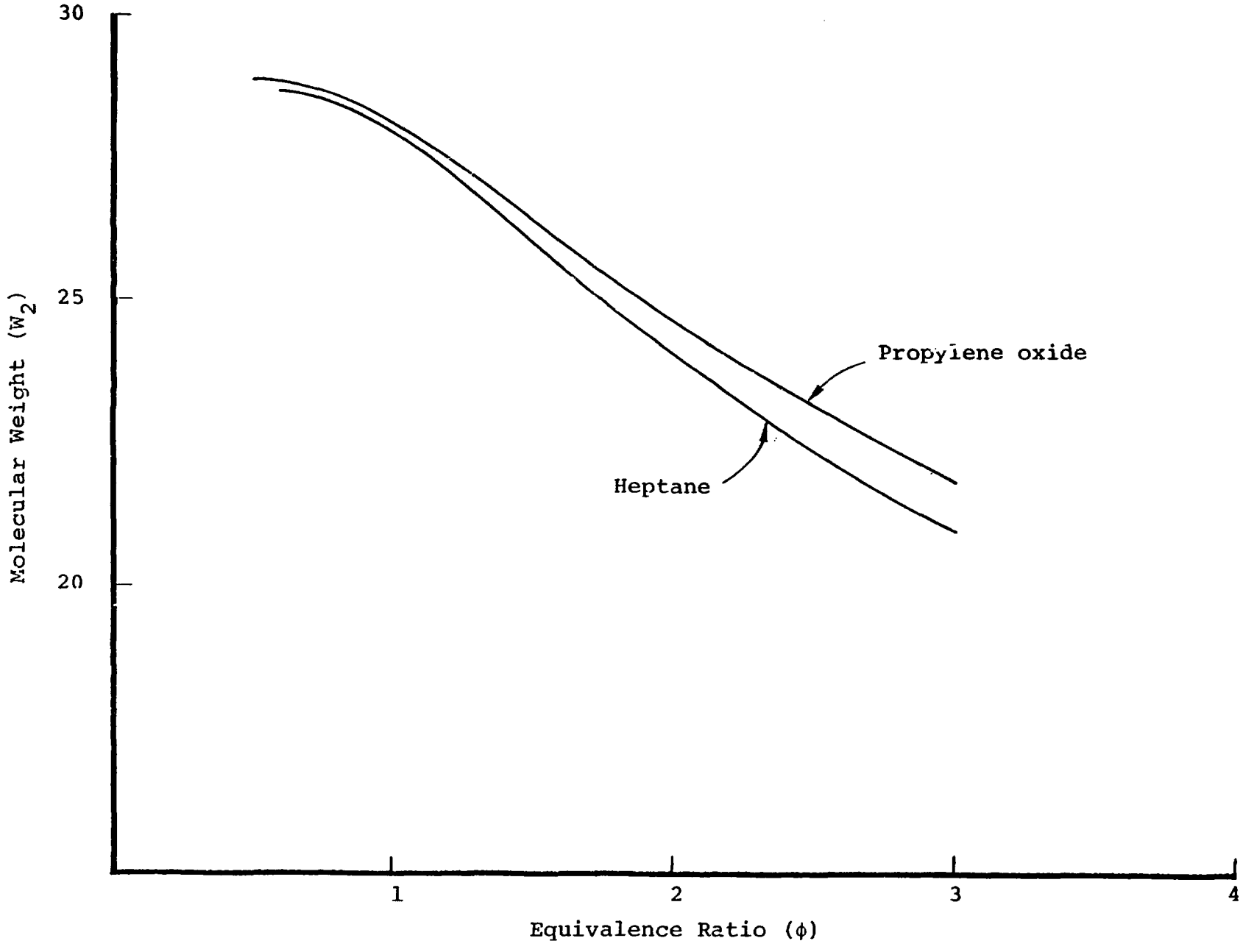

Figure 67. Product mixture molecular weight behind unconfined two-phase heptane and propylene oxide detonations in air.

5.3.2 Initial Conditions

For most purposes it is not necessary to numerically evaluate the flowfield behind the detonation front throughout the period in which it propagates from the explosion center to the cloud boundary. During this period, the internal flowfield (expansion wave) is usually self-similar to a reasonable degree of approximation. Therefore, the self-similar profiles need to be calculated only once. This calculation was carried out following the development in Reference 65 which is summarized here.

The physical pressure, density, and gas velocity are written in terms of dimensionless quantities Π, Γ, and Ω by the definitions

$$P = \rho_1 \lambda^2 U_s^2 \Pi(\lambda) \tag{58}$$

$$\rho = \rho_1 \Gamma(\lambda) \tag{59}$$

$$u = \lambda U_s \Omega(\lambda) \tag{60}$$

where

$$\lambda \equiv R/R_s \quad . \tag{61}$$

The detonation front velocity is U_s and its instantaneous position is R_s. A dimensionless sound speed is also defined by

$$z = \frac{\gamma \Pi}{\Gamma} \quad . \tag{62}$$

The Euler equations of mass and momentum conservation can then be reduced to

$$\frac{dz}{d\Omega} = \frac{z[2(\Omega-1)^2 + (\omega-1)(\gamma_2-1)\ \Omega(\Omega-1) - 2z]}{\Omega[(\Omega-1)^2 - \omega z]} \tag{63}$$

and

$$\frac{d(\ell n\lambda)}{d\Omega} = \frac{z - (\Omega-1)^2}{\Omega[(\Omega-1)^2 - \omega z]} \quad , \tag{64}$$

where $\omega = 1,2,3$ for planar, cylindrical, and spherical (or hemispherical) geometries, respectively. Also, since the flowfield in the rarefaction behind the detonation front is assumed to be isentropic, the entropy equation, derived from energy conservation, integrates to

$$\frac{p}{\rho^{\gamma_2}} = \text{constant}$$

or in terms of the dimensionless variables,

$$\frac{\lambda^2 z}{\Gamma^{(\gamma_2-1)}} = \frac{z_2}{\Gamma_2^{(\gamma_2-1)}} \quad . \tag{65}$$

In these equations, the subscript "2" refers to conditions at $R = R_s$ ($\lambda = 1$). This is the C-J point and so

$$\Gamma_2 = \left[\frac{\gamma_2}{\gamma_2+1}\left(1 + \frac{z_1}{\gamma_1}\right)\right]^{-1} \quad , \tag{66}$$

and

$$z_2 = \frac{\gamma_2^2}{(\gamma_2+1)^2}\left(1 + \frac{z_1}{\gamma_1}\right)^2 \quad , \tag{67}$$

where the subscript "1" refers to conditions in the unburned fuel-air mixture. In particular,

$$z_1 = \frac{\gamma_1 \Pi_1}{\Gamma_1} \tag{68}$$

becomes $z_1 = M_s^{-2}$ since $R = R_s$ at the front and $R_s = U_s t$.

To generate the self-similar profiles, the detonation properties computed previously were used as input. First, z_1 was calculated from Eq. (68), z_2 from Eq. (67), and Γ_2 from Eq. (66). Next, the value of Ω_2 was found from

$$\Omega_2 = 1 - z_2^{1/2} \tag{69}$$

which expresses the C-J condition at point 2; i.e., the gas velocity relative to the front is sonic at the end of the reaction zone. Now Eqs. (63) and (64) are integrated starting from the point (z_2, Ω_2) and going through decreasing values of Ω (with increasing values of z) to the point $(z = 1, \Omega = 0)$. The value of γ used in this integration is γ_2. Note that

$$\frac{d(\ell n \lambda)}{d\Omega} = 0$$

at (z_2, Ω_2) for $\omega = 2,3$, and that this derivative is indeterminate at that point for $\omega = 1$. This implies $du/dR \to \infty$ at (z_2, Ω_2) for $\omega = 2,3$. Also, note that the point $(z = 1, \Omega = 0)$ does not occur at the explosion center (center of symmetry), but rather at $\lambda \sim 0.5$. For values of λ less than this, all properties of the flow are constant and $u = 0$. There is a discontinuity in the slope of all variables at $(z = 1, \Omega = 0)$.

Integration of Eqs. (63) and (64) effectively yields $z = z(\lambda)$ through quadrature. Also, from Eq. (64), $\Omega = \Omega(\lambda)$ is

obtained. Then $\Gamma = \Gamma(\lambda)$ can be calculated from Eq. (65) and $\Pi = \Pi(\lambda)$ can be obtained from Eq. (62) with $\gamma = \gamma_2$. With Π, Γ, and Ω known as functions of λ, the physical variables P, ρ, and u can be determined as functions of λ by means of Eqs. (58)-(60). Finally, when a value for R_s is specified, these profiles can be expressed in terms of physical radius R in view of Eq. (61).

The self-similar profiles of P, ρ, and u behind a stoichiometric heptane-air detonation at R_s = 4.42 m (14.5 ft) are plotted in Figures 68-70. This fuel and radius were chosen because it is expected in forthcoming experimental FAE work to test neptane clouds of that size. The time for the detonation to reach R_s = 4.42 m (14.5 ft) is 2.47 ms. The self-similar profiles at this time were used as initial conditions for the solution of the subsequent airblast.

Two observations regarding these initial conditions should be noted. First, the peak values for the variables as shown in Figures 68-70 are actually those which obtain at the end of the detonation reaction zone, that is, at the Chapman-Jouget point. In reality, however, the peak pressure, density, and particle velocity in a detonation occur just behind the leading shock, before any reaction is initiated. The actual peak pressure, for example, is about twice that shown in Figure 68. This is usually referred to as the von Neumann spike. The flowfield between the von Neumann spike and the C-J point can generally be ignored when the reaction zone width is small compared to the overall wave radius, including the expansion wave (i.e., R_s). The impulse imparted by this very small segment of the overall wave is negligible in that case. For that reason, the von Neumann spike was not included in the detonation profiles. However, in terms of initiating the airblast calculation, it should be noted that the changes in (P,ρ,u) across the detonation front as shown in Figures 68-70 are not consistent with those of any simple shock wave. Thus,

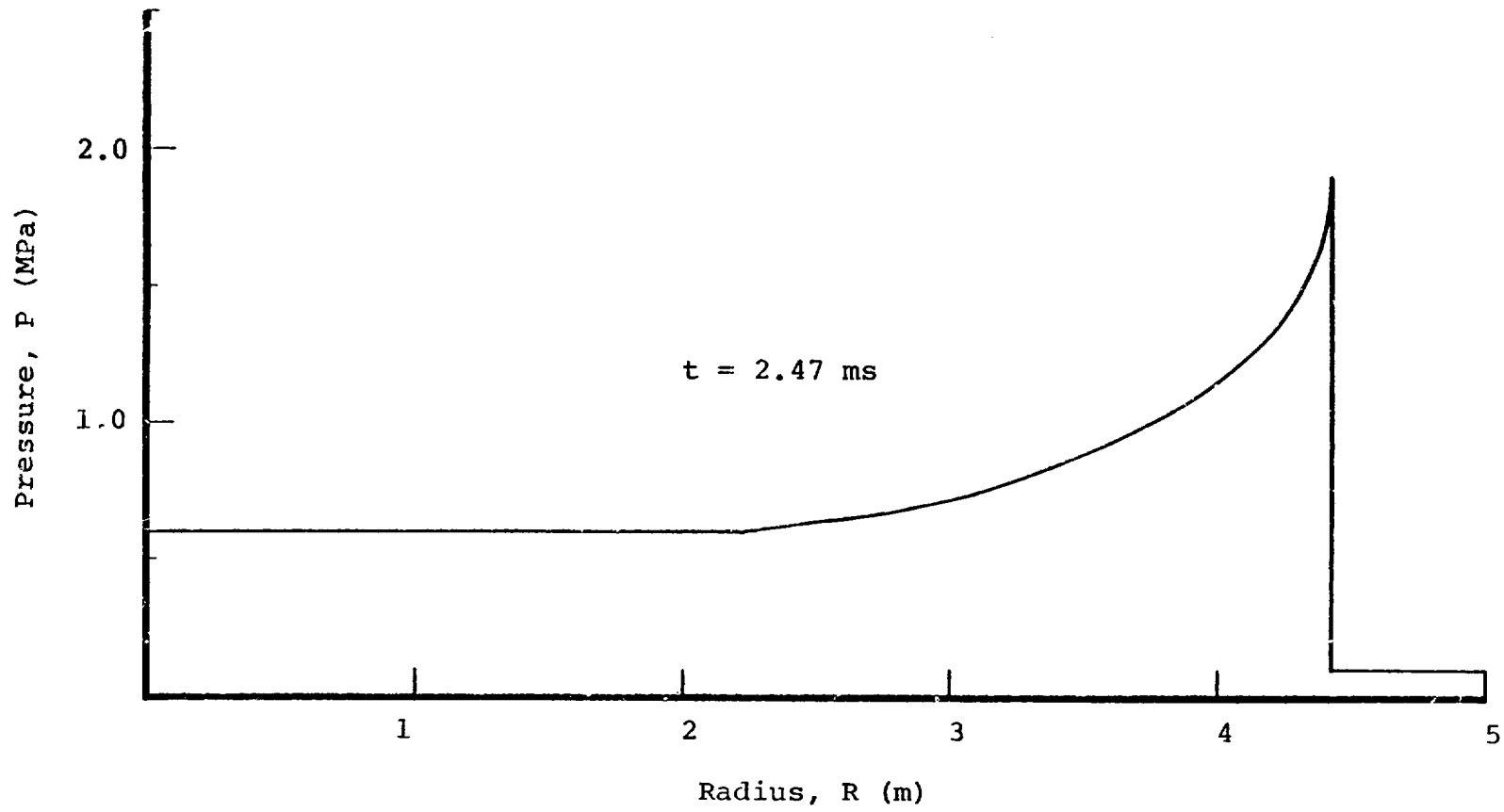

Figure 68. Self-similar absolute static pressure profile within expansion wave behind stoichiometric, unconfined, two-phase heptane-air detonation.

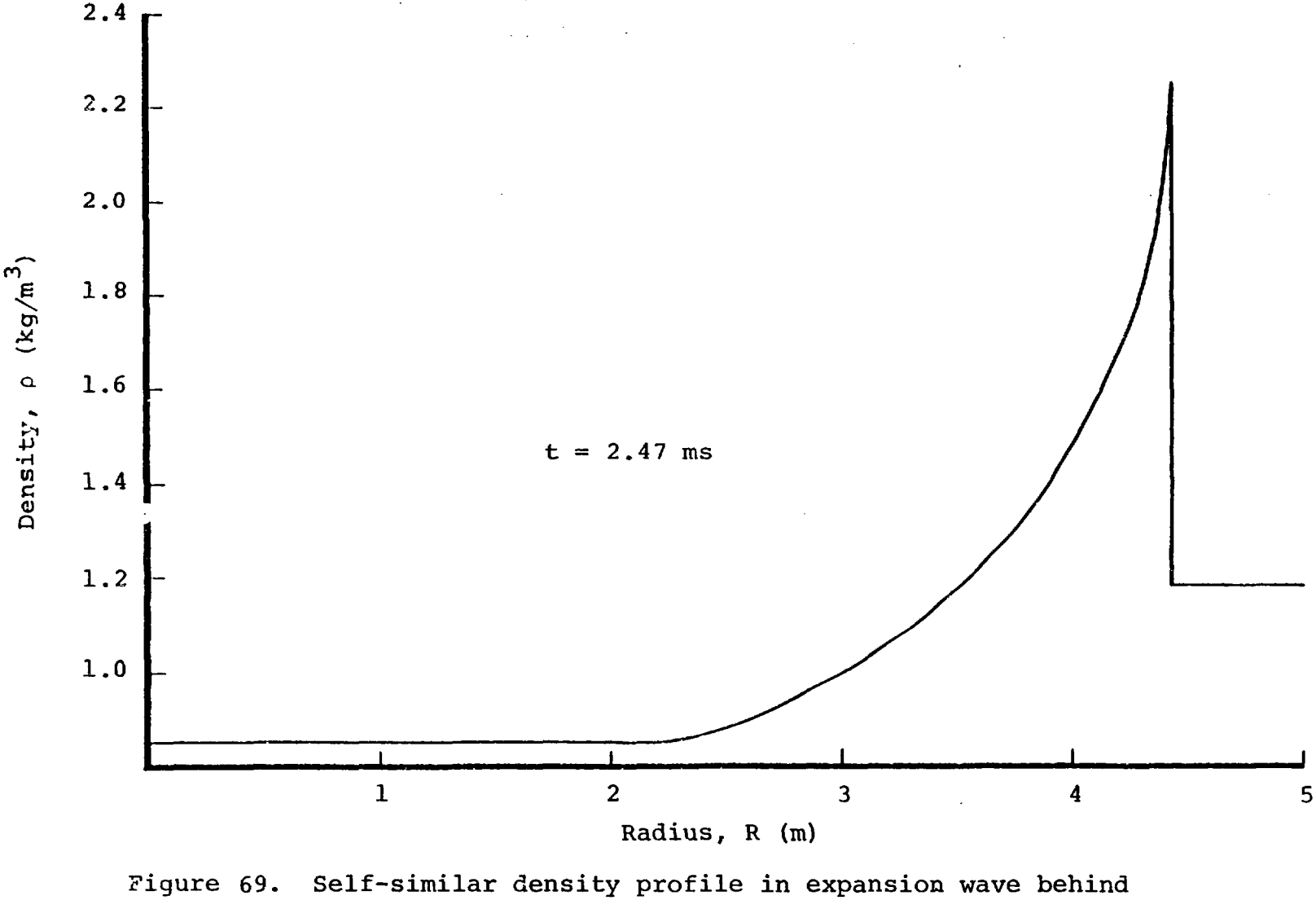

Figure 69. Self-similar density profile in expansion wave behind stoichiometric, unconfined, two-phase heptane-air detonation.

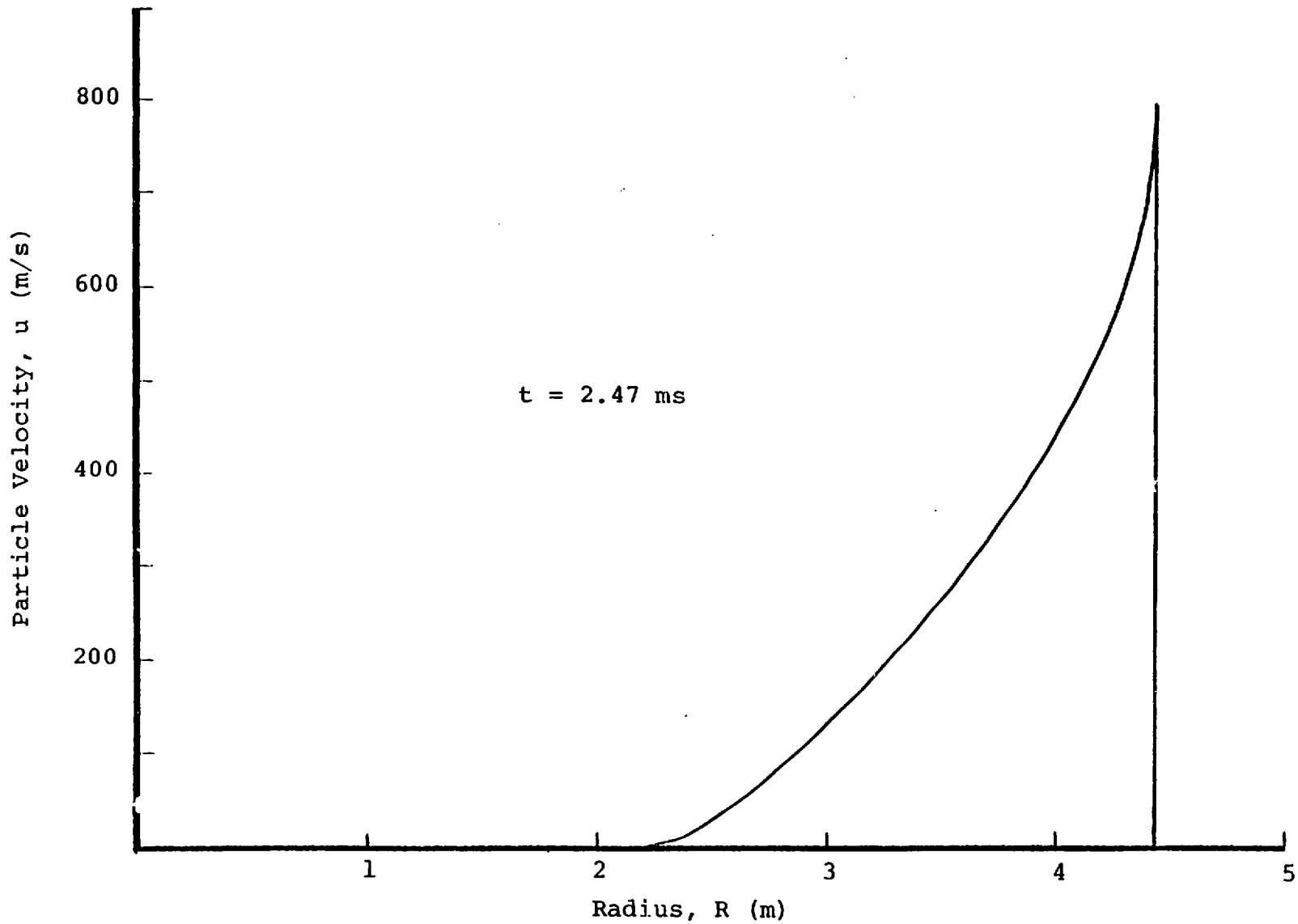

Figure 70. Self-similar absolute (particle) velocity profile in expansion wave behind stoichiometric, unconfined, two-phase heptane-air detonation.

in the first moment following t = 2.47 ms a perturbation was expected in the numerical airblast calculation. This did in fact occur, but the perturbation was rapidly damped.

The second comment concerns a related observation. The flowfield comprising a detonation and its trailing expansion wave cannot actually be exactly self-similar except in the limiting case of vanishing reaction zone width. For non-zero reaction zone widths, a certain quantity of mass is carried at all times within the reaction zone. This mass is effectively removed from the expansion wave flow which must, therefore, have a density profile that differs from the self-similar profile. That is, the expansion wave must be stronger than the self-similar wave (more rapid density drop-off) as the reaction zone width increases. Normally, in gas-phase detonations the amount of mass in the reaction zone can be ignored except at very small radii. However, two-phase detonations in sprays of 2 mm (0.08 in.) droplets (for example) have reaction zones on the order of 0.5 m (20 in.) in length. In that case, the amount of mass in the reaction zone is not negligible when the wave radius is 4.42 m (14.5 ft).

This observation may be of some significance to the detonation initiation question. Presumably, there must exist a minimum wave radius below which it would not be possible to establish a C-J detonation. This is because there would not be enough mass at smaller radii to fill the reaction zone to C-J levels even if a vacuum existed throughout the region from the explosion center to the reaction zone. To illustrate this point it was assumed, for simplicity, that the density variation between the von Neumann spike and the C-J point is linear. Values of the densities at these points in a stoichiometric vapor-phase heptane-air detonation are ρ_{2s} = 6.25 kg/m^3 (0.391 lbm/ft^3) and ρ_2 = 2.23 kg/m^3 (0.139 lbm/ft^3). The upstream mixture density is ρ_1 = 1.23 kg/m^3 (0.0769 lbm/ft^3). It is readily shown by mass conservation that the

detonation wave radius for which all of the mass initially between $0 \leq R \leq R_s$ would be contained within the C-J reaction zone in this example is $R_s^* = 9.46\ \delta$, where δ is the reaction zone thickness. Thus, if the heptane were dispersed as a vapor so that $\delta \sim 5$ mm (0.2 in.), then a Chapman-Jouget detonation could not exist at radii smaller than $R_s^* \sim 47$ mm (1.9 in.).

At the other extreme, if the heptane were dispersed as a fairly coarse spray such that $\delta \sim 0.5$ m (20 in.), then $\rho_1 = 1.25$ kg/m^3 (0.0781 lbm/ft^3), $\rho_{2s} = 6.01$ kg/m^3 (0.376 lbm/ft^3), and $\rho_2 = 2.25$ kg/m^3 (0.14 lbm/ft^3). A Chapman-Jouget detonation could not, in this case, be achieved within $R_s^* \sim 4.5$ m (15 ft). It is noted that in this last case, R_s^* would exceed the experimental cloud size. The structure within the expansion wave of a vapor-phase detonation would be well represented by the self-similar profiles of Figures 68-70 at a radius of 4.42 m (14.5 ft). On the other hand, very significant departures from self-similarity would be expected in the two-phase case. The impact of these departures on the airblast generated is not presently known. However, the reduction in the rarefaction wave pressures and densities would seem certain to influence the airblast development. It seems clear that to produce truly self-similar detonation waves in two-phase media, very fine droplets are required if the clouds are of small scale. In clouds that are very large ($R_c >> R_s^*$), the effect of drop size would be small, but the airblast would differ from that generated by a small cloud ($R_c \sim R_s^*$).

5.3.3 Airblast Calculation

The airblast that develops from the detonation was calculated using the S^3 SKIPPER code (Reference 66). This is a one-dimensional Lagrangian code operable in any of the three geometries. The code was executed for the present calculation using quadratic artificial viscosity. No linear artificial

viscosity was required. Shock waves thereby retained fairly steep slopes in the solution. The calculation was begun at R_s = 4.42 m, t = 2.57 ms using the self-similar detonation profiles as initial conditions. It was stopped when the positive phase ended at the position R = 30 m (98.4 ft). This is the position of the most distant instrumentation trough on the experimental test pad. The peak overpressure at that location is about 35 kPa (5 psi).

The calculated pressure profiles within the airblast at various stages of its decay are presented in Figures 71 and 72. The profiles were plotted at times that correspond to the arrival of the front at radii equal to the experimental transducer locations. The times shown in the figures are times of arrival. Note the change in scale between figures. Beyond about three cloud radii the positive-phase pressure profile assumes the general character of a point source blastwave. Secondary and tertiary shocks and expansions are confined to the negative phase.

The static overpressures experienced at each transducer position are plotted as functions of time in Figures 73-78. Again, it can be seen that secondary shocks are confined to the negative phase. Also, the curvature of the initial pressure drop-off is positive even close to the cloud. This is important in simulating nuclear airblasts because the way in which impulse develops in the early period of pressure decay may affect damage mechanisms in some cases.

The path of the interface that separates combustion products from the surrounding air is plotted in Figure 79. The detonated cloud first expands to roughly twice its initial radius and then contracts slightly. The outward travel of the interface extends to a location at which the peak overpressure is about 0.283 MPa (41 psi).

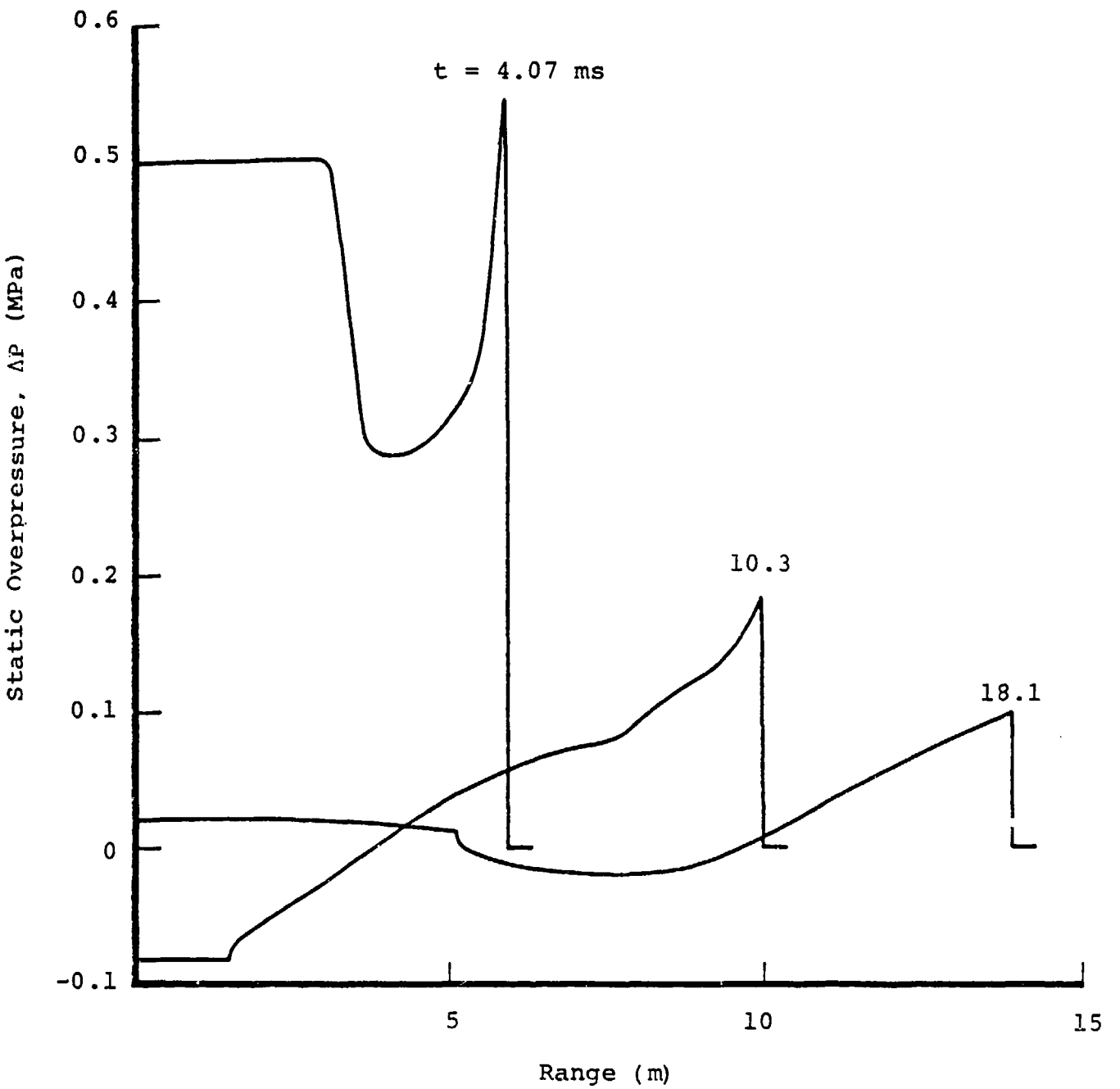

Figure 71. Calculated static overpressure profile within FAE airblast at fixed times.

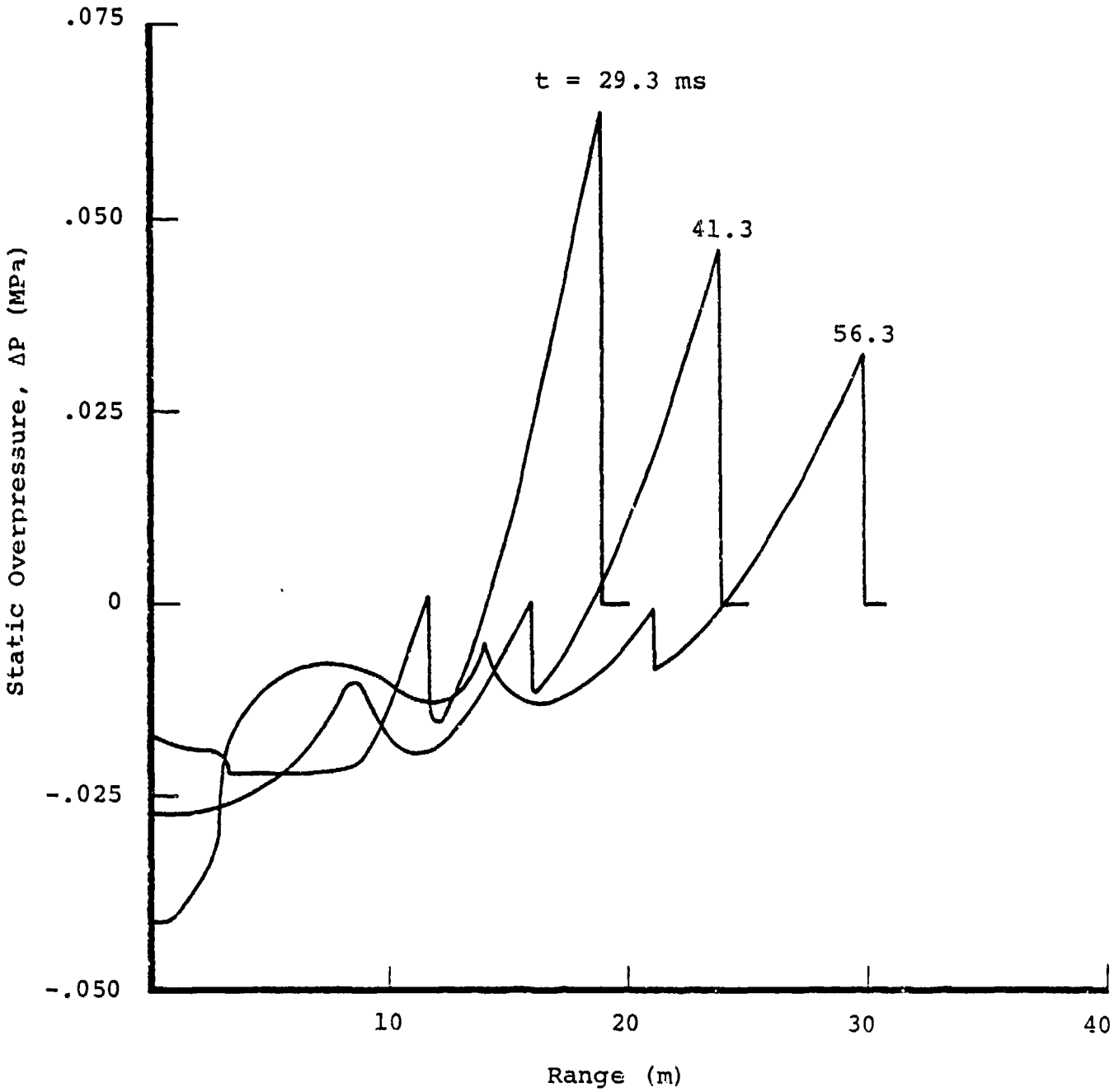

Figure 72. Calculated static overpressure profiles within FAE airblast at fixed times.

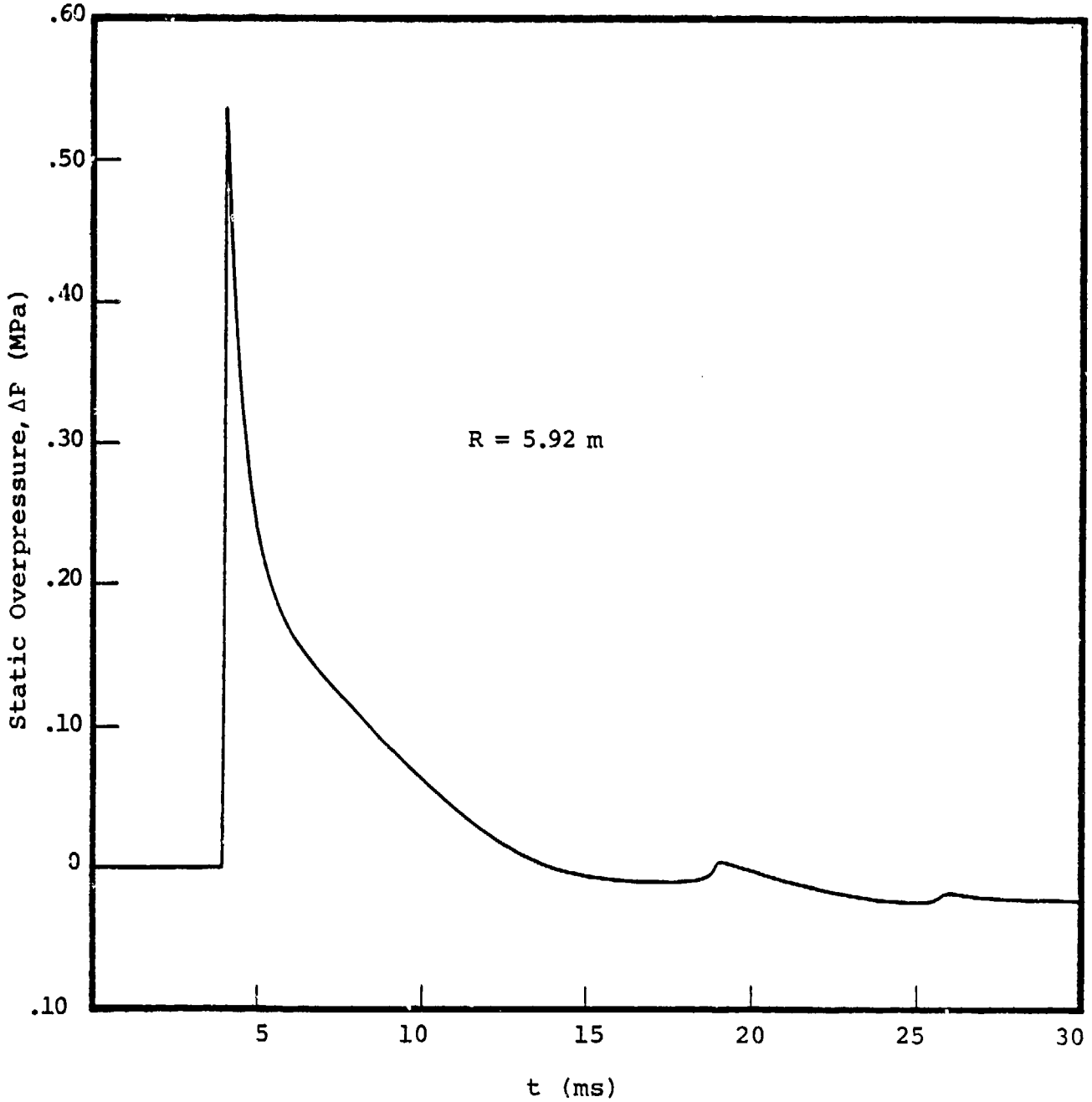

Figure 73. Calculated static overpressure versus time at fixed range from hemispherical FAE airblast.

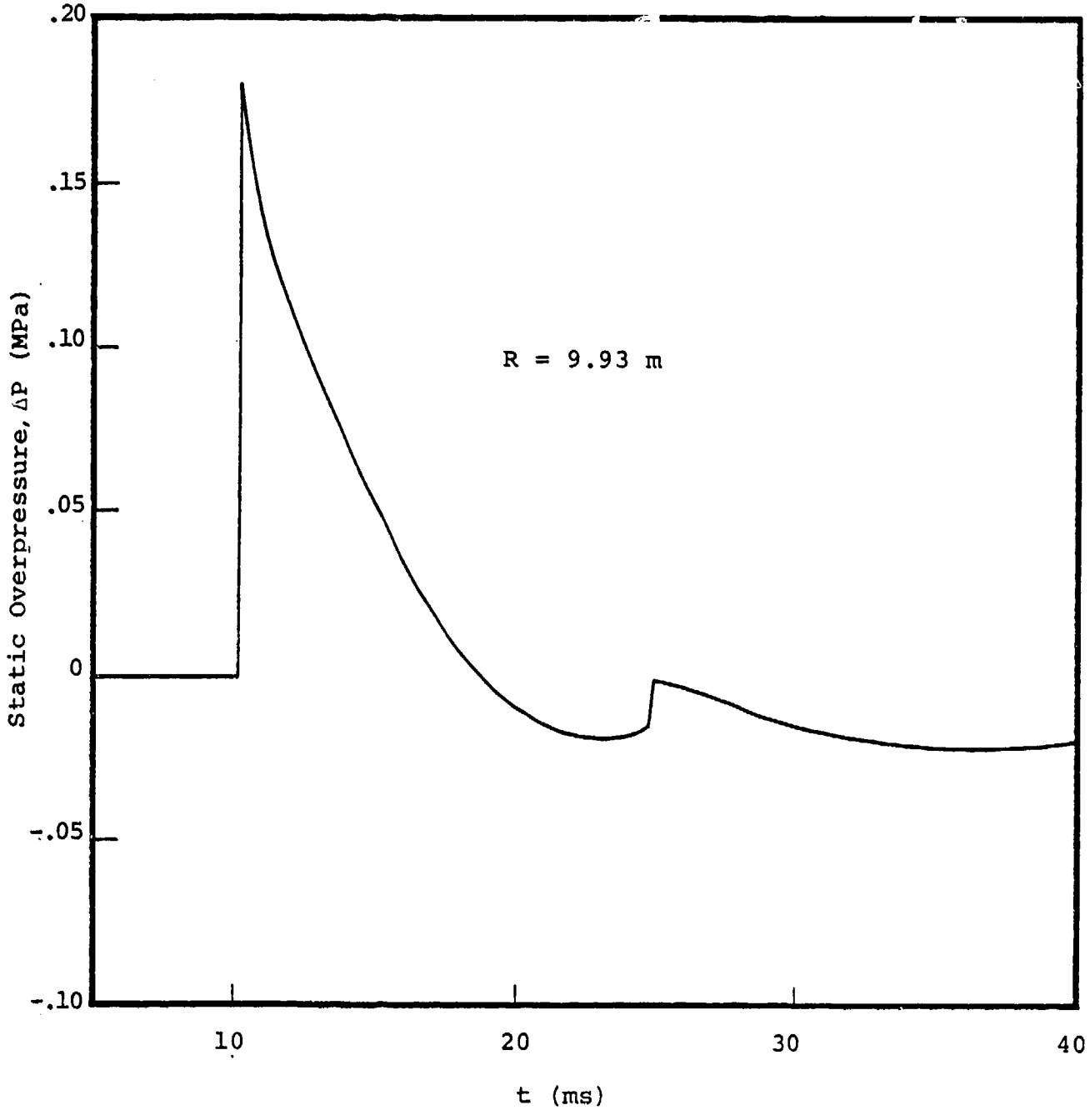

Figure 74. Calculated static overpressure versus time at fixed range from hemispherical FAE airblast.

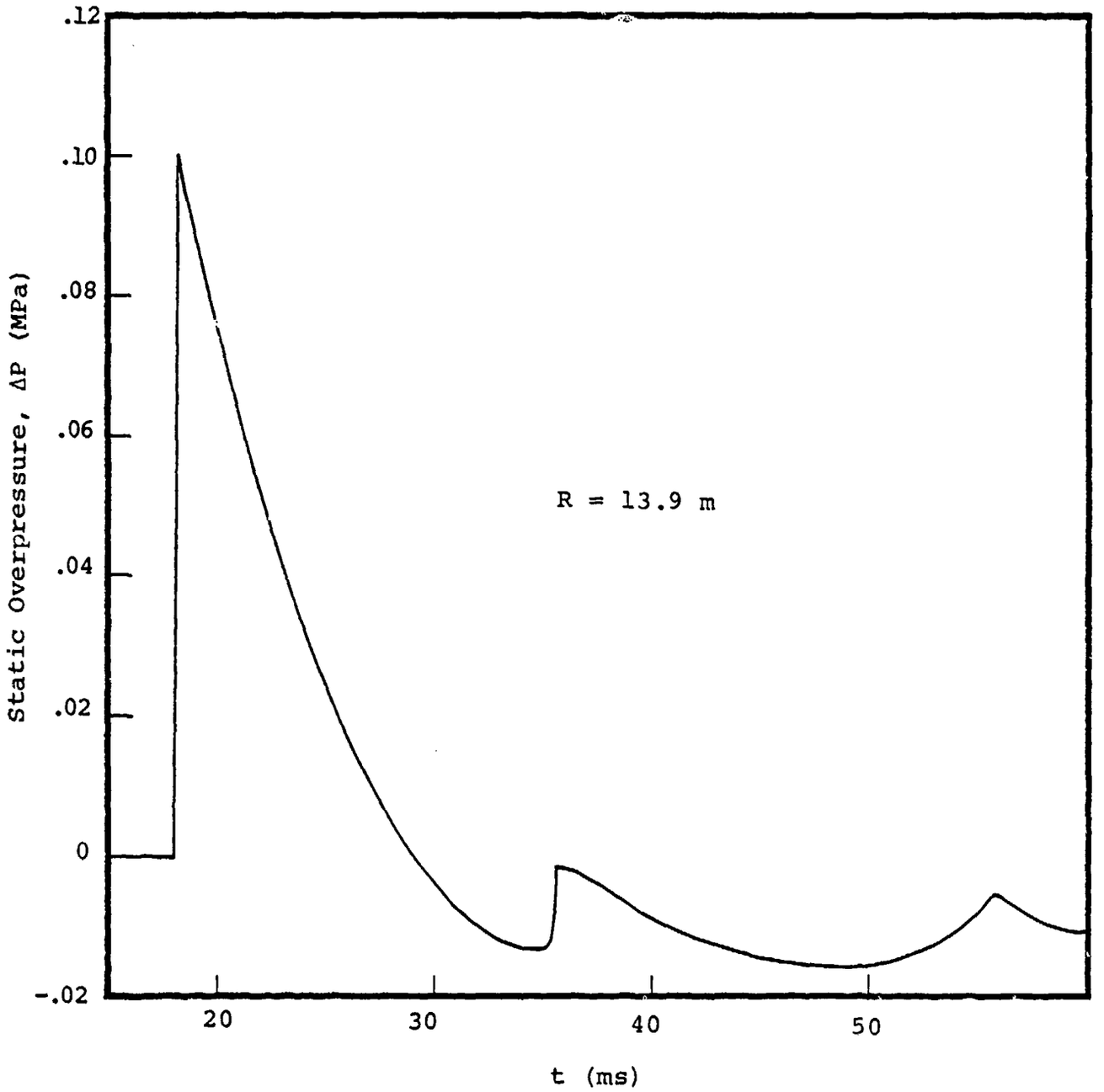

Figure 75. Calculated static overpressure versus time at fixed range from hemispherical FAE airblast.

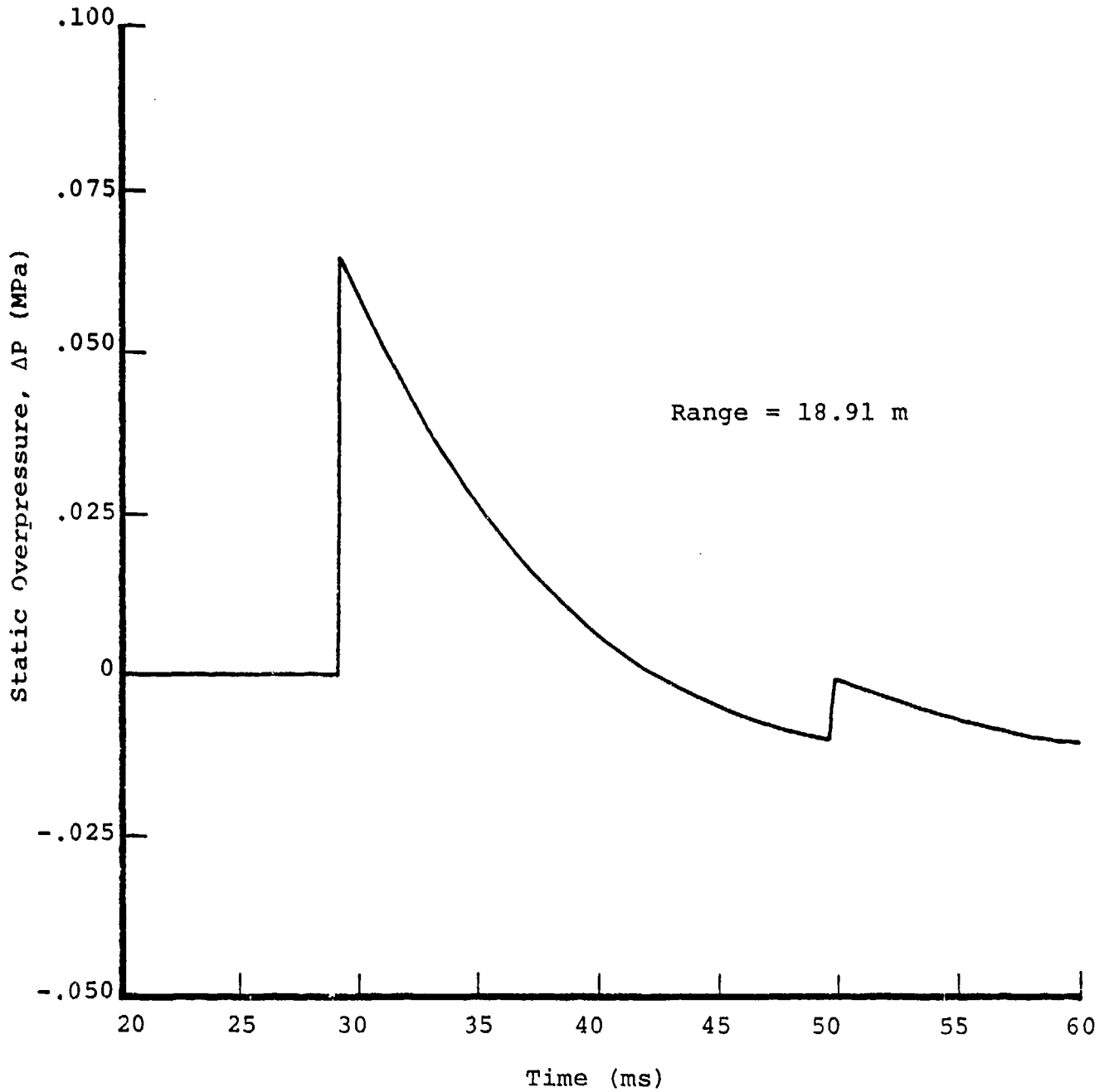

Figure 76. Calculated static overpressure versus time at fixed range from FAE airblast.

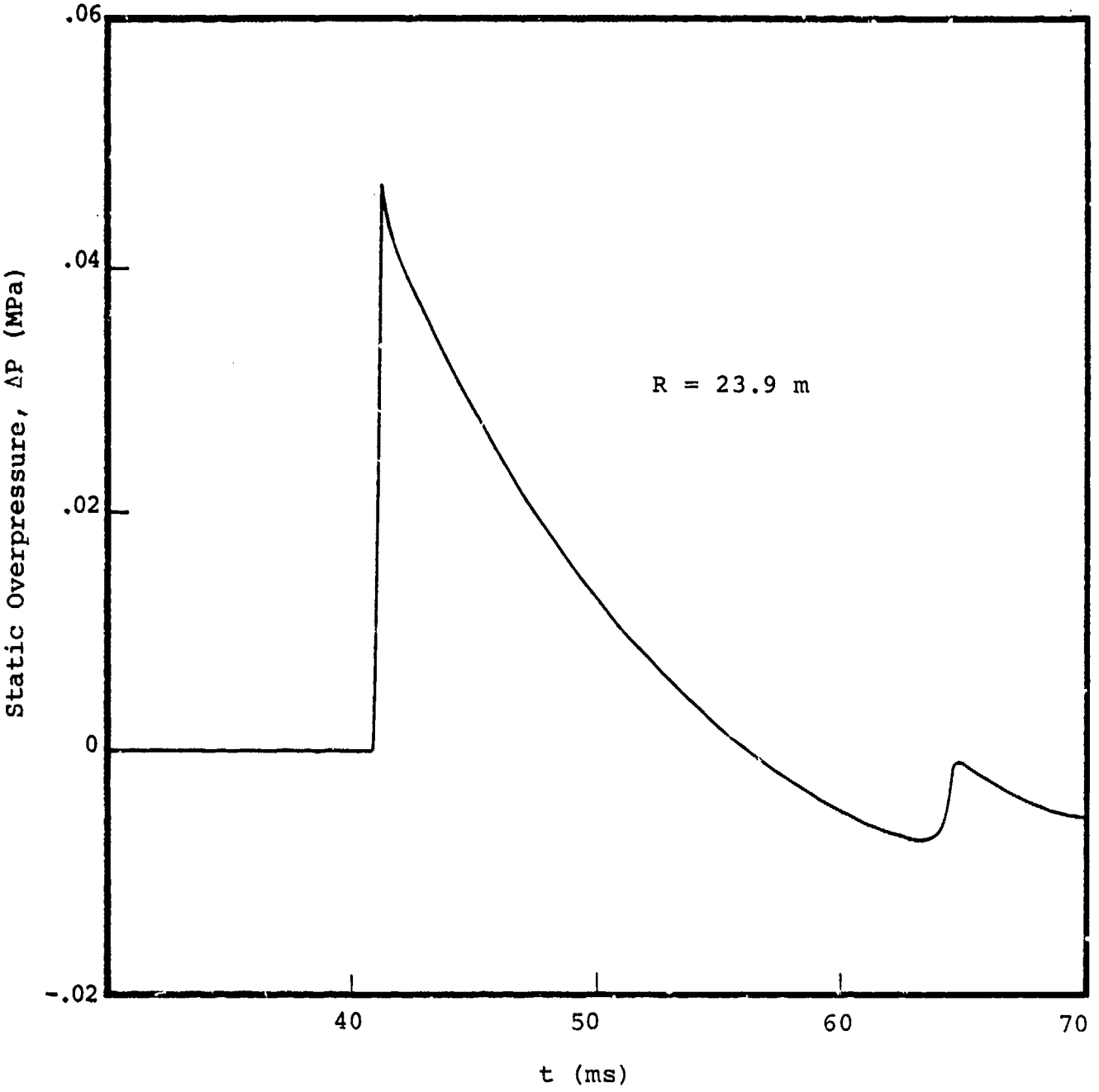

Figure 77. Calculated static overpressure versus time at fixed range from hemispherical FAE airblast.

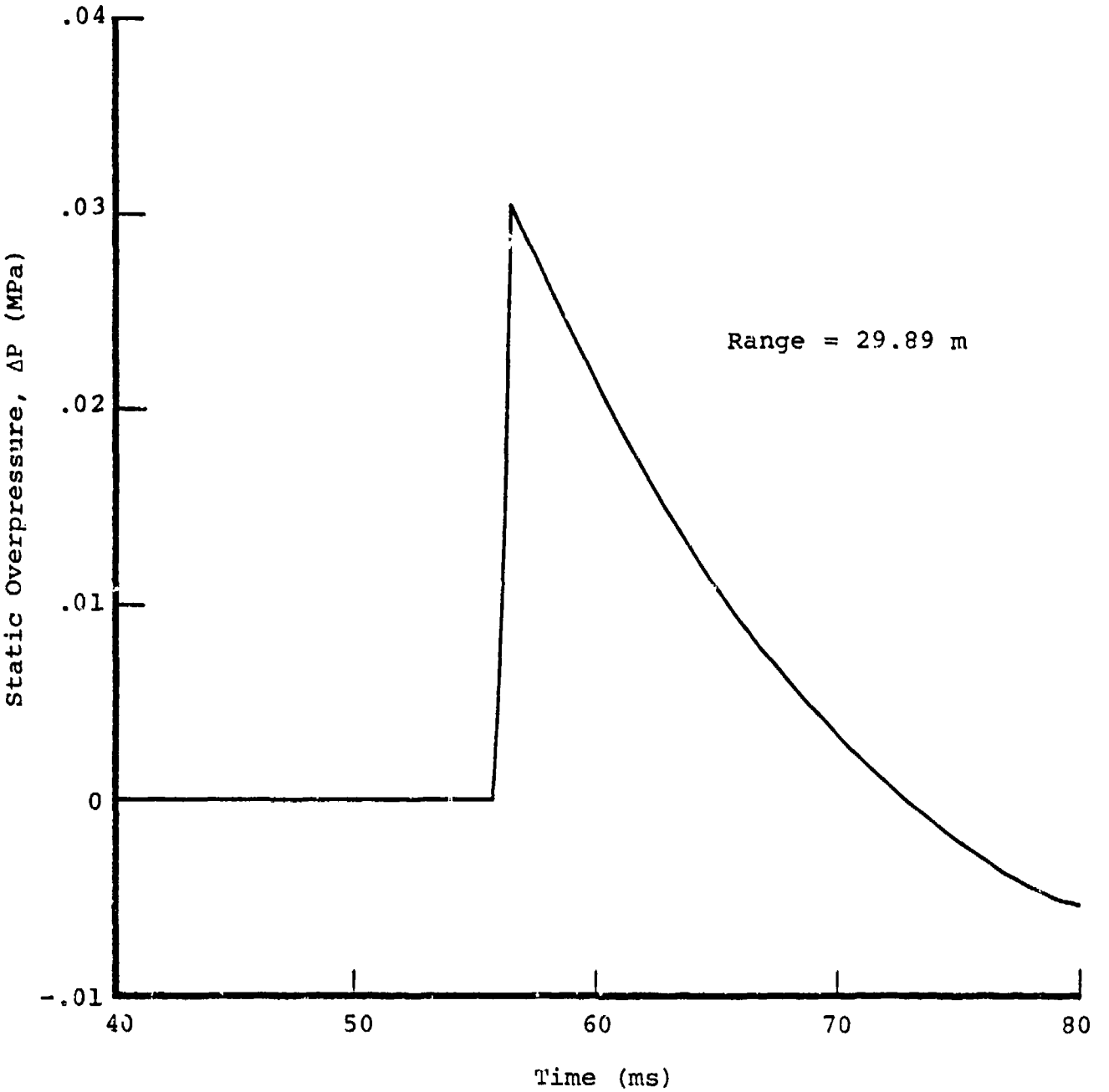

Figure 78. Calculated static overpressure versus time at fixed range from FAE airblast.

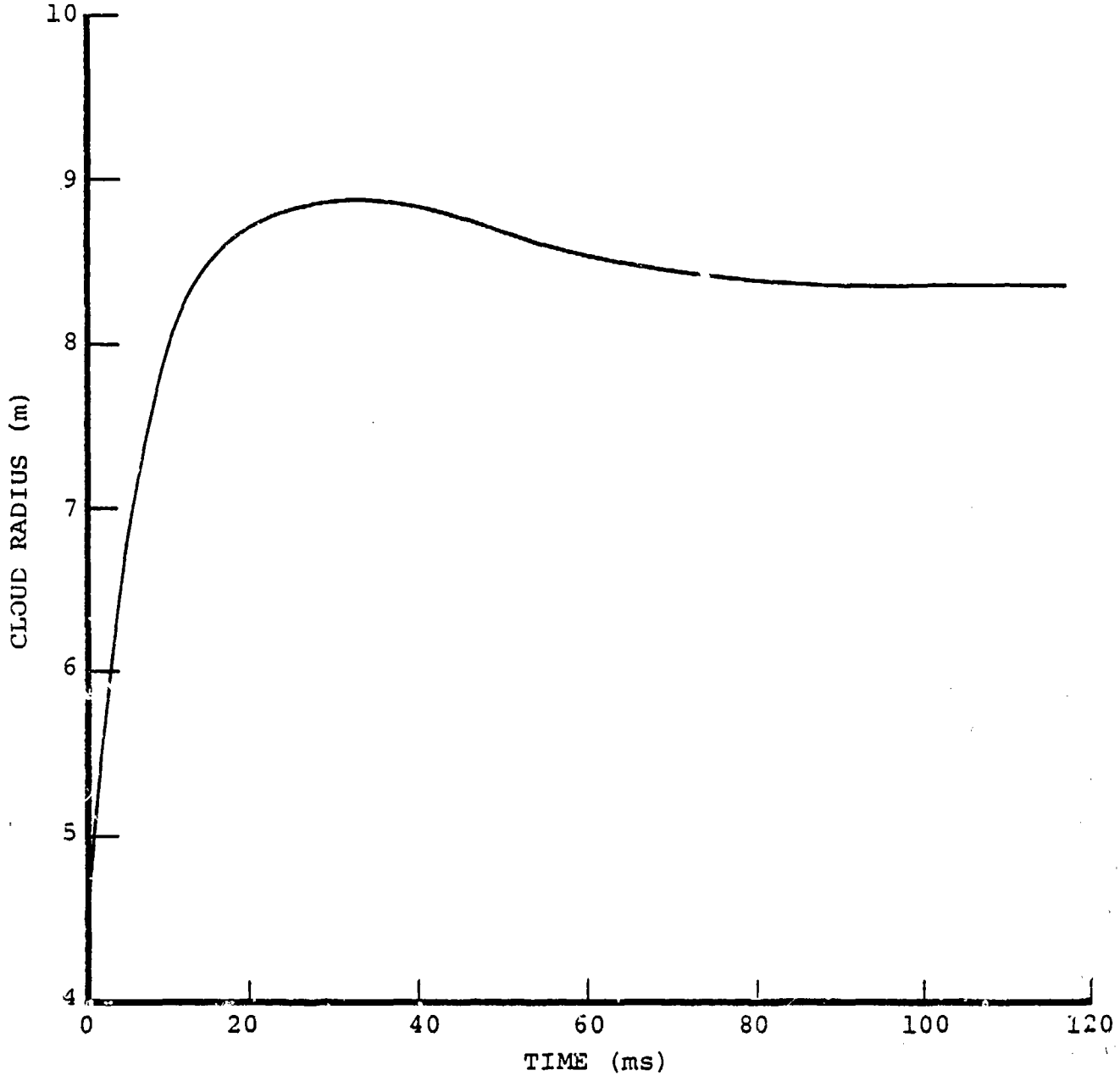

Figure 79. Trajectory of interface between combustion products and air in terms of time after detonation reaches cloud boundary.

The calculated results were evaluated further by treating them as though they had been acquired as experimental data. Stagnation probe pressures were determined from the computed flow Mach numbers and static pressures using Eq. (52). The theoretical data were then input to the data reduction program that was described earlier. The results appear on the next several figures.

It was found that $R_{O_{E,F}}$ values that were determined from matching overpressure positive-phase duration, t_p^+, differed widely from those inferred from peak overpressures and from overpressure impulses. It was decided as an interim measure to use only impulse and peak overpressure to determine $R_{O_{E,F}}$ until somewhat greater confidence in the nuclear reference curve for t_p^+ is established. The values of $R_{O_{E,F}}$ are plotted at each transducer position in Figure 80. The average of all these values is $R_{O_{E,F}}$ = 9.83 m (32.2 ft). This value was used in the remaining data reduction. The corresponding scale factor and effective blast coupling efficiencies were found to be s = 15.2, η_F = 0.867.

Peak static overpressure and total static impulse are presented in Figures 81 and 82. The peak pressures generally fall below and the impulses generally above the nuclear reference curves. This is due to the choice of average R_o. Agreement with the nuclear curves improves with radius up to the point at which the calculation was stopped. This was also the case with peak dynamic pressure and with overpressure positive phase duration, which appear in Figures 83 and 84.

In the next series of figures, Figures 85-96, the dimensionless static overpressures and dynamic pressures are plotted as functions of dimensionless time and compared

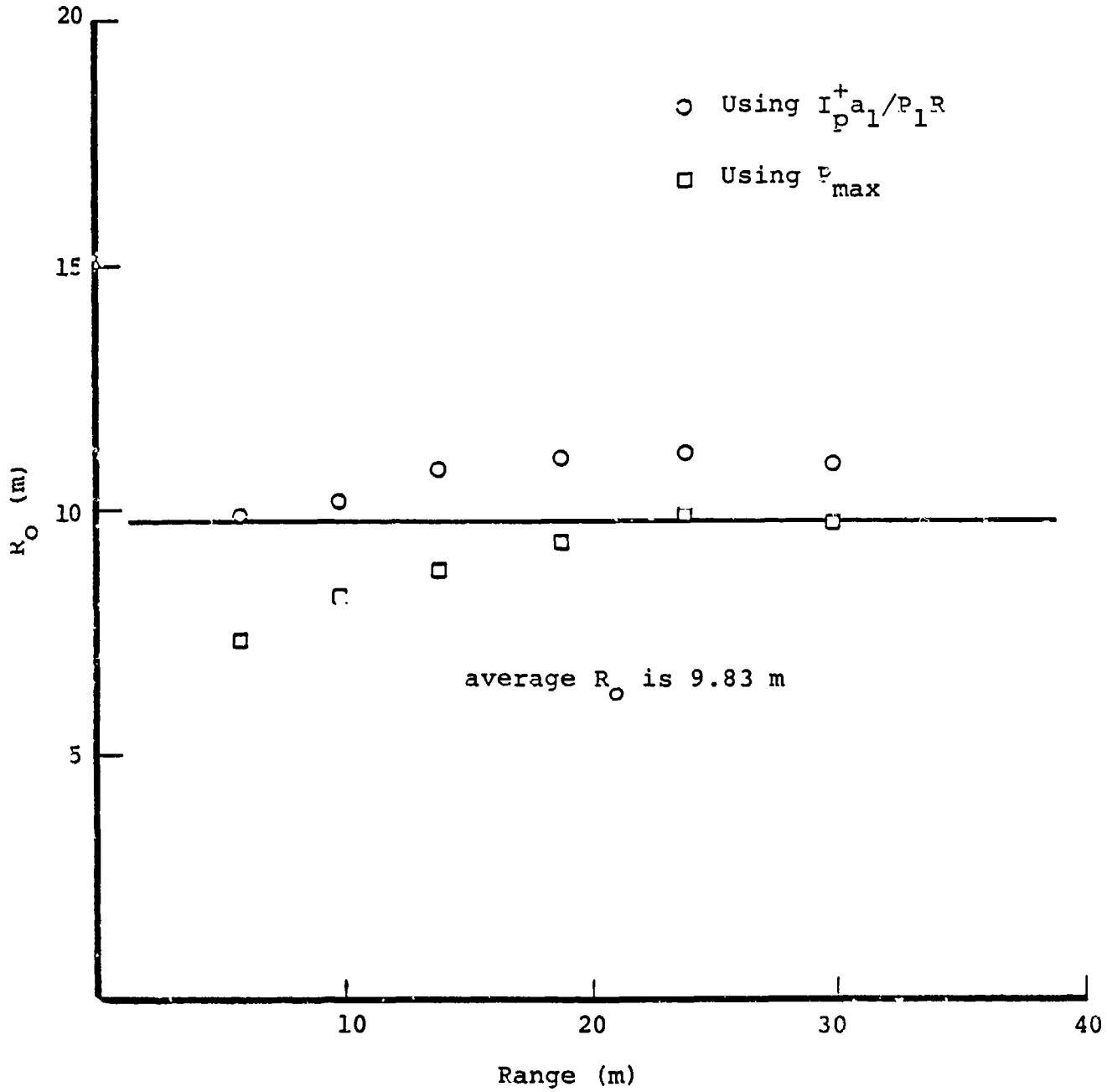

Figure 80. Inferred characteristic blastwave radius in hemispherical geometry for experimental scale stoichiometric heptane-air FAE.

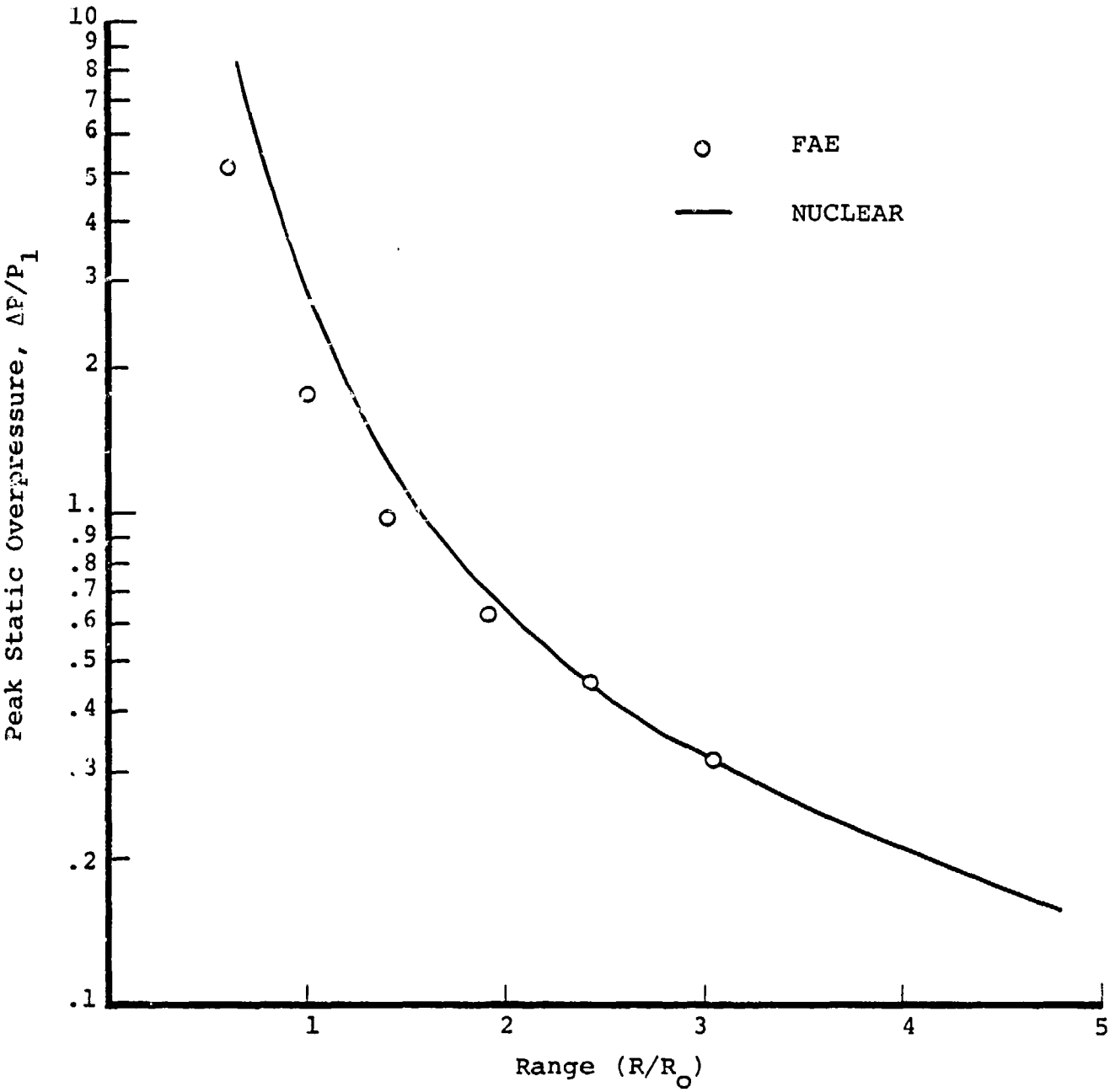

Figure 81. Calculated peak static overpressure from FAE versus range, compared against nuclear reference curve.

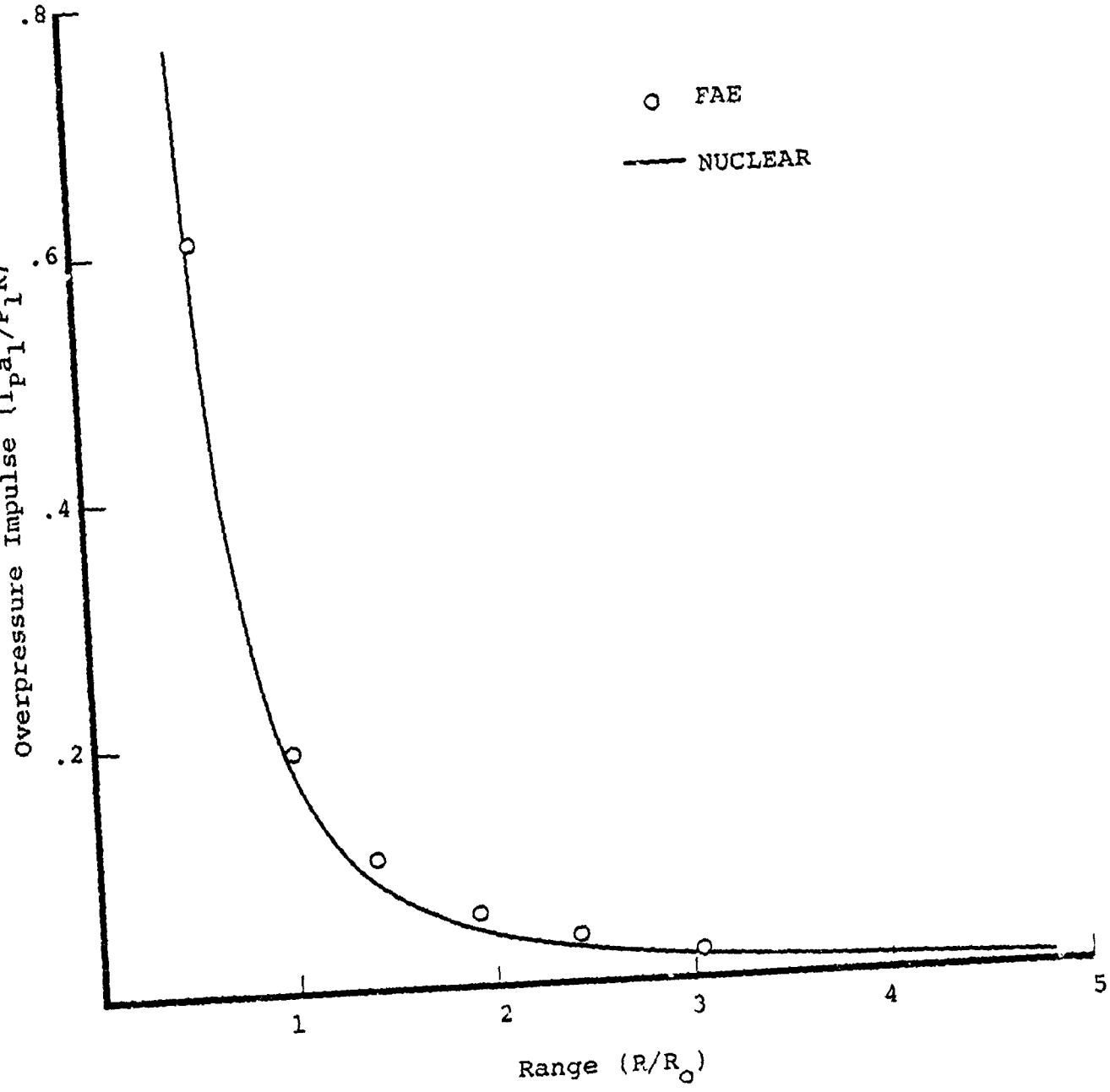

Figure 82. Calculated positive-phase static overpressure impulse from FAE versus range, compared against nuclear reference curve.

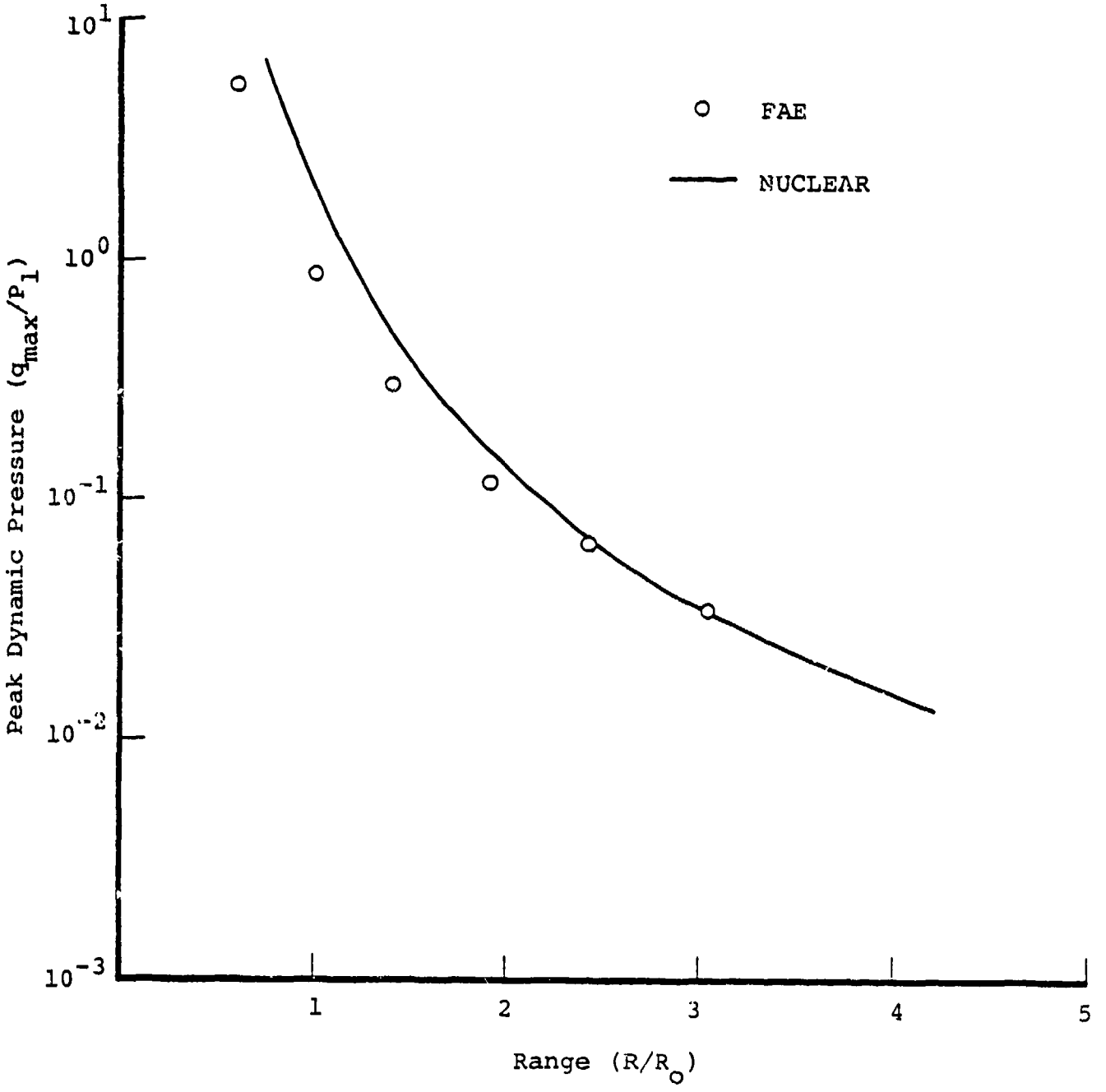

Figure 83. Calculated peak dynamic pressure from FAE versus range, compared with nuclear reference curve.

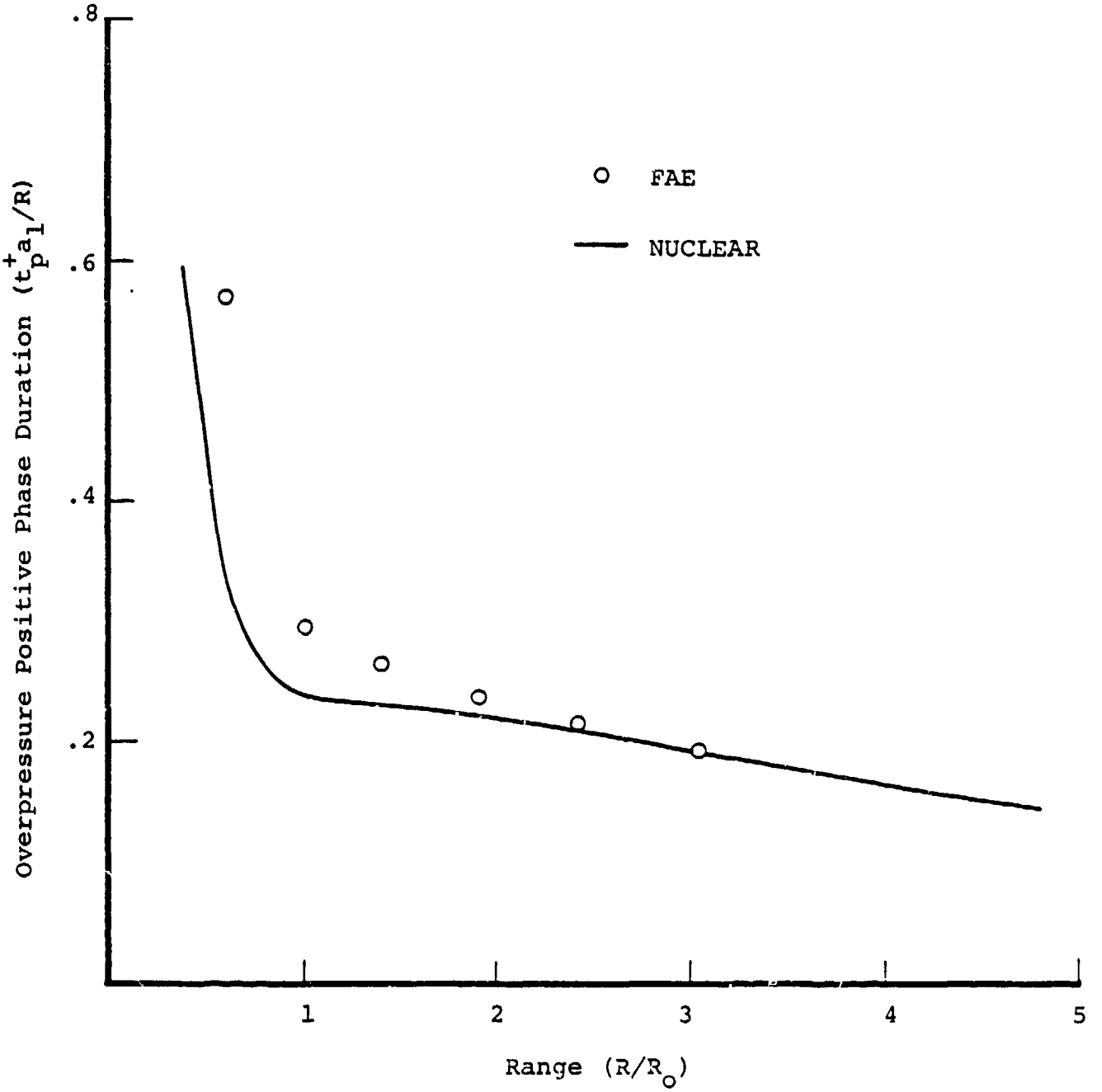

Figure 84. Calculated static overpressure positive-phase duration versus range from FAE, compared with nuclear reference curve.

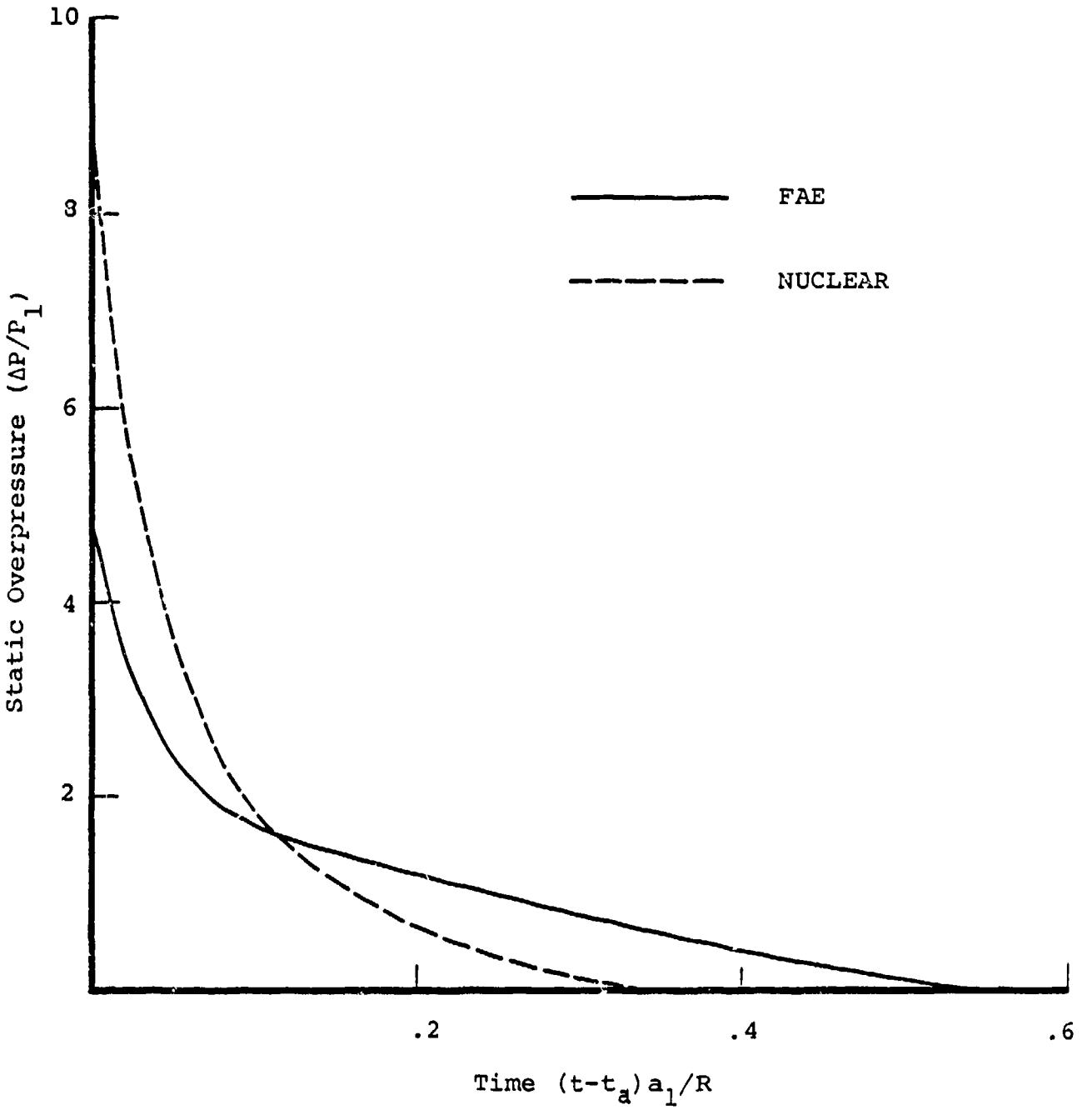

Figure 85. Calculated heptane-air FAE static overpressure versus time after shock arrival compared with nuclear reference curve, at $R/R_o = 0.603$.

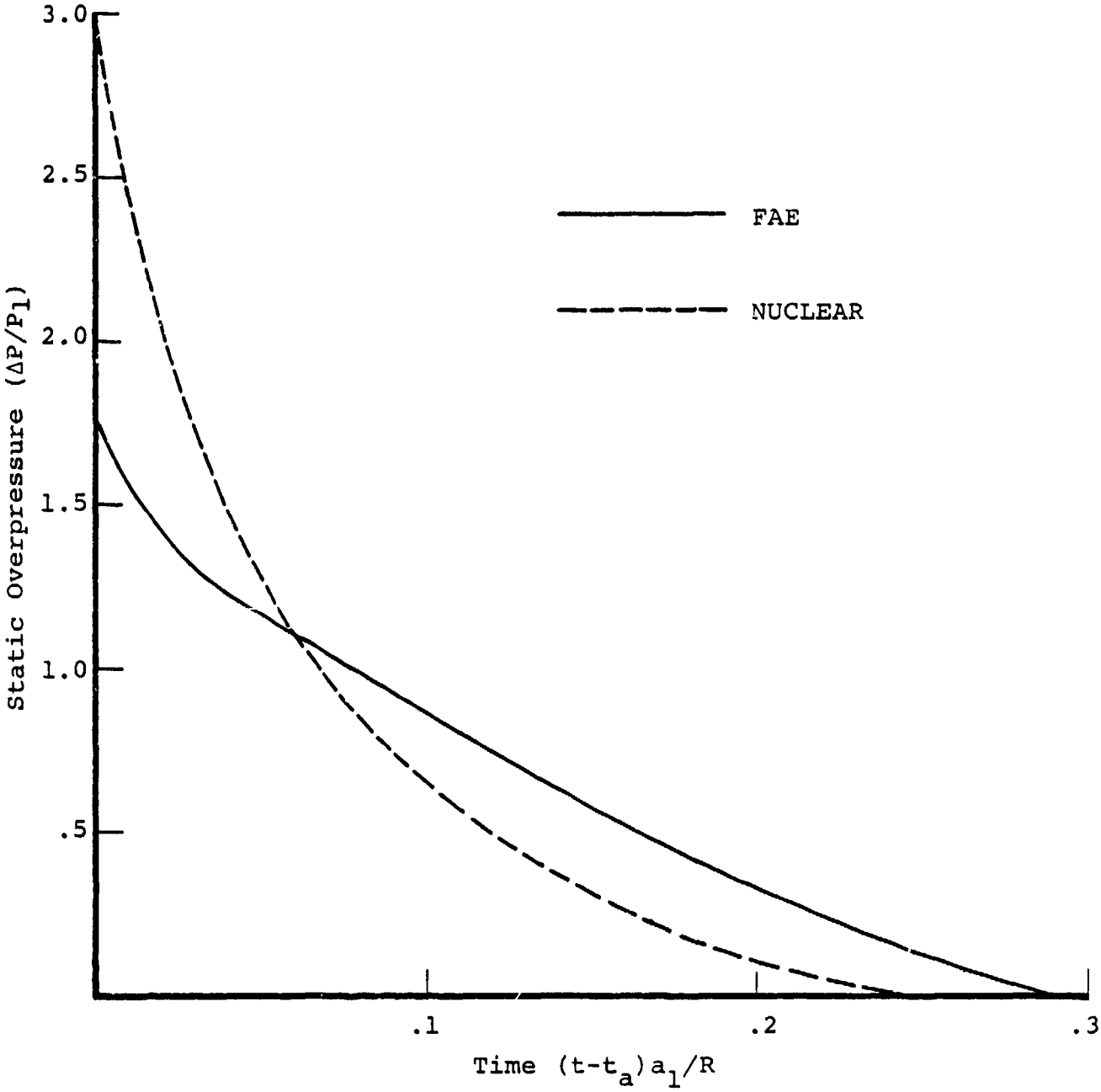

Figure 86. Calculated heptane-air FAE static overpressure versus time after shock arrival compared with nuclear reference curve, at R/R_o = 1.01.

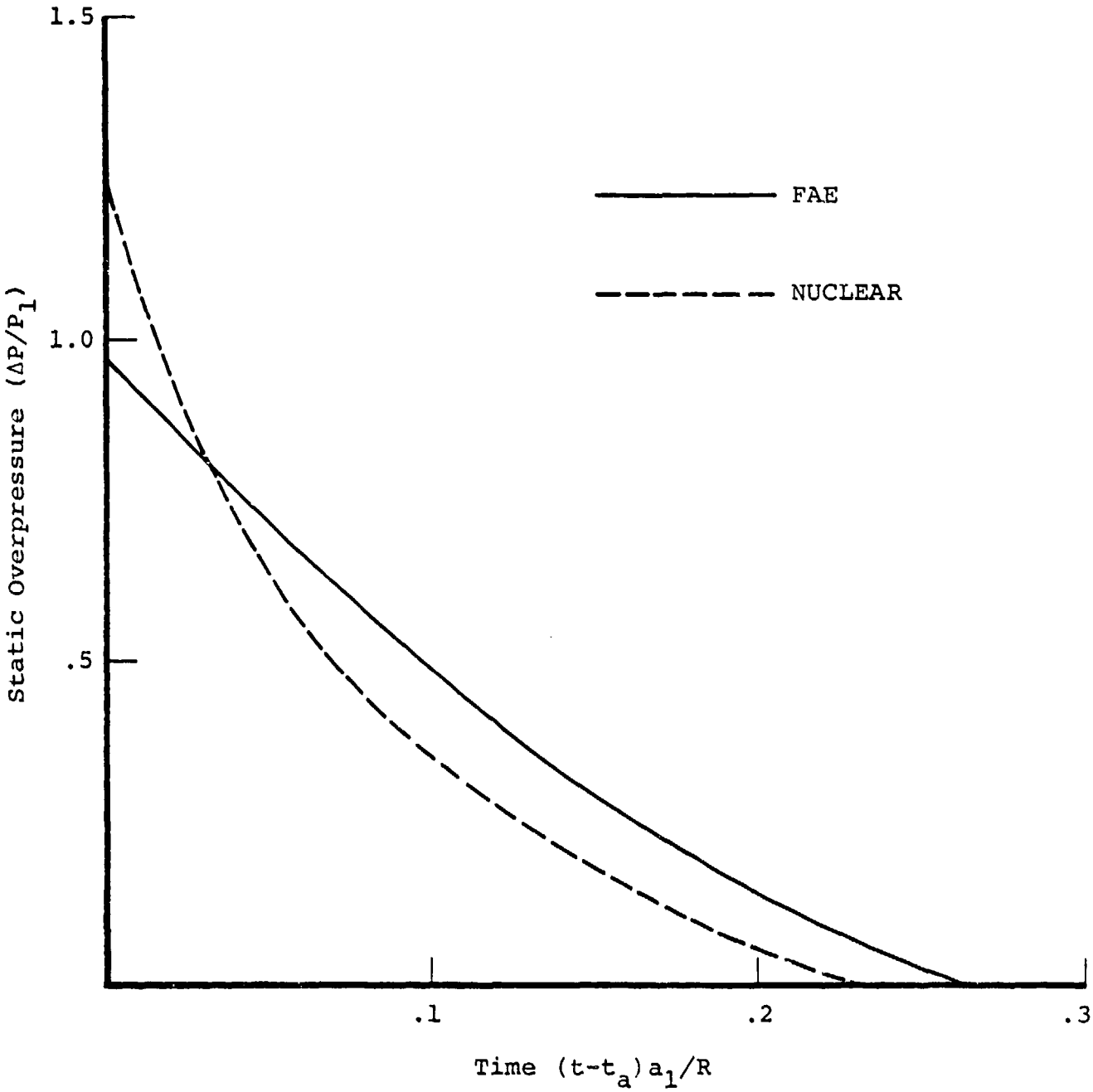

Figure 87. Calculated heptane-air FAE static overpressure versus time after shock arrival compared with nuclear reference curve, at R/R_o = 1.42.

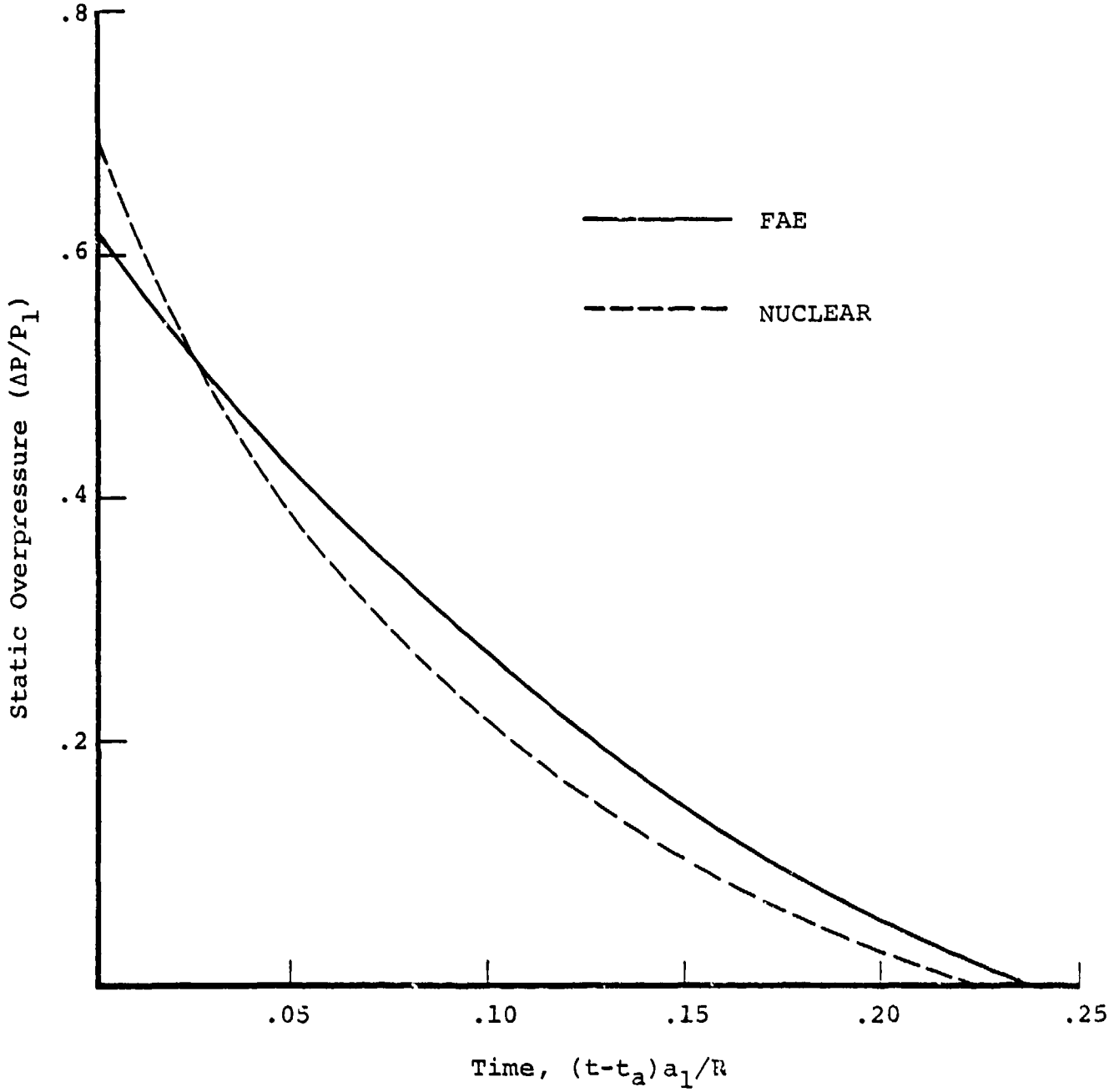

Figure 88. Calculated heptane-air static overpressure versus time after shock arrival compared with nuclear reference curve, at R/R_o = 1.93.

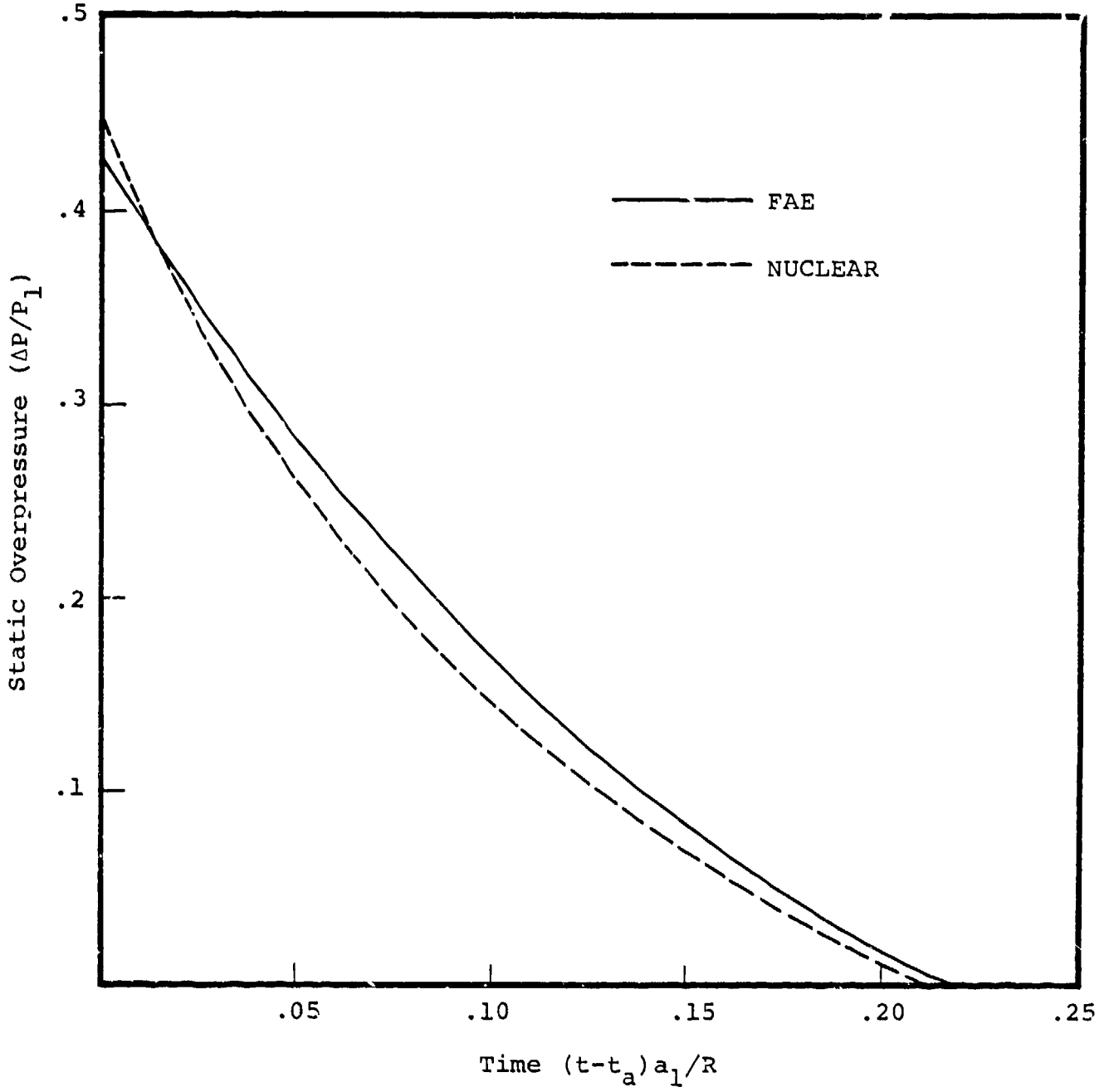

Figure 89. Calculated heptane-air side-on overpressure versus time after shock arrival compared with nuclear reference curve, at R/R_o = 2.43.

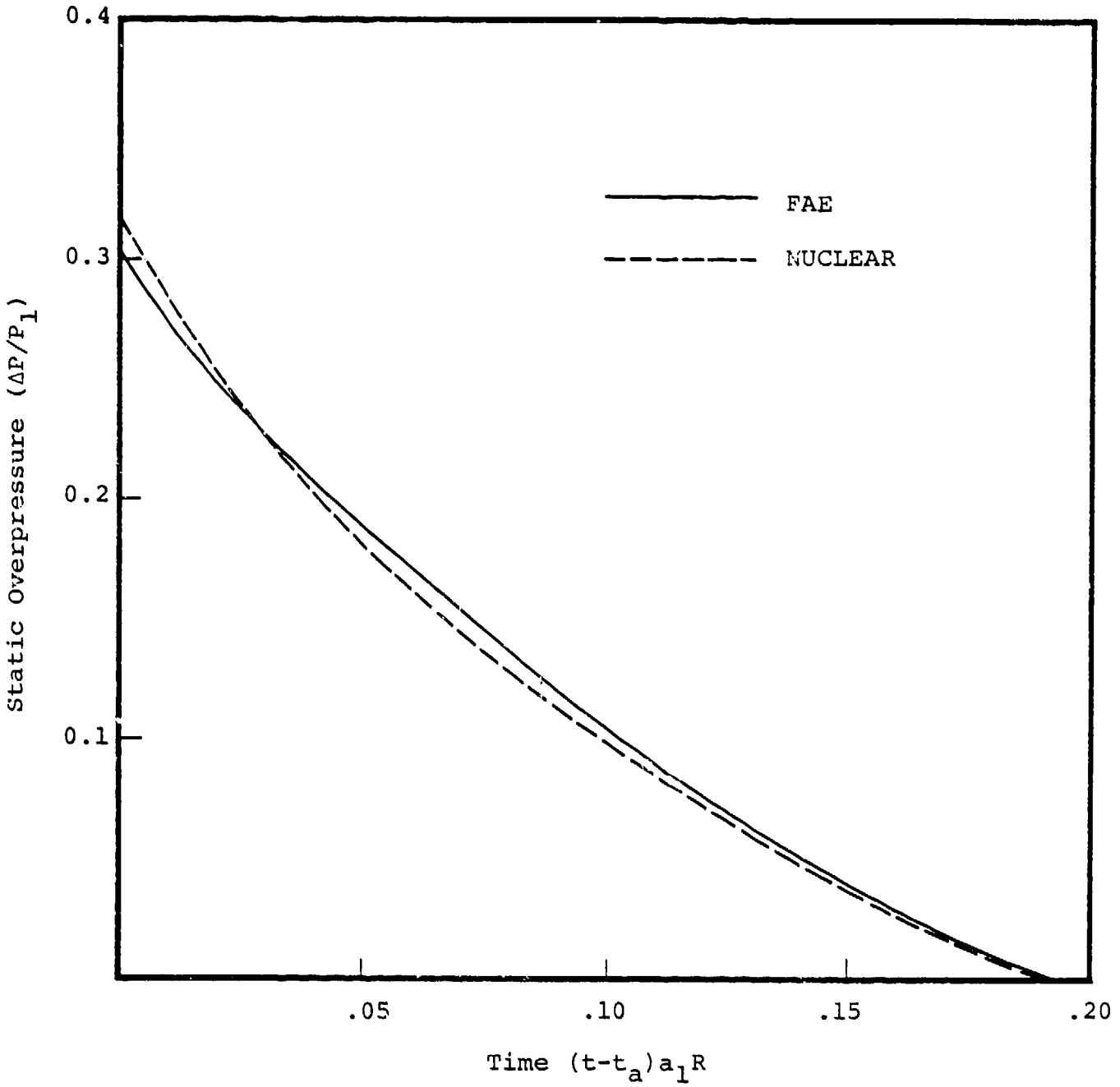

Figure 90. Calculated heptane-air static overpressure versus time after shock arrival compared with nuclear reference curve, at R/R_o = 3.04.

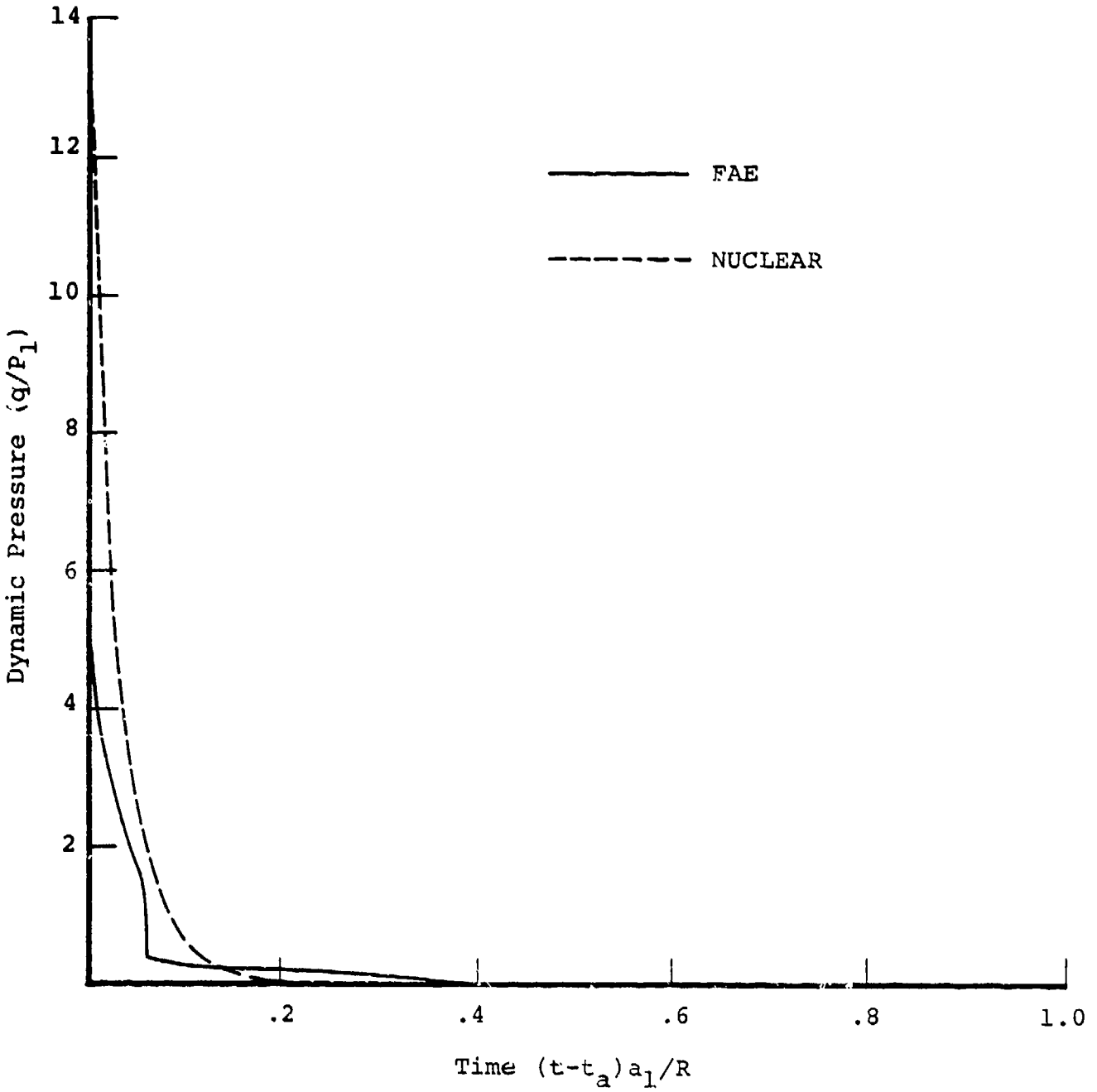

Figure 91. Calculated heptane-air dynamic pressure versus time after shock arrival compared with nuclear reference curve, at $R/R_o = 0.603$.

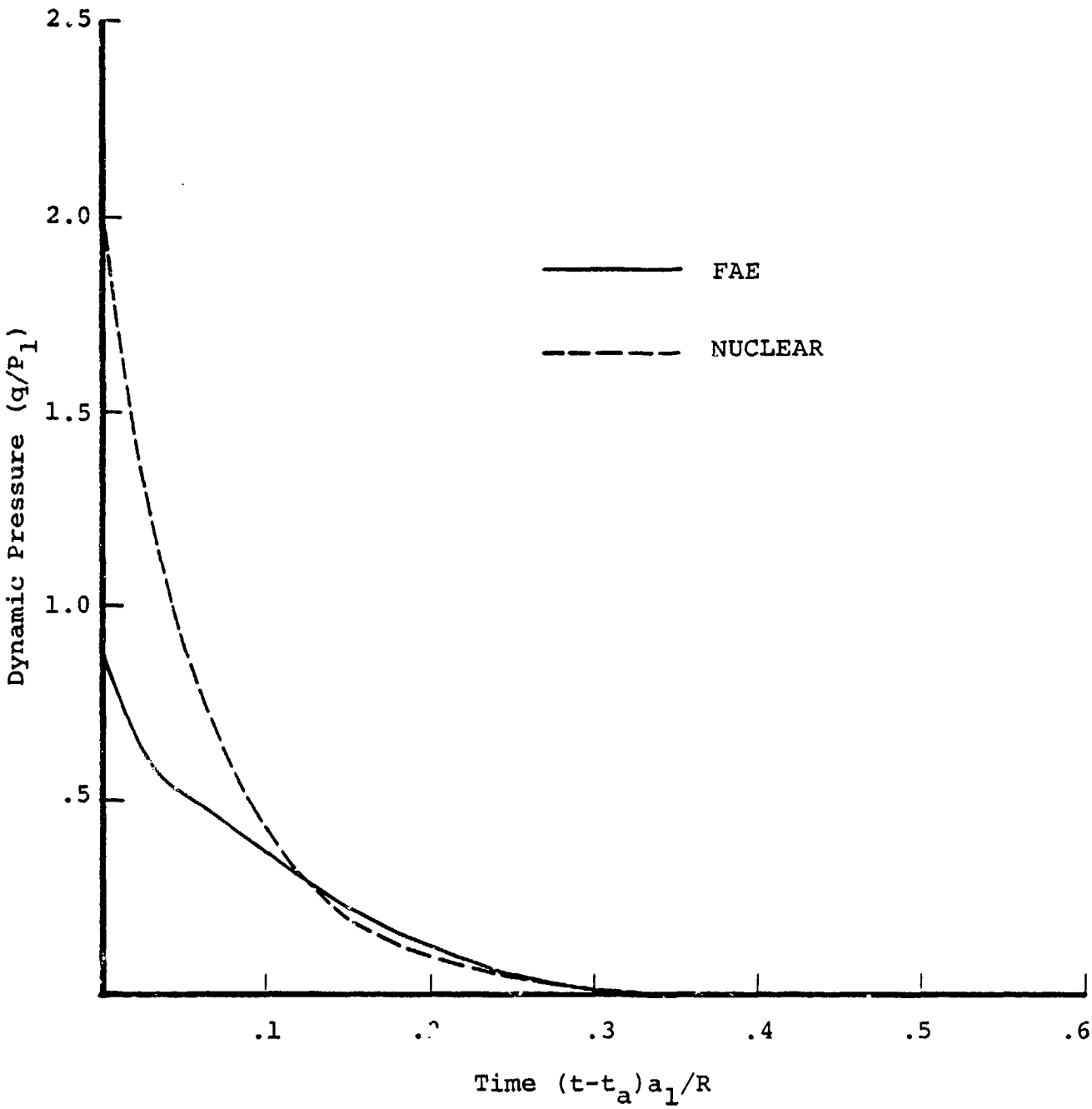

Figure 92. Calculated heptane-air dynamic pressure versus time after shock arrival compared with nuclear reference curve, at R/R_o = 1.01.

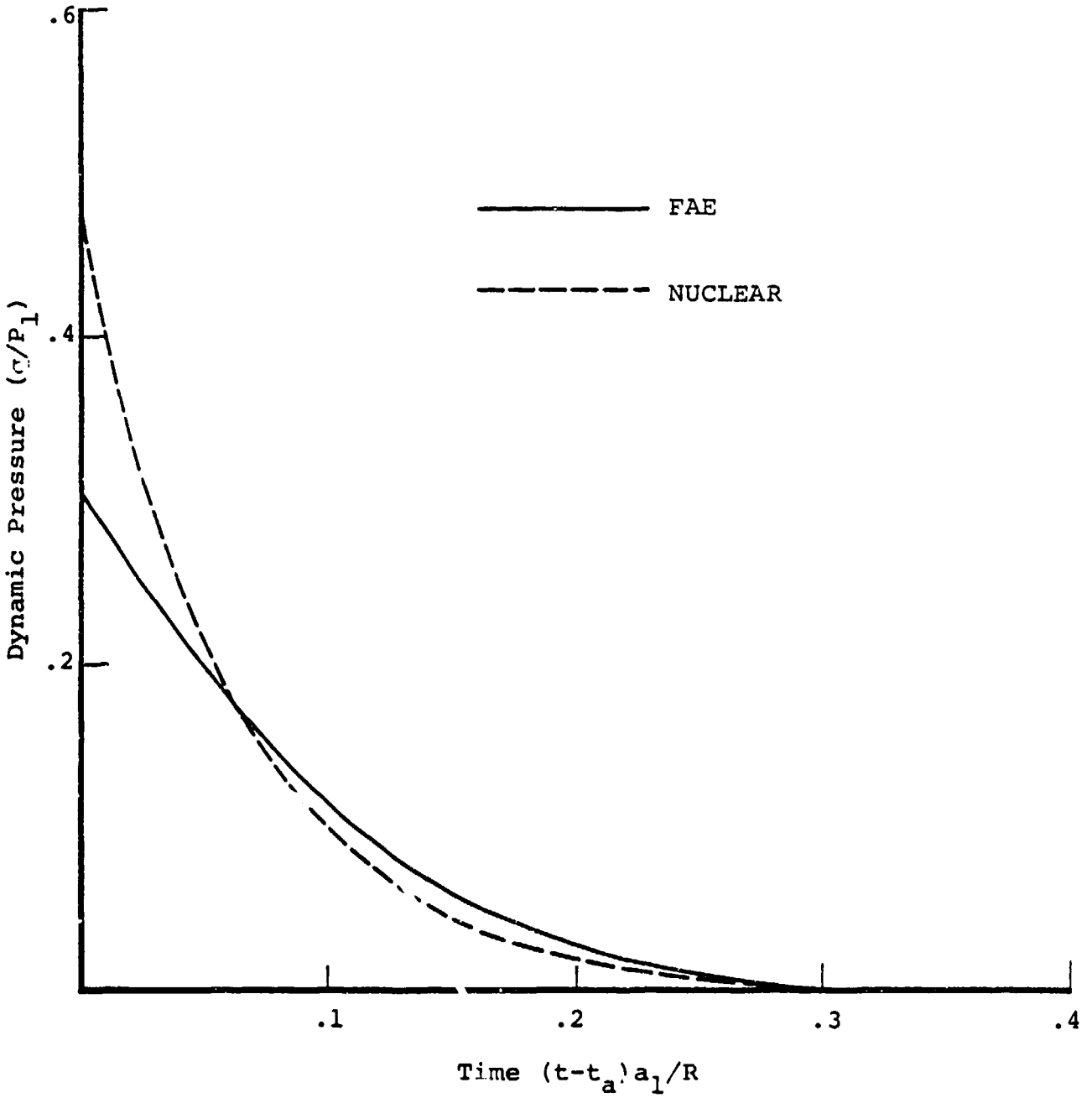

Figure 93. Calculated heptane-air dynamic pressure versus time after shock arrival compared with nuclear reference curve, at R/R_0 = 1.42.

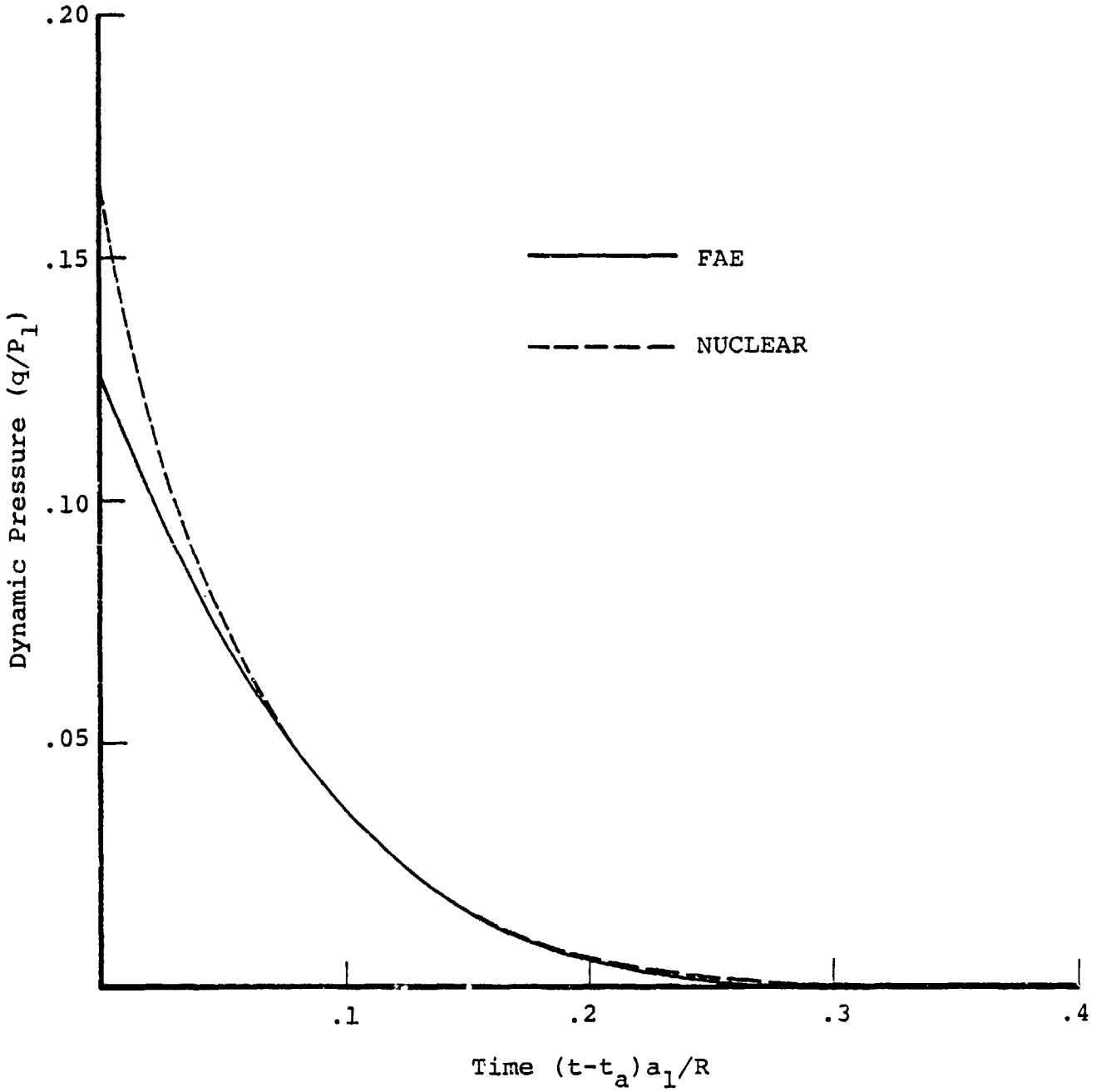

Figure 94. Calculated heptane-air dynamic pressure versus time after shock arrival compared with nuclear reference curve, at R/R_o = 1.93.

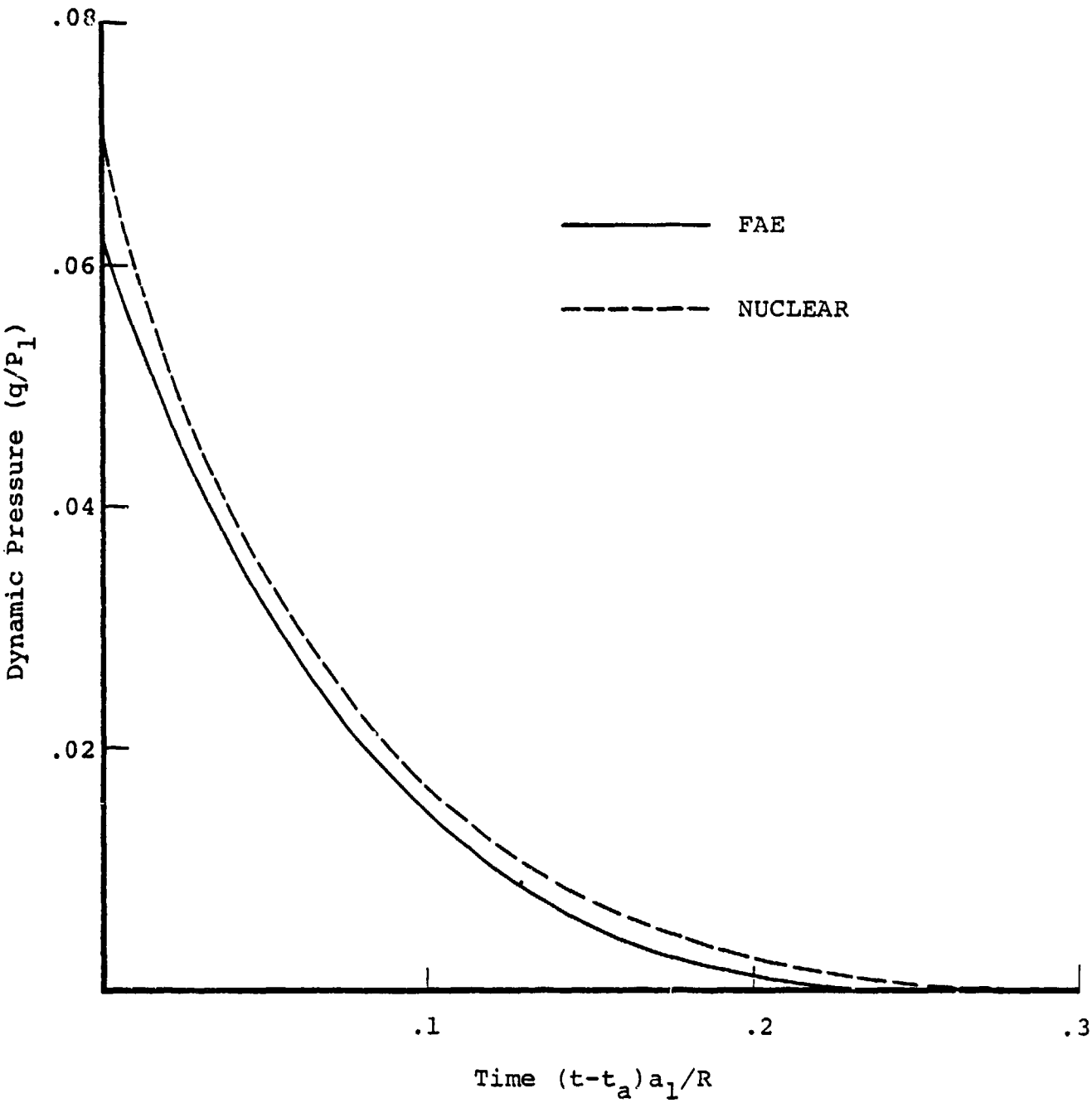

Figure 95. Calculated heptane-air dynamic pressure versus time after shock arrival compared with nuclear reference curve, at $R/R_o = 2.43$.

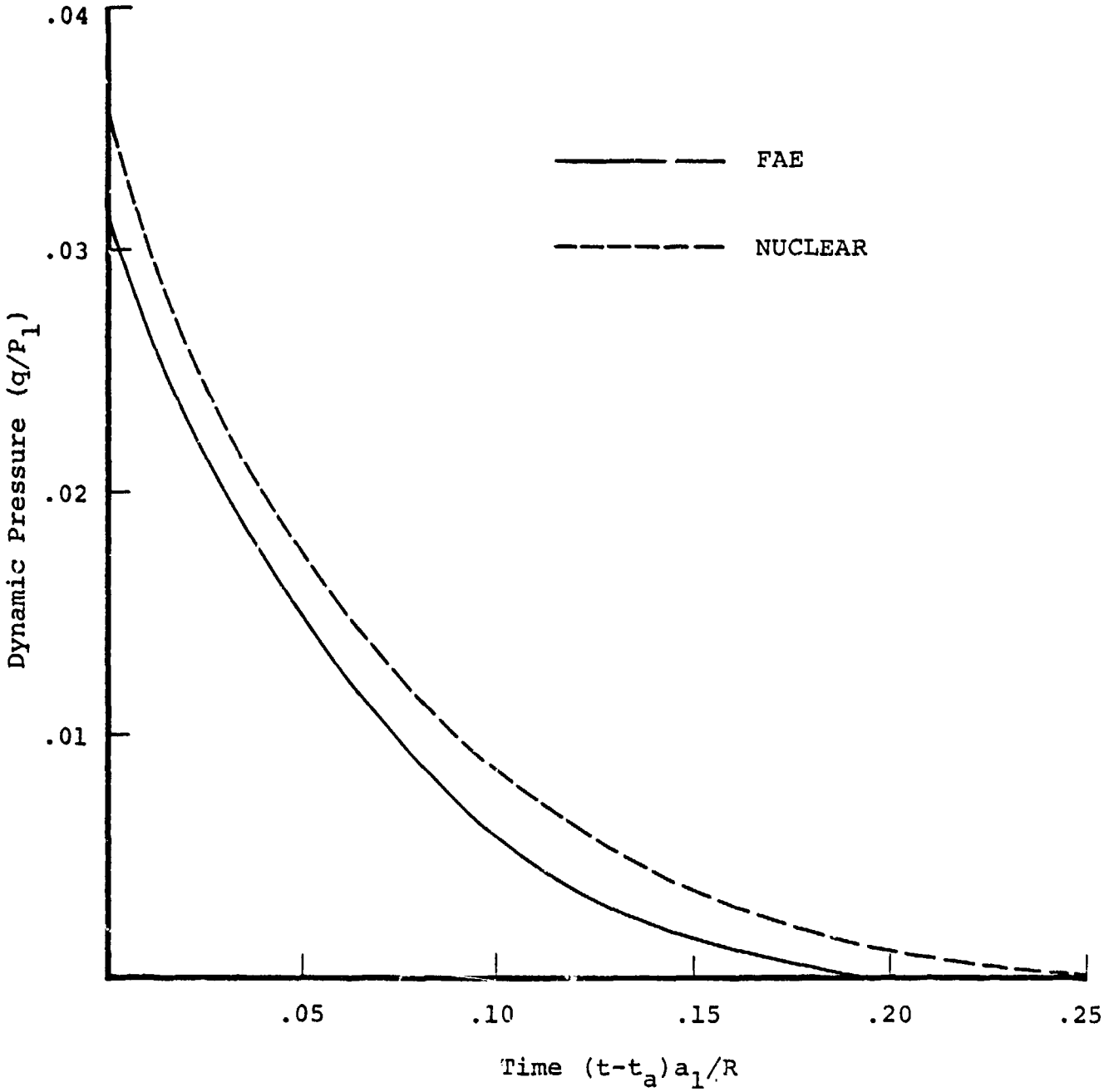

Figure 96. Calculated heptane-air dynamic pressure versus time after shock arrival compared with nuclear reference curve, at $R/R_o = 3.04$.

against the fully smoothed nuclear curves. The theoretical FAE data have also been fully smoothed. The agreement between the FAE and nuclear profiles becomes quite reasonable at ranges corresponding to overpressures below about 70 kPa (10 psi). Closer to the explosion center the FAE overpressure curves are flatter than the respective nuclear profiles. That is, the FAE peak overpressures are lower and the overpressure positive-phase durations are longer. The greater durations result in impulses that are above the nuclear values in spite of the lower peak overpressures.

Finally, it should be noted that two simplifications in the FAE calculation may have a significant impact on these results. In the calculation, the chemical composition of the cloud was assumed to be invariant with time, and the specific heats within the cloud and in the air, while not equal, were assumed to be constants. The chemical composition of the cloud was taken to be that calculated by the ORAKL code for the detonation products. The fixed specific heats (and γ) in the cloud were taken to correspond to these products.

In reality, the substantial pressure and temperature excursions in the exploded FAE cloud would result in continuously shifting local chemical equilibrium. This, in itself, would alter local specific heats and would result in additional local heat release as dissociated species recombine. The specific heats, both within the cloud and in the surrounding air, would also change as the local temperatures change.

The accuracy of gas-phase detonation calculations has long been known to be strongly dependent on product composition assumptions (Reference 67). This is due to the considerable dissociation that occurs at the very high temperatures attained in detonations. The initial shock compression of air surrounding an FAE cloud also produces large temperature increases during the early stages of blastwave development. Subsequent

expansion then reduces these temperatures markedly. Therefore, a dissociation/reassociation cycle can be expected in the air outside the cloud as well as in the detonation products. A more accurate FAE calculation would include local chemical equilibrium and variable specific heats, both within the cloud and in the surrounding air.

SECTION 6

CONCLUDING REMARKS

A reusable 1/4-ton nuclear equivalent FAE airblast simulator has been built. Symmetrical fuel-air clouds of propylene oxide and heptane have been formed impulsively from clusters of 600-1400 nozzles located at the cloud center. These clouds have been routinely detonated and the scaled blast waveforms are in reasonably good agreement with nuclear waveforms at the scaled ranges. Theoretical calculations have yielded similar results. Results from survey experiments with large-diameter single nozzles are preliminary but indicate that it should be possible to form clouds large enough to simulate the far-field airblast of a 1 KT surface nuclear explosion.

Scaleup to the 1 KT level involves many issues. Theoretically, the scale of an FAE cloud should not affect its airblast characteristics unless the detonation reaction zone contains a significant proportion of the total cloud mass (when the detonation reaches the cloud boundary). This is a possible problem at the 1/4-ton scale with coarsely atomized liquid jets. The two-phase detonation in these small clouds may possess expansion-wave flowfields that are very different from the self-similar flowfields in larger detonated clouds. As a result, the effective airblast coupling efficiency may differ with scale.

Beyond this effect, however, fuel droplet size should have little impact on the fuel-air detonation or on the airblast that is produced by it, provided that initiation is possible. Initiation is a relatively greater problem in small-scale than in large-scale clouds. The droplets of the atomized jets do not scale linearly with cloud size, although

somewhat larger mean initial droplet diameters are expected from the breakup of larger jets. Therefore the initiation requirements of large clouds should not be far removed from those for much smaller clouds. If the fuel were allowed to vaporize the initiation requirements would be identical. The total energy release of the initiator and its physical size can be made negligible in both cases but this is especially so in the case of large clouds.

The size of the fuel-air cloud and the minimum quantity of fuel needed to simulate a nuclear explosion of specified yield is determined by the effective blast efficiency. This efficiency was found experimentally to be about 74% for propylene oxide FAE clouds. Theoretically it was found to be 87% for a heptane cloud. Experiments with small scale heptane-air clouds have yielded efficiencies of about 40%. These values are defined with respect to the constant-pressure heat of combustion which is used as a reference. It should be emphasized that the effective airblast efficiency is in essence determined by a process of best fit matching of theoretical or experimental FAE data with the respective nuclear curvefits. The values that are obtained in this way are very sensitive to the nuclear curvefit choice. For example, the nuclear curvefits used presently are those of Reference 52 (Brode, 1964). If instead the curvefits of Reference 51 (Brode, 1970) are used, the effective blast efficiency of the theoretical heptane FAE is found to be 68% rather than 87%.

Nuclear airblast simulation by fuel-air explosions is limited to ranges at which the overpressures are below the Chapman-Jouget detonation pressure. As examples the C-J overpressures of stoichiometric heptane/air and propylene oxide/air detonations under standard conditions are 1.78 MPa (258 psi) and 1.86 MPa (270 psi) respectively. The peak detonation pressure increases with decreasing initial air temperature so that simulation could be extended to somewhat higher overpressures

if tests are conducted during cold weather. It might also be feasible to increase the center-cloud pressure by dispersal of a liquid high explosive with the fuel spray.

FAE/nuclear airblast simulation may also be limited by the extent of expansion of the detonated fuel-air cloud. The degree of this expansion was not investigated experimentally, but in the theoretical heptane FAE calculation the cloud expanded to a radius at which the peak overpressure was about 0.283 MPa (41 psi). Testing would have to be confined to ranges having peak overpressures below this level, if the effect of hot combustion products on the target being tested were a matter of concern.

Ultimate limitations on the maximum scale of hemispherical FAE clouds are not presently known. It seems likely that cost would in practice limit the scale. While it appears feasible to achieve a 1 KT simulation, it is not known what additional engineering difficulties would have to be overcome to reach, say, the 10 KT level. One possible technique to attain higher level simulation would be to locate the fuel-air cloud in the vertex of a large natural earth formation in the shape of a spherical wedge. This would reduce the size of the required dispenser hardware but all testing would have to be confined to regions inside the wedge.

A second alternative to reach larger scales is to abandon the hemispherical FAE cloud geometry. The hemispherical shape is the most efficient in terms of ground-level airblast coupling. It also minimizes unwanted secondary shocks and permits point symmetrical test hardware layout, maximizing the data yield per test. If these advantages can be compromised, FAE cloud shaping could be used to produce large-scale (long positive-phase duration) simulation in localized spacial volumes of restricted size.

It should also be noted that in the extreme far-field (≤14 KPa (2 psi) overpressure) the influences of cloud shape are almost entirely lost. Large-diameter, pancake-shaped FAE clouds of virtually unlimited yield could be formed by a dispensing system comprising for example a number of point source dispensers such as that described in this report. Very large-yield testing of aeronautical systems in the extreme far-field might be accomplished in this way.

In all cases, FAE clouds formed from the impulsive dispensing of a large number of liquid fuel jets are subject to many constraints, some of which are conflicting. In most respects dispensing at the highest practical jet velocity is advantageous. This improves atomization which enhances fuel distribution uniformity. It also reduces the cloud formation time which is important in minimizing cloud shape distortions due to winds, and it increases the jet spray column width which decreases the required number of jets needed to fill in the cloud. Unfortunately, high velocity injection leads to interactions between the spray and the air which can severely distort the cloud. Whether or not accurate cloud shape is considered a critical requirement, the volume of air engulfed by these distorted clouds differs from that intended and this influences the effective FAE yield. One possible remedy to the problem of distortions due to high velocity jets may lie in tailored aiming of the injector nozzles, with some nozzles directed downward. The distortion can also be reduced by decreasing the number of nozzles, but if too few nozzles are used the jet sprays will not overlap at the outermost portions of the cloud. Overlap in this region is necessary since a large fraction of the total cloud mass is contained in it. It appears that 1400-1600 nozzles are needed for complete overlap in a cloud produced by point source injection.

While it is probably not necessary to fully understand all details of jet breakup and cloud formation in order to build a successful FAE/nuclear simulator, basic engineering data relating to certain rudimentary features are essential. The reach and width of individual spray columns formed under conditions that produce adequate atomization are needed as is the formation time. Reach, width, and formation time are in general functions of injection velocity, nozzle diameter, fuel properties, and, it appears, the quantity of fuel dispensed. For each fuel and nozzle size there is a minimum injection velocity below which atomization is poor. The minimum appears to increase with nozzle diameter. Above this velocity atomization continuously improves while the jet reach changes only slightly. Increasing the nozzle diameter increases both reach and spray column width. Jet reaches are typically 1000-2000 nozzle diameters, while jet spray widths are typically 100 nozzle diameters. It may be possible to increase jet reach through the use of additives such as long-chain polymers but it is anticipated that this would adversely affect atomization, particularly near the nozzle. Fuel distribution in individual jet sprays is unknown but the spray density appears visually to increase with distance along the jet. This should permit rather uniform clouds to be formed when a large number of such jets overlap after point source injection.

One feature of jet breakup that has emerged during the survey experiments is the influence on jet reach of jet tail breakup. When the end of the jet emerges from a nozzle, material from the jet tail appears to continuously be torn off. It has been postulated that this phenomenon, which may be due to vortex shedding at the tail, will reduce the jet reach if an insufficient quantity of fuel is dispensed. Some experimental evidence has been generated in support of this postulate which, however, is presently considered unproven. If the effect is real it could have a major impact on dispenser design. The implication would be that there is a minimum

quantity of fuel that must be dispensed through each nozzle in order for the jet to attain full reach. Thus the minimum quantity of fuel needed to form a fuel-air cloud of specified radius would equal the number of nozzles needed multiplied by the minimum quantity of fuel per nozzle. This could well exceed the quantity of fuel required calculated on the basis of effective airblast efficiency.

It is recommended that systematic experiments with single jets be conducted in which jet velocity, nozzle diameter, and fuel quantity are varied over a reasonably wide range. This will require impulsive dispensers that are larger and smaller than the existing U-tube and linear dispensers. It has been found that each dispenser is limited to a narrow range of jet sizes that can be tested. The largest jet that can be produced is limited by the fuel capacity of the dispenser. The smallest jet is limited by flow non-uniformities when too little fuel is dispensed. In the latter case multiple nozzles can be attached to the dispenser in a single test to increase the quantity of fuel dispensed, provided the layout is such that the jets do not interfere with one another.

It is also recommended that FAE tests using the 1/4-ton reusable facility be continued to generate a better data base for comparison with nuclear explosions. Additional areas that must be addressed before a full-scale FAE blast simulator can be constructed are more engineering-oriented and include hardware configuration, fuel handling techniques, repeatability, safety, and construction and life-cycle costs.

SECTION 7

REFERENCES

1. Sauer, F. and Stubbs, T., "Application of FAE Technology to the Design of Nuclear Airblast Simulation Experiments," DNA 4327F, August 1977.

2. Sedgwick, R. T., et al., "Feasibility Investigation of a Permanent Fuel-Air Explosive Blast Simulator," DNA 5059, August 1978.

3. Kratz, H. R., Sedgwick, R. T. and Pierce, T. H., "The Use of Fuel-Air Explosives as a Nuclear Blastwave Simulator," Proceedings, Tenth Symposium on Explosives and Pyrotechnics, Franklin Institute, Philadelphia, February 1979.

4. Sedgwick, R. T., Pierce, T. H. and Kratz, H. R., "The Use of Fuel-Air Explosives as a Nuclear Blastwave Simulator," Sixieme Symposium International sur Les Applications Militaires de La Simulation de Souffle, Centre D'Etudes de Gramat, Gramat, France, June 1979.

5. Sedgwick, R. T., et al., "Feasibility Investigation of a Permanent Fuel-Air Explosive Blast Simulator," Proceedings of the Nuclear Blast and Shock Simulation Symposium, DNA 4797P-1, p. 206, December 1978.

6. Balcerzak, M., "Detonable Gas Explosion," Operation Distant Plain Symposium, DASA 1947-1, September 1967.

7. Reisler, R. and Ethridge, N., "Airblast Overpressure Phenomena," Operation Distant Plain Symposium, DASA 1947-1, September 1967.

8. Fields, S. F. and Fugelso, L. E., "Blast Simulation with Balloons Containing Detonable Gas," DNA 3432F, December 1974.

9. Hartenbaum, B. A., "Nuclear Airblast Simulation Using Fuel-Air Explosives," DNA4839F, December 1978.

10. Sedgwick, R. T., unpublished data, Systems, Science and Software, 1977.

11. Ohnsorge, W., "Die Bildung vol Tropfen Düsen und Die Auflösung Flussiger Strahlen," ZaMM, Bd. 16, Heft 6, p. 355-358, December 1936.

12. Rayleigh, J. W. S., "On the Instability of Jets," Proc. London Math. Soc., vol. 10, p. 4-13, 1878.

13. Haenlein, A., "Über den Zerfall Eines Flüssigkeitsstrahles," Forsch., A. D., Gebiet d. Ingenieurwes, 2, 1931.

14. Grant, R. P. and Middleman, S., "Newtonian Jet Stability," A.I.Ch.E. J., vol. 12, no. 4, p. 669 ff, July 1966.

15. Phinney, R. E., "Breakup of a Turbulent Liquid Jet in a Low-Pressure Atmosphere," A.I.Ch.E. J., vol. 21, no. 5, p. 996-999, September 1975.

16. Rouse, H., et al., "Experimental Investigation of Fire Monitors and Nozzles," Proc. A.S.C.E., vol. 77, October 1951.

17. Chen, T. F. and David, J. R., "Disintegration of a Turbulent Water Jet," Journal of the Hydraulics Division, Proc. Amer. Soc. of Civil Engineering, vol. 90, no. HY1, p. 175, January 1964.

18. Schweitzer, P. H., "Mechanism of Disintegration of Liquid Jets," J. Appl. Phys., vol. 8, p. 513, August 1937.

19. Zakin, J. L. and Summers, D. A., "The Effect of Viscoelastic Additives on Jet Structures," Third Intl. Symp. on Jet Cutting Technology, Paper A4, BHRA Fluid Engineering, Cranfield, Bedford, England, 1976.

20. Hoyt, J. W. and Taylor, J. J., "A Photographic Study of Polymer Solution Jets in Air," Intl. Conf. on Drag Reduction, Paper E3, BHRA Fluid Engineering, Cranfield, Bedford, England, 1974.

21. Freeman, J. R., "Experiments Relating to Hydraulics of Fire Streams," Trans. Amer. Soc. Civil Engineering, vol. 21, November 1889.

22. Lee, D. W. and Spencer, R. C., "Photomicrographic Studies of Fuel Sprays," NACA Report No. 454, 1933.

23. Phinney, R. E., "The Breakup of a Turbulent Liquid Jet in a Gaseous Atmosphere," J. Fluid Mech., vol. 60, part 4, p. 689-701, 1973.

24. Lafrance, P., et al., "Drop Spectrometry of Laminar and Turbulent Jets," Phys. Fluids, vol. 17, no. 7, p. 1469-1470, 1974.

25. Reinecke, W. G. and Waldman, G. D., "Shock Layer Shattering of Cloud Drops in Reentry Flight," A.I.A.A. 13th Aerospace Sciences Mtg., Paper No. 75-152, January 1975.

26. National Fire Protection Association, Fire Protection Handbook, 14th ed., 1976.

27. Box, T., Practical Hydraulics, Sixth Ed., Spon., London, 1882.

28. Advertisement Brochure "The Worlds Highest Fountain," Prepared by or for Pratt Properties, Inc., Phoenix, Arizona.

29. Franz, N. C., "Fluid Additives for Improving High Velocity Jet Cutting," 1st Intl. Symp. on Jet Cutting Technolcgy, Paper No. A7, British Hydromechanics Research Assoc., Cranfield, Bedford, England, 1972.

30. Lienhard, J. H., "An Influence of Superheat Upon the Spray Configurations of Superheated Liquid Jets," Transactions of the A.S.M.E., Journal of Basic Engineering, p. 685, September 1966.

31. Bowen, J. R., et al., "Heterogeneous Detonations Supported by Fuel Fogs or Films," Thirteenth Symposium (International) on Combustion, The Combustion Institute, Pittsburgh, p. 1131-1139, 1971.

32. Dabora, E. K., Ragland, K. W. and Nicholls, J. A., "A Study of Heterogeneous Detonations," Astronautica Acta 12, p. 9-16, 1966.

33. Dabora, E. K., Ragland, K. W. and Nicholls, J. A., "Drop-size effects in spray detonations," Twelfth Symposium (International) on Combustion, Combustion Institute, Pittsburgh, p. 19-26, 1969.

34. Kauffman, C. W. and Nicholls, J. A., "Shockwave Ignition of Liquid Fuel Drops," A.I.A.A. Journal 9, 5, p. 880-885. 1971.

35. Pierce, T. H. and Nicholls, J. A., "Two-phase Detonations With Bimodal Drop Distributions," Astronautica Acta 17, p. 703, 1972.

36. Pierce, T. H. and Nicholls, J. A., "Time variation in the Reaction-Zone Structure of Two-Phase Spray Detonations," Fourteenth Symposium (International) on Combustion, Combustion Institute, Pittsburgh, p. 1277-1284, 1972.

37. Pierce, T. H. and Nicholls, J. A., "Hybrid Gas-Phase/Two-Phase Detonations," Combustion Science and Technology, vol. 9, p. 119-128, 1974.

38. Wagner, H. G.: "Gaseous Detonations and the Structure of a Detonation Zone," in Fundamental Data Obtained from Shock Tube Experiments (A. Ferri, Ed.), Pergamon Press, 1961.

39. Fraser, R. P., "Detonation Velocities in Liquid Fuel Vapors With Air or Oxygen at 100°C and Atmospheric Pressure," Seventh Symposium (International) on Combustion, Butterworths, p. 783, 1959.

40. Komov, V. F. and Troshin, Ya. K.: Dokl. Akad. Nauk SSSR 175, 109, 1967.

41. Kingery, C. N. and Kellner, R. C., "Airblast Overpressure vs. Time Histories Nuclear and TNT Surface Bursts," BRL Report 1638, AD 912092, March 1973.

42. Kingery, C. N., "Parametric Analysis of Sub-Kiloton Nuclear and High Explosive Air Blast," BRL Report 1393, AD 833698, February 1968.

43. Lehto, D. L. and Larson, R. A., "Long Range Propagation of Spherical Shockwaves from Explosions in Air," NOLTR 69-88, AD 698121, July 1969.

44. Ellis, P. A., et al., "Nuclear Weapons Blast Phenomena," DASA 1200-1, vol. 1-5, March 1971.

45. Glasstone, S. and Dolan, P. J., The Effects of Nuclear Weapons, 3rd Ed., DOD & DOE; USGPO 1977-0-213-794.

46. Needham, C., et al., "Nuclear Blast Standard (1 KT)," AFWL-TR-73-55 (Ref.), April 1975.

47. Sauer, F. and Stubbs, T., "Application of FAE Technology to the Design of Nuclear Airblast Simulation Experiments," DNA 4327F, May 1977.

48. Brode, H., "Point Source Explosion in Air," Rand Corp. RM-1824, December 1956.

49. Brode, H., "Numerical Solutions of Spherical Blast Waves," J. Appl. Phys., vol. 26, no. 6, p. 766, June 1955.

50. Brode, H., "Theoretical Description of the Blast and Fireball for a Sea Level Kiloton Explosion," Rand Corp. Memo. RM-2246-PR, January 1966.

51. Brode, H., "Height of Burst Effects at High Overpressures," DASA 2506, July 1970.

52. Brode, H., "A Review of Nuclear Explosion Phenomena Pertinent to Protective Construction," Rand Corp., R-425-PR, May 1964.

53. Brode, H. L., "Review of Nuclear Weapons Effects," Annual Rev. of Nuclear Science, vol. 18, p. 153-202, 1968.

54. Johnson, M. R. and Balcerzak, M. J., "Modified Atmosphere Effects on Air Blast Project 1.09, Operation Distant Plain," DASA 2008, November 1967.

55. Bryant, E. J. and Keefer, J. H., "Basic Airblast Phenomena," Wt-1401, June 1962.

56. Sachs, D. C., Swift, L. M. and Sauer, F. M., "Airblast Overpressure and Dynamic Pressure over Various Surfaces," Wt-1109, September 1957.

57. Teel, G. D., "Airblast Measurements," BRL Report 1477, February 1970.

58. Kingery, C. N., "Air Blast Parameters Versus Distance for Hemispherical TNT Surface Bursts," BRL Report 1344, September 1966.

59. Shreve, J. D., "Pressure-Distance-Height Study of 250-LB TNT Spheres," WT-520, March 1953.

60. Needham, C. E. and Burghard, T. H., "Air Blast Calculations-Event Mine Under," AFWL-TR-69-105, October 1969.

61. Teel, G. D., "Airblast Measurements from a 100 ton TNT Detonation over Granite-Mineral Rock Event, Mine Shaft Series," BRL Report 1502, October 1970.

62. Goldstein, H. and von Neumann, J., "Blast Wave Calculation," Collected Works of J. von Neumann, vol VI, Pergamon Press, Oxford, p. 386-412, 1963.

63. Guirao, C. M., Bach, G. G. and Lee, J. H. S., "On the Scaling of Blast Waves from Fuel-Air Explosives," Sixieme Symposium International sur les Applications Militaires de la Simulation de Souffle, Deuxieme Partie, Centre d'Etudes de Gramat, Gramat, France, p. 4.2.1, June 1979.

64. Cooperwaithe, M. and Zwisler, W. H., "TIGER Computer Program Documentation," NTIS AD-A002-791, March 1974.

65. Nicholls, J. A., et al., "Theoretical and Experimental Study of Cylindrical Shock and Heterogeneous Detonation Waves," Acta. Astro., vol. 1, p. 385-404, 1974.

66. Rimer, N., "A Users Guide to SKIPN, a One-Dimensional Lagrangian Material Response Code," Systems, Science and Software, SIR-2115, February 1974.

67. Lewis, B. and Friauf. J. B., "Explosions in Detonating Gas Mixtures, I, Calculation of Rates of Explosions in Mixtures of Hydrogen and Oxygen and the Influence of Rare Gases," J. Am. Chem. Soc., vol. 52, 1930, p. 3905.

APPENDIX A

EXPERIMENTAL FACILITY

Preliminary experimental work performed at Systems, Science and Software (Reference 2) examined the basic technological feasibility of a point-source dissemination, FAE airblast-simulation concept. For that purpose relatively coarse measurements were acceptable and an undeveloped test area adjacent to an existing bunker was used for the experiments. Although reasonably level, this test area had not been fully graded or surfaced. Strain gage transducers, buried directly in the soil were used to measure static pressures.

This simple arrangement proved adequate to establish concept feasibility. However, it was felt that additional refinements would be necessary in order to generate more conclusive data. A number of facility improvements were accordingly undertaken. The present facility is described in this section. The facility is located at the Green Farm Test Site which is managed by Systems, Science and Software for the Defense Nuclear Agency. Green Farm is a part of the Camp Elliot Naval Reservation near San Diego, California.

A.1 TEST PAD

A concrete test pad was built to provide a smooth blastwave path from the explosion center. This was intended to minimize measurement aberations that might otherwise result from wave reflections in the vicinity of pressure transducers.

A schematic of the pad layout is shown in Figure A-1 and a photograph appears in Figure A-2. The test area, which has the approximate overall dimensions of 37 m x 46 m (120 ft x 150 ft), is graded level, smoothed, and covered with a 2 1/2 cm (1 in.) layer of pea gravel. Two perpendicular steel-reinforced concrete legs extend continuously from an octagonal center area. The shorter of these two legs was included to permit blastwave symmetry testing.

Abrupt slopes surround the test area. However, it was possible to find an orientation for the concrete pad such that the arrival of reflected waves from these slopes would not interfere with measurements during a 20 ms minimum period following the arrival of the blast front at each location on the pad. This exceeds the longest positive phase duration of blastwaves at the experimental scale (1/4-ton nuclear equivalent).

The average thickness of the concrete pad is 15 cm (6 inches). A rectangular opening in the center area is provided for emplacement of the fuel dispenser in the ground. Since rain water runoff from adjacent hills could flood the test area, ditching is provided and a sump pump system has been installed.

Instrumentation troughs were installed at several locations along each runway, with approximate positional correspondence between the two legs. A cross-section of a trough is shown in Figure A-3 and a photograph is given in Figure A-4. In each trough, a 15.2 cm x 61 cm x 1.9. cm (6 in. x 24 in. x 3/4 in.) steel cover plate is securely fastened with six recessed machine screws. The cover plates were individually milled for each trough so that their upper surfaces are flush with the concrete. Side-on transducers and stagnation pressure probes (stings) are installed on these plates. A transducer location schedule is given in Table A.1.

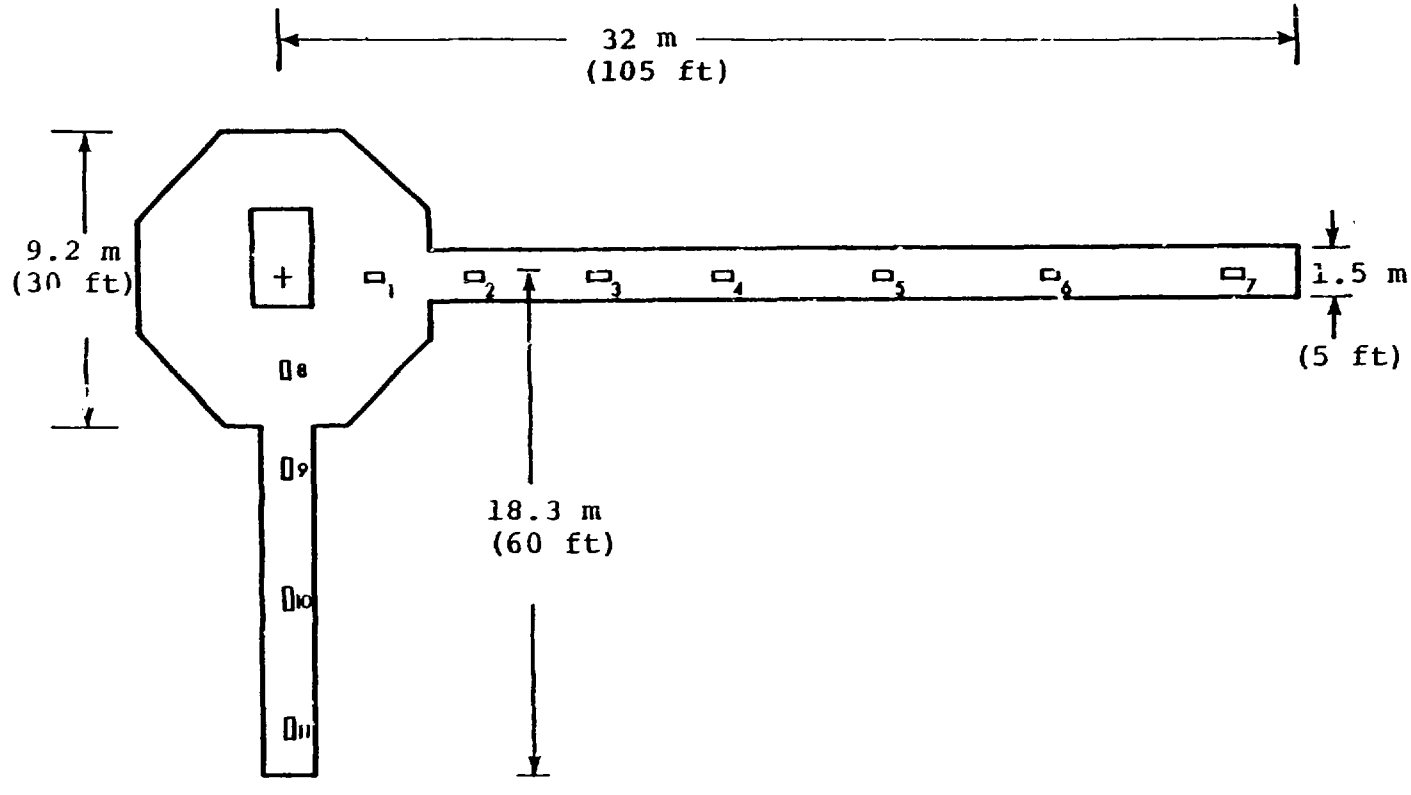

Figure A-1. Plan view of concrete FAE test pad showing instrumentation trough locations (see Table 1).

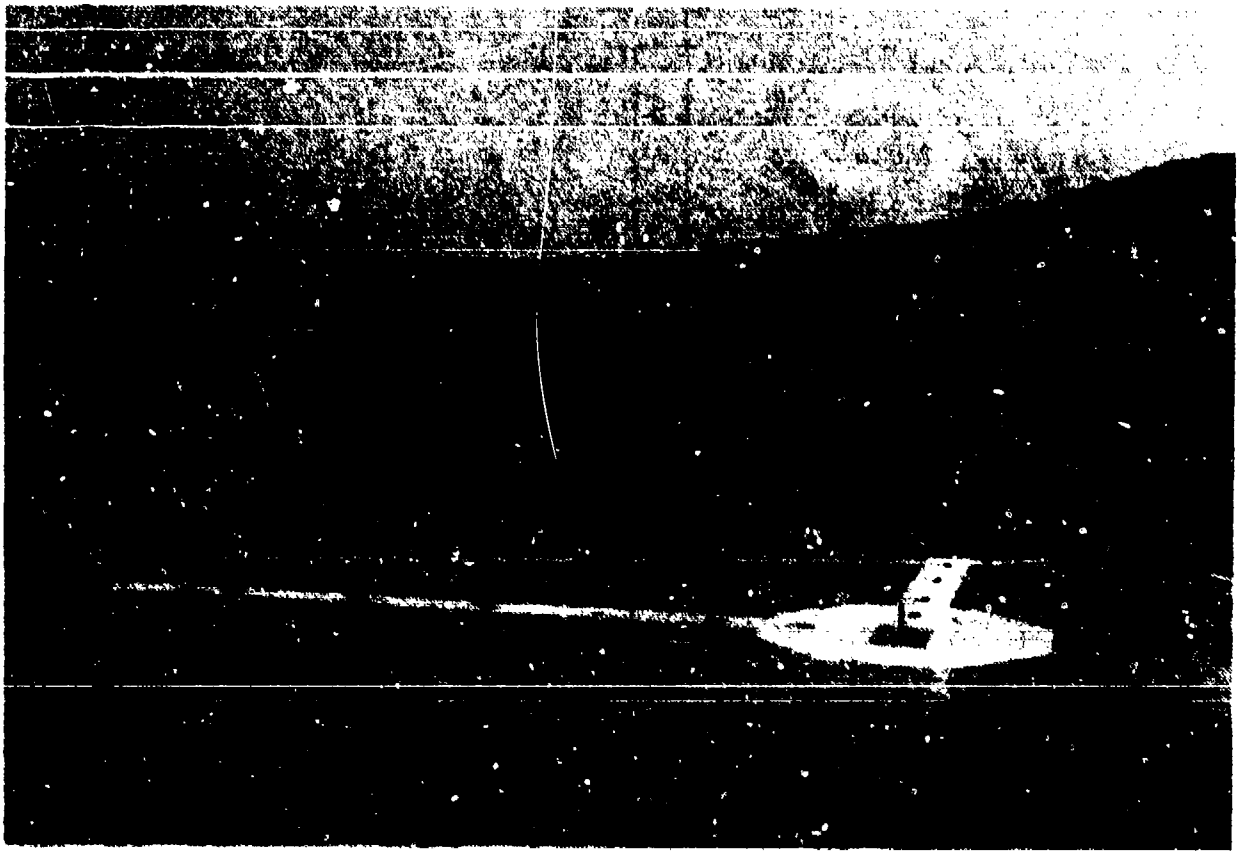

Figure A-2. Photograph of FAE test pad. Stagnation pressure gages are shown installed at four locations.

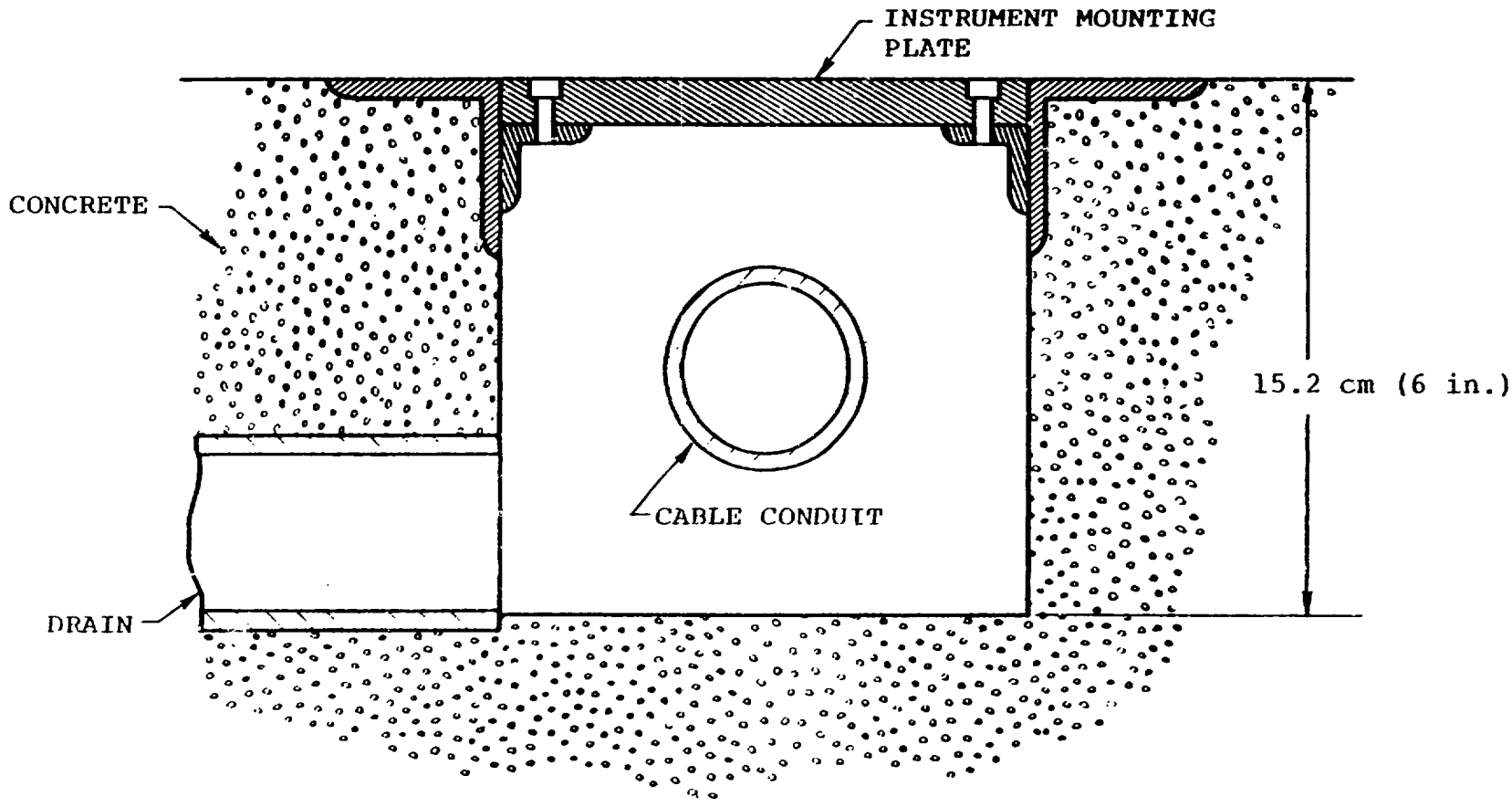

Figure A-3. Cross-sectional view of instrumentation trough.

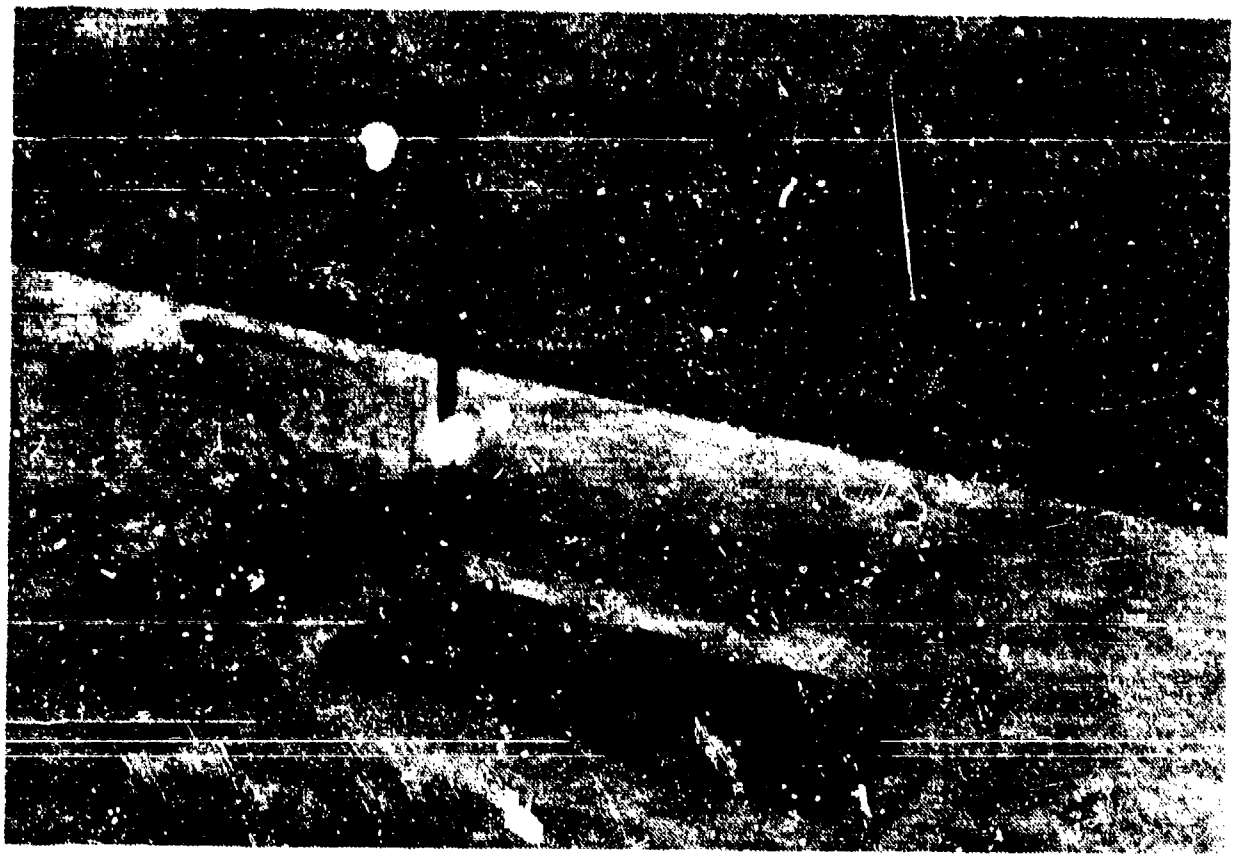

Figure A-4. Photograph of stagnation pressure sting mounted in instrumentation trough. A static pressure transducer is flush mounted directly below sting face.

Table A.1. Location of transducers on FAE test pad (see Figure A.1).

INSTRUMENTATION TROUGH NUMBER	DISTANCE FROM PAD CENTER (DISPENSER)	
	METERS	FEET
1	2.91	9.54
2	5.92	19.40
3	9.93	32.60
4	13.90	45.60
5	18.90	62.00
6	23.90	78.30
7	29.90	98.00
8	3.05	10.00
9	6.04	19.80
10	10.10	33.00
11	14.10	46.10

The troughs are joined with 5.1 cm (2 in.) ID conduit that is inlaid in the concrete runways. Coaxial instrumentation cables are permanently installed in the conduit, with two terminations (BNC-type) available at each trough. The troughs also have drain openings into the rain ditches.

Two additional conduit lines service the center pad area. These are buried in the ground adjacent to the longer runway. One of these carries the high voltage line used with the high explosive detonators (to initiate FAE clouds). The other is used to route auxiliary 110 VAC power, intercom, and control cables. A buried 0.7 MPa (100 psi) compressed air line also services the center pad area.

A.2 CONTROL AND INSTRUMENTATION

The event sequence during a particular test is controlled by a set of adjustable, precision time-delay relays. These are part of a control console that also includes provisions for low and high voltage detonator ignition, a low-voltage power supply, and a fiducial pulse generator. A photograph of this console is given in Figure A.5.

Instrumentation during an FAE test currently consists of static and stagnation pressure history measurements at various ranges from the cloud center. The static transducers are flush mounted in the trough cover plates. The stagnation pressure transducers are mounted in stings fabricated from 1.27 cm (1/2 in.) schedule 40 steel pipe. The stings are 76 cm (30 in.) high and have a 43 cm (14 in.) horizontal extension to the transducer face. The stagnation pressure transducers are located directly above companion static pressure transducers on each plate.

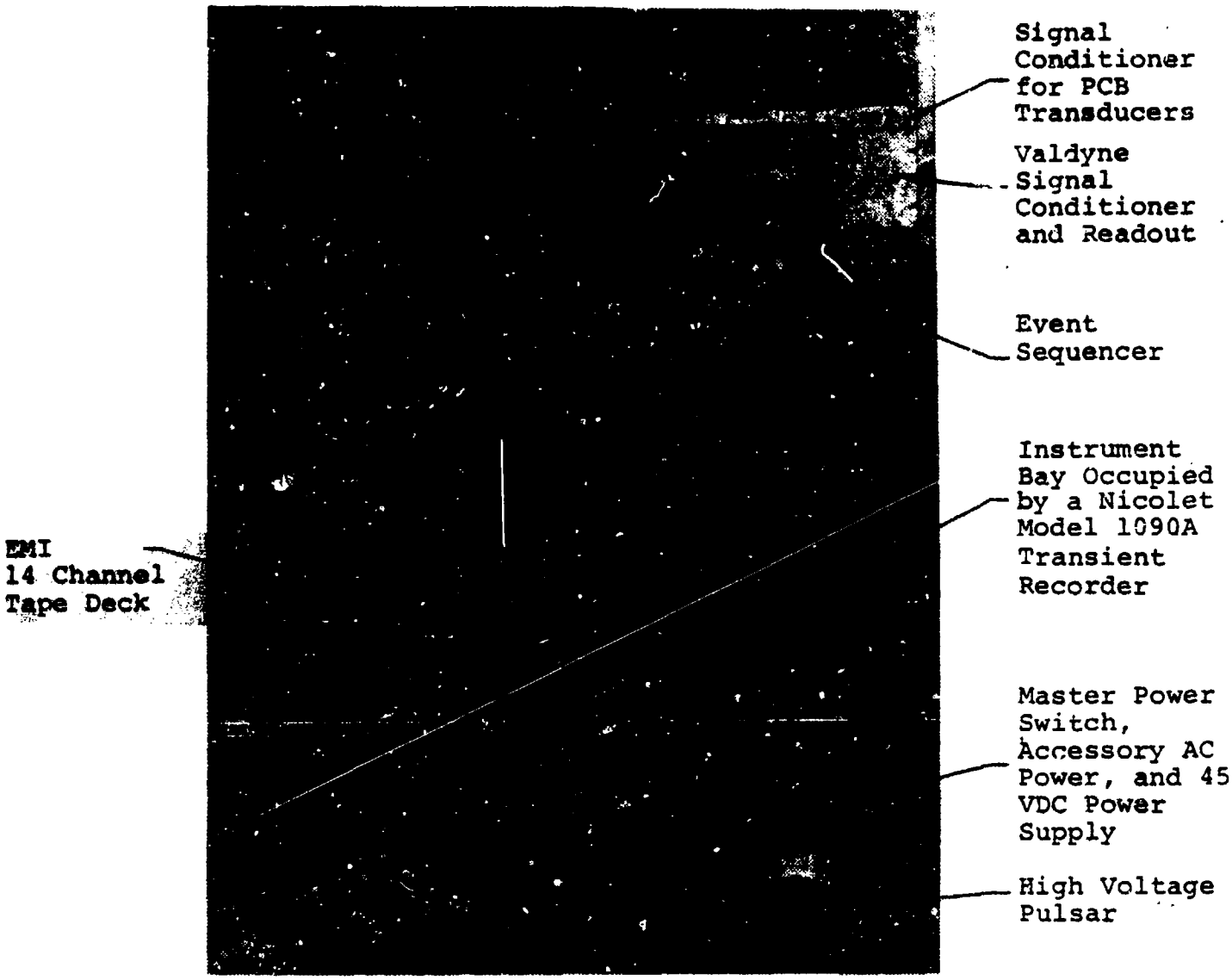

Figure A-5. Photograph of FAE control console.

The static pressure transducers presently in use are PCB Model 102A12. These are high frequency piezoelectric transducers with a built-in voltage-follower amplifier. The rise time of these transducers is ∿1 μs. Resonant ringing resulting from step pressure inputs is suppressed by built-in electronics. The head-on transducers have equivalent performance specifications. They were supplied by PCB as Model 113M49, including aerodynamic sting termination mounting. The transducers are powered by a modified twelve-channel, 20 MA constant current supply, PCB Model 483A. For low frequency pressure measurements a Validyne Model DP-15 variable reluctance transducer is used with a model CD12 indicating signal conditioner. The output from all transducers is recorded on an EMI Model SE7000A 14-channel tape deck, using Scotch 2.54 cm (1 in.) instrumentation tape. At a recording velocity of 305 cm/s (120 in./s), this instrument has a frequency response to 80 KHz and is the limiting component in the data acquisition chain. When faster response is needed signals are recorded individually on oscilloscopes or fast-transient recorders. All transducers are periodically tested in a shock tube to verify that they are operating properly.

A.3 PHOTOGRAPHY

In addition to pressure measurements, high speed films are taken during many of the tests. For framing rates to 400 fr/s a Milliken Model DBM-4A is used. Framing rates up to 7500 fr/s are obtainable with a Fastax Model WF45. However, this highest speed requires a 120 m (400 ft) length of film. For a 38 m (125 ft) roll of film, the framing rate reaches 3500 fr/s. Negative films are processed at the test site using a Cramer Mark I Cine Processer.

The filming of high-reach vertical jets has presented some difficulty when portions of the jets stand against a background of sky. Little success has been realized in obtaining high resolution films on cloudy or hazy days, in spite of many attempts with various film, filter, and polarizer combinations. However, when the sky is blue it has been found that satisfactory results can be achieved by using a film with extended red sensitivity in conjunction with a deep red filter. Polarizing filters were found not to be effective in this application. At present, Kodak RAR 2479 or 2475 film and a Tiffen #29 red filter are used. The film is processed for five minutes in Kodak D-19 developer at 25°C (75°F). Under these conditions an assumed effective film speed of ASA 300 gives the necessary contrast of the jets against the sky.

APPENDIX B

LINEAR DISPENSER GAS GENERATOR

The gas generator presently in service with the linear dispenser burns Hercules Red Dot smokeless powder in a 15 cm (6 in.) OD by 33 cm (13 in.) long breech. The size of the combustion chamber is about 5 cm (2 in.) ID by 18 cm (7 in.) long. An end cap or nut having a right-angle, 2.5 cm (1 in.) diameter nozzle passage directs the product gases downward into the dispenser free volume (the gas generator is mounted horizontally). The gas generator was fabricated from 4340 steel, heat treated to 1.17 GPa (170,000 psi) and Rockwell-C hardness of 38. An outline sketch is given in Figure B-1, and a photograph is provided in Figure B-2.

Smokeless powder was chosen over more exotic fast-burning, stable propellants because of the high cost of the latter. However, the low burning velocity of smokeless powder presented considerable difficulty. The burning velocity of Red Dot is given in Figure B-3. Even at 138 MPa (20,000 psi) is is only about 10 cm/s (4 in./s). This means that if the breech combustion chamber were filled with this powder and ignited at one end, combustion would be complete in about 1.75 seconds. Since the required fuel dispensing times are on the order of a few hundred milliseconds at most, this lengthy burning time could not be tolerated. Therefore, to enable the use of smokeless powder as a propellant, the breech is mounted horizontally and the combustion chamber is only partially filled with powder. The powder depth is then about 2.5 cm (1 in.). The igniter, which is mounted at one end, produces a flame that traverses the entire upper surface of the powder, initiating it in many locations simultaneously. A sketch of the igniter appears in Figure B-4. The depth of the powder then determines the burning time, reducing it by about an order of magnitude.

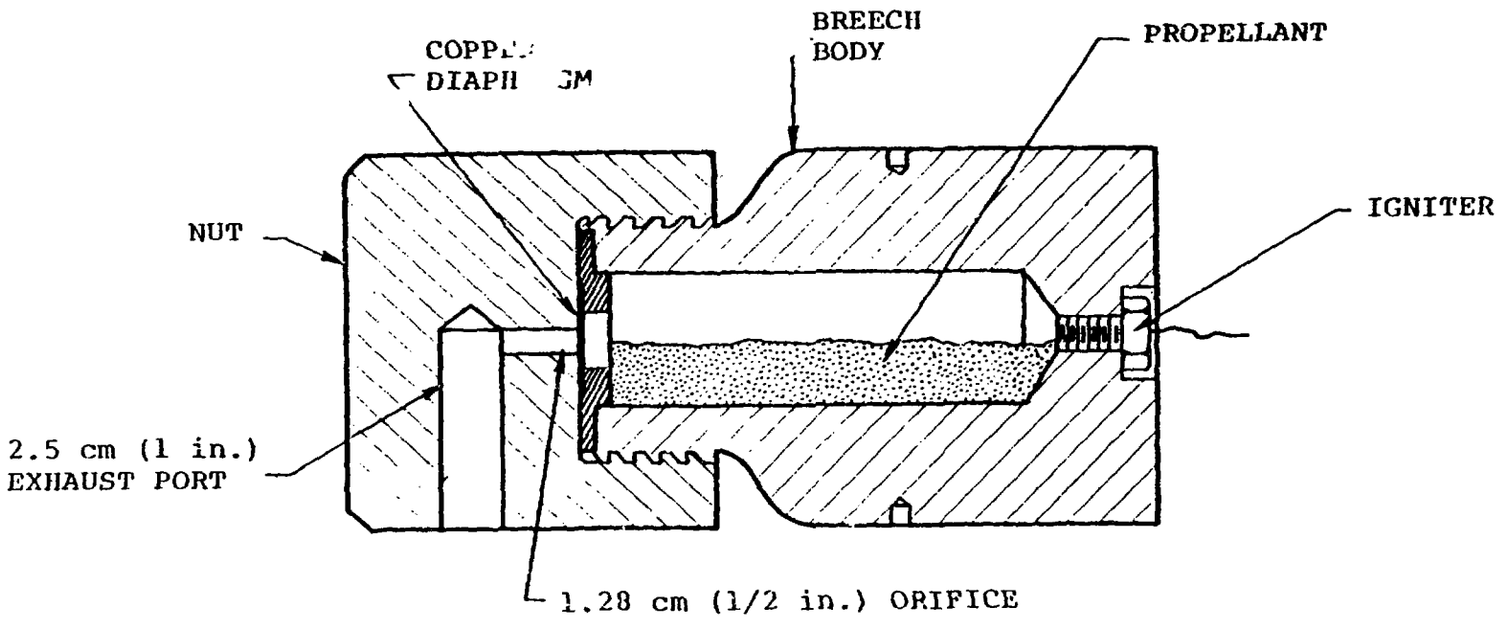

Figure B-1. Sketch of linear fuel dispenser gas generator (breech).

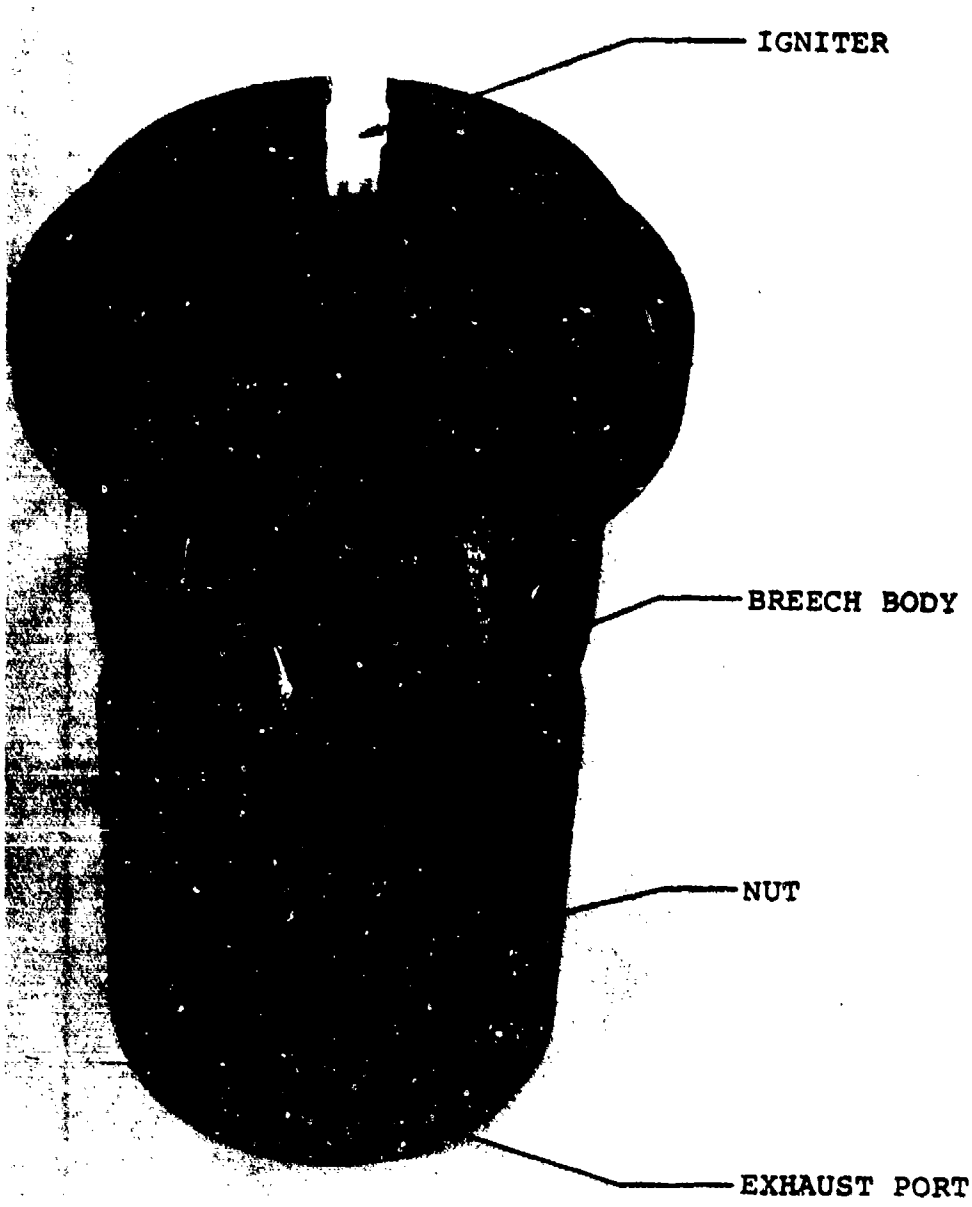

Figure B-2. Photograph of gas generator used with linear fuel dispenser.

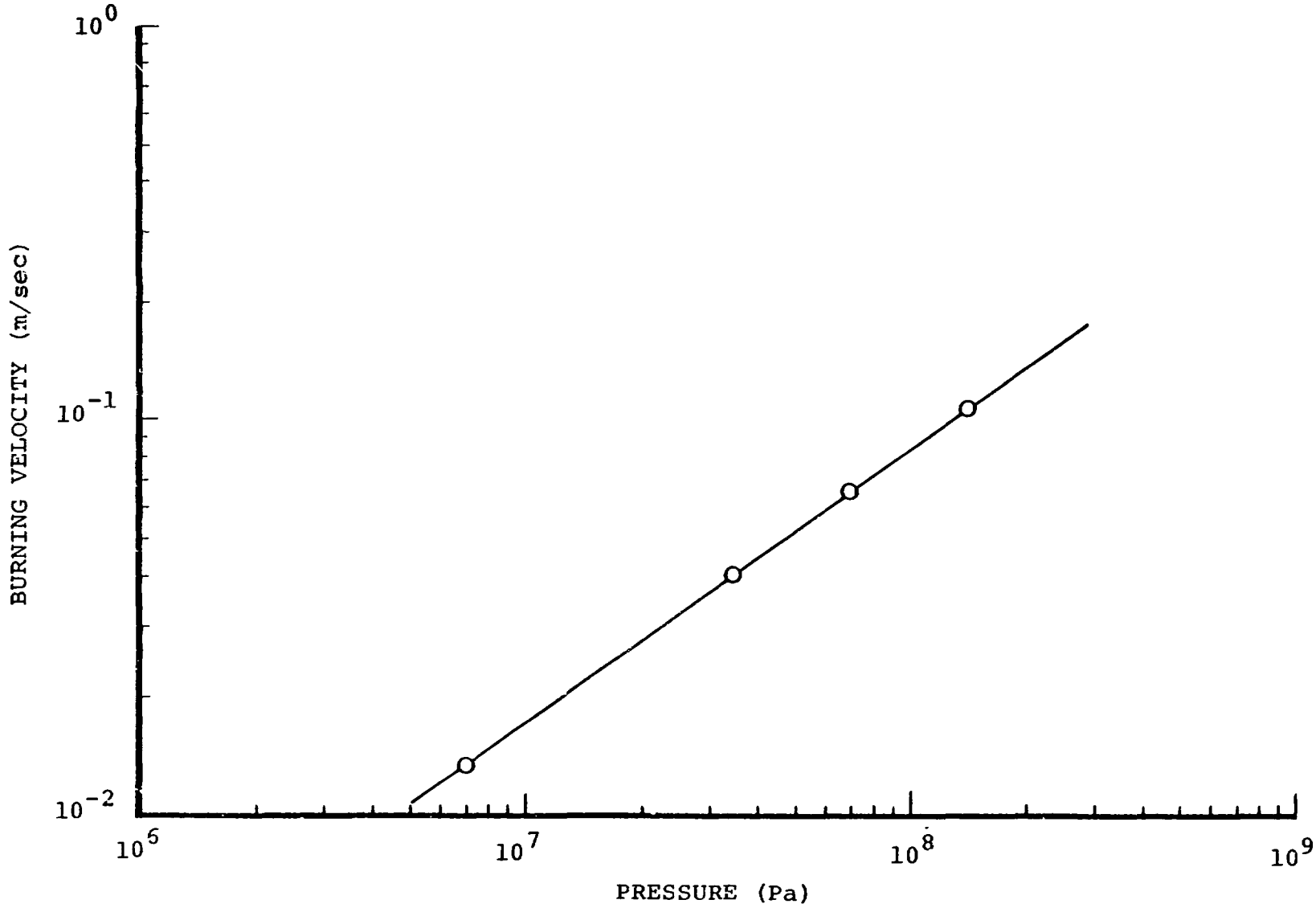

Figure B-3. Burning velocity of Red Dot smokeless powder (data supplied by Hercules, Inc.).

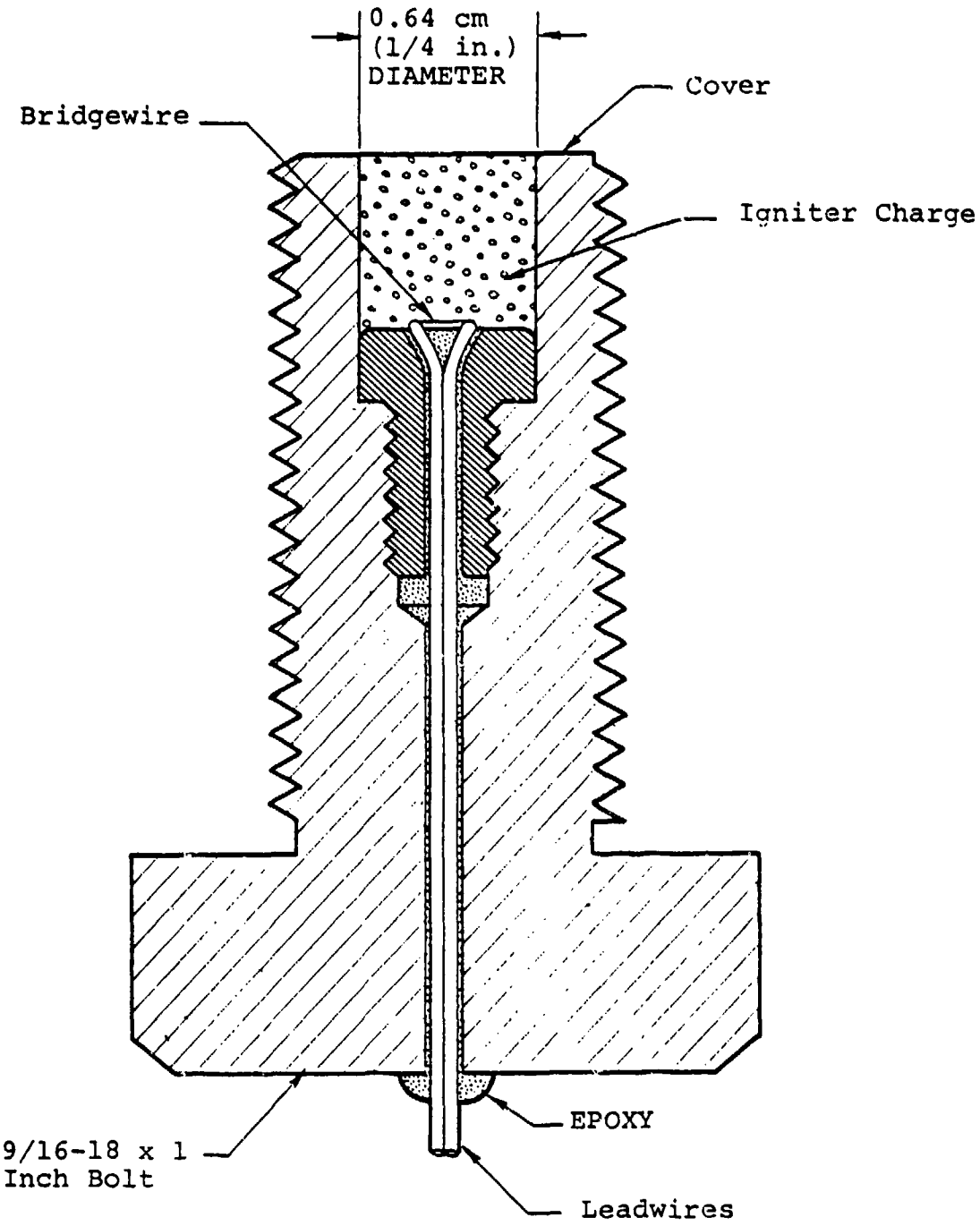

Figure B-4. Cross-sectional view of gas generator igniter.

In addition, the Red Dot products are prevented from immediately exhausting from the breech by a 1.8 mm (0.070 in.) thick copper diaphragm that separates the combustion chamber from the right-angle exhaust nozzle. The diaphragm is designed to burst after combustion is completed thus delaying the start of blowdown. The higher combustion pressures prior to blowdown also improve the combustion efficiency and produce a cleaner product exhaust.

The gas generator size was determined from a simple thermodynamic analysis for the quantity of smokeless powder required. All of the powder, mass m_B, is assumed to first burn to completion in the breech. At that time the temperature and pressure in the breech are T_B and P_B. The diaphragm then ruptures and the breech gases blow down into and mix uniformly with the air that is initially in the free volume tank (mass m_A). This process is adiabatic. The final mixture contained in both the breech and free volume has uniform composition, and the final pressure and temperature, P_2 and T_2, are uniform throughout. For the system comprising the breech plus free volume, the process is work-free so that the First Law is simply

$$E_2 = E_1$$

or

$$m_A e_{A_2} + m_B e_{B_2} = m_A e_{A_1} + m_B e_{B_1}$$

where e_i is the mass-specific internal energy of specie i and states 1 and 2 correspond to conditions just prior to and after breech blowdown. Thus

$$m_A(e_{A_2} - e_{A_1}) + m_B(e_{E_2} - e_{B_1}) = 0 \quad ,$$

or assuming that both the air and the breech gases behave as calorically perfect gases,

$$m_A C_{V_A} (T_2 - T_1) + m_{B_1} C_{V_B} (T_2 - T_{B_1}) = 0$$

where T_1 is the initial air temperature and C_{V_i} is the constant-volume specific heat of specie i. Solving for T_2 gives

$$T_2 = \frac{m_{B_1} C_{V_B} T_{B_1} + m_A C_{V_A} T_1}{m_{B_1} C_{V_B} + m_A C_{V_A}} \quad . \tag{B.1}$$

The final state equilibrium pressure is simply

$$P_2 = \frac{m_2 \bar{R} T_2}{W_2 V_{FV}} \tag{B.2}$$

where $m_2 = m_A + m_B$, and W_2 is the final mixture molecular weight. However, for the mixture,

$$\frac{m_2}{W_2} = \frac{m_A}{W_A} + \frac{m_{B_1}}{W_B} \quad . \tag{B.3}$$

Combining Eqs. (B.1)-(B.3) gives

$$P_2 = \left(\frac{m_A}{W_A} + \frac{m_{B_1}}{W_B}\right) \left(\frac{\bar{R}}{V_{FV}}\right) \left[\frac{m_{B_1} C_{V_B} T_{B_1} + m_A C_{V_A} T_1}{m_{B_1} C_{V_B} + m_A C_{V_A}}\right] \quad . \tag{B.4}$$

To calculate P_2, the breech temperature reached after combustion but before blowdown, T_{B_1}, must be known. This can be estimated by treating the combustion process as an external heat addition. The energy equation for that process is

$$E_{B_1} - E_{B_0} = Q \quad .$$

That is, the increase in energy inside the breech above its initial value equals the heat added. On a unit mass basis, this is approximated by

$$e_{B_1} - e_{B_0} = H_c$$

where H_c is the heat of combustion per unit mass of smokeless powder. Treating the combustion products as calorically perfect, this becomes

$$C_{V_B}(T_{B_1} - T_{B_0}) = H_c$$

or with $T_{B_0} = T_1$,

$$T_{B_1} = \frac{H_c}{C_{V_B}} + T_1 \quad . \tag{B.5}$$

The corresponding pressure in the breech at this time is

$$P_{B_1} = \frac{m_{B_1}\bar{R}T_{B_1}}{W_B V_B} \quad , \tag{B.6}$$

in which V_B is the volume of the breech combustion chamber. Finally, the mass of air in the free volume tank behind the piston, also required in Eq. (B.4), is simply

$$m_A = \frac{P_1 V_{FV} W_A}{\bar{R} T_1} \quad , \tag{B.7}$$

where P_1 is the initial free volume pressure.

During preliminary design of the dispenser, a maximum free volume of $V_{FV} = 0.085\ m^3$ ($3\ ft^3$) was assumed for these estimates. It was hoped to achieve a maximum initial pressure of $P_2 \doteq 2.8$ MPa (400 psig) in this volume. Using data for Red Dot powder supplied by the manufacturer ($H_c = 5.14 \times 10^6$ J/KG (2210 btu/lbm), $C_{V_B} = 1471$ J/(KG-°K) (0.352 btu/(lbm-°R)), and $M_B = 24.9$), the quantity of powder required according to Eq. (B.4) is $m_{B_1} = 0.16$ kg (0.35 lbm). This calculation assumes $T_1 = 300$°K (540°R), so that $T_{B_1} = 3794$°K (6830°R) from Eq. (B.5). The combustion chamber volume required for the breech was $V_B = m_{B_1}/\rho_B = 2.72 \times 10^{-4} m^3$ ($16.6\ in^3$), since the bulk density of Red Dot is $\rho_B = 5.88\ kg/m^3$ ($0.368\ lbm/ft^3$). The actual breech volume as built is approximately $3.6 \times 10^{-4} m^3$ ($22\ in^3$). The pressure developed in the breech with $m_{B_1} = 0.16$ kg (0.35 lbm) of powder is $P_{B_1} = 561$ MPa (81,400 psi), according to Eq. (B.6). Theoretical free volume pressures corresponding to other quantities of smokeless powder are plotted in Figure B-5.

The gas generator blowdown time after rupture of the copper diaphragm is a function of the exhaust nozzle orifice size. Since a maximum blowdown time of 10-20 ms was considered requisite for impulsive dispenser operation (relative to the shortest liquid dispensing times of about 100 ms), this would suggest as large an orifice as possible. However there was

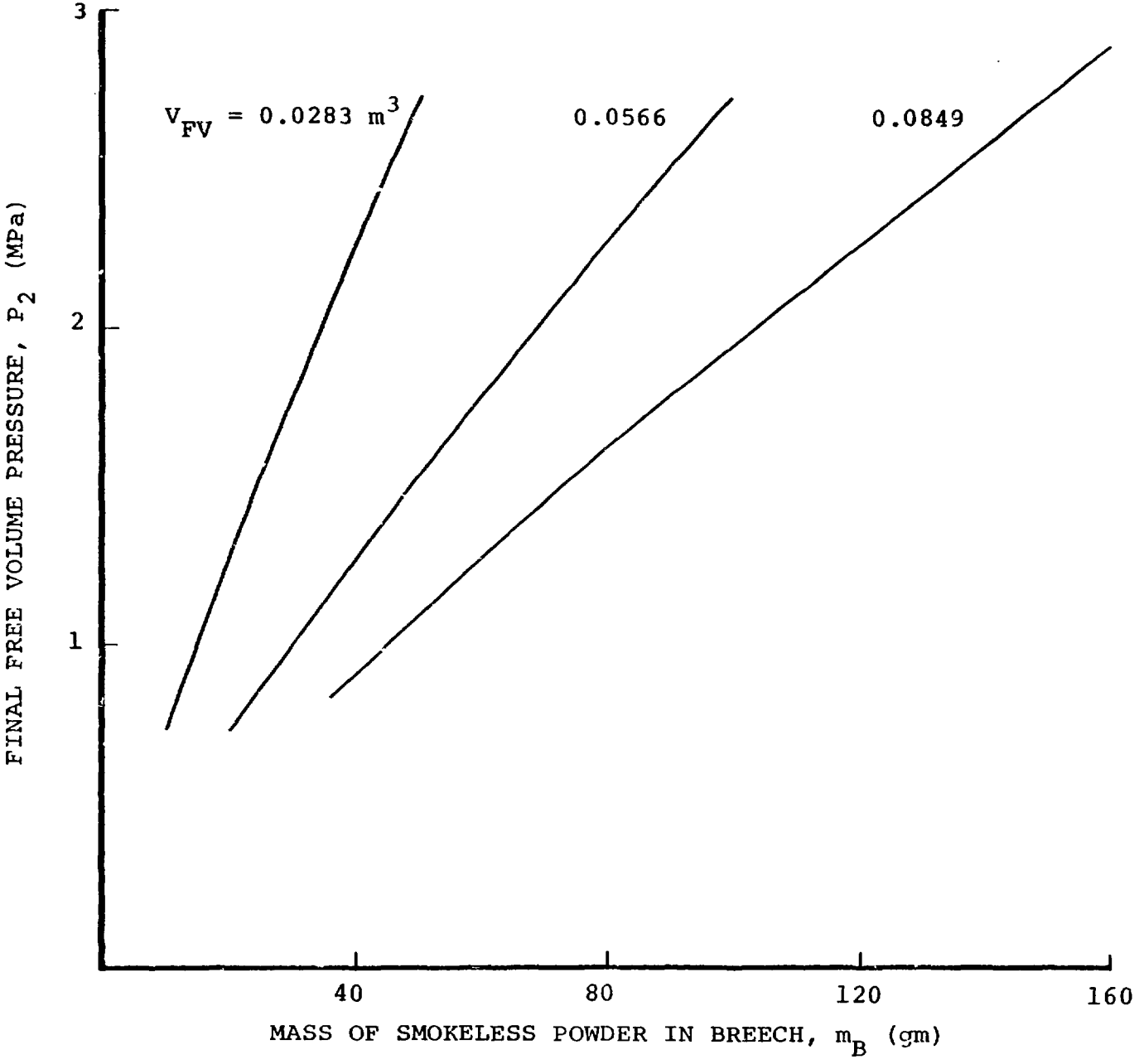

Figure B-5. Loss-free theoretical pressure developed in free volume tank after gas generator blowdown.

concern that with too large an orifice the blowdown times might be so short as to produce blastwaves of damaging strength inside the free volume tank. It was therefore decided to limit the blowdown rate.

To calculate the required orifice size, the gas-generator blowdown was assumed to be isentropic and quasi-steady. For a control volume that coincides with the gas generator surface, conservation of mass is

$$\frac{dm_B}{dt} = -\dot{m} \tag{B.8}$$

where the mass flow through the orifice of area A* is

$$\dot{m} = P_B A^* \left(\frac{\gamma_B W_B}{\bar{R} T_B}\right)^{1/2} \left(\frac{2}{\gamma_B + 1}\right)^{\frac{\gamma_B + 1}{2(\gamma_B - 1)}} , \tag{B.9}$$

and γ_B is the ratio of specific heats of the combustion product gases. Eq. (B.9) assumes that the orifice is choked. The breech pressure at any time during blowdown is related to the instantaneous temperature and mass of product gases by

$$P_B = \frac{m_B \bar{R} T_B}{\bar{W}_B V_B} . \tag{B.10}$$

In addition, conservation of energy can be expressed by

$$\frac{dE_B}{dt} = -\dot{m}(h^* + u^{*2}/2)$$

where h* and u* are the enthalpy and velocity of the products when they reach the orifice. Since $E_B = m_B e_B$, and since

$$h^* + u^{*2}/2 = h_B \quad ,$$

where h_B is the enthalpy inside the combustion chamber, the energy equation can be written as

$$m_B \frac{de_B}{dt} + e_B \frac{dm_B}{dt} = -\dot{m} h_B \quad .$$

Making use of Eq. (B.8), and with $h_B = e_B + P_B v_B$ (where v_B is the specific volume of the breech gases), this last equation can be written as

$$m_B \frac{de_B}{dt} = -\dot{m} P_B v_B \quad .$$

Finally, assuming a calorically perfect gas so that

$$\frac{de_B}{dt} = C_{v_B} \frac{dT_B}{dt} \quad ,$$

and using $P_B v_B = R_B T_B$, the energy equation can be written as

$$\frac{dT_B}{dt} = -\frac{\dot{m}_B}{m_B} (\gamma_B - 1) T_B \quad . \qquad \text{(B.11)}$$

Equations (B.8)-(B.11) can be integrated analytically. The solution for the breech pressure as a function of time was found to be

$$P_B = P_{B_1}(1 + Ct)^{-\frac{2\gamma_B}{\gamma_B - 1}} \qquad (B.12)$$

where

$$C \equiv \left(\frac{\gamma_B - 1}{2}\right) \frac{A^*}{V_B} \left(\frac{\gamma_B \bar{R} T_{B_1}}{W_B}\right)^{1/2} \left(\frac{2}{\gamma_B + 1}\right)^{\frac{\gamma_B + 1}{2(\gamma_B - 1)}},$$

and P_{B_1}, T_{B_1} are values at t = 0 (following combustion but just prior to blowdown).

Estimates of the nozzle orifice size required for a specified blowdown time were obtained by solving Eq. (B.12) for A* in terms of P_B and t. The blowdown time was defined as the time at which $P_B = P_2$. In fact this equality occurs only as t approaches infinity. Eq. (B.9) and therefore Eq. (B.12) become invalid before $P_B = P_2$ because the orifice becomes unchoked. However, extrapolation of Eq. (B.12) to $P_B = P_2$ does provide a characteristic time. The values of P_{B_1} and m_{B_1} are related to P_2 and V_{FV}, according to Eq. (B.4) and (B.6). With T_{B_1} computed from Eq. (B.5) and with $\gamma_B = 1.23$, the required nozzle orifice diameter for 20 ms blowdown time was calculated as a function of P_2 and V_{FV}. The result appears in Figure B-6. On the basis of these calculations, a gas generator exit orifice diameter of 13 mm (0.5 in.) was selected.

No attempt was made to measure pressures developed inside the breech. However, an approximate measure of the blowdown time was obtained by observing the gas generator exhaust with a photoelectric cell. The exhaust gases remained luminous for about 18 ms in most tests, in reasonable agreement with the predicted value of blowdown time.

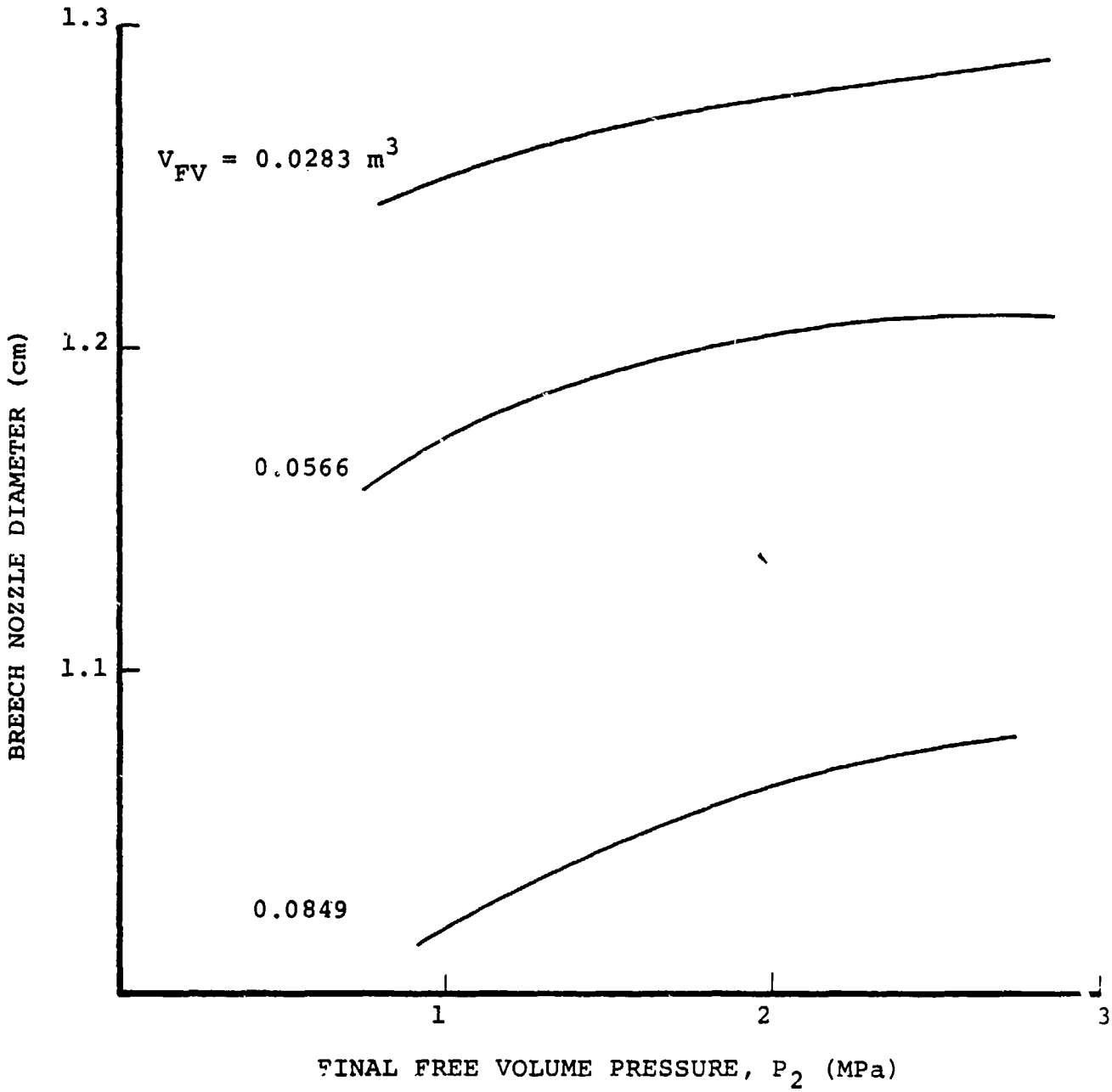

Figure B-6. Required gas generator orifice as a function of free volume and pressure in the free volume, for 20 ms blowdown time.

While the gas generator performance was encouraging in this respect, it was found to be marginal in others. One minor difficulty resulted from the absence of high pressure seals between the breech body and the orifice retainer nut. When stainless steel and aluminum diaphragms were tested initially, their vapor condensed while leaking between the threads of the nut. The gas generator was then very difficult to disassemble. This particular problem was eliminated simply by changing to copper diaphragms.

A more serious problem was experienced during operation of the gas generator with a full load of Red Dot powder (m_{B_1} = 0.16 kg (0.352 lbm)). On separate occasions both the nut and the breech body failed and were damaged beyond repair. There has been some speculation as to whether in these cases the smokeless powder may have detonated, although the deflagration to detonation transition distance for Red Dot powder is much greater than the 18 cm (7 in.) chamber length, according to the powder manufacturer. In any case, the gas generator was redesigned to eliminate all sharp corners before being rebuilt. (The current version is shown in Figure B-2.) Subsequent operation has also been limited to m_B = 0.10 kg (0.22 lbm) of smokeless powder.

The most troublesome problem with this type of gas generator is a consequence of the relatively slow burning rate of smokeless powder. The total burning time in the breech is estimated as 250 ms. However luminous exhaust is detected beginning at only 80 ms after ignition (which indicates diaphragm rupture), and the blowdown time is then about 20 ms. Presumably a substantial amount of powder is expelled in an unburned or partially burned condition. The result is that pressure levels actually reached in the free volume tank are about 20-40% below the predicted values.

DISTRIBUTION LIST

DEPARTMENT OF DEFENSE

Assistant to the Secretary of Defense
Atomic Energy
ATTN: Executive Assistant

Defense Intelligence Agency
ATTN: DT-2
ATTN: DB-4C, E. O'Farrell
ATTN: DT-1C

Defense Nuclear Agency
ATTN: SPTD
2 cy ATTN: SPSS
4 cy ATTN: TITL

Defense Technical Information Center
12 cy ATTN: DD

Department of Defense Explo Safety Board
ATTN: Chairman

Field Command
Defense Nuclear Agency, Det 1
Lawrence Livermore Lab
ATTN: FC-1

Field Command
Defense Nuclear Agency
ATTN: FCTT, G. Ganong
ATTN: FCTXE
ATTN: FCTT, W. Summa
ATTN: FCT
ATTN: FCTX
ATTN: FCTT
ATTN: FCPR

Field Command Test Directorate
ATTN: FCTC

Under Secy of Def for Rsch & Engrg
ATTN: Strategic & Space Sys, OS

DEPARTMENT OF THE ARMY

Chief of Engineers
ATTN: DAEN-MPE-T
ATTN: DAEN-RDL

Harry Diamond Laboratories
ATTN: DELHD-NW-P
ATTN: 00100 Commander/Tech Dir/Div Dir

US Army Ballistic Research Labs
ATTN: DRDAR-BLT, W. Taylor
ATTN: DRDAR-BLT, J. Keefer
ATTN: DRDAR-TSB-S

US Army Concepts Analysis Agency
ATTN: CSSA-ADL

US Army Engr Waterways Exper Station
ATTN: WESSA, W. Flathau
ATTN: WESSD, J. Jackson
ATTN: Library

DEPARTMENT OF THE ARMY (Continued)

US Army Material & Mechanics Rsch Ctr
ATTN: Technical Library

US Army Materiel Dev & Readiness Cmd
ATTN: DRXAM-TL

US Army Mobility Equip R&D Cmd
ATTN: DRDME-WC

US Army Nuclear & Chemical Agency
ATTN: Library

USA Missile Command
ATTN: Documents Section

DEPARTMENT OF THE NAVY

David Taylor Naval Ship R&D Ctr
ATTN: Code L42-3, Library
ATTN: Code 1844
ATTN: Code 1770
ATTN: Code 17
2 cy ATTN: 1740.5, B. Whang

Naval Civil Engineering Laboratory
ATTN: Code L51, J. Crawford
ATTN: Code L51

Naval Facilities Engineering Command
ATTN: Code 04B

Naval Material Command
ATTN: MAT 08T-22

Naval Research Laboratory
ATTN: Code 2627, Tech Lib
ATTN: Code 8440, G. O'Hara

Naval Sea Systems Command
ATTN: SEA-55X
ATTN: SEA-09G53, Lib
ATTN: SEA-0351

Naval Surface Weapons Center
ATTN: Code R15
ATTN: Code R14
ATTN: Code F31
ATTN: Code R40, I. Blatstein

Naval Surface Weapons Center
ATTN: Tech Library & Info Svcs Br

Ofc of the Deputy Chief of Naval Ops
ATTN: NOP 981
ATTN: OP 03EG

Office of Naval Research
ATTN: Code 474, N. Perrone

DEPARTMENT OF THE AIR FORCE

Air Force
ATTN: INT

DEPARTMENT OF THE AIR FORCE (Continued)

Air Force Geophysics Laboratory
ATTN: LWH, H. Ossing

Air Force Institute of Technology
ATTN: Library

Air Force Systems Command
ATTN: DLW

Air Force Weapons Laboratory
ATTN: NTE, M. Plamondon
ATTN: NTED, E. Seusy
ATTN: NTES
ATTN: SUL
ATTN: NTEO

Air University Library
ATTN: AUL-LSE

Ballistic Missile Office
ATTN: ENBF, D. Gage

Deputy Chief of Staff
Research, Development, & Acq
ATTN: AFRDQI

Strategic Air Command
ATTN: NRI-STINFO Library

DEPARTMENT OF ENERGY

Albuquerque Operations Office
ATTN: CTID
ATTN: D. Richmond

Office of Military Application
ATTN: OMA/RD&T

Nevada Operations Office
ATTN: Doc Con for Technical Library

OTHER GOVERNMENT AGENCY

Central Intelligence Agency
ATTN: OSWR/NED

NATO

NATO School, SHAPE
ATTN: US Documents Officer

DEPARTMENT OF ENERGY CONTRACTORS

University of California
Lawrence Livermore National Lab
ATTN: Technical Info Dept Library

Los Alamos National Laboratory
ATTN: J. Hopkins
ATTN: Reports Library

Sandia National Lab
ATTN: Tech Lib 3141

Sandia National Labs, Livermore
ATTN: Library & Security Classification Div

DEPARTMENT OF DEFENSE CONTRACTORS

Aerospace Corp
ATTN: Technical Information Services

Applied Research Associates, Inc
ATTN: N. Higgins
ATTN: J. Bratton

Applied Research Associates, Inc
ATTN: J. Shinn

Applied Research Associates, Inc
ATTN: D. Piepenburg

Applied Research Associates, Inc
ATTN: B. Frank

BDM Corp
ATTN: Corporate Library

Boeing Co
ATTN: Aerospace Library

California Research & Technology, Inc
ATTN: M. Rosenblatt
ATTN: K. Kreyenhagen

California Research & Technology, Inc
ATTN: D. Orphal

Cushing Associates
ATTN: V. Cushing

EG&G Wash Analytical Svcs Ctr, Inc
ATTN: Library

Electro-Mech Systems, Inc
ATTN: L. Piper

Electro-Mech Systems, Inc
ATTN: R. Shunk

Geo Centers, Inc
ATTN: E. Marram

H-Tech Labs, Inc
2 cy ATTN: B. Hartenbaum

IIT Research Institute
ATTN: Documents Library

Institute for Defense Analyses
ATTN: Classified Library

JAYCOR
ATTN: Library

Kaman Sciences Corp
ATTN: Library

Kaman Sciences Corp
ATTN: D. Sachs

Kaman Tempo
ATTN: DASIAC

DEPARTMENT OF DEFENSE CONTRACTORS (Continued)

Lockheed Missiles & Space Co, Inc
ATTN: S. Taimuty Dept 81-74/154
ATTN: TIC-Library

Martin Marietta Denver Aerospace
ATTN: D-6074, G. Freyer

Mitre Corp
ATTN: MS E190

National Technical Systems
ATTN: P. Lieberman

University of New Mexico
ATTN: N. Baum
ATTN: CERF, G. Leigh

Pacific-Sierra Research Corp
ATTN: H. Brode, Chairman SAGE

Pacifica Technology
ATTN: G. Kent

Physics Applications, Inc
ATTN: F. Ford

Physics International Co
ATTN: F. Sauer
ATTN: Technical Library
ATTN: E. Moore

R&D Associates
ATTN: Technical Information Center
ATTN: R. Port
ATTN: J. Lewis

S-CUBED
ATTN: D. Grine
ATTN: Library
4 cy ATTN: R. Sedgwick
4 cy ATTN: T. Pierce

Science Applications, Inc
ATTN: J. Dishon

DEPARTMENT OF DEFENSE CONTRACTORS (Continued)

Science Applications, Inc
ATTN: Technical Library

Science Applications, Inc
ATTN: M. Knasel
ATTN: W. Layson
ATTN: J. Cockayne

Southwest Research Institute
ATTN: A. Wenzel
ATTN: W. Baker

SRI International
ATTN: J. Colton
ATTN: G. Abrahamson

Structural Mechanics Associates, Inc
ATTN: R. Kennedy

Teledyne Brown Engineering
ATTN: F. Leopard
ATTN: J. Ford
ATTN: D. Ormond

TRW Electronics & Defense Sector
ATTN: D. Baer
ATTN: Technical Information Center
2 cy ATTN: N. Lipner

TRW Electronics & Defense Sector
ATTN: E. Wong
ATTN: P. Dai

Weidlinger Assoc, Consulting Engrg
ATTN: M. Baron

Weidlinger Assoc, Consulting Engrg
ATTN: A. Misovec

Weidlinger Associates
ATTN: J. Isenberg

Lockheed Missiles & Space Co, Inc
ATTN: Technical Library
ATTN: T. Geers